

AFRL-SN-HS-TR-2006-0047 Volume II

**PROCEEDINGS OF THE 2006 ANTENNA APPLICATIONS SYMPOSIUM
Volume II of II**

Daniel Schaubert et al.

**University of Massachusetts at Amherst
Electrical and Computer Engineering
100 Natural Resources Road
Amherst MA 01003**

Final Report

26 February 2007

APPROVED FOR PUBLIC RELEASE; DISTRIBUTION UNLIMITED



**AIR FORCE RESEARCH LABORATORY
Sensors Directorate
Electromagnetics Technology Division
80 Scott Drive
Hanscom AFB MA 01731-2909**

NOTICE AND SIGNATURE PAGE

Using Government drawings, specifications, or other data included in this document for any purpose other than Government procurement does not in any way obligate the U.S. Government. The fact that the Government formulated or supplied the drawings, specifications, or other data does not license the holder or any other person or corporation; or convey any rights or permission to manufacture, use, or sell any patented invention that may relate to them.

This report was cleared for public release by the Electronic Systems Center Public Affairs Office for the Air Force Research Laboratory Electromagnetic Technology Division and is available to the general public, including foreign nationals. Copies may be obtained from the Defense Technical Information Center (DTIC) (<http://www.dtic.mil>).

AFRL-SN-HS-TR-2006-0047 HAS BEEN REVIEWED AND IS APPROVED FOR PUBLICATION IN ACCORDANCE WITH ASSIGNED DISTRIBUTION STATEMENT.

//signature//

HARVEY TOBIN
Monitor

//signature//

DAVID D. CURTIS
Acting Chief, Antenna Technology Branch

//signature//

MICHAEL N. ALEXANDER
Technical Advisor
Electromagnetic Technology Division

This report is published in the interest of scientific and technical information exchange, and its publication does not constitute the Government's approval or disapproval of its ideas or findings.

REPORT DOCUMENTATION PAGE

*Form Approved
OMB No. 0704-0188*

Public reporting burden for this collection of information is estimated to average 1 hour per response, including the time for reviewing instructions, searching existing data sources, gathering and maintaining the data needed, and completing and reviewing this collection of information. Send comments regarding this burden estimate or any other aspect of this collection of information, including suggestions for reducing this burden to Department of Defense, Washington Headquarters Services, Directorate for Information Operations and Reports (0704-0188), 1215 Jefferson Davis Highway, Suite 1204, Arlington, VA 22202-4302. Respondents should be aware that notwithstanding any other provision of law, no person shall be subject to any penalty for failing to comply with a collection of information if it does not display a currently valid OMB control number. **PLEASE DO NOT RETURN YOUR FORM TO THE ABOVE ADDRESS.**

1. REPORT DATE (DD-MM-YYYY) 26-02-2007		2. REPORT TYPE FINAL REPORT		3. DATES COVERED (From - To) 20 Sep 2006 - 22Sep 2006	
4. TITLE AND SUBTITLE Proceedings of the 2006 Antenna Applications Symposium, Volume II				5a. CONTRACT NUMBER F33615-02-D-1283	
				5b. GRANT NUMBER	
				5c. PROGRAM ELEMENT NUMBER	
6. AUTHOR(S) Daniel Schaubert et al.				5d. PROJECT NUMBER	
				5e. TASK NUMBER	
				5f. WORK UNIT NUMBER	
7. PERFORMING ORGANIZATION NAME(S) AND ADDRESS(ES) University of Massachusetts Amherst Electrical and Computer Engineering 100 Natural Resources Road Amherst, MA 01003		8. PERFORMING ORGANIZATION REPORT			
9. SPONSORING / MONITORING AGENCY NAME(S) AND ADDRESS(ES) Electromagnetics Technology Division Sensors Directorate Air Force Research Laboratory 80 Scott Drive Hanscom AFB MA 01731-2909		10. SPONSOR/MONITOR'S ACRONYM(S) AFRL-SN-HS			
		11. SPONSOR/MONITOR'S REPORT NUMBER(S) AFRL-SN-HS-TR-2006-0047			
12. DISTRIBUTION / AVAILABILITY STATEMENT APPROVED FOR PUBLIC RELEASE; DISTRIBUTION UNLIMITED; ESC 07-0269, 22 FEB 2007					
13. SUPPLEMENTARY NOTES Volume I contains pages 1 - 239 Volume II contains pages 240 - 494					
14. ABSTRACT The Proceedings of the 2006 Antenna Applications Symposium is a collection of state-of-the art papers relating to antenna arrays, millimeter wave antennas, simulation and measurement of antennas, integrated antennas, and antenna bandwidth and radiation improvements.					
15. SUBJECT TERMS Antennas, phased arrays, digital beamforming, millimeter waves, antenna measurements					
16. SECURITY CLASSIFICATION OF:		17. LIMITATION OF ABSTRACT UU	18. NUMBER OF PAGES 267	19a. NAME OF RESPONSIBLE PERSON Harvey Tobin	
a. REPORT Unclassified	b. ABSTRACT Unclassified			c. THIS PAGE Unclassified	19b. TELEPHONE NUMBER (include area code) N/A

TABLE OF CONTENTS

2006 ANTENNA APPLICATIONS SYMPOSIUM (Volume I & II), 20 - 22 September 2006, Monticello, Illinois

Wideband Printed Antenna for Tactical Terrestrial Vehicles R.B. Waterhouse and D. Novak	1
Some Matched Resonators with Applications to Small Antennas Paul E. Mayes and Paul W. Klock	23
Planar and Conical Projections of Multifunctional Two-Arm Sinuous Antennas Michael C. Buck and Dejan S. Filipovic	37
Some Considerations for Compact Resonant UHF PIFAs Sergey N. Makarov, Shashank D. Kulkarni and Reinhold Ludwig	56
UHF Band RFID Tag Antenna with a Symmetric Structure Mountable on Metallic Platforms Sung-Joo Kim, Hanphil Rhyu, Seung-Hoon Baek, Frances J. Harackiewicz and Byungje Lee	68
Small Antennas and Arrays for Wireless Communications Yuanxun Ethan Wang	80
Development of a Slotted Substrate Integrated Waveguide (SIW) Array Antennas for Mobile DBS Applications Songnan Yang, Aly E. Fathy and Shady H. Suleiman	103
Direct Modulation of an L-Band Microstrip Patch Antenna Using Integrated Pin Diodes Steven D. Keller, W. Devereux Palmer and William T. Joines	132
Tri-band Reconfigurable Antenna for Active RFID Wonbin Hong, Nader Behdad and Kamal Sarabandi	141
A Wide Band, Low Profile Array of End Loaded Dipoles with Dielectric Slab Compensation Ben A. Munk	149

On the Performance Trade-Offs Associated with Modular Element of Single- and Dual-Polarized DmBAVA	166
M.W. Elsallal and D.H. Schaubert	
New Results Using Polyomino-Tiled Subarrays for Time-Delay Control of Wideband Arrays	188
R.J. Mailloux, S.G. Santarelli and T.M. Roberts	
High Efficiency SATCOM and MILSTAR Solid State Power Amplifiers	203
Paul J. Oleski and Sarjit S. Bharj	
A Constrained Pattern Synthesis Technique for a Circular IFF Array Antenna	210
Matthew S. Lasater and Herbert M. Aumann	
Generalized CoCo Antennas	240
Branislav M. Notaros, Miroslav Djordjevic and Zoya Popovic	
A Model for MEMS-Based Perturbations in Open (Leaky) Waveguide Structures: Application to the Trough Waveguide Antenna	258
G.H. Huff and J.T. Bernhard	
On Losses Due to an Air Gap and Lateral Displacements in a Junction of Two Collinear Rectangular Waveguides	272
Jari Paunonen	
Time/Space-Probing Interferometer for Plasma Diagnostics	281
V.A. Manasson, A. Avakian. A. Brailovsky, W. Gekelman, A. Gigliotti, L. Giubbolini, I. Gordion, M. Felman, V. Khodos, V. Litvinov, P. Pribyl and L. Sadovnik	
Near Field Target DOA Simulation Using Antenna Arrays	294
Louis Botha and Jacques Cilliers	
Wideband Folded Horn Antenna Array for 20kV Impulse	314
Jin-Seong Lee, Jin-Woo Park, Byungwoon Jung, Frances J. Harackiewicz and Byungje Lee	
Development of Conformal Antenna Materials Technology to Enable ‘Paint-On’ Antenna Arrays for Air Force Aerospace Applications	330
Thomas G. Campbell, C.J. Reddy and Robert C. Boyd	

Design, Analysis, and Experimental Test Results of a Conformal Phased Array Painted on a Composite Wing	358
M.C. Bailey, C.B. Ravipati, T.G. Campbell and C.J. Reddy	
Impedance Bandwidth of a Wire Dipole with the Split-Coaxial Balun	388
Sergey N. Makarov and Reinhold Ludwig	
Progress in the Design of a Small Wideband Antenna	411
Steven R. Best	
The Multi-Lens Array Architecture	429
Danh Luu	
Surface-Micromachined Ka-Band Phase-Array Antenna	455
Milan Lukic, Daniel Fontaine, Christopher Nichols and Dejan Filipovic	
Design and Development of Aircraft Antenna Interface Adapters – Conformal Couplers for USM-464 (EW) Test Applications	470
Thomas G. Campbell, M.C. Bailey and C.J. Reddy	

Identifiers for Proceedings of Symposia
The USAF Antenna Research and Development Program

Year	Symposium No.	Identifier
1951	First	
1952	Second	ADB870006
1953	Third	ADB283180
1954	Fourth	AD63139
1955	Fifth	AD90397
1956	Sixth	AD114702
1957	Seventh	AD138500
1958	Eighth	AD301151
1959	Ninth	AD314721
1960	Tenth	AD244388 (Vol. 1) AD319613 (Vol. 2)
1961	Eleventh	AD669109 (Vol. 1) AD326549 (Vol. 2)
1962	Twelfth	AD287185 (Vol. 1) AD334484 (Vol. 2)
1963	Thirteenth	AD421483
1964	Fourteenth	AD609104
1965	Fifteenth	AD474238L
1966	Sixteenth	AD800524L
1967	Seventeenth	AD822894L
1968	Eighteenth	AD846427L
1969	Nineteenth	AD860812L
1970	Twentieth	AD875973L
1971	Twenty-First	AD888641L
1972	Twenty-Second	AD904360L
1973	Twenty-Third	AD914238L

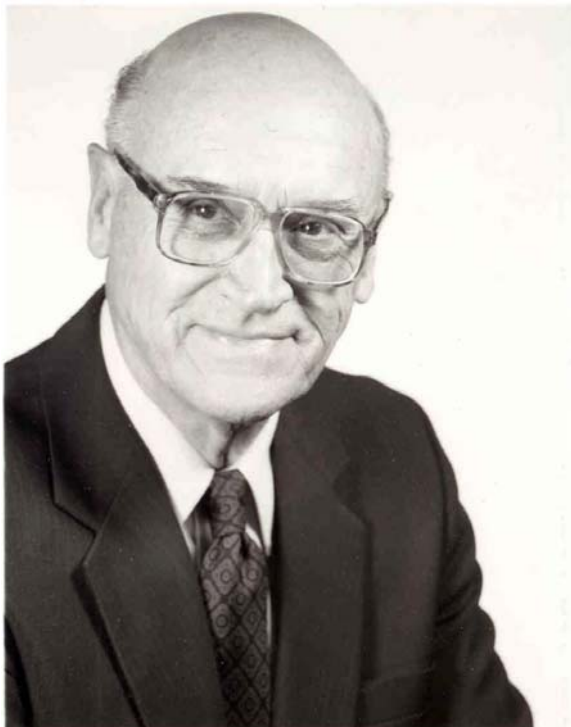
Antenna Application Symposium

Year	Symposium No.	Technical Report No.	Identifier
1977	First	_____	ADA955413
1978	Second	_____	ADA955416
1979	Third	_____	ADA077167
1980	Fourth	_____	ADA205907
1981	Fifth	_____	ADA205816
1982	Sixth	_____	ADA129356
1983	Seventh	_____	ADA142003; 142754
1984	Eighth	85-14	ADA153257; 153258
1985	Ninth	85-242	ADA166754; 165535
1986	Tenth	87-10	ADA181537; 181536
1987	Eleventh	88-160	ADA206705; 206704
1988	Twelfth	89-121	ADA213815; 211396
1989	Thirteenth	90-42	ADA226022; 226021
1990	Fourteenth	91-156	ADA237056; 237057
1991	Fifteenth	92-42	ADA253681; 253682
1992	Sixteenth	93-119	ADA268167; 266916
1993	Seventeenth	94-20	ADA277202; 277203
1994	Eighteenth	95-47	ADA293258; 293259
1995	Nineteenth	96-100	ADA309715; 309723
1996	Twenty First	97-189	ADA341737
1997	Twenty Second	1998-143	ADA355120
1998	Twenty Third	1999-86	ADA364798
1999	Twenty Fourth	2000-008 Vol. I & II	ADA386476; 386477
2000	Twenty Fifth	2002-001 Vol. I & II	ADA405537; 405538
2001	Twenty Sixth	2002-002 Vol. I & II	ADA405328; 405327
2002	Twenty Seventh	2005-001 Vol. I & II	ADA427799; 427800
2003	Twenty Eighth	2005-005 Vol. I & II	ADA429122; _____
2004	Twenty Ninth	2005-016 Vol. I & II	ADA431338; 431339
2005	Thirtieth	2005-039 Vol. I & II	ADM001873
2006		2006-0047 Vol. I & II	

2006 Author Index

Aumann, H.M.	210	Mayes, P.E.	23
Avakian, A.	281	Munk, B.A.	149
Baek, S-H.	68	Nichols, C.	455
Bailey, M.C.	358,470	Notaros, B.M.	240
Behdad, N.	141	Novak, D.	1
Bernhard, J.T.	258	Oleski, P.J.	203
Best, S.R.	411	Palmer, W.D.	132
Bharj, S.S.	203	Park, J-W.	314
Botha, L.	294	Paunonen, J.	272
Boyd, R.C.	330	Popovic, Z.	240
Brailovsky, A.	281	Pribyl, P.	281
Buck, M.C.	37	Ravipati, C.B.	358
Campbell, T.G.	330, 358, 470	Reddy, C.J.	330, 358, 470
Cilliers, J.	294	Rhyu, H.	68
Djordjevic, M.	240	Roberts, T.M.	188
Elsallal, M.W.	166	Sadovnik, L.	281
Fathy, A.E.	103	Santarelli, S.G.	188
Felman, M.	281	Sarabandi, K.	141
Filipovic, D.S.	37,455	Schaubert, D.H.	166
Fontaine, D.	455	Suleiman, S.H.	103
Gekelman, W.	281	Wang, Y.E.	80
Gigliotti, A.	281	Waterhouse, R.B.	1
Giubbolini, L.	281	Yang, S.	103
Gordion, I.	281		
Harackiewicz, F.J.	68, 314		
Hong, W.	141		
Huff, G.H.	258		
Joines, W.T.	132		
Jung, B.	314		
Keller, S.D.	132		
Khodos, V.	281		
Kim, S-J.	68		
Klock, P.W.	23		
Kulkarni, S.D.	56		
Lasater, M.S.	210		
Lee, B.	68, 314		
Lee, J-S.	314		
Litvinov, V.	281		
Ludwig, R.	56, 388		
Lukic, M.	455		
Luu, D.	429		
Mailloux, R.J.	188		
Makarov, S.N.	56, 388		
Manasson, V.A.	281		

We Remember: John Dyson, the “Spiral-antenna Man”



John Dyson, a University of Illinois, Urbana-Champaign faculty member from 1957 to 1985, died on April 28 in Urbana at age 87.

Dyson was a key member of the famed Antenna Lab, where frequency-independent antennas were pioneered.

At the Fifth USAF Antenna Symposium in 1955 Dyson gave the paper, “The equiangular-spiral antenna” that was the first in a life-long series of publications that led to numerous applications of spiral antennas.

Generalized CoCo Antennas

Branislav M. Notaroš,¹ Miroslav Djordjević,² and Zoya Popović³

¹Colorado State University, ECE Department, notaros@colostate.edu

²University of Massachusetts Dartmouth, ECE Department, miroslav@ieee.org

³University of Colorado at Boulder, ECE Department, zoya@colorado.edu

Abstract – This paper presents recent contributions to the theory and design of generalized colinear (GeCo) transmission-line antennas. The main feature of these narrowband antennas, which radiate essentially as colinear arrays of wire dipoles driven in phase, is their extremely simple feed. They are excited at a single port, but behave as if excited at a number of ports. This is achieved by making the antenna in the form of series-connected segments of asymmetric two-conductor lines, with alternating 180-degree phase shifts at the series connections. The classical coaxial collinear (CoCo) antenna, made of sections of coaxial cable, is a special case of this new, much broader, antenna class. The paper presents generalized colinear antennas implemented in a multitude of forms, and some designs have properties that cannot be achieved with conventional CoCo antennas. Examples include antennas made of different combinations of asymmetric strip lines and two-wire lines with “inverse connections” between the segments, as well as printed antenna arrays based on the CoCo concept. The analysis of GeCo antennas is carried out using the method of moments. Numerical and experimental results are shown to be in reasonable agreement.

1. Introduction

The coaxial colinear (CoCo) antenna, introduced in 1956 by H. A. Wheeler [1], has been used over the past few decades mostly in atmospheric and ionospheric radar applications, e.g., for wind profilers, as well as in commercial communication applications. The CoCo antenna is inherently narrowband, and as such intended for practically single-frequency operation. It radiates essentially as a colinear array of wire dipoles driven in phase, providing a narrow broadside beam and an omnidirectional pattern in the plane perpendicular to the antenna axis. It is used both as an isolated antenna element and in large arrays [2-10].

The CoCo antenna consists of a sequence of colinear sections of a coaxial cable that are half-wave long (measured in terms of the guided wavelength). The antenna has a single simple feed, but the driving voltage is transmitted to the secondary “ports” of the assembly (ports between adjacent segments of the antenna) via cable segments, which are half of a guided wavelength long. The inner and outer conductors of one segment are

connected to the outer and inner conductors of the next segment, respectively. With this, approximately cophasal current distribution along the outer surface of the coaxial-cable segments (the antenna radiating current) is obtained.

In 1996-1998, based on a new understanding of the physical basis of operation of the CoCo antenna, we proposed a new wide class of cophasal antenna arrays with simple compact feeds, with the classical CoCo antenna being just a special case and one of many realizations, not at all based on the coaxial-cable geometry [11-13]. Since such antennas are excited at a single port, but behave as if excited at a number of ports, we refer to them as OPOMEX (One-Port-Multiply-Excited) antennas, or simply as generalized colinear (GeCo) antennas. The OPOMEX antenna concept has subsequently been used by other authors [14, 15]. It is important to have in mind that, in all applications, the main advantage of using both classical and generalized CoCo antennas for narrowband operation is their extremely simple feed. For example, it was shown that an electronically reconfigurable OPOMEX antenna for diversity wireless communications can exploit spatial diversity in a multipath channel using only a single simple feed (which is not a lossy dispersive corporate feed) and a single low-noise amplifier [16].

This paper presents several forms of generalized colinear antennas, using segments of transmission lines of several types, with the two conductors in a segment having different equivalent electrical radii. Examples include antennas made of different combinations of asymmetric strip lines and two-wire lines with “inverse connections” between the segments, as well as printed antenna arrays based on the CoCo concept. The analysis of GeCo antennas is carried out using the method of moments (MoM). In particular, we use WireZeus, a computer program for analysis of wire antennas and related radiating structures [17]. WireZeus can very effectively analyze a number of forms of OPOMEX antennas, including narrow-strip versions, possibly printed on a thin dielectric substrate. We present two independent techniques, based on using WireZeus, for the analysis of GeCo antennas: (i) a direct numerical method (direct use of WireZeus to model GeCo antennas as wire antennas) and (ii) a multiport-network method (with a use of WireZeus to compute the admittance matrix of the antenna multiport network) [13]. Numerical and experimental results are shown to be in reasonable agreement in all cases.

We show that GeCo antennas can have properties that cannot be achieved with CoCo antennas. For example, numerical optimum of sidelobe levels for a 2×5 -element free-space CoCo antenna appears to be at the most -14 dB. A 2×5 -element GeCo antenna is described in the paper, obtained by numerical optimization, for which all sidelobes are at a level of -25 dB or less. As another example, it is possible to design GeCo antennas having very high and approximately real impedance (over 1 k Ω), which does not appear possible with CoCo antennas. Such high values of impedances are of interest when feeding several GeCo antennas in parallel in a two-dimensional aperture.

2. Principle of Operation of Generalized CoCo Antennas

Consider first the classical CoCo antenna, consisting of a sequence of collinear sections of a coaxial cable (Fig.1). The lengths of segments are approximately half a wavelength along the line. The segments are transposed, i.e., the inner and outer conductors of one segment are connected to the outer and inner conductors of the next segment, respectively. We will refer to the cable interconnections as “ports”. The last cable segment is short-circuited at a distance of about a quarter-wavelength (along the line) from the interconnection with the preceding segment. The last port along the collinear antenna then sees an open circuit in that direction. Since all the preceding segments are (approximately) half-wave long, this high impedance as seen by the line towards the ends of the antenna arms will be transmitted to the generator. As can be observed from Fig.1, all the ports then have a voltage of amplitude and phase (with respect to the indicated reference direction) close to the antenna driving voltage. Approximately cophasal current distribution along the outer surface of the coaxial segments (the antenna radiating current) should therefore be expected. Of course, the same effect can be obtained if the last segment is half a wavelength long (along the line) and open-circuited.

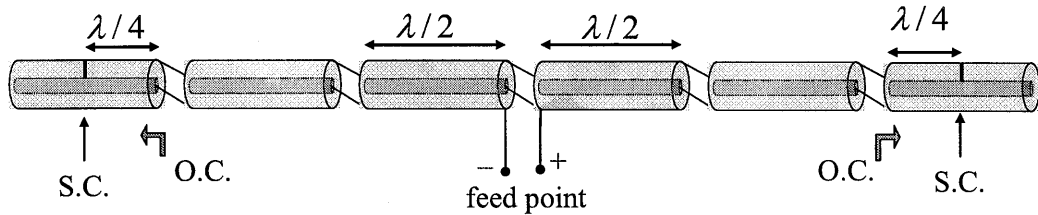


Figure 1. Sketch of a classical CoCo antenna. The excited port is referred to as the feed port, while the places where the cable sections are connected are referred to as “ports”.

In order to answer a simple question—why an antenna made of a cable would radiate at all—we first realize that it consists, in fact, of two antennas, one within the other (the inner and outer coaxial-line conductors), connected to the same feed point and source. The currents in the two antennas are in opposite directions. Transposition of the coaxial-line conductors at certain intervals does not change the propagation along the line, and is intended to produce proper voltages across the gaps between adjacent line segments. It is a simple matter to conclude that if the characteristic impedance of the coaxial-line sections were made to approach zero (i.e., the radius of the inner conductor to approach that of the outer conductor), the CoCo antenna would not radiate any more. This indicates that the CoCo antenna radiates because the two parallel antennas which make it have different current magnitudes at the feed, i.e., the feed-port currents are unbalanced.

Consequently, antennas of the form shown in Figs.2(a) and (b), made of close segments of wires of different radii, will have properties similar to those of a CoCo antenna [13]. Indeed, the antenna in Fig.2(a) can be considered as obtained from that in Fig.1 by

“pulling out” the inner line conductors and placing them outside and parallel to the outer conductors. Voltages will therefore appear between the two thicker (and two thinner) conductors at the ports. The antenna will behave as if excited not only by the actual generator, but also by concentrated voltage generators at all the ports.

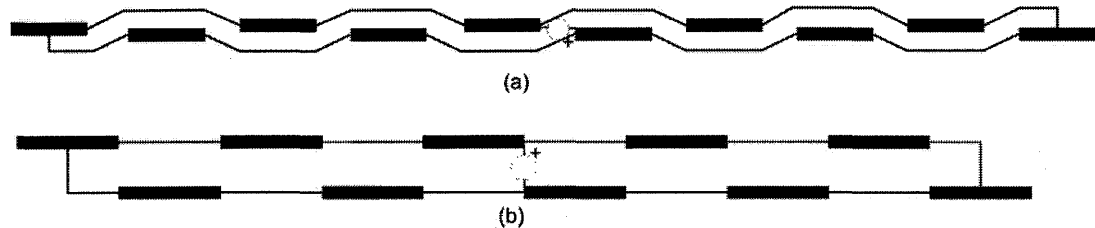


Figure 2. *Two possible forms of the GeCo antenna. Both forms (a) and (b) are constructed of segments of two-wire lines with conductors of different radii or with strips of different widths.*

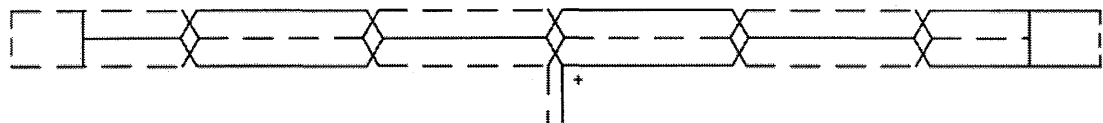


Figure 3. *Another possible form of the GeCo antenna. The antenna is constructed of wire segments of the same radius. The planes of the two antenna parts (indicated in solid and in dashed lines) are separated by a small distance.*

This in turn means that the GeCo antennas can be constructed in a multitude of forms, which only must comply with the general philosophy mentioned. For example, another antenna of this type, constructed entirely of the same wire, is sketched in Fig.3. With the GeCo antennas we have a number of relatively easily adjustable parameters. For example, if the conductors in Fig.2 or Fig.3 are wires, there is a wide range of available wire radii, and we can choose the distance between them in a relatively wide range. Further, the GeCo-antenna conductors need not be round wires. For example, one conductor may be tubular (of any cross-section, not necessarily circular), and the other a thin wire running parallel to the tube, outside it or inside it. If placed inside the tube, it need not run along the tube axis, as it does in CoCo antennas. The two conductors may also be strips of different widths, which is very simple to obtain. The strips can be glued onto a styrofoam support, on the same side or on the opposite sides of the support, with the propagation coefficient of the equivalent line being very nearly that for air. Alternatively, they can be printed on a thin dielectric substrate, in which case the propagation coefficient may also be a parameter for design. The strips can be printed on

the same side or on the opposite sides of the substrate; in the latter case, the strips need not be staggered, but may be one above the other.

3. Modeling and Analysis of GeCo Antennas

In principle, generalized coaxial colinear antennas of the forms shown in Figs.2 and 3, as well as of some other suggested forms (including printed versions), can be analyzed as wire structures, using the method of moments. However, one should be aware of the fact that most wire-antenna MoM analysis programs, assume a uniform current distribution around the wire circumference. For GeCo antennas this is not a good assumption, since the thick and thin wires of any GeCo segment are quite close (axis-to-axis distance on the order of the diameter of the thick wire). In addition, we have interconnections of wires with greatly differing radii, which is difficult to accurately take into account. Finally, the radius of the short segment with the generator influences significantly the antenna susceptance. Consequently, although techniques for direct analysis of wire antennas can be used for approximate analysis of GeCo antennas, one cannot expect very accurate results, in particular for the antenna impedance.

On the other hand, we can perform a modified wire-antenna analysis of GeCCo antennas based on the multiport-network theory [13]. To this end, we first realize that the thick and thin wires (or wide and narrow strips, etc.) form an (asymmetrical) transmission line. The principle of superposition can then be applied to decompose the current in thick wires (I_{thick}) as follows:

$$I_{\text{thick}} = -I_{\text{thin}} + \Delta I. \quad (1)$$

The first component ($-I_{\text{thin}}$) is equal to the current in the adjacent thin wire, but in the opposite direction. This is a transmission-line current, and since the line conductors are very close, it practically does not radiate. The other component (ΔI), i.e., the unbalanced part of the total current in the thick wires is the actual radiating current.

We next note that in both Figs.2 and 3 the points of the wire transposition can be considered as additional ports, with unknown voltages. We also note that these voltages are “connected” (measured) between the antenna segments (i.e., thick-wire segments) on one hand and between the transmission-line conductors on the other hand. This is sketched in Fig.4. The transmission-line assembly and the antenna assembly of a GeCo antenna can be considered as two multiport networks connected in parallel. This parallel connection can, in turn, be considered as a single equivalent multiport network. It is evident from Fig.4 that in the ports of the equivalent network there is current only in the actual excitation port (labeled 1), while the other (additional) ports of the equivalent multiport network are open-circuited.

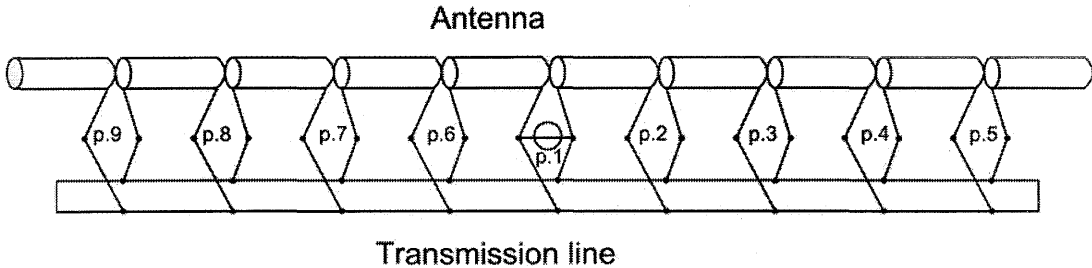


Figure 4. The GeCo antenna represented as a parallel connection of two multiport networks, with common ports ($p.1, p.2, \dots$). If this combination is considered as a single equivalent multiport network, all ports of the equivalent network except $p.1$ are open-circuited.

Based on this reasoning, it is possible to develop another approximate method for the analysis of GeCo antennas (which can also be used for the analysis of CoCo antennas). Briefly, the currents at the transmission-line multiport-network assembly can be represented as

$$[I_{\text{line}}] = [Y_{\text{line}}][V], \quad (2)$$

where $[Y_{\text{line}}]$ is the transmission-line admittance matrix. The elements of this matrix can be calculated with relative ease from the transmission-line equations. The left-hand side of Eq.(2) is a single-column matrix of currents at the transmission-line ports, and $[V]$ is the matrix of voltages at these ports.

The currents at the ports of the antenna multiport network can likewise be expressed as

$$[I_{\text{antenna}}] = [Y_{\text{antenna}}][V]. \quad (3)$$

The admittance matrix of the antenna multiport network, $[Y_{\text{antenna}}]$, can be obtained only numerically, and requires a full numerical analysis of the antenna. The evaluation of $[Y_{\text{antenna}}]$ is therefore incorporated in the method-of-moments analysis (an in-house code WireZeus). Here, we need to determine the antenna-assembly equivalent radius prior to the analysis. It is not difficult to conclude that, by decomposing the total current into the transmission-line current and the antenna current, we are left with the thick-wire assembly as the antenna. Therefore, the equivalent radius of the thick wire should be used as the antenna wire radius [17].

Referring to Fig.4, the total currents at the ports of the equivalent multiport network are obtained from the following matrix equation:

$$[I] = ([Y_{\text{line}}] + [Y_{\text{antenna}}]) [V] = [Y_{\text{equivalent}}] [V], \quad (4)$$

where the sum of two admittance matrices represents the admittance matrix, $[Y_{\text{equivalent}}]$, of the network obtained as the parallel connection of the transmission-line and the antenna multiport networks. As explained, all ports except p.1 of the equivalent network are open-circuited, so that all the elements of the column matrix $[I]$ are zero except the first one,

$$[I] = [I_1 \ 0 \ 0 \ \cdots \ 0]^T, \quad (5)$$

and that is the total current in the generator. We can assume any current I_1 in port 1, and solve for voltages V_1, V_2, \dots, V_{N+1} ($N+1$ is the total number of ports). The GeCo-antenna impedance is then obtained as

$$Z_{\text{GeCo}} = \frac{V_1}{I_1}. \quad (6)$$

Note that this impedance is, in fact, the parallel connection of the impedance of the antenna proper and the transmission-line assembly. This impedance is observed by the generator.

If the relative port voltages are known, the voltages that drive the antenna proper are known as well. We can assume any voltage at the input antenna port, scale the other voltages accordingly, calculate the antenna current distribution, and hence the antenna radiation field. [Note that the impedance of the antenna proper calculated in this manner is not the impedance of the GeCo antenna from Eq.(6).]

To make a qualitative comparison between the two presented methods for the analysis of GeCo antennas in terms of the accuracy of the simulation, we note that the excitation zone in the two models is quite different. In the direct method (direct use of a numerical solver, in this case MoM WireZeus program), a delta-function generator is connected at the starting point of a short segment of the thin wire. This segment, in turn, is connected in a complex way to the adjacent thin and thick antenna segments. In the multiport-network approach, the antenna proper is excited between two thick wire segments by a delta-function generator. The excitation mechanisms being so different, we cannot expect excellent agreement in the antenna impedance obtained by the two methods. We can expect, however, relatively good agreement of the radiation patterns. We can also expect that both methods should predict the antenna operating frequency with reasonable accuracy.

Finally, note that the GeCo antenna general philosophy is intuitive and can easily be exploited in different practical realizations also starting from the network model of a

standard antenna array feed shown in Fig.5(a). In this model, an N -port antenna array is excited by an $(N+1)$ -port feed network with a generator at one port. However, we can add one port to the antenna array to make it a $(N+1)$ -port network as indicated in Fig.5(b), and then, to make it as simple as possible, open-circuit all other ports – this is a GeCo or OPOMEX antenna (see Fig.4). So, the antenna indeed does not have to be based on the coaxial-line geometry, but on any other structure that allows this type of network-feed interconnect.

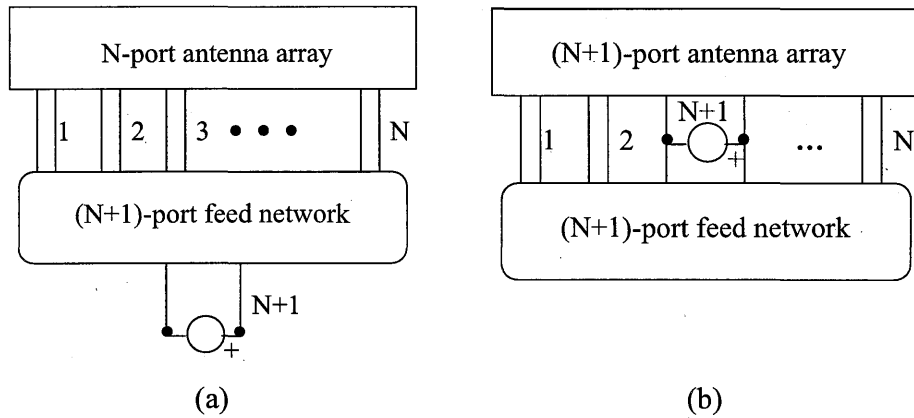


Figure 5. *Principle of operation of generalized coaxial colinear antennas based on the network model of a standard antenna array feed with a generator at one of the ports of the feed network (a), which can be transformed into a GeCo or OPOMEX antenna by adding a generator port to the antenna array network and open-circuiting all other ports for simplicity (b).*

4. Specific GeCo Antenna Designs

4.1. Two-Wire-Line Colinear Antenna

The first example of a GeCo antenna design is a two-wire-line colinear antenna of the form shown in Fig.2(b). The antenna is composed of 2×5 segments, radii of the thick and thin wires are 0.9 cm and 0.5 mm, respectively, and the distance between the wire axes is 2 cm. The characteristic impedance of the two-wire-line segments is about 255Ω , which cannot be implemented with a coaxial cable. The design objective is to obtain an antenna that operates at 300 MHz, matched at 200Ω , and with a high gain in the E-plane.

Interactive optimization is used in conjunction with each of the two methods for analysis of GeCo antennas described in the previous section, with the segment lengths (including that of the last, short-circuited segment) as the optimization parameters. The optimal antennas obtained by the two methods are of somewhat different dimensions. The direct

method (full-wave analysis) results in the first four segment lengths of 48.5 cm, the length of the last segment 42 cm, and the length of the short-circuited segment of 20 cm. With the indirect method (the use of multiport-network approach), these lengths are 45 cm, 45 cm, and 24 cm, respectively. The simulation results for the two optimal antennas are summarized in Fig.6. It is seen that the two antennas have similar VSWR's and gains. This indicates that the results obtained by the two methods are in a reasonable agreement, and that, in general, both methods should be used in the CAD of GeCo antennas, to get an insight into possible errors in each of the methods.

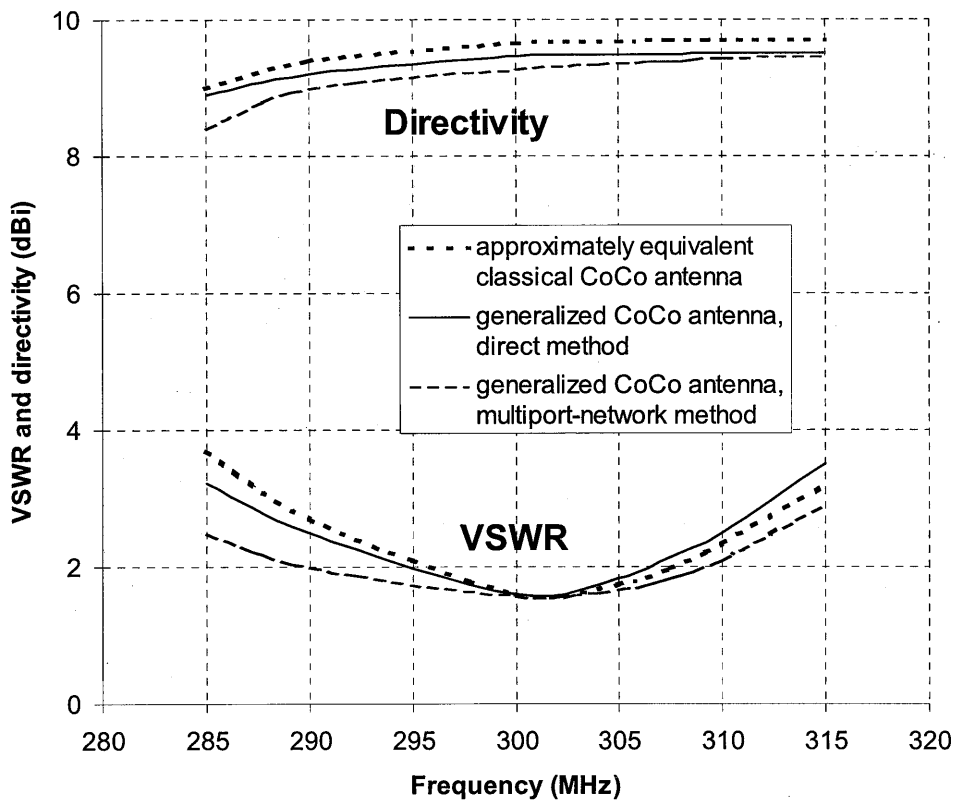


Figure 6. Directivity and VSWR (with respect to 200Ω) of the 300-MHz optimized GeCo antennas described in the text using the direct method and multiport-network method, respectively. Also shown are directivity and VSWR (with respect to 50Ω) for an approximately equivalent classical CoCo antenna, made of commercial coaxial-line segments and described in Subsection 4.2.

Fig.7 shows the co-polarized E-plane radiation pattern of the GeCo antenna obtained by the direct analysis method. Note that the largest sidelobe is about -13 dB below the main lobe. The antenna is bi-directional.

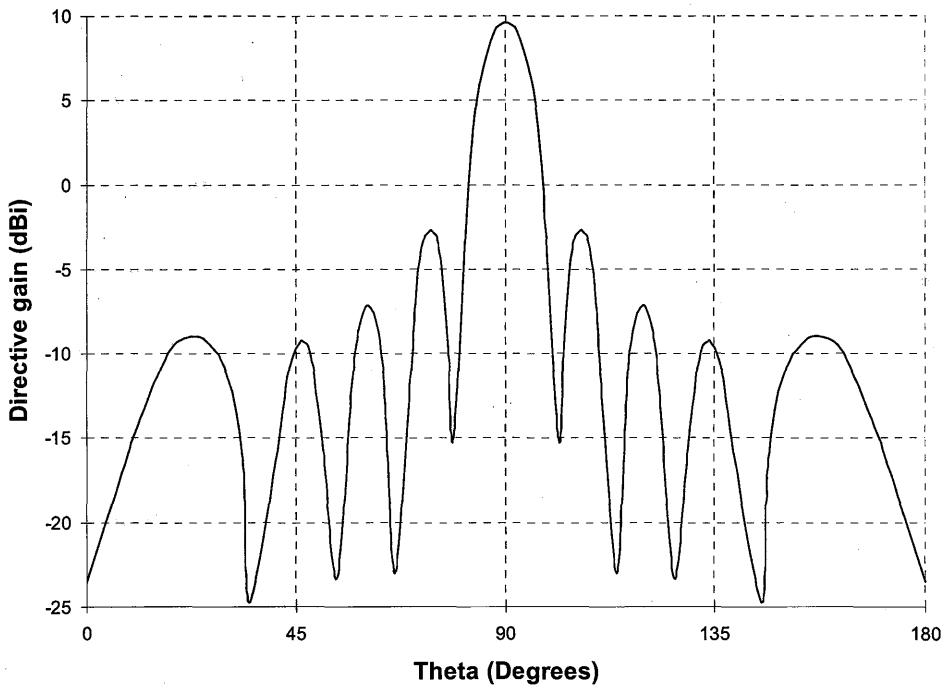


Figure 7. Radiation pattern in the plane containing the long axis of the 300-MHz GeCo antenna described in the text, calculated by the direct analysis method.

4.2. Comparison of GeCo and Classical CoCo Antennas

It is of considerable interest to compare the results of the preceding example with those for a true CoCo antenna (made of sections of a realistic coaxial line). Note that the results of the multiport-network method in the preceding example correspond to those for a CoCo antenna made of line segments with a characteristic impedance $Z_0 = 255 \Omega$ situated in air. This can, in principle, be also a coaxial line. However, such a high characteristic impedance is obtained for the ratio of radii of outer and inner coaxial-line conductors of about 70, which is not commercially available and is quite difficult to realize. Our goal is to design a CoCo antenna made of sections of an available coaxial line. Therefore, the following coaxial-line parameters are adopted: $Z_0 = 75 \Omega$, $v/c = 0.67$, and the line attenuation constant $\alpha = 0.03 \text{ dB/m}$.

Since the wavelength along this coaxial line is only 0.67 that in free space (assumed in the preceding example), to obtain approximately the same gain it is necessary to adopt the length of the CoCo antenna to be about the same as before, i.e., about $2 \times 5 \times 45 \text{ cm} = 450 \text{ cm}$. Therefore the CoCo antenna is adopted with 2×7 segments, each 33.5 cm long (i.e., half a wavelength along the line at 300 MHz), making a total

length of 469 cm. The length of the short-circuited line segments is adopted to be half this length (16.7 cm).

The computed VSWR (with respect to 50Ω) and gain of this antenna are shown in Fig.6 along with the results for the two optimized GeCo antennas described in Subsection 4.1. It can be observed from the figure that this approximately equivalent CoCo antenna has very nearly the same properties as the GeCo antennas. This conclusion is found to be true in many other cases of parallel analysis of CoCo and GeCo antennas. However, GeCo antennas not only can be made of lines having practically arbitrary characteristic impedance, but this impedance can also be varied very easily between the segments of an antenna if desired. For example, this is a valuable tool for controlling sidelobe levels, as the next example will demonstrate.

4.3. GeCo Antenna with Minimized Sidelobes

As explained, the two-wire-line colinear antennas in Figs.2(a) and (b) will practically not radiate if made of conductors of the same radius; a difference in radii of the line conductors is essential for the GeCo-antenna operation. One can expect, therefore, that the antenna current component along the GeCo antenna can be tapered if the difference in the conductor radii (or in strip widths) is decreased towards the antenna ends. The following numerical example will show theoretically that this is indeed true. In Subsection 4.5, a fabricated printed GeCo antenna of this type will be described and it will be shown that the measured results also confirm this reasoning.

A printed antenna for 3 GHz is considered using the direct method, with the objective to design an antenna with minimized sidelobes. The antenna shown in Fig.2(b) can also be considered to be made of strips printed on a thin dielectric substrate. This type of GeCo printed antenna is optimized interactively using WireZeus, in order to obtain the best possible match, possibly with added narrow-band matching network, and as low sidelobes as possible. The antenna is assumed to be printed on a 0.508-mm substrate with $\epsilon_r = 2.17$, having 2×5 sections. The distance of the axes of the printed strips is adopted to be 5 mm, and their lengths 44 mm. The distance of the short circuit from the last interconnection is 22.2 mm, and the distance from the short circuit to the array end 24 mm. The width of all the narrow strips (including the ones that contain the generator) is 0.3 mm. The optimization of the widths of the wider strips results in widths of 3 mm, 2.8 mm, 2.3 mm, 1.5 mm, and 0.5 mm, starting from the feed point. The antenna matching network is simultaneously optimized, with the objective that at 3 GHz the antenna is well matched to 50Ω .

The optimized antenna radiation pattern in the plane containing the long antenna axis is shown in Fig.8. Comparing the sidelobe levels in Figs.7 and 8, it is concluded that the sidelobes in Fig.8 are more than -25 dB below the main beam, while in Fig.7 they are

only about -13 dB below the main beam. Note that the latter result corresponds approximately to that for the classical CoCo antenna, where it is practically impossible to suppress the sidelobes by more than about -14 dB. The compensated optimal antenna VSWR is about 1.14 at 3 GHz, and below 2.2 in the frequency range (3.00 ± 0.02) GHz.

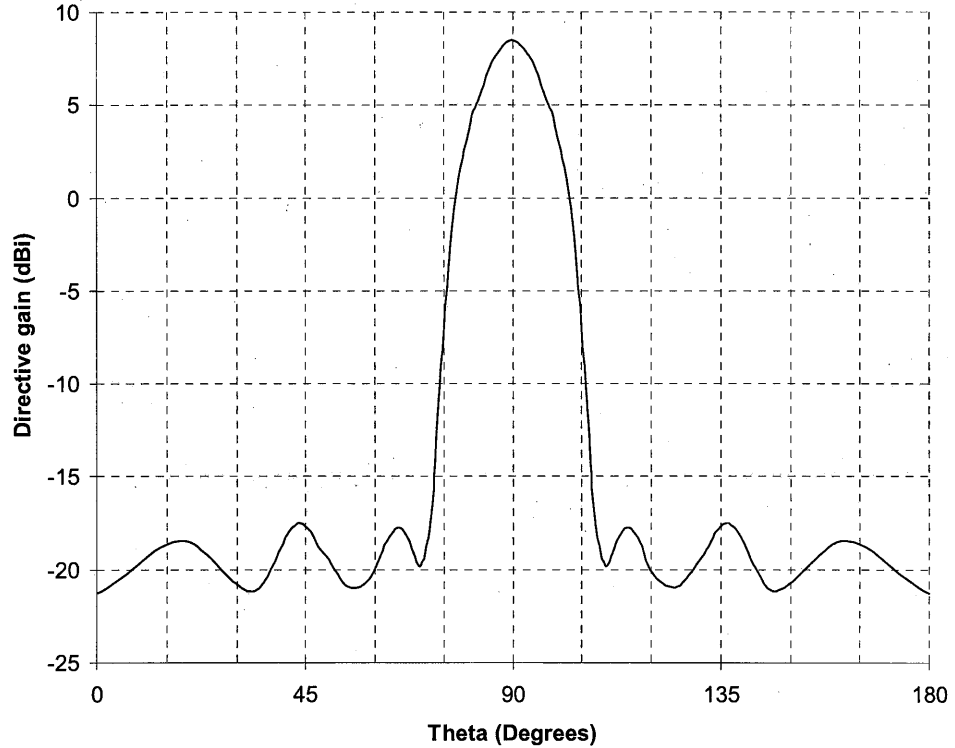


Figure 8. Directive gain of the 3-GHz printed GeCo antenna optimized for low sidelobe levels, calculated by the direct method.

4.4. Quasi-GeCo Strip Antenna

As the next example and another check of the accuracy of the direct analysis method, consider the structure sketched in Fig.9, which represents a half of the antenna in Fig.2(b), mounted above a ground plane. The structure is manufactured from thin wires and thin rectangular strips. It is glued on a styrofoam support, and the thin-wire conductor is connected to the inner coaxial line conductor protruding through the ground plane. Note that this is not a GeCo antenna, since the image of the wide conductor in the ground plane is also a wide (instead of a narrow) conductor, and the image of the thin conductor is also a thin (instead of a wide) conductor. However, this configuration enables measurement of the impedance for a structure that is very similar to the GeCo antenna.

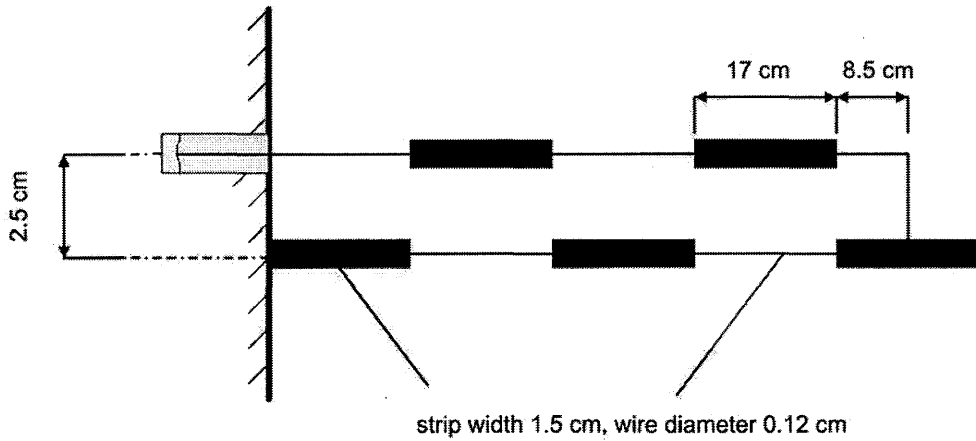


Figure 9. Sketch of a half of the GeCo antenna in Fig.2(b) (with dimensions), mounted on a ground plane.

Fig.10 shows the theoretical and measured VSWR of the antenna, with respect to 50Ω . The theoretical results are obtained using the direct method, and are corrected for the estimated difference in the capacitance between the generator model (delta-function generator) and the actual N-connector used in measurements. Good agreement between the two sets of results can be observed.

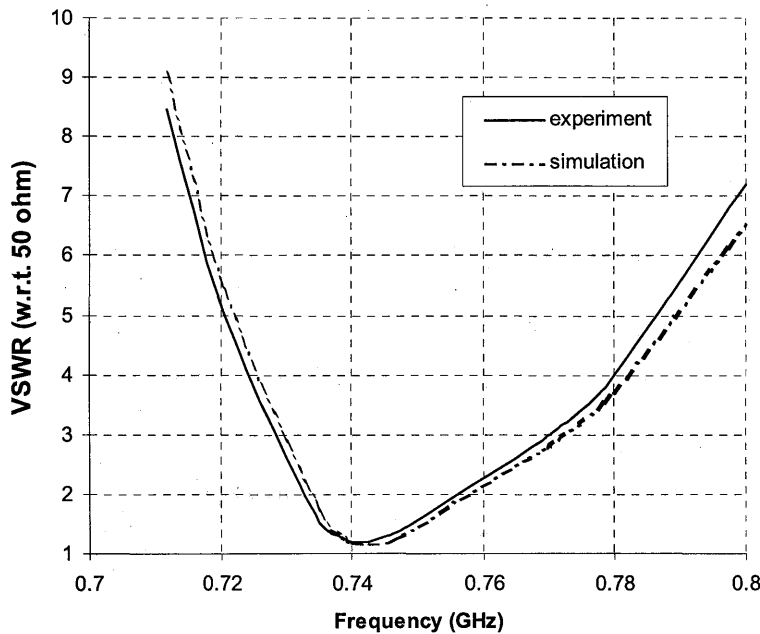


Figure 10. Experimental and theoretical VSWR, with respect to 50Ω , of the antenna in Fig.9, versus frequency.

4.5. Printed GeCo Antenna

The last example is a printed 3-GHz GeCo antenna of the type shown in Fig.2(b), with the number of segments and their lengths as described in Subsection 4.3. The antenna is fabricated on a substrate of thickness $t = 0.508$ mm and relative permittivity $\epsilon_r = 2.17$ (produced by “Arlon”). The strip widths after etching differ from those in Subsection 4.3 due to fabrication limitations. The thin strip width is about 0.7 mm (instead of 0.3 mm), and the widths of the wider strips, from the feeding point towards the antenna arm ends, are 4.0 mm, 3.0 mm, 2.5 mm, and 1.0 mm (instead of 3.0 mm, 2.8 mm, 2.3 mm, 1.5 mm, and 0.5 mm), respectively. The antenna is matched to the $50\ \Omega$ feeder by a $200\ \Omega$ two-wire line quarter-wave matching section followed by a coaxial balun. Note that, although the difference in desired and actual strip widths is relatively large, the strip-width tapering rates in the two cases are almost the same, which should imply that the sidelobe levels should not be dramatically different.

Fig.11 shows the normalized measured antenna E-plane copolarized power pattern. The crosspolarization level for all angles is at most -16 dB with respect to the main lobe copolar power. Note that the level of the first sidelobe is about -21 dB, in spite of the relatively crude experimental model when compared to the mathematical model, indicating that the design has good tolerance.

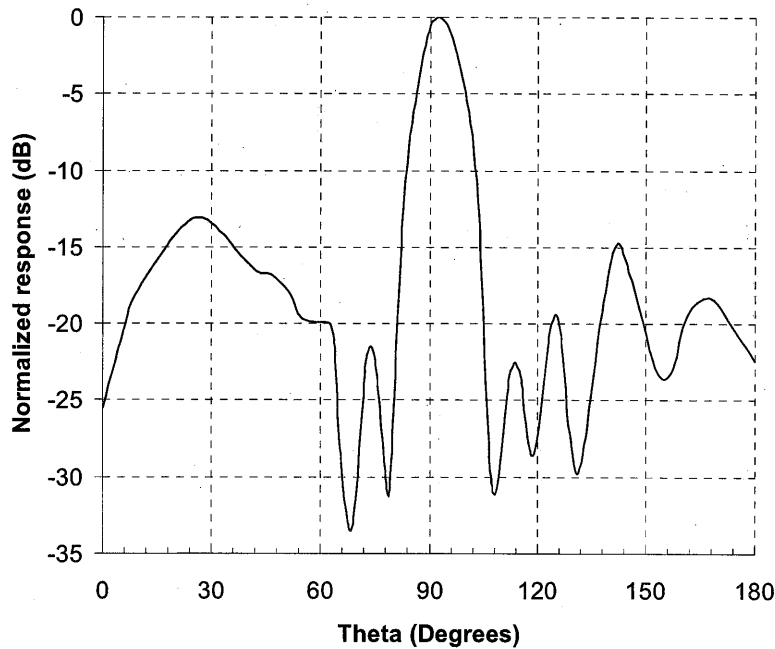


Figure 11. Normalized measured copolarized E-plane power pattern of the experimental 3-GHz printed GeCo antenna described in the text. The H-plane pattern has no gain, as the antenna is a linear array. The cross-polarization is better than -16 dB for all angles.

Finally, shown in Fig.12 is the measured reflection coefficient of the antenna with its matching network. Note an excellent match of the antenna to $50\ \Omega$ at about 2.92 GHz with a return loss of -31 dB. Theoretically, it should have the reflection coefficient of 0.064 (i.e., -24 dB) at 3.0 GHz. The deviation from the predicted operating frequency is less than 3%.

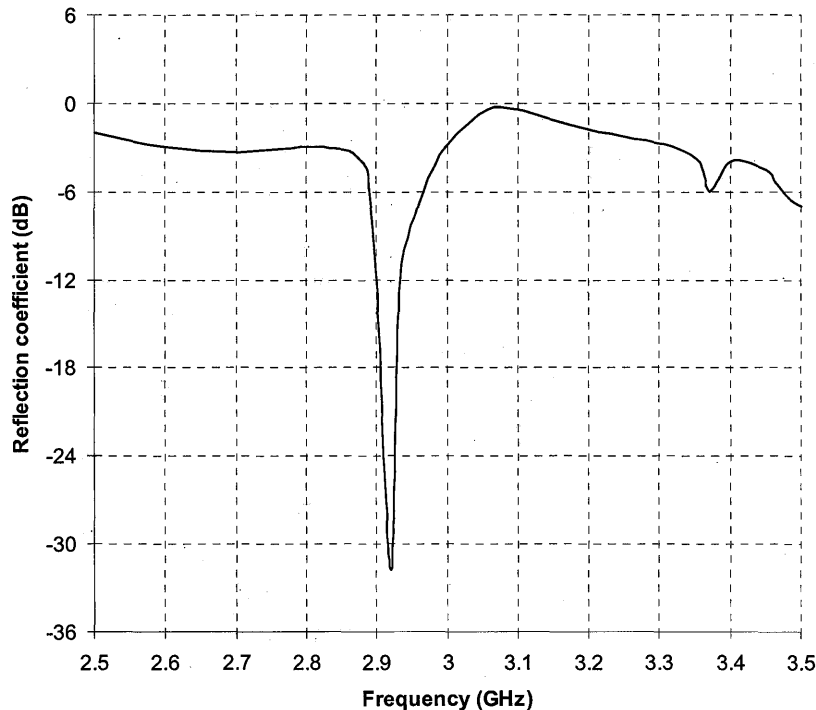


Figure 12. *Measured reflection coefficient of the experimental 3-GHz printed GeCo antenna.*

5. Conclusions and Discussion

This paper has presented recent contributions to the theory and design of generalized colinear antennas. The main feature of these antennas, which radiate essentially as colinear arrays of wire dipoles driven in phase, is their extremely simple feed. They are excited at a single port, but behave as if excited at a number of ports. Effectively, the feed network is integrated with the antenna itself and requires no additional real-estate. This is achieved by making the antenna arms in the form of segments of asymmetrical two-conductor lines, with exchanged places of the conductors at certain (regular or irregular) intervals. The classical CoCo antenna is a special case of this new class of narrowband antennas.

The GeCo antennas offer greater design flexibility than classical CoCo antennas, which have been made only of segments of coaxial lines. In contrast, the GeCo antennas can be made in a wide variety of forms, using segments of any two-conductor transmission line with conductors of different equivalent electrical radii. For example, a strip-line with strips of different widths, a two-wire line with wires of different radii, and two strips of different widths on the two sides of a dielectric substrate are possible building-blocks for a GeCo antenna. Finally, the GeCo antenna can be made of successive segments of different lines, resulting in a further possibility to modify the current distribution along the antenna, and thus the radiation pattern. Specifically, tapering of the current amplitude can result in sidelobe reduction.

The paper presents two methods for the analysis of GeCo antennas. According to the first method, the structure is analyzed as a wire antenna. The other method uses the principle of superposition and the basics of the multiport-network theory, combined with the numerical analysis of wire antennas. We show results using an in-house MoM code (WireZeus), but simple and fast CAD tools such as MiniNEC can also be used. Numerical and experimental results are presented for several GeCo antennas, and are shown to be in reasonable agreement in all cases.

The main published applications of CoCo arrays have been at lower MHz frequencies for meteorology and weather prediction. The limitations in available impedances of coaxial cables, and the parasitic reactance associated with the interconnection of the cable sections have made high-frequency applications difficult. However, these antennas may have large advantages at higher frequencies, where a narrow percentage bandwidth is still several hundred MHz, and where feed networks become lossy. Recently, revolutionary planarized wafer-scale fabrication technology advances have made it possible to fabricate air-filled micro-coaxial cables with square and rectangular cross-sections on the order of 200 μm on the side [18-20]. The loss of these quasi-planar micro-coaxial cables is below 0.1 dB/cm at Ka-band, and the TEM mode is dominant up to around 400 GHz. In addition, parasitic reactances associated with interconnections are greatly reduced. GeCo antennas with varying characteristic impedances of sections between 20 and 120 Ω are possible, thus enabling sidelobe reduction. In addition, several such linear antennas can be fed in parallel with an integrated micro-coaxial feed. The design of GeCo antennas in this new technology, as well as in different printed-circuit technologies, are topics of current and future work.

References

- [1] H. A. Wheeler, "A vertical antenna made of transposed sections of coaxial cable," *IRE Conv. Rec.*, Vol.4, Pt.1, 1956, p.160.
- [2] G. R. Ochs, 'The large 50 Mc/s dipole array at Jicamarca radar observatory,' *NBS Rep. 8772*, Boulder, CO, Mar.1965.

- [3] B. B. Balsley and. W. L. Ecklund, "A portable coaxial colinear antenna," *IEEE Transactions on Antennas and Propagation*, Vol.20, 1972, pp.513-516.
- [4] B. B. Balsley, W. L. Ecklund, D. A. Carter, and P. E. Johnston, "MST radar at Packer Flat, Alaska," *Radio Sc.*, Vol.15, Mar.-Apr. 1980, pp.213-223.
- [5] T. J. Judasz, W. L. Ecklund, and B. B. Balsley, "The coaxial colinear antenna: current distribution from the cylindrical antenna equation," *IEEE Transactions on Antennas and Propagation*, Vol. 35, No. 3, March 1987, pp.327-331.
- [6] B. B. Balsley, W. L. Ecklund, D. A. Carter, and A. C. Riddle, "A note on reducing the horizontal sidelobes of near-vertically directed COCO arrays," *IEEE Transactions on Antennas and Propagation*, Vol. 36, No. 1, January 1988, pp.139-141.
- [7] T. J. Judasz and B. B. Balsley, "Improved theoretical and experimental models for the coaxial colinear antenna," *IEEE Transactions on Antennas and Propagation*, Vol. 37, No. 3, March 1989, pp.289-296.
- [8] B. Lagoun and L. Bertel, "A modular coaxial colinear antenna," *Proc. HF Radio Systems and Techniques 1994*, United Kingdom, July 1994 (IEE Conf. Publ. No. 392), pp.234-238.
- [9] B. Lagoun and L. Bertel, "Bandwidth investigation of coaxial colinear antennas," *Proc. ICAP 1995*, United Kingdom, April 1995 (IEE Conf. Publ. No. 407), pp.410-414.
- [10] Sinclair Radio Labs, Inc., "Fibreglass collinear antennas," *SRL Series*, Tonawanda, N. Y., U.S.A.
- [11] B. D. Popovic and B. M. Notaros, "New class of wire antennas with approximately cophasal current distribution," *Proc. Trans Black Sea Region Symposium on Applied Electromagnetism*, Metsovo, Epirus, Greece, 17-19 April 1996, p.ANPR-14.
- [12] B. D. Popovic and B. M. Notaros, "Two-wire-line colinear (TWILCO) antennas," *Proc. 40th Yugoslav ETRAN Conf.*, Budva, Yugoslavia, June 1996, pp.II-AP.363-366.
- [13] B. D. Popovic, B. M. Notaros, and Z. B. Popovic: "A new class of cophasal antenna arrays with simple compact feeds," *Electromagnetics*, 1998, Vol. 18, (5), pp.507-518.
- [14] R. Bancroft and B. Bateman, "An omnidirectional planar microstrip antenna," *IEEE Transactions on Antennas and Propagation*, Vol. 52, No. 11, November 2004, pp.3151-3153.

- [15] M. Polivka, A. Holub, and M. Mazanek, "Collinear microstrip patch antenna," *Radioengineering*, Vol. 14, No. 4, December 2005, pp.40-42.
- [16] M. T. Oswald, S. C. Hagness, B. D. Van Veen, and Z. Popovic, "Reconfigurable single-feed antennas for diversity wireless communication," *2002 IEEE Antennas and Propagation Society International Symposium Digest*, June 16-21, 2002, San Antonio, TX, U.S.A., pp.I.469-472.
- [17] B. D. Popovic, *CAD of wire antennas and related radiating structures*, New York - Chichester, Research Studies Press (John Wiley & Sons), 1991.
- [18] J. Reid, E. D. Marsh, and R. T. Webster, "Micromachined rectangular coaxial transmission lines," *IEEE Transactions on Microwave Theory and Techniques*, Vol. 54, No. 8, August 2006, pp.3433-3442.
- [19] D. S. Filipovic, Z. Popovic, K. Vanhille, M. Lukic, S. Rondineau, M. Buck, G. Potvin, D. Fontaine, C. Nichols, D. Sherrer, S. Zhou, W. Houck, D. Fleming, E. Daniel, W. Wilkins, V. Sokolov, and J. Evans, "Modeling, design, fabrication, and performance of rectangular μ -coaxial lines and components," in *2006 IEEE MTT-S International Microwave Symposium Digest*, San Francisco, California, June 2006, pp.1393-1396.
- [20] K. J. Vanhille, D. L. Fontaine, C. Nichols, D. S. Filipovic, and Z. Popovic, "Quasi-planar high-Q millimeter-wave resonators," *IEEE Transactions on Microwave Theory and Techniques*, Vol. 54, No. 6, June 2006, pp.2439-2446.

A MODEL FOR MEMS-BASED PERTURBATIONS IN OPEN (LEAKY)
WAVEGUIDE STRUCTURES: APPLICATION TO THE TROUGH
WAVEGUIDE ANTENNA

G. H. Huff¹ and J. T. Bernhard²

¹Electromagnetics and Microwave Laboratory, Department of Electrical and Computer Engineering, Texas A&M University, College Station, TX 77840

²Electromagnetics Laboratory, Department of Electrical and Computer Engineering, University of Illinois at Urbana-Champaign, Urbana, IL 61801

Abstract: This work provides an analytical framework that is well suited for examining MEMS-based perturbations in open (leaky) waveguide structures. This continues previous studies of a trough waveguide antenna using cantilever-type perturbations that was designed to provide fixed frequency beam steering. The modeling technique utilizes physical symmetry conditions and the electric/magnetic field structure to approximate a closed (guiding) geometry, thereby allowing the fields to be expressed as an expansion of orthogonal modes. Perturbation theory and the Compensation Theorem are then used to analyze the effects of the perturbations within the equivalent guiding structure, providing a closed-form relationship between the perturbation's geometry, position, and orientation and the resulting leaky-wave power that is radiated from the physical open structure. This technique is easily generalized, it provides a great deal of physical insight, and is well suited for other applications at mm-wave frequencies that use moving or other non-static components in this fashion. A trough waveguide antenna, designed for W-Band operation and fixed frequency beam steering using electromechanically actuated cantilever perturbations, is analyzed using this framework and the results compared to commercially available full-wave solvers and similar structures (circa 1957) obtained in literature.

I. Introduction

This work develops an analytical framework based on variational quantities, perturbational techniques, and network concepts for analyzing MEMS based perturbations (specifically the cantilever) in micromachined leaky-wave

structures. The perturbational techniques used in this analysis are geared to characterize very complex transverse cross-sections and provide physical insight into the operation and application of the structures. Many of the fundamental concepts in variational techniques, reaction concepts, Fourier expansions, and perturbational techniques [e.g., 1-10] have proven very effective for analyzing the open waveguide structure and offer many different approaches and experience that can be drawn from. They represent the basis for many different formulations and much can be said about these methods and the means by which they obtain the solution to this problem, but the underlying principles in all of these techniques rely on accurately interpreting the physical structure. The procedure in this paper also interprets the physical structure to assign variational quantities and use perturbational techniques, but examines the radiation (leaky-wave) and guidance (traveling-wave) from a network perspective using the Compensation Theorem [11-13] and a complete modal set based on the cross-section of the physical structure.

The small aspect ratios and feature sizes from potential micromachined geometries (e.g., a cantilever) motivate this discussion – specifically those that are suitable for mm-wave and THz applications. These structures can be periodically (antipodal spacing) actuated to enhance and utilize the radiation from leaky-wave structures to facilitate reconfigurable radiation on a large aperture scale. This concept – the reconfigurable radiation line source antenna – was first examined in [14-17] and resulted in the electromechanically scannable trough waveguide antenna [17]. This device used periodically spaced perturbations with a fixed length a (antipodal spacing with a period $2a$) to reconfigure the guided wavelength λ_g and steer the beam direction θ according to Equation 1 [14] (fixed frequency beam steering). The designs in [16] use metallic block perturbations that are mechanically driven by a cam and gear drive to adjust the heights of the blocks, which altered the guided wavelength and allowed the beam to be steered at a fixed frequency. This structure was later considered in [18-20] for the application of electrostatically actuated metallic cantilever perturbations that can alter both the periodicity (in discrete steps based on the design of the cantilever) and the guided wavelength (based on the degree of actuation). The additional degree of freedom in the nominal design has the potential to reconfigure the frequency and maintain fixed frequency beam steering characteristics. These concepts can be extended to other antenna designs and novel micromachined radiators – including those incorporating the properties of tunable materials, small feature sizes, and high aspect ratios – whose analysis can benefit from the analytical technique presented in this paper.

$$\sin \theta = \frac{\lambda_0}{\lambda_g} - \frac{\lambda_0}{2a}$$

1

The organization of this paper follows. The analytical framework and methods to approximate the leaky-wave structure as a closed waveguide are covered first, including the network description of the traveling wave antenna. Following this, application of the Compensation Theorem provides the relationship between the actuation of the cantilever and the power converted into the leaky-wave mode. Next, an analysis of the trough waveguide antenna's cross-section using these methods demonstrates this process, and includes a comparison to results obtained from a commercially available full-wave solver. The work concludes with a summary of current work.

II. Formulation

A. Approximating a Complete Set of Mode Vectors

The assignment of variational quantities first requires an accurate understanding of the field structure in the leaky-wave device, such that it can be accurately represented by a closed structure capable of guidance. Approximating the electric/magnetic fields that are primarily tangential and at a maximum value as magnetic/electric walls and the use of symmetry planes or similar physical conditions are two commonly used methods for achieving this. This process remains specific to the individual geometry – applicable to both standing wave and traveling wave structures – for which numerous examples exist (e.g., the cavity model of the microstrip patch antenna [21] or the transverse resonance technique for the slotted waveguide [e.g., 6]). Closing the geometry allows the assignment of a complete modal set [22] expressed through the wave function Ψ , which satisfy the transverse Helmholtz equation (Equation 2, assuming propagation in the +y-direction) for the cross section of the closed structure. This set represents the orthogonal mode vectors \vec{e} or \vec{h} (Equation 3) that are normalized according to Equation 4. These procedures are commonly used so further discussion can be found in literature.

$$(\nabla_t^2 + k_c^2)\Psi = 0$$

2

$$\vec{e}^{TE} = \hat{u}_y \times \nabla_t \Psi^{TE} \quad \text{and} \quad \vec{e}^{TM} = -\nabla_t \Psi^{TM}$$

$$\vec{h}^{TE} = -\nabla_t \Psi^{TE} \quad \text{and} \quad \vec{h}^{TM} = -\hat{u}_y \times \nabla_t \Psi^{TM} \quad 3$$

$$\iint \vec{e}_i \cdot \vec{e}_j dS = \iint \vec{h}_i \cdot \vec{h}_j dS = \begin{cases} 1 & \text{for } i=j \\ 0 & \text{for } i \neq j \end{cases} \quad 4$$

B. Power Flow and Dissipation

The power flow (assuming propagation in the \hat{u}_y direction) and power dissipated by radiation into the upper half-plane ($z > 0$) are considered next for the (approximate) closed guiding structure. The fields of this structure are described by variational quantities based on a complete set of orthogonal mode vectors. Equation 5 shows the relationship between the electric \vec{E} and magnetic \vec{H} fields to the mode vectors \vec{e} (TM) and \vec{h} (TE) and mode voltages V and currents I . Using the relationship in Equation 4, Equation 6 demonstrates that each of these modes propagates power independently (since they are orthogonal [22]). Then, recalling that physical structure has leaky wave properties, the power will then be the sum of the propagating (traveling-wave) power P_P and dissipated (leaky-wave) power P_D (Equation 7).

$$\vec{E}_t = \vec{e}V \quad \text{and} \quad \vec{e} = \vec{h} \times \hat{u}_z$$

$$\vec{H}_t = \vec{h}I \quad \text{and} \quad \vec{h} = \hat{u}_z \times \vec{e} \quad 5$$

$$P = \iint \vec{E} \times \vec{H}^* \cdot \hat{u}_z dS = \sum_{i,j} V_i I_j^* \iint \vec{e}_i \cdot \vec{e}_j dS = \sum_i V_i I_i^* \quad 6$$

$$P = P_P + P_D \quad 7$$

All of the power will be propagated in the closed structure if the excitation of the waveguide corresponds to the fundamental mode of the guide, therefore the ports associated with the higher order modes will propagate no power since they are in cut-off. Recalling again that the physical structure is leaky, and power in higher-order modes is dissipated in the form of evanescent radiation (neglecting other losses from conductivity or dielectric loss tangent), an expression for the dissipated power can be obtained. Using Equation 5 and restating Equation 6 (neglecting the intrinsic losses, and assuming a means to couple power into the higher order modes), the total power P can be decomposed into the sum of the

propagating power P_P in the fundamental mode (denoted with the subscript $i = I$) and the radiated power P_{RAD} (denoted with the subscripts $i > I$) which represents power coupled into higher-order modes (Equation 8).

$$P = P_P + P_{RAD} = V_1 I_1^* + \sum_2^N V_i I_i^* \quad 8$$

C. Network Representation

Within the closed structure, the power in each one of the N -modes propagates independently (Equation 6) because they are orthogonal. Therefore, the guide can be viewed as a N -port network [22] – assigning a “port” on for every mode vector. Each of these ports gets terminated in its characteristic impedance to approximate an infinite extent in the direction of propagation. Figure 1 shows the multi-port network representation of waveguide cross-section excited in its fundamental mode.

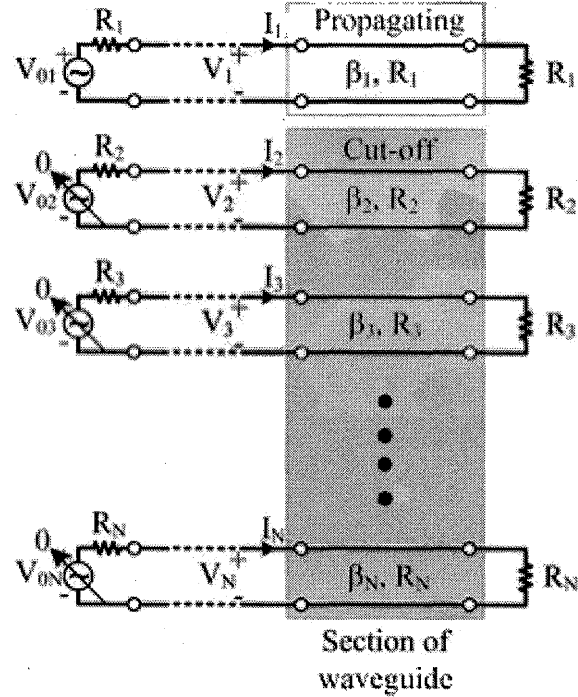


Figure 1. Equivalent network representation of the waveguide (assuming N -ports, or modes).

D. Compensation

The N -port network representation of the waveguide obtained in the previous section provides an opportunity to apply the Compensation Theorem [11, 12] and refine the expression for the radiated power (Equation 8). As a preface, the Compensation Theorem states that a small change in the impedance ΔZ_i (shown as R_i in Figure 1) at port i – or mode i for the waveguide – results in a compensating mechanism in the rest of the $N-1$ ports of the network to satisfy conservation of power arguments. The power associated with this compensation can be calculated by (1) terminating the remaining ports in their characteristic impedance (the modal impedance in the case of a waveguide modes) and (2) driving these ports with a voltage source equivalent to the product of the driving current I_i at port i and the differential impedance ΔZ_i . Assuming the guide operates in the fundamental mode ($i = 1$) and the differential impedance and current are for port 1 (with no other losses present), the evanescent behavior of the higher order modes accounts for the dissipated power. Equation 10 shows the rearranged power term from Equation 9 that represents the power dissipated by radiation (recalling again that the actual structure is open and leaky).

$$P_{Rad} = \sum_2^N V_i I_i^* = \sum_2^N \frac{V_i^2}{Z_i} = \sum_2^n \frac{(\Delta Z_i I_i^*)^2}{Z_i} \quad 9$$

E. Perturbations

Perturbing the fields in the fundamental mode of the guiding structure can be viewed as a mechanism for creating the differential impedance of the corresponding port in the network description. The network compensates this change in impedance through the excitation of higher order modes that dissipate this power in the form of radiation from the open structure. The perturbations must not significantly alter the field structure to avoid significant impedance reflections (maintaining the conservation of power), so their type and placement in the waveguide must reflect this constraint. This can be accomplished by using a properly placed inward metallic perturbation (i.e., a wall perturbation) – similar to that provided by the cantilever geometry. Figure 2 depicts an original and perturbed guiding structure, where \vec{E}_0 , C , and S represent the electric field, contour, and surface of the original guide in the transverse direction and \vec{E} , ΔC , and S' represent the electric field, contour resulting from the perturbation, and remaining surface of the perturbed guide in the transverse direction. Equation 10 (and equivalent forms) can be used to calculate the effect of this perturbation.

Equations 11 and 12 from [11, 12, 22] translate the result of this perturbation into the desired change in the port (modal) impedance required for the application of the Compensation Theorem.

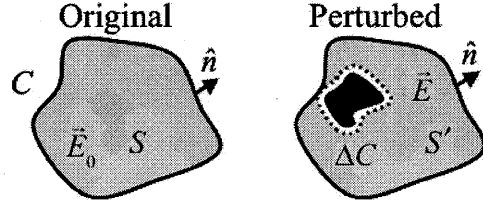


Figure 2. Transverse cross-section of the original and perturbed waveguide.

$$\beta - \beta_0 = -j \frac{\oint (\vec{E}_0^* \times \vec{H}) \cdot \hat{n} dl}{\iint_{S'} (\vec{E}_0^* \times \vec{H} + \vec{E} \times \vec{H}_0^*) \cdot \hat{u}_y ds} \quad 10$$

$$\gamma = jk_y = \begin{cases} j\beta = jk\sqrt{1 - (f_c/f)^2} & \text{for } f > f_c \\ \alpha = k_c\sqrt{1 - (f_c/f)^2} & \text{for } f < f_c \end{cases} \quad 11$$

$$Z_i = \frac{j\omega\mu}{\gamma_i} \text{ for TE-modes} \quad 12$$

$$Z_i = \frac{\gamma_i}{j\omega\epsilon} \text{ for TM-modes}$$

III. Reconfigurable W-Band Trough Waveguide (Fixed Frequency Beam Switching)

A. Analysis

The left side of Figure 3 shows the transverse cross section of the trough waveguide antenna and the electric field structure of its fundamental mode. Physically, the guide is composed of an open rectangular waveguide with a center fin that bisects the bottom of the guide; the resulting dimensions reflect this and the antenna dimensions are typically comparable to the size of a rectangular waveguide covering the same frequency range (although the trough waveguide

has up to 1.5x the bandwidth of the equivalent rectangular waveguide). Figure 3 shows the guide and a field structure similar to that of a rectangular waveguide folded in half and pivoted along the symmetry plane of the electric field – assuming propagation in the fundamental TE₀₁ mode. The electric fields can be considered completely tangential at the open end of the guide, so assuming the presence of a magnetic wall at this location can close the structure. Equation 13 provides the normalized fundamental mode vector of the simplified structure shown on the right side of Figure 3 (the effects of perturbations are analyzed using this transverse cross-section). The mode vector results from the electric and magnetic boundary conditions that support a quarter-wavelength in the z -direction. The discussion in [14-17] provides a comprehensive description of both the design and operation of the guiding structure so further discussion will be left for the presentation.

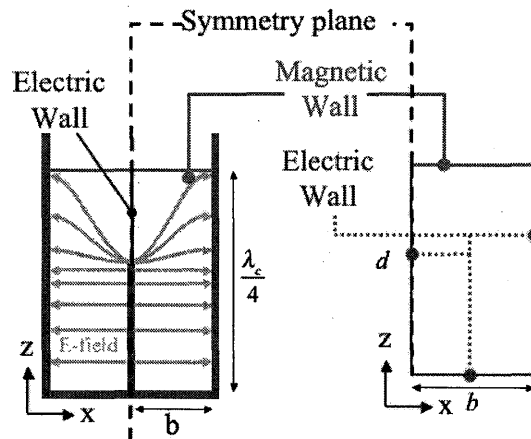


Figure 3. Cross-section of the trough waveguide (left) and the simplified structure used to analyze the effects of perturbations (right).

$$\vec{e}_1(z) = 2 \sqrt{\frac{2}{b\lambda_c}} \sin\left(\frac{2\pi z}{\lambda_c}\right) \hat{x} \quad 13$$

B. Cantilever Perturbation

By asymmetrically perturbing the trough waveguide, the physical structure becomes asymmetric and the compensating mechanism for this generates a corresponding loosely bound (radiating) TEM-mode that is also asymmetric with

respect to the guide. The left side of Figure 4 shows the radiating TEM mode. The left side of Figure 4 depicts the transverse cross-section of the trough waveguide with a metallic cantilever perturbation located in the bottom of the right-hand trough, which remains hinged to the corresponding exterior wall. The placement of the cantilever at the bottom of the guide provides a small perturbation to the fundamental mode vector (Equation 13), and has a similar effect as the metallic blocks in [16]. The length of the cantilever spans the entire length b , has a thickness Δ , and its actuation assumes coverage across the full available range from 0° (no actuation, resting horizontally on the bottom of the guide) to 90° (fully actuated and vertically oriented with the trough). For this work, the elasticity of the cantilever has been neglected and does not physically deform (and ideal hinged surface) from the actuation forces that would normally result in a nominal degree of curvature. Other effects can be easily included with information regarding the specific material stiffness and elasticity and the actuation method.

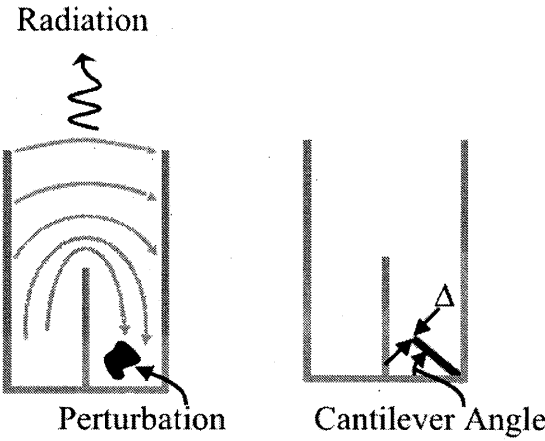


Figure 4. Transverse cross-section of the trough waveguide including the metallic cantilever perturbation (thickness Δ).

C. Results

This section demonstrates the analytical technique developed in this paper (Compensation Theorem and perturbational techniques) using the trough waveguide wall perturbation discussed in the previous section. The dimensions of the trough waveguide in this example are the 2.686 mm, 0.861 mm, 0.05 mm, and 0.562 mm for the height of the outer sidewalls, center fin height, center fin thickness, and width of both troughs (Figure 3), respectively. Figure 5 shows a plot of the results for the cantilever perturbation (thickness $\Delta = 0.0025$ mm),

actuated through the available range of angles at $f = 93.5$ GHz, which has been normalized by the free-space wave number β_0 . This analysis effectively results in a closed form expression (Equation 9) for the leakage constant as a function of the actuation angle. Measurements have not been completed at the time of this manuscript so the calculated results are compared against those obtained from a full-wave solver [23], and are in excellent agreement. Additionally, the normalized leakage constant in this work remains comparable to the calculated and measured results in [17] (transverse-resonance procedure) for the metallic block perturbations, but the cantilever provides a lesser perturbation the cavity than the metallic blocks due to the degree of visibility (or exposure) that each provides in the guide.

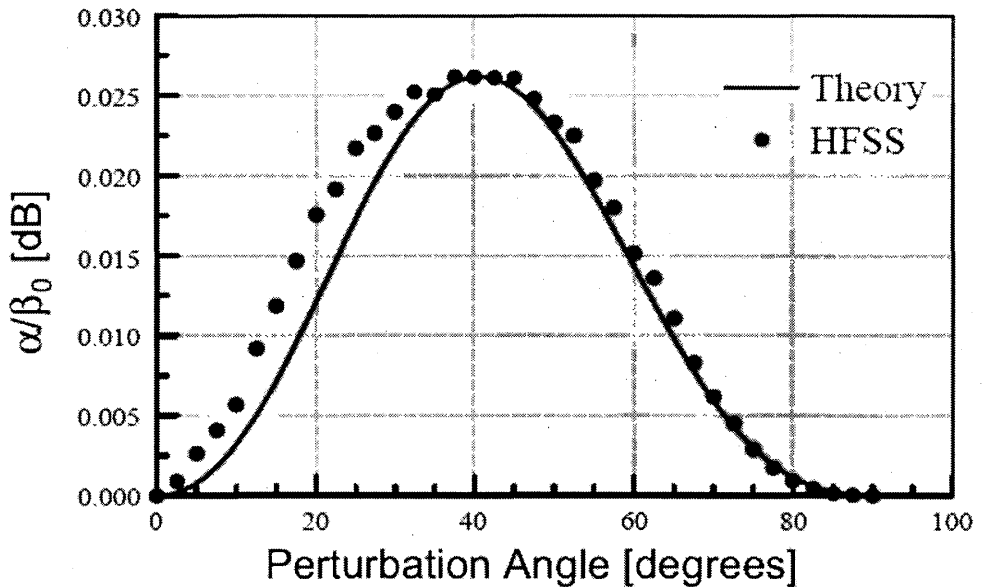


Figure 5. Results obtained in this work (solid) and a full-wave solver [23] (normalized to the free-space wave number β_0) for a cantilever perturbation in a trough waveguide operating at $f = 93.5$ GHz (W-band).

Periodically spacing the cantilevers (discretized into sub-wavelength dimensions in both troughs) and actuating sets of them (e.g., “one at time,” “two at a time,” and so on) in a periodic antipodal fashion to the same angle allows the adjustment of the argument α in Equation 1 – creating the reconfigurable radiation line source antenna. Figure 6 shows this type of arrangement. Since previous work in [18-20] has demonstrated the use of cantilever perturbations in the trough waveguide

antenna (after the original demonstration in [14-17] using fixed-length metallic blocks) the radiation behavior will be highlighted in the presentation.

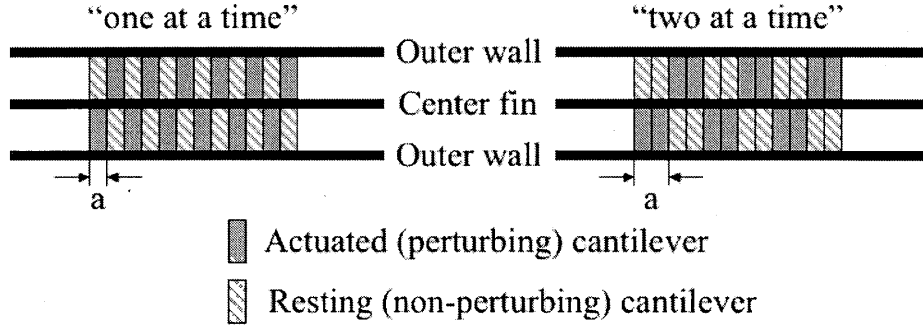


Figure 6. Top-view of the trough waveguide antenna showing two periodic antipodal actuation schemes (“one at a time” on the left and “two at a time” on the right) for the cantilever geometries used to achieve fixed frequency beam steering.

IV. Conclusions

An analytical method based on variation quantities has been covered in this work to calculate the effects of MEMS based perturbations in mm-wave and THz leaky-wave structures. The process begins by briefly identifying the necessary steps for approximating a leaky-wave device as a closed structure, which allows the transverse section to be characterized by a complete set of modal vectors. Power arguments then provide a multi-port network description of the structure, leading to an expression for the radiated power (assuming the guide operates in the fundamental mode) by using the Compensation Theorem. Perturbational techniques that are suitable for analyzing the small feature size and potential material compositions of micromachined structures are then used to calculate the differential impedance of the perturbed guide. The compensation in the network for the change in impedance equates to the excitation of higher order modes that dissipate the power in the form of radiation. A brief example using the trough waveguide antenna using cantilever perturbations (for antipodal actuation schemes and fixed frequency beam steering) demonstrates the potential of this method. The agreement between simulated data and calculated data for this structure have excellent agreement, and future work will aim to fabricate the trough waveguide antenna and validate these results with experimental data.

V. Acknowledgements

The authors would like to thank Profs. Andreas Cangellaris, Paul Mayes, and Paul Klock from the Electromagnetics Laboratory at the University of Illinois in Urbana-Champaign for their insightful discussions. Funding for Gregory H. Huff is provided through the Vodafone-U.S. Foundation Graduate Fellowship for the 2005 – 2006 academic year.

VI. References

- [1] S. Silver and W. K. Saunders, “The external fields produced by a slot in an infinite circular cylinder,” *Journal of Applied Physics*, Vol. 21, pp. 153 – 158, February 1950.
- [2] V. H. Rumsey, “Traveling wave slot antennas,” *Journal of Applied Physics*, Vol. 24, pp. 1358-1365, November 1953.
- [3] V. H. Rumsey, “Reaction concept in electromagnetic theory,” *Physical Review*, Vol. 94, pp. 1483 – 1491, June 1954.
- [4] A. D. Berk, “Variational principle for electromagnetic resonators and waveguides,” *IEEE Transactions on Antennas and Propagation*, pp. 104 – 111, Vol. 4, April 1956.
- [5] V. H. Rumsey, “Variational principle for electromagnetic resonators and waveguides,” *IEEE Transactions on Antennas and Propagation*, Vol. 5, p. 146, January 1957.
- [6] R. F. Harrington, “Propagation along a slotted cylinder,” *Journal of Applied Physics*, Vol. 24, pp. 1366 – 1371, November 1953.
- [7] R. E. Collin, “Variational Integral for Propagation Constant of Lossy Transmission Lines,” *IEEE Transactions on Microwave Theory and Techniques*, Vol. 8, pp. 339 – 342, May 1960.
- [8] L. O. Goldston and A. A. Oliner, “Leaky wave antennas I: Rectangular waveguide,” *IEEE Transactions on Antennas and Propagation*, Vol. 7, pp. 307 – 319, Oct. 1959.

[9] A. A. Oliner, "Equivalent circuits for small symmetrical longitudinal apertures and obstacles," *IRE Transactions on Microwave Theory and Techniques*, Vol. 8, pp. 72 – 80, Jan. 1960.

[10] L. N. Tao, "On variational principles for electromagnetic theory," *Journal of Mathematical Physics*, Vol. 7, pp. 526 – 530, March 1966.

[11] A. Cangellaris, class notes for ECE 598, *Analytical Foundations of Electromagnetic Theory*, Department of Electrical and Computer Engineering, University of Illinois at Urbana-Champaign, Spring 2003.

[12] A. Cangellaris, class notes for ECE 598, *Advanced Topics in Electromagnetic Theory*, Department of Electrical and Computer Engineering, University of Illinois at Urbana-Champaign, Fall 2005.

[13] R. Mittra, "A vector form of Compensation Theorem and its application to boundary-value problems," *Applied Scientific Research*, Vol. 11, pp. 26 - 42, January 1965.

[14] W. Rotman and N. Karas, "Some new microwave antenna designs based on the trough waveguide," *IRE International Convention Record*, Vol. 4, March 1956, pp. 230 – 235.

[15] W. Rotman and A. A. Oliner, "Asymmetrical trough waveguide antennas," *IRE Transactions on Antennas and Propagation*, Vol. 7, pp. 153 – 162, April 1959.

[16] W. Rotman and A. A. Oliner, "Periodic structures in trough waveguide," *IRE Transactions on Microwave Theory and Techniques*, Vol. 7, pp. 134 – 142, Jan. 1959.

[17] W. Rotman and A. Maestri, "An electromechanically scannable trough waveguide array," in proc. *IRE International Convention Record*, Vol. 8, March 1960, pp. 67 – 83.

[18] "Electromechanical beam steering of a W-band trough waveguide antenna for use in integrated automated radar systems," G. H. Huff and J. T. Bernhard, *Ansoft Converge - Applications Workshop for High Performance Design*, Detroit, MI, Nov. 2005, p. 8.

[19] "Electromechanical beam steering of a trough waveguide antenna using cantilever perturbations," G. H. Huff and J. T. Bernhard, *Proc. 2005 Antenna Applications Symposium*, Allerton Park, Monticello, IL, Sept. 2005, pp. 152 – 165.

[20] (Invited paper) G. H. Huff and J. T. Bernhard, "Radiation and beam-steering of a W-band trough waveguide antenna using MEMS perturbations," in *Proc. URSI 2006 National Radio Science Meeting*, January 2006, p. 20.

[21] Y. T. Lo, D. Solomon, and W. Richards, "Theory and experiment on microstrip antennas," *IEEE Transactions on Antennas and Propagation*, vol. 27, pp. 137 – 145, July 1979.

[22] J. R. Harrington, *Time Harmonic Electromagnetic Fields*. New York, NY: McGraw-Hill Book Company, 1961.

[23] Ansoft, HFSS[®] v9.1, Pittsburgh, PA 15219.

ON LOSSES DUE TO AN AIR GAP AND LATERAL DISPLACEMENTS IN A JUNCTION OF TWO COLLINEAR RECTANGULAR WAVEGUIDES

Jari Paunonen

Electronics and Information Technology Division
Finnish Defence Forces Technical Research Centre
FIN-11311 Riihimäki, Finland

Abstract: Losses due to an air gap and lateral misalignments in a standard WR-28 waveguide line are studied using finite element method simulations. Losses are mainly caused by the radiation from the gap, which behaves like a resonant antenna. Resonant wavelength of a narrow gap is approximately three times the average perimeter of the waveguide. Accordingly, for WR-28 waveguide line the resonant frequency is about 35 GHz. Increasing gap width widens the resonance and lowers the resonant frequency. The gap width does not affect loss at resonance, but outside the resonance a wider gap induces more radiation loss than a narrower one. For example, the loss can be almost 1.5 dB at resonance, and below 0.1 dB on the band edges. Lateral displacements generally increase reflection loss and may increase or decrease radiated power. The resonant frequency may increase or decrease with the displacements.

1. Introduction

Waveguide switches of more than three ports are usually pin-diode devices. If very low loss or capability to handle very high power levels is required, pin-diode devices cannot be used. Hence, mechanical switching may be the only possible solution [1]. Displacements, if large enough, in the junction of moving parts of the switch may deteriorate performance. This is important in low-cost designs because of relatively large manufacturing tolerances. However, studies on the effects of these misalignments are not readily found in the literature, but only some faint references, e.g. [2]. This

is understandable since it is usually more or less trivial to adjust waveguides well enough. Probably the only problem that may arise in connecting two waveguides is the leakage of power, which is easily handled with choke flanges.

In this paper, the simplest possible example is chosen for studying the phenomena introduced by an air gap and lateral displacements in a waveguide line. The structure of actual switching device is of course considerably more complicated, but also more laborious to study. Moreover, the fundamental relationships between geometry parameters and electromagnetic effects are easier to discover with a simple model.

2. Simulations

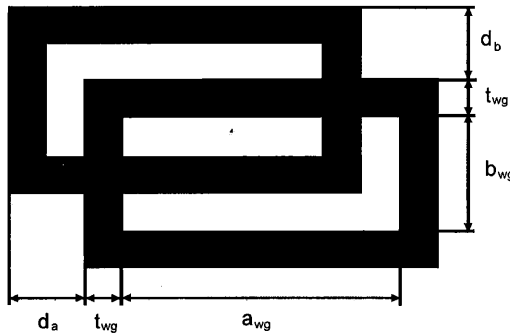


Figure 1. Waveguide dimensions and lateral displacements.

The case study consists of a junction of two collinear standard WR-28 waveguides having a longitudinal displacement (d_l) and lateral displacements (d_a, d_b), see Fig. 1. Scattering parameters of the transmission line were simulated with Ansoft HFSS 10. Absorbing boundary condition was used on the edges of the problem region, and ports were considered as perfectly matched. As a criterion for convergence, maximum change in the elements of the scattering matrix between successive iterations was set to 0.002. Frequency response was calculated on the Ka-band (27 - 40 GHz) with 0.1 GHz resolution.

A waveguide line with an air gap is a two-port device which has one resonance within its operating frequency band (higher resonances occur outside the band). In order to obtain accurate frequency response, adaptive solution has to be calculated quite near the resonant frequency. Hence, simulation is very time consuming because locating the resonance requires a series of adaptive solutions at different frequencies. If the resonant frequency is known, built-in frequency sweeps of the HFSS software can be used with sufficient accuracy.

Effects of the displacements d_l , d_a and d_b were studied by sweeping them as design parameters. In addition, effects of the waveguide width a_{wg} and height b_{wg} on the resonant frequency were studied.

3. Results

3.1 Effects of gap width

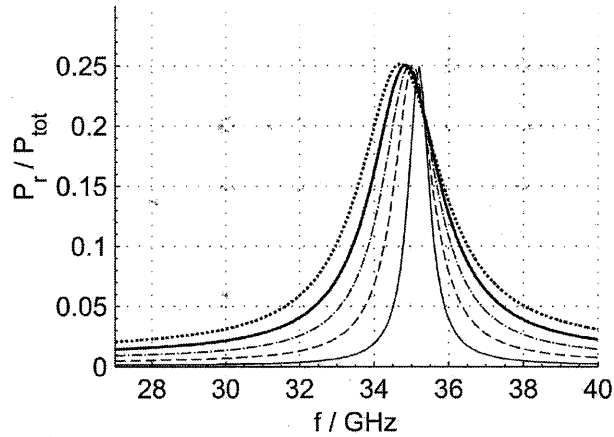


Figure 2. Ratio of radiated power and total power of the waveguide line for gap widths d_l of 0.05 mm (thin solid), 0.10 mm (thin dashed), 0.15 mm (thin dash-dotted), 0.20 mm (thick solid) and 0.25 mm (thick dotted).

An air gap in a waveguide line radiates a substantial portion of the total power fed in to the waveguide, as shown in Fig. 2. In this case, almost one fourth of the total power is radiated at the resonance. The gap also induces some reflection, which is shown in Fig. 3. The highest reflection occurs at the resonance and the best matching is generally achieved at frequencies below the resonance.

Figs. 2, 3 and 4 all show the effect of gap width. Relative portion of radiated power seems to remain constant at resonance. Widening the gap seems to increase reflection and thus overall loss slightly, but the effect is hardly noticeable. Far from the resonance a narrower gap induces clearly less loss than a wider one, because of a sharper resonance.

Fig. 5 shows that increasing gap width slightly decreases resonant frequency. Similar frequency shifting occurs if the width of a slot antenna is increased. For a dipole antenna (which is dual to a slot antenna) and also for a loop antenna, resonance

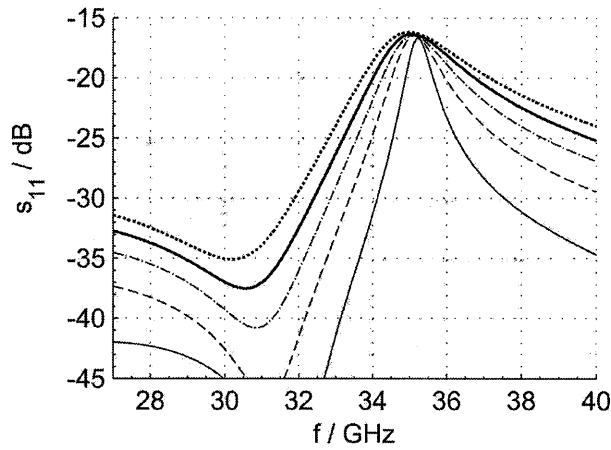


Figure 3. S_{11} of the waveguide line for gap widths d_l of 0.05 mm (thin solid), 0.10 mm (thin dashed), 0.15 mm (thin dash-dotted), 0.20 mm (thick solid) and 0.25 mm (thick dotted).

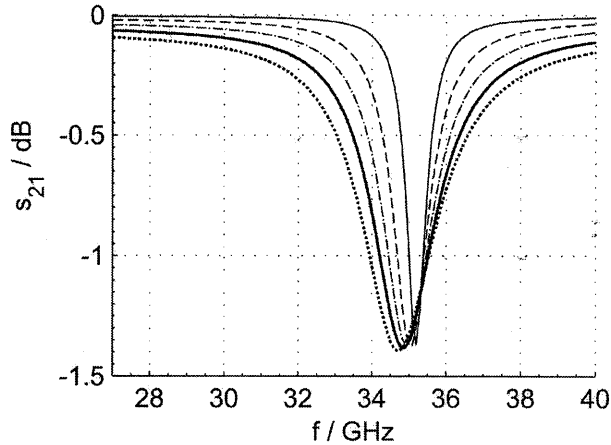


Figure 4. S_{21} of the waveguide line for gap widths d_l of 0.05 mm (thin solid), 0.10 mm (thin dashed), 0.15 mm (thin dash-dotted), 0.20 mm (thick solid) and 0.25 mm (thick dotted).

shifts in opposite direction as the diameter is increased [3]. In this sense the gap is dual to a loop antenna. For standard WR-28 dimensions, resonance occurs annoyingly near the atmospheric window on the Ka-band.

3.2 Effects of lateral displacements

The effects of lateral displacements on resonant frequency in both the E-plane (d_b) and

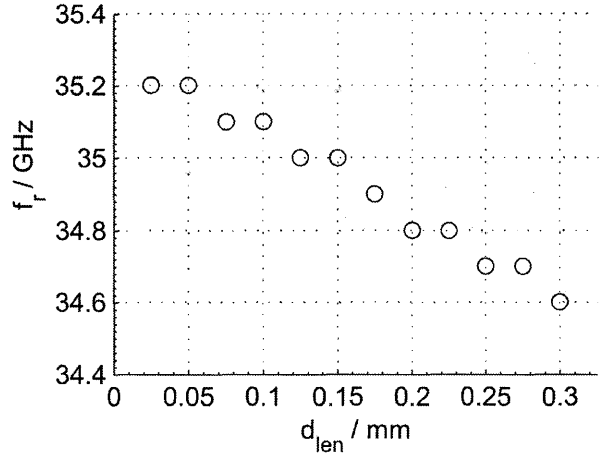


Figure 5. Resonant frequency of the waveguide line as a function of gap width d_l .

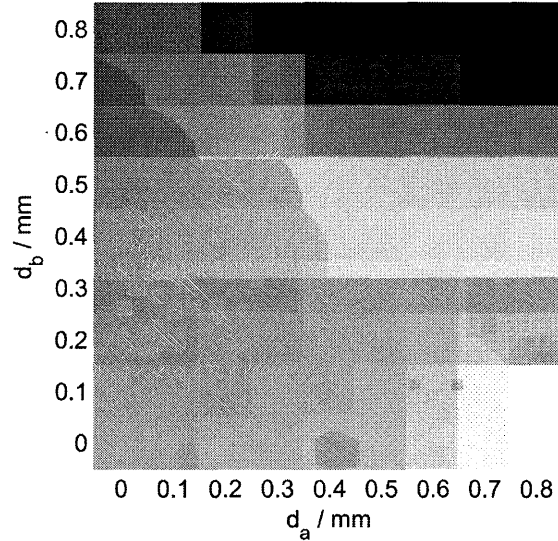


Figure 6. Resonant frequency of the waveguide line as a function of displacements d_a and d_b . The highest value is 35.6 GHz at the bottom right corner, the lowest value is 34.0 GHz at the top right corner and value at bottom left corner is 35.1 GHz.

the H-plane (d_a) are shown in Fig. 6. Displacement in the E-plane decreases resonant frequency whereas displacement in the H-plane increases it. If both displacements are present simultaneously, resonant frequency may increase or decrease. Worst case situation occurs when both displacements are large.

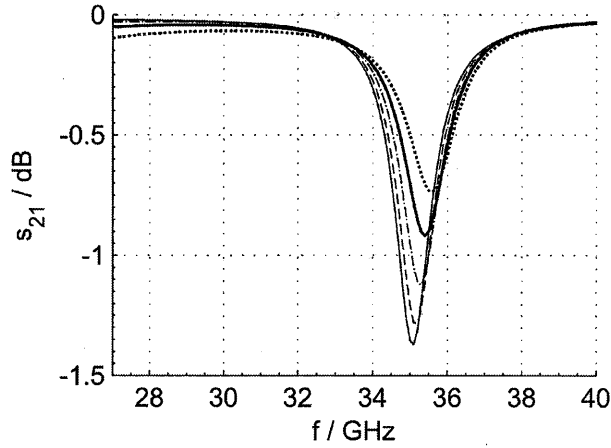


Figure 7. S_{21} of the waveguide line for lateral displacement d_a of 0 mm (thin solid), 0.2 mm (thin dashed), 0.4 mm (thin dash-dotted), 0.6 mm (thick solid) and 0.8 mm (thick dotted).

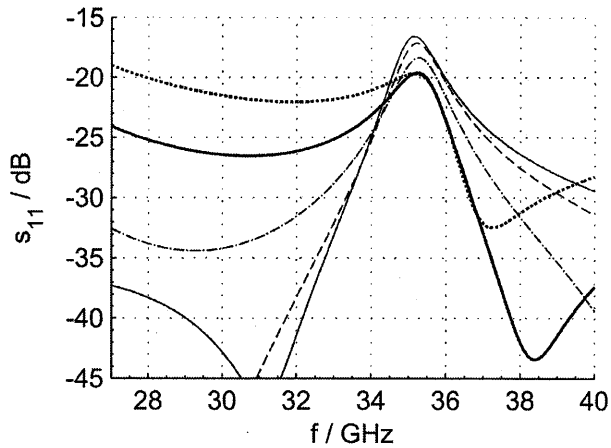


Figure 8. S_{11} of the waveguide line for lateral displacement d_a of 0 mm (thin solid), 0.2 mm (thin dashed), 0.4 mm (thin dash-dotted), 0.6 mm (thick solid) and 0.8 mm (thick dotted).

Fig. 7 shows transmission characteristics of the waveguide line with the H-plane displacement only. Increasing d_a increases resonant frequency. Losses due to both radiation and reflection are decreased with increasing d_a . As shown in Fig. 8, displacement generally reduces reflection at resonance and above it. For lower frequencies reflection is dramatically increased.

Transmission and reflection characteristics of the waveguide line for the E-plane dis-

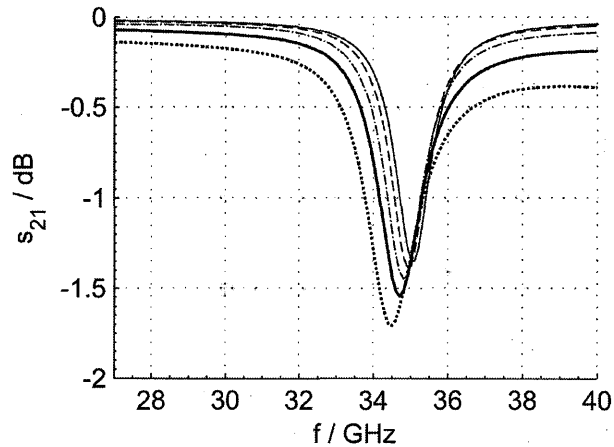


Figure 9. S_{21} of the waveguide line for lateral displacement d_b of 0 mm (thin solid), 0.2 mm (thin dashed), 0.4 mm (thin dash-dotted), 0.6 mm (thick solid) and 0.8 mm (thick dotted).

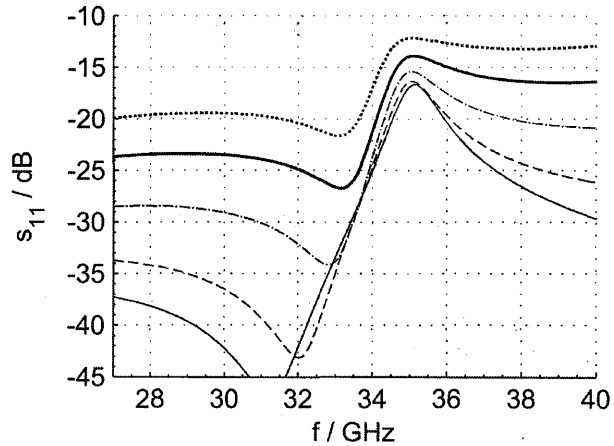


Figure 10. S_{11} of the waveguide line for lateral displacement d_b of 0 mm (thin solid), 0.2 mm (thin dashed), 0.4 mm (thin dash-dotted), 0.6 mm (thick solid) and 0.8 mm (thick dotted).

placement are shown in Figs. 9 and 10. The resonance shifts towards the lower end of the band and also deepens while d_b is increased. Larger displacement causes more reflection for all frequencies within the band.

3.3 Effects of waveguide dimensions

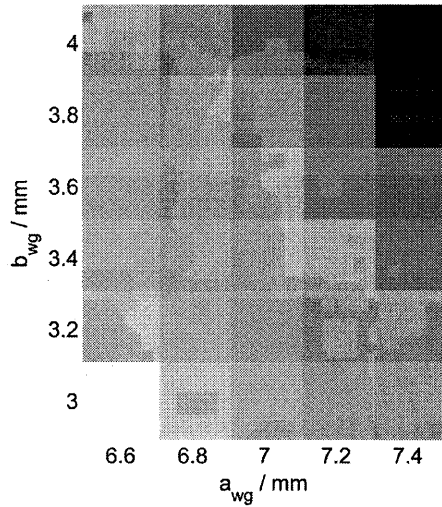


Figure 11. Resonant frequency of the waveguide line as a function of width a_{wg} and height b_{wg} . The highest value is 38.2 GHz at bottom left corner; the lowest value is 32.3 GHz at top right corner.

The effects of waveguide width and height on resonant frequency are shown in Fig. 11. It can be seen that increase in both a_{wg} and b_{wg} decrease the resonant frequency similarly. This leads to a thought of a "gap antenna" which perimeter determines its resonant frequency.

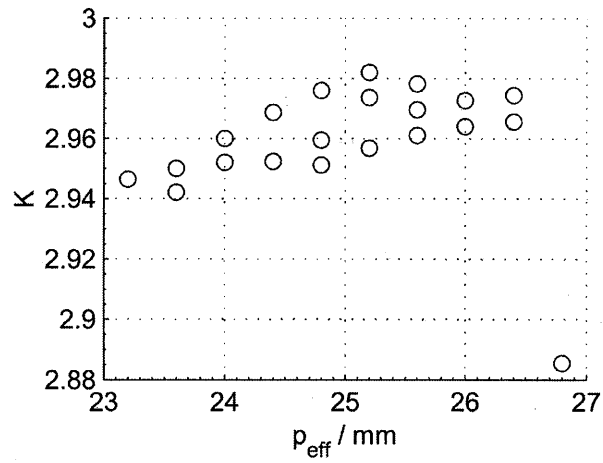


Figure 12. Electrical length of the "gap antenna".

The electrical length of the "gap antenna" plotted versus the average of the perimeters along inner and outer surfaces of the waveguide wall is shown in Fig. 12. The ratio of average perimeter and resonant wavelength, denoted by K , is about 2.97. Higher resonances can also be found but they appear outside the frequency band of interest. Factor K increases when the perimeter is increased while keeping wall thickness constant, i.e., increasing imaginary length-to-diameter ratio. It should be noted that similar relative increase in resonant frequency is obtained if this length-to-diameter ratio is increased by decreasing gap width.

4. Conclusions

An air gap in a waveguide line causes additional loss due to reflection and radiation. If narrow band signals are used, it is possible to minimize the loss by choosing operating frequency sufficiently far from resonance. If this is not possible or sufficient, resonant frequency can be shifted by properly changing the dimensions of the waveguide. The resonant frequency of the "gap antenna" is determined mainly by the width and the height of the waveguide. Lateral displacements, gap width and wall thickness all have minor effects on the resonant frequency. Resonant wavelength seems to be about three times the average perimeter of the waveguide.

The absolute loss is affected by both the width of the gap and lateral displacements. At resonance, gap width does not affect loss. However, sharper resonance of a narrower gap appears as lower loss outside the resonance if compared with a wider gap. Lateral displacement in the E-plane deepens the resonance and deteriorates feed matching. Displacement in the H-plane does not have as severe effect on reflection, and it actually reduces loss at resonance. Therefore, if lateral displacement cannot be avoided, it is better to occur in the H-plane.

References

- [1] H. Eskelinen and P. Eskelinen, *Microwave Component Mechanics*. Norwood, MA: Artech House, 2003.
- [2] A. F. Harvey, *Microwave Engineering*. Bristol: Academic Press, 1963.
- [3] R. C. Johnson, *Antenna Engineering Handbook (3rd ed.)*. USA: McGraw-Hill, 1993.

TIME/SPACE-PROBING INTERFEROMETER FOR PLASMA DIAGNOSTICS

V. A. Manasson, A. Avakian, A. Brailovsky, W. Gekelman*, A. Gigliotti*,
L. Giubbolini, I. Gordion, M. Felman, V. Khodos, V. Litvinov, P. Pribyl*, L. Sadovnik

(WaveBand, a Business Unit of Sierra Nevada Corporation, 15245 Alton Pkwy, Ste. 100,
Irvine, California, 92618

* UCLA Basic Plasma Science Facility, 1000 Veteran Ave.,
Los Angeles, California, 90095)

Rapid progress in plasma applications requires new instrumentation. Plasma density distribution is a key characteristic in fusion devices and in applications related to plasma processing. The plasma dielectric constant depends on the plasma density. The latter is subject to rapid local changes. Millimeter-wave (MMW) interferometry can be used for measuring such variations. It is desirable that the interferometer be capable to track both time and space plasma density variations. The latter typically requires a rather long time for changing the position of the instrument. We propose a new device that provides fast spatial probing. The new instrument is based on electronically controlled MMW beam-formers recently developed at WaveBand-SNC. The major advantages of this device are fast data acquisition and holographically flexible beam-forming. In future, an array of the proposed interferometers will be used as a key subsystem in plasma diagnostics tomography.

We have built a prototype of the new interferometer, which is planned to be installed for testing and for exploring the capability of the new approach at the Large Plasma Device (LAPD) at UCLA. The prototype comprises a heterodyne type reflectometer-interferometer operating at 76 GHz and two synchronously operating electronically controlled scanning antennas, one for transmitting MMW radiation and the other for receiving the radiation reflected back from a mirror placed behind the plasma tube. The antennas scan beams over a 30° angular range and can switch beam position within 3 μ s. Preliminary demonstration of the new instrument was performed at LAPD with a plasma density of $1 - 4 \times 10^{12} \text{ cm}^{-3}$. The new instrument can find applications in plasma diagnostics in scientific research as well as in commercial applications of plasma.

1. Introduction

Millimeter wave (MMW) interferometry is an established means for measurements of electron density in plasmas [1-3]. The underlying principle is the phase shift attained by a MMW beam traversing a plasma volume. The phase shift is proportional to the plasma index of refraction integrated along the beam path. The plasma refractive index according to the Drude model is

$$n = \sqrt{1 - \frac{f_p^2}{f^2}} \quad (1),$$

where $f_p \equiv \sqrt{\frac{Ne^2}{m_e}}$ is the electron plasma frequency; N is the plasma density, e is the

elementary charge, and m_e is the electron mass. For electromagnetic waves with frequencies higher than the plasma frequency (and for "O" mode in magnetized plasmas with $f \gg f_{pe}$), the plasma is almost transparent and the effect is a phase delay for the propagating wave. This makes MMW interferometry applicable for diagnostics of plasmas with densities lower than $N \sim (10^{11} - 10^{12}) \text{ cm}^{-3}$.

A conventional interferometer measures the phase delay of an electromagnetic wave passing through the plasma volume in a single direction (single channel), with respect to a wave which does not. Having these measurements performed in different directions and applying tomography makes it possible to recover 2-D or 3-D plasma density distributions. Using a single interferometer for tomography, with the inevitable repositioning of the instrument, makes the measurement process slow and inefficient. Using several conventional interferometers and parallel data acquisition speeds up the process but makes it much more costly.

We propose an alternative solution to the problem. Radical improvement in data acquisition time, at a moderate increase in the instrument cost, can be achieved by using a new type of device, a multi-channel interferometer (MCI). This is an instrument that can quickly switch from one direction of plasma probing to another (one measurement channel to another), thus eliminating the need for moving the entire device to a new position. The switched multi-channel device makes it possible to use an inexpensive conventional interferometer to probe many directions, each for a short time. In this paper we describe a prototype of the new multi-channel instrument that was built and installed for exploration and testing of the new approach at the UCLA Large Plasma Device.

The key elements of the new instrument are fast, operating almost in real-time, flexible beam-formers, based on a Electronically Reconfigurable Aperture (ERA) recently developed at WaveBand (a business unit of Sierra Nevada Corporation).

2. Interferometer

The block-diagram of the interferometer is shown in Figure 1. It comprises a transmitter, a receiver, and phase detector. The receiver is configured as a heterodyne operating at IF=19 GHz.

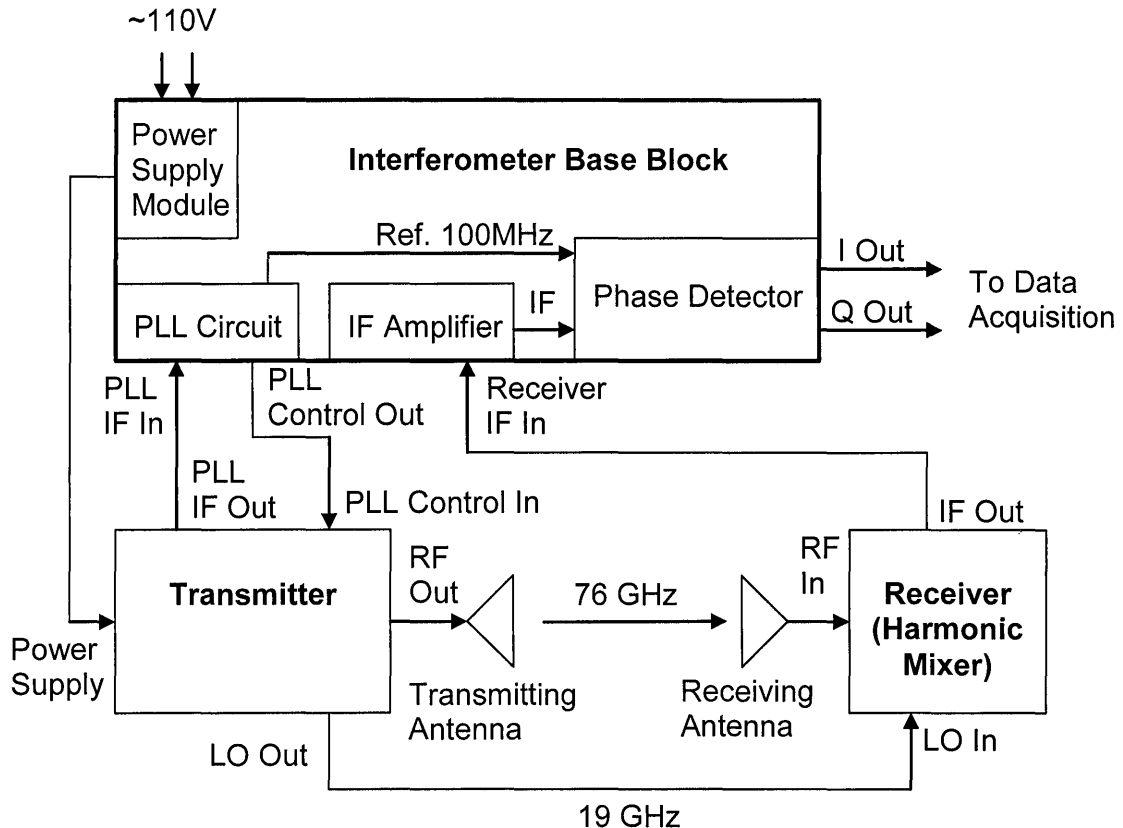


Figure 1. Block-diagram of the heterodyne interferometer.

The transmitter is based on a tunable Gunn oscillator with a central frequency of 75.9 GHz and a power level of 17 dBm. A magic tee distributes the source power between two channels. One channel goes to the transmitting antenna while the other one drives the harmonic mixer and is used for Phase Lock Loop (PLL), which synchronizes the Gunn oscillator with the reference oscillator. The reference oscillator is a 9.5 GHz dielectric resonator oscillator with an active frequency multiplier. Output 19 GHz signal from the multiplier goes to the reference input of the harmonic mixer. IF signal from the mixer output has a frequency of $4 \times 19 \text{ GHz} - F_{tr}$, where F_{tr} is the Gunn source frequency. The IF-signal goes to PLL circuit where it is compared to the 100 MHz clock oscillator signal. The PLL circuit output signal goes to varactor-biased input of the Gunn oscillator and sets its frequency to $F_{tr} = 4 \times 19 \text{ GHz} - 100 \text{ MHz} = 75.9 \text{ GHz}$. Received radiation is collected by the receiving antenna. A 2nd harmonic mixer is identical to the mixer used in

the transmitter. A coaxial cable is used to provide the reference 19 GHz signal from the transmitter to the receiver. Conversion loss in the harmonic mixer is less than 20 dB so that the received signal is large enough to provide the required signal-to-noise ratio. The quadrature phase detector (QPD) operating at 100 MHz is used to increase the accuracy of phase measurement to a level of better than 1°. The IF signal is amplified by the IF Amplifier. The phase detector measures the phase difference between the IF signal and the reference signal generated by the PLL Circuit.

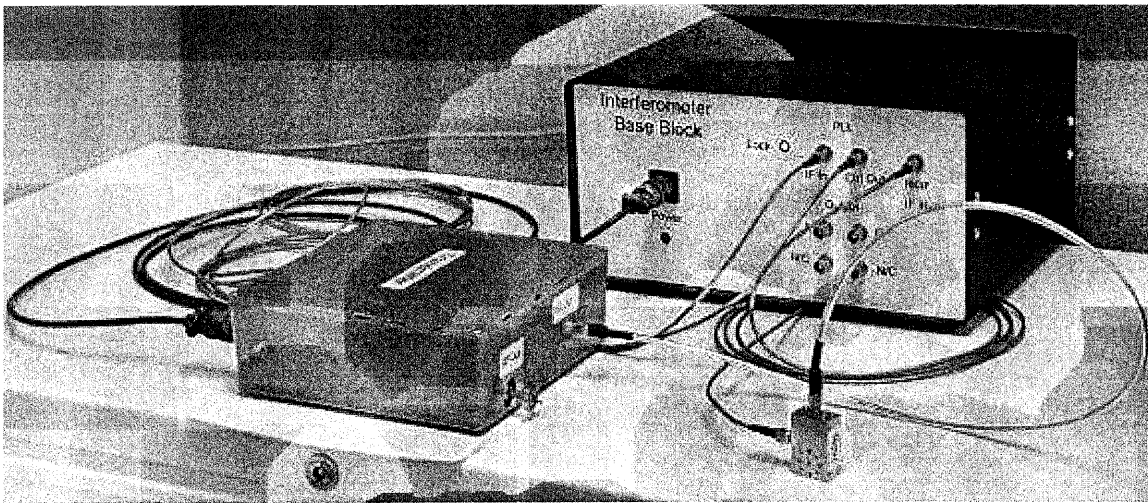


Figure 2. Interferometer assembly.

Signals from the Interferometer's I and Q outputs (U_I and U_Q) provide phase information. The phase shift accumulated by the MMW signal passing through the plasma is given by the equation:

$$\phi = \tan^{-1}(U_I/U_Q). \quad (2).$$

The prototype interferometer was assembled as a three unit system: Interferometer Base Block, Transmitter, and Receiver, and is shown in Figure 2.

3. Electronically Reconfigurable Aperture: Simulation

A traditional beamforming/beam steering antenna utilizes a phased array architecture, and represents a set of distributed elementary antenna elements coupled to phase shifters. Typically, each antenna element is individually controlled via the respective phase shifter. Phased array antennas are cumbersome, prohibitively expensive, and unacceptably lossy in the W-band.

We used an alternative approach where the antenna aperture represents a reconfigurable hologram and electronic control occurs due to the injection, and extraction, of electron-hole plasmas (not to be confused with the gaseous plasma under the test!) into, and out

of, a semiconductor waveguiding medium. The aperture hologram can be varied continuously (WaveBand has developed a method for continuous aperture variations in mechanically controlled antennas and in optically controlled plasma grating antennas [4,5]) or varied digitally in a pixelized aperture. Pixels, in turn, can be controlled either continuously or digitally. The pixelized Electronically Reconfigurable Aperture (ERA) with digital control, combines high stability and beam-forming flexibility. The ERA beam-forming flexibility is at the same level as the flexibility of traditional phased array antennas, however, ERA's temperature stability is much better.

For the plasma interferometer prototype we have developed a monolithic 1-dimensional (1D) ERA. The development process included Ansoft HFSS simulations. A typical simulated far-field beam pattern is shown in Figure 3.

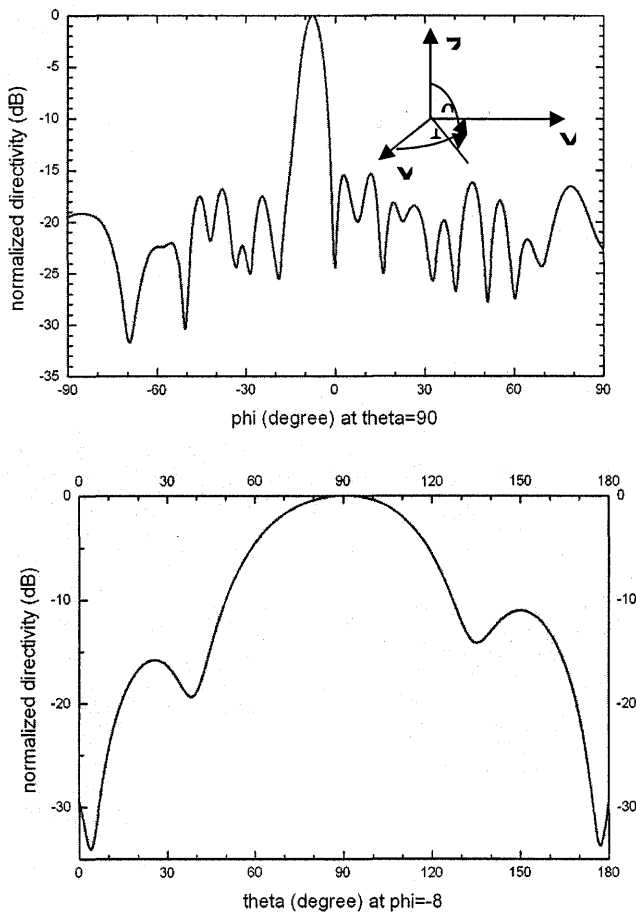


Figure 3. Simulated far field antenna beam pattern for 1D ERA: upper curve represents the azimuth beam pattern, lower curve represents the elevation beam pattern.

4. ERA Test Results

Two monolithic ERA chips were fabricated for installation in the interferometer. Each chip was 3-inches long, or approximately 19 wavelengths at 76 GHz. The chips were coupled to RF electronics via dielectric waveguides. The required hologram patterns were created by using a programmable electronic driver-controller. Beam shape in the H-plane was controlled by selecting the appropriate hologram pattern. Beam shape in V-plane was fixed and determined by the cylindrical lens attached to the aperture. The antenna assembly with the attached driver-controller is shown in Figure 4.

Each antenna was capable of creating a sequence of beams covering a wide angle span. The beam width at -3 dB level in the H-plane was on the order of 3-3.5 deg. Samples of measured H-plane beam patterns are shown in Figures 5 and 6.

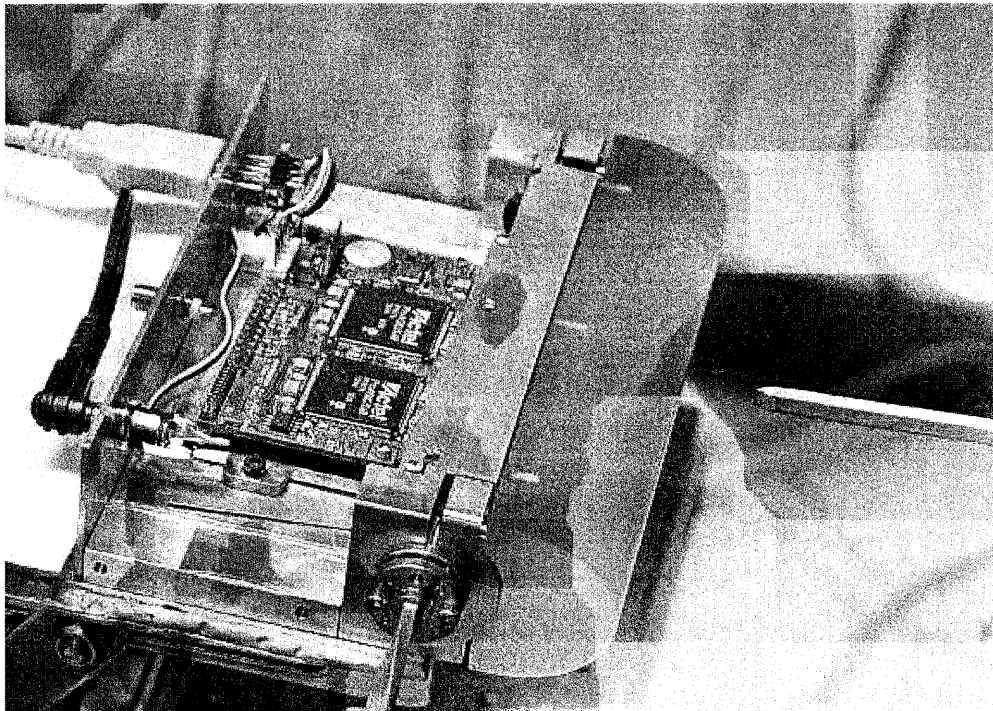
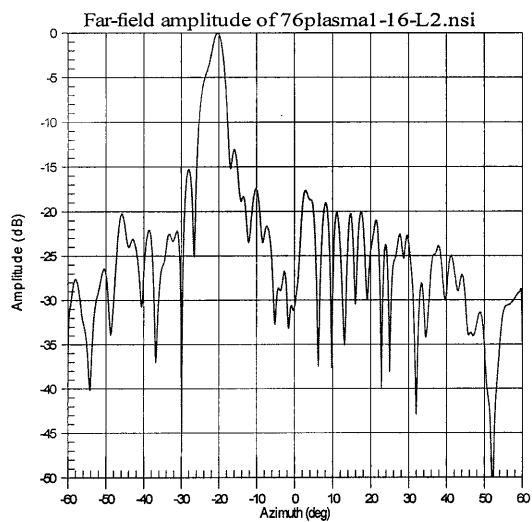
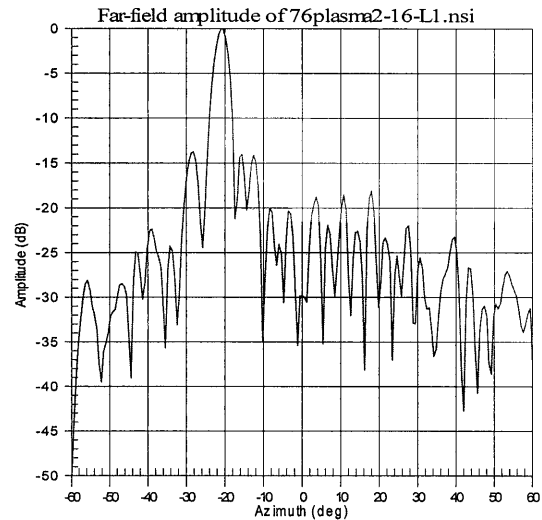


Figure 4. Antenna assembly at the near-field antenna measurement test setup.

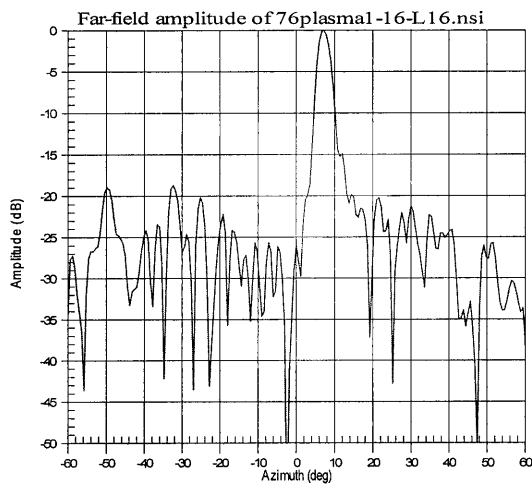
Hpeak at: -20.33018 deg
 Directivity = 29.662 dB,
 -3. dB beam width: 3.52 deg



Hpeak at: -20.78409 deg
 Directivity = 30.170 dB,
 -3. dB beam width: 3.42 deg



Hpeak at: 7.04725 deg
 Directivity = 30.644 dB,
 -3. dB beam width: 3.16 deg



Hpeak at: 7.02295 deg
 Directivity = 31.231 dB,
 -3. dB beam width: 3.09 deg

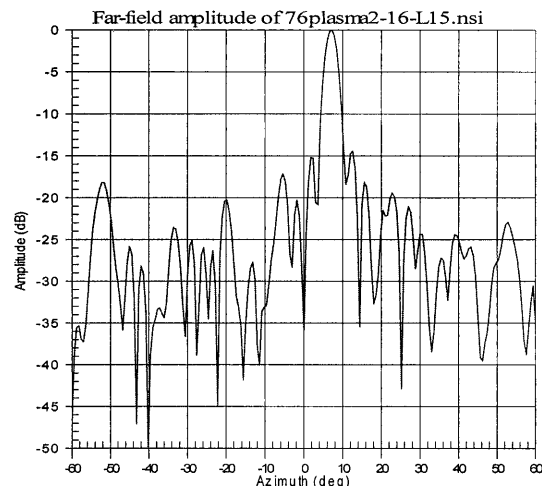


Figure 5. Measured H-plane beam patterns for two antennas
 (left curves and right curves correspondingly)
 with two hologram patterns
 (upper and lower curves).

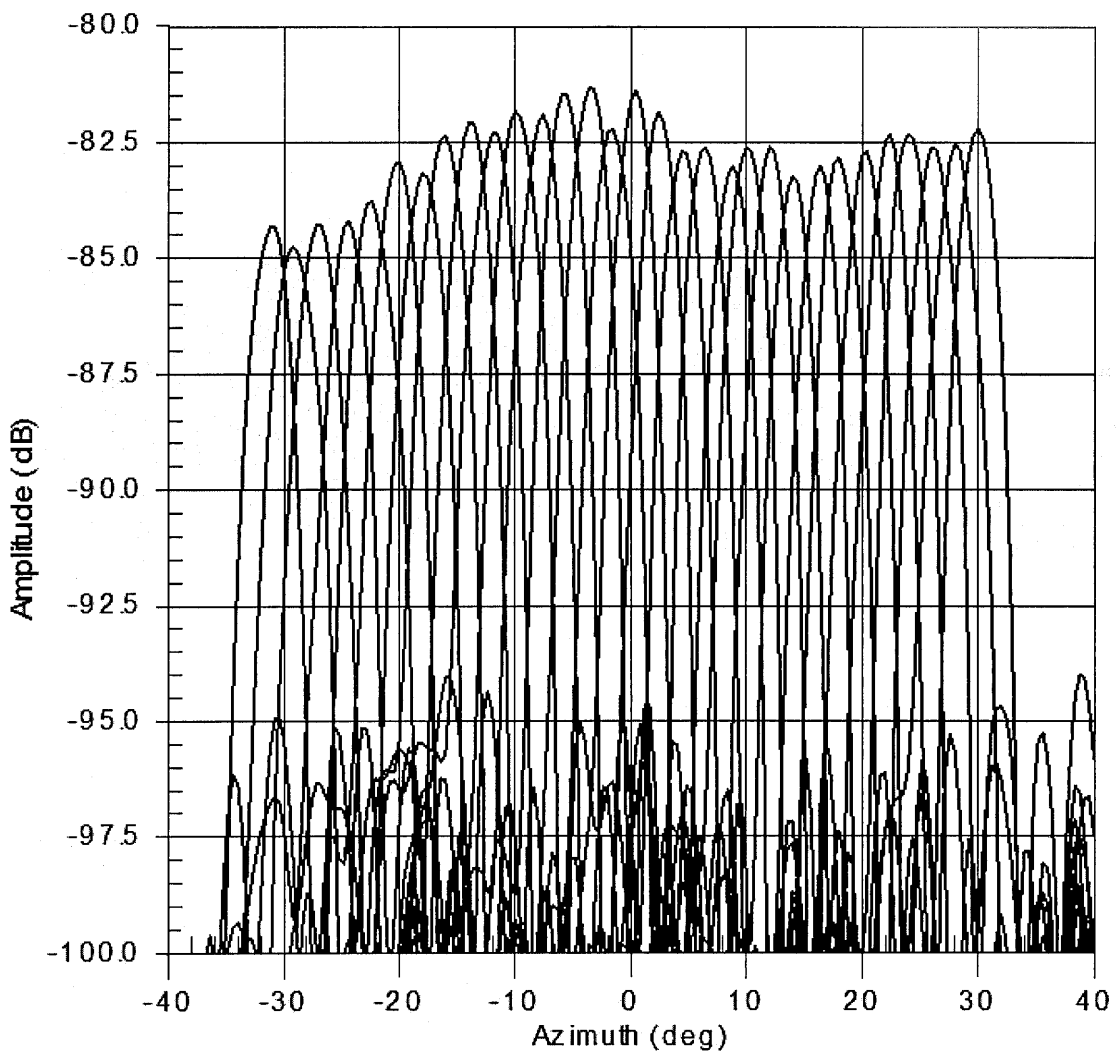


Figure 6. Selected H-plane beam-patterns corresponding to different hologram patterns.

To measure the time needed for switching from one beam position to another, we used a setup consisting of the interferometer receiver and the transmitter radiating toward the antenna via a pyramidal horn. The ERA was programmed to be positioned toward the horn and was located at a distance of 1 m from the horn. Two hologram patterns were loaded into the driver memory, one for the antenna pointing toward the horn, the other for the antenna pointed in a different direction. The harmonic mixer was connected to the antenna output. A 19 GHz RF signal was fed into the reference input of the mixer. The differential frequency from the mixer output was amplified and recorded by oscilloscope. The oscillogram is shown in Figure 7.

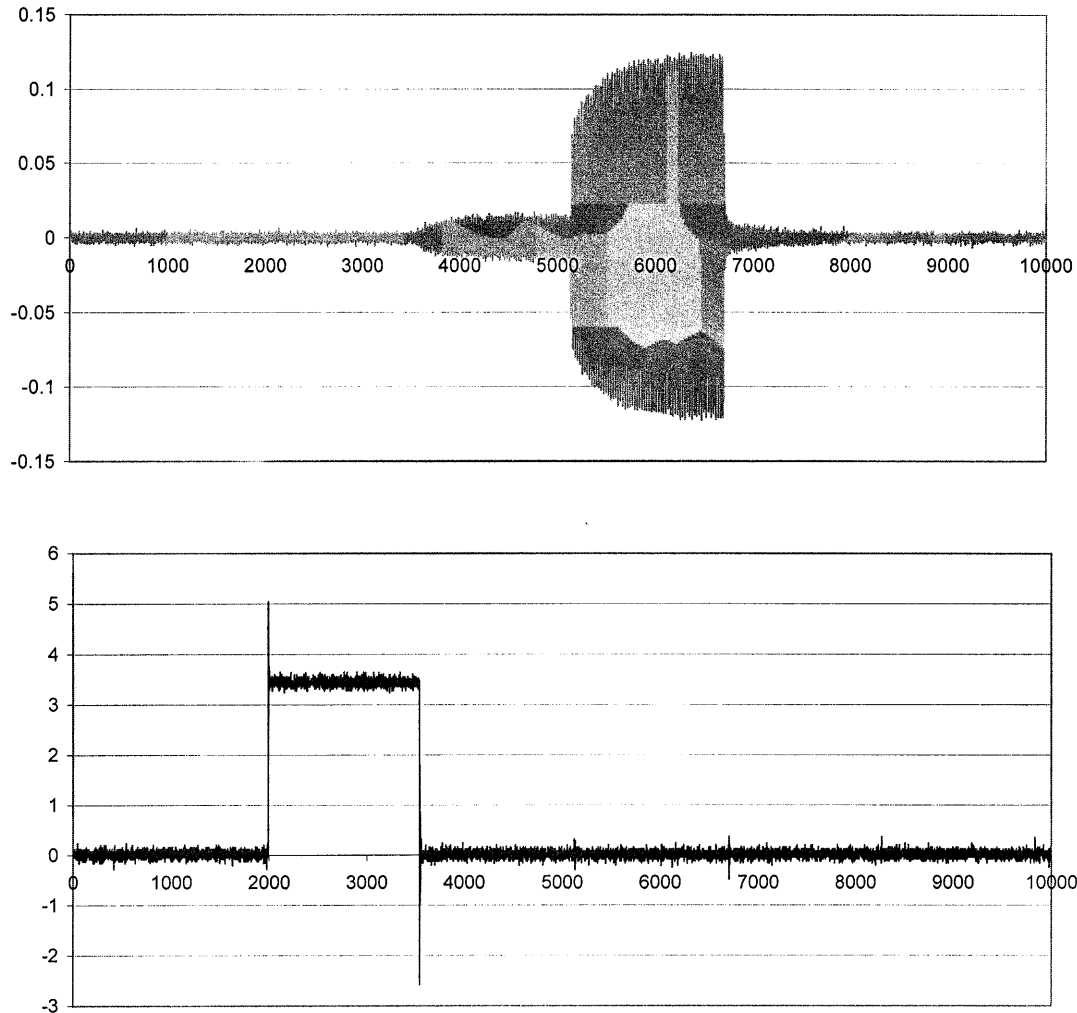


Figure 7. Switching time measurements: upper curve is the antenna response, lower curve is pulse generated by the antenna driver.

The driving pulse duration was 6.6 microseconds (lower curve). The signal generated by the antenna has a rise time on the order of 3 microseconds (the upper curve).

5. MCI Assembly and Test Results

The transmit and receive antennas were assembled on a common mount as shown in Figure 8. The overall size matched the size of the LAPD window. The antennas were

synchronized by synchronization of their drivers. The antenna hologram patterns and their sequences were identical for both antennas.

We initially tested the instrument using a corner reflector placed at a distance of 1 m from the antennas (Figure 8). The interferometer's I and Q outputs were connected to the oscilloscope, which was synchronized with the antenna drivers. The antennas scanned in the vertical plane. The beginning of the scan corresponded to bottom beam position. Signals detected by the antenna appeared with a time delay depending on the vertical position of the reflector: the higher the reflector the longer the time delay. This can be seen by comparing the upper and the lower photos in Figure 8. Phase shift was determined by comparing I and Q outputs. By inserting thin dielectric films between the antenna and the reflector we found that the phase sensitivity is better than half a degree.

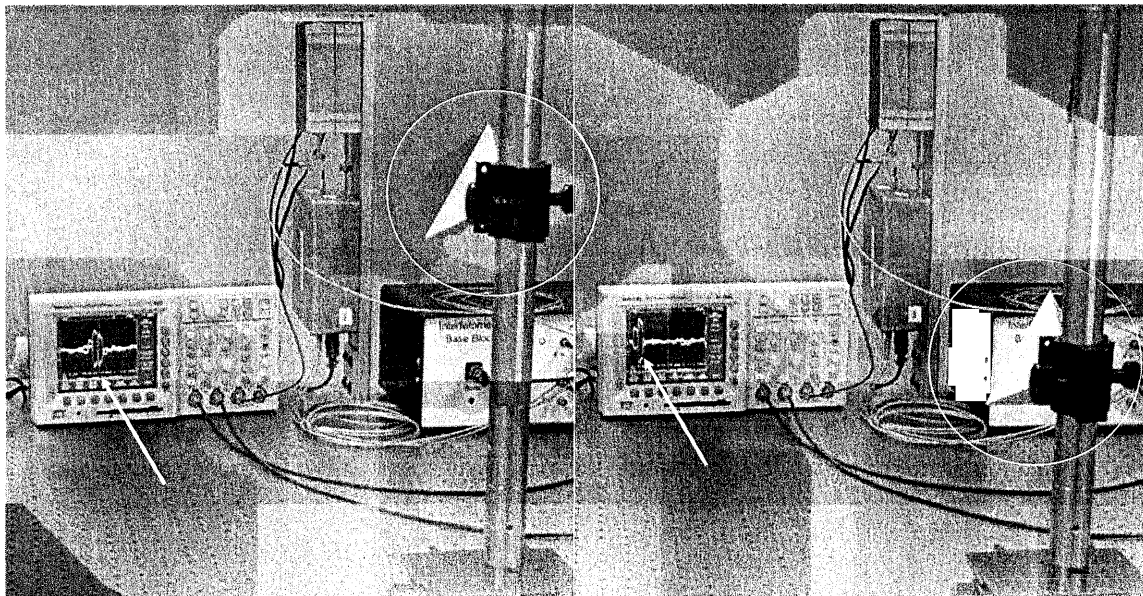


Figure 8. MCI preliminary test.

Two pictures taken for different positions of the corner reflector.
I and Q signals recorded on the oscilloscope screen appear at different times,
depending on the position of the corner reflector.

We have tested the instrument with a real plasma at the UCLA Large Plasma Device (LAPD). The interferometer antennas were attached to the LAPD window and the detected signals are shown in Figure 9. They are illustrative of plasma dynamics during plasma production and decay.

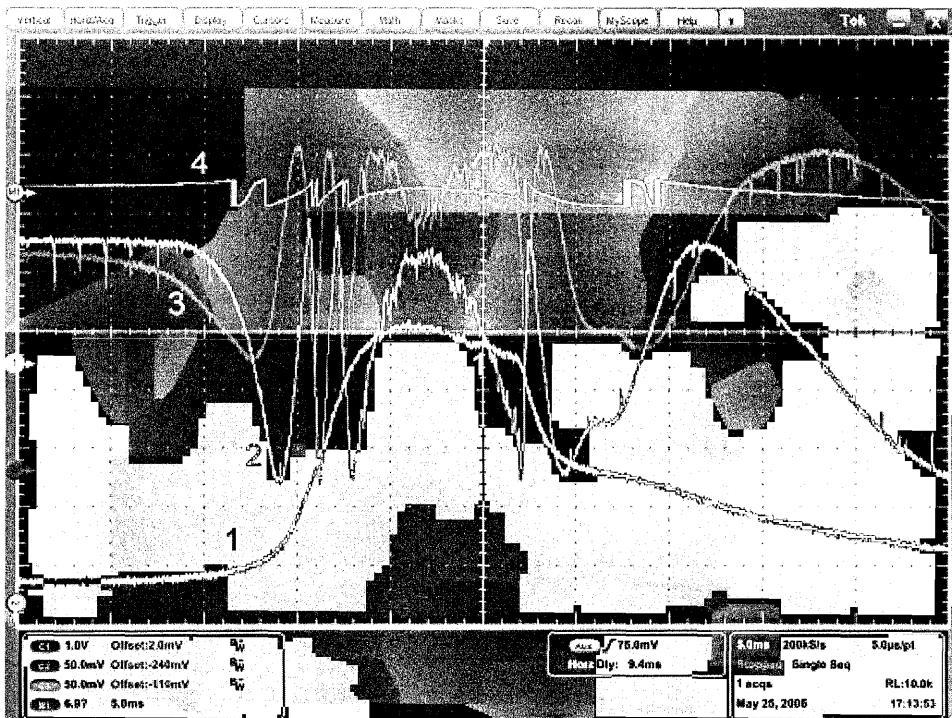


Figure 9. Data obtained while testing the interferometer at the LAPD. Curve 1 is a reference signal from an independent 56 GHz interferometer. Curves 2 and 3 are, respectively, I and Q signals from the interferometer. Curve 4 is the calculated phase shift obtained using formula (2).

Results presented in Figure 9 show that the phase dynamics measured by the MCI are correlated with the plasma density dynamics. However, the data are affected by parasitic reflections from the plasma reactor window. The accumulated phase shift inserted by plasma greatly exceeds 2π . Without window reflection, all curves would have a vertical span equal to 2π . However, reflection from the reactor window creates a parallel reflection channel that screens the plasma phase variations. In future operation, the window reflection will be minimized by optimization of the window material and its geometry.

The effect of the window reflection can be accounted for, and the corrected data have been used to estimate plasma density. The resulting curves are presented in Figures 10 and 11.

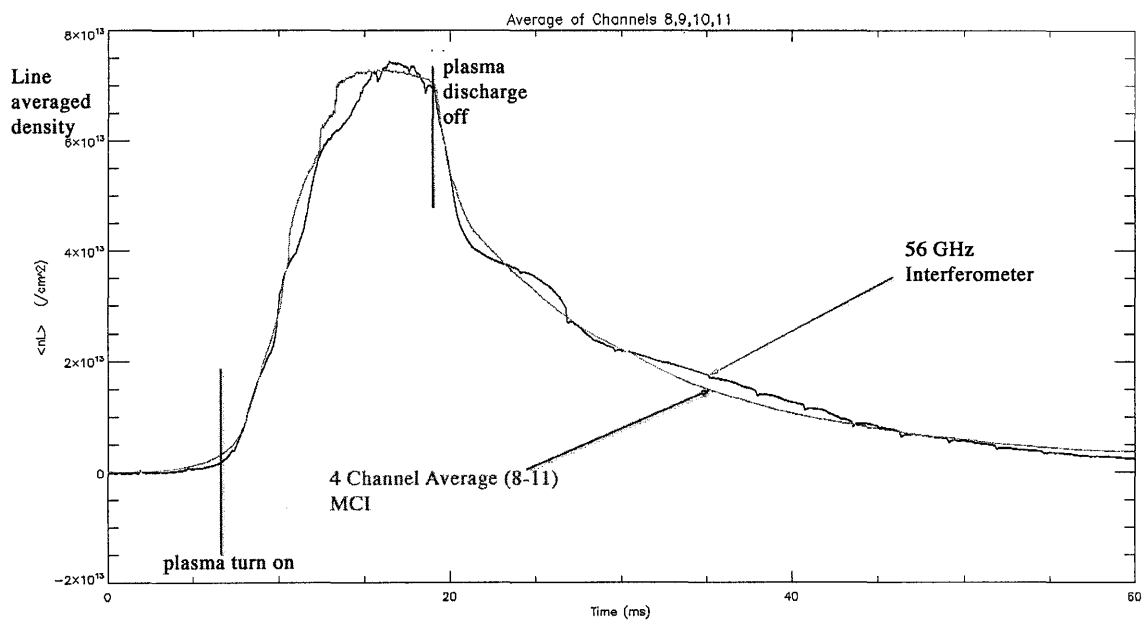


Figure 10. Plasma density dynamics obtained with the new interferometer in comparison with the reference device (56 GHz).

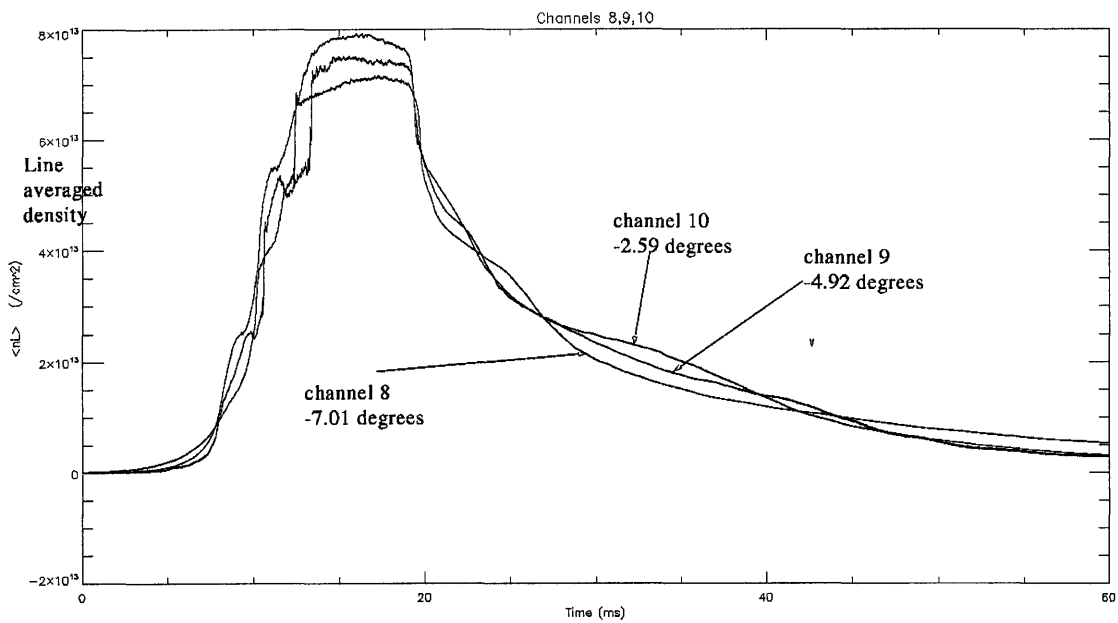


Figure 11. Plasma density dynamics in different directions obtained with the new interferometer.

6. Conclusions

We have designed, fabricated and preliminarily tested a scanning interferometer for plasma tomography. The device utilizes novel beam steering antennas based on WaveBand's ERA technology. Preliminary test at the Large Plasma Device at UCLA was successfully completed.

7. Acknowledgment

This work was supported by the US Department of Energy (contract DE-FG02-03ER83843).

8. References

- [1] D. Veron, "Submillimeter Interferometry of High-Density Plasmas", in Infrared and Millimeter Waves, K.J. Button, ed., Vol. 2, pp. 67-135, NewYork, Academic Press, 1979.
- [2] N.C. Luhmann, Jr. "Instrumentation and Techniques for Plasma Diagnostics: An Overview", in Infrared and Millimeter Waves, K.J. Button, ed., Vol. 2, pp. 1-65, NewYork, Academic Press, 1979.
- [3] C.W. Domier, W.A. Peebles, and N.C. Luhmann, "Millimeter-wave interferometer for measuring plasma electron density," Rev. Sci. Instrum., vol. 59, No.8, pp.1588-1590, 1988.
- [4] V.A. Manasson, L. S. Sadovnik, K. Spariosu, "Compact Version of an Optically Scanning MMW Antenna," 20th Antenna Application Symposium, Allerton Park, Monticello, IL, pp. 1-11, 1996
- [5] V. A. Manasson, L. S. Sadovnik, V.A. Yepishin, L. Timashpolsky, and R. Mino, "Spinning-Array 2-D Beam-Steering MMW Antenna," 23rd Antenna Application Symposium, Allerton Park, Monticello, Illinois, pp. 243-250, 1999

Near Field Target DOA Simulation Using Antenna Arrays

Louis Botha and Jacques Cilliers
CSIR

PO Box 395, Pretoria, South Africa, 0001
Tel: +27 12 841 2899 Fax +27 12 379 1766
Email: lbotha@csir.co.za

Abstract

This paper presents a feasibility study into the concept of generating the correct angle of arrival for a simulated radar target by making use of an array of antennas in the near field of the radar's antenna. The target's range delay and Doppler shift is simulated by means of a Digital Radio Frequency Memory (DRFM) coupled to the antenna array. This architecture will thus enable the generation of more realistic test flight profiles, which include target angle, and not just "inbound" and "outbound" profiles that can be generated by a DRFM.

The phase and amplitude of each antenna can be controlled to induce a distorted wave front over the aperture of the radar antenna. This will have the effect of producing a target with an apparent angle of arrival that is not aligned with either of the antennas in the array, but is somewhere between them. The possibility also exists to generate targets that are outside the area bounded by the antennas.

As the aim of this paper is to determine the feasibility of this concept, only simulation results will be presented for an X-band tracking radar antenna.

1. Problem description

When testing modern radar systems it is desirable to simulate the environment in which the radar is to operate as realistically as possible. The amount of testing which can be conducted against real military type targets during the development of a radar is usually limited from a budgetary and aircraft availability point of view. This is especially true in developing countries. All threat aircraft types might also not be available. Testing of the radar with hardware-in-the-loop (HIL) simulators is thus necessary to reduce cost and to ensure thorough testing of the radar system.

The radar designers would like to simulate at least the following aspects of a target when testing the tracking performance of a radar:

- Range delay

- Doppler shift
- RCS variation
- Angular movement of the target.

A popular technique of simulating the first three parameters above is to make use of a Digital Radio Frequency Memory (DRFM). The DRFM system (shown in Figure 1) down-converts the radio frequency (RF) signal to an intermediate frequency (IF) with a bandwidth that covers the agility bandwidth of the radar. The IF signal is then band-limited and sampled at a high sampling rate (usually 2 Gsamples/s). The data samples are read into a fast memory and can be accurately time delayed with high resolution. The delayed data is converted back to the intermediate frequency and can be up-converted to the original RF frequency. During the up-conversion process a programmable Doppler shift can be introduced, as well as pseudo random fluctuations in the signal level that can be used to simulate the RCS fluctuations of targets.

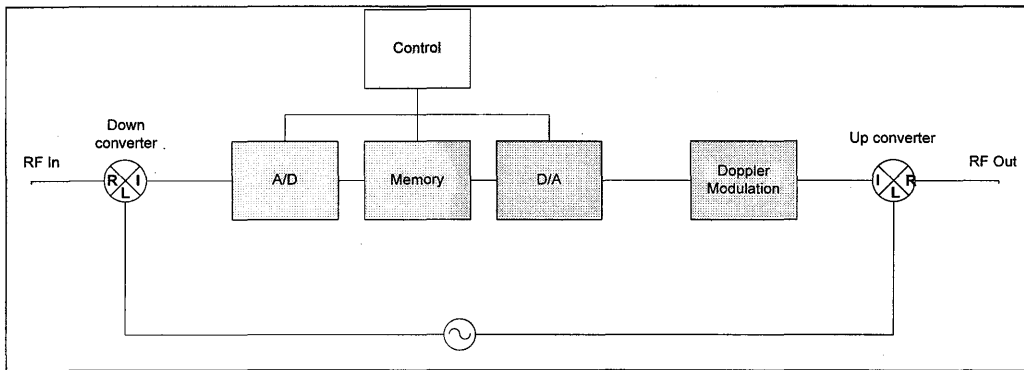


Figure 1 Block diagram of a typical DRFM system.

Monopulse radars make use of the amplitude and/or phase differences between the antenna ports to determine the angle of arrival of a target return. This technique allows the radar to calculate a single target's angle to an accuracy which is much higher than the beamwidth of the antenna. Figure 2 shows a typical antenna pattern with sum pattern and azimuth difference pattern. By taking the ratio of the difference channel voltage to the sum channel voltage (amplitude comparison) a function is obtained that will give the angle of arrival of the target very accurately. This function is depicted in Figure 3. This shows the relationship between the ratio of the patterns and the off boresight (OBT) angle.

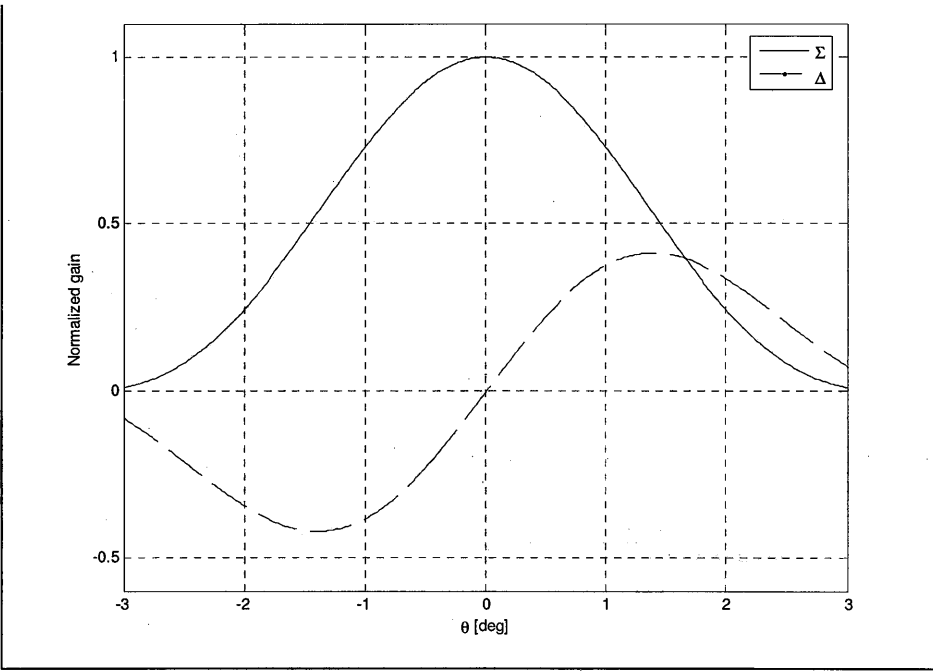


Figure 2 Principal plane monopulse patterns.

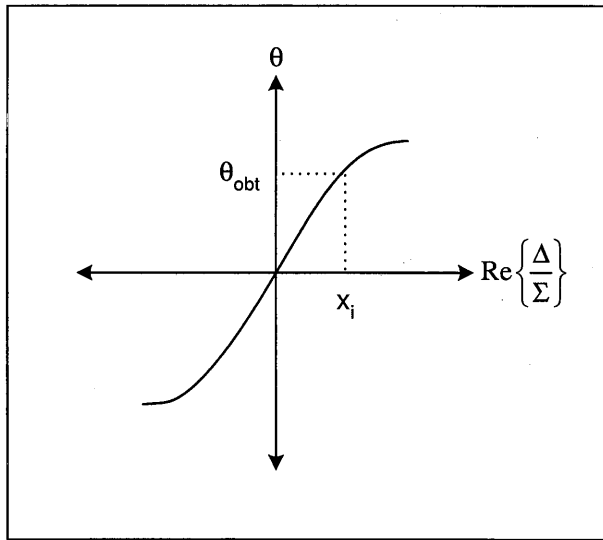


Figure 3 Monopulse error slope.

If the antenna can be removed, the antenna can be bypassed and replaced with an antenna simulator. Such an antenna simulator will typically split the RF returned from the DRFM into a number of channels equal to the number of channels of the antenna system. Typical channels will include a sum channel, azimuth difference channel, elevation difference channel and sidelobe blanking channels. Each of the channels can then be manipulated to induce an amplitude and phase change that is a function of angle, so as to introduce the magnitude and phase changes that would have been introduced by the antenna system. One of the necessary conditions for an antenna simulator to work is that the antenna-pointing angle must be available from the radar, so that the angle between the target and antenna boresight can be calculated and given as an input to the antenna simulator.

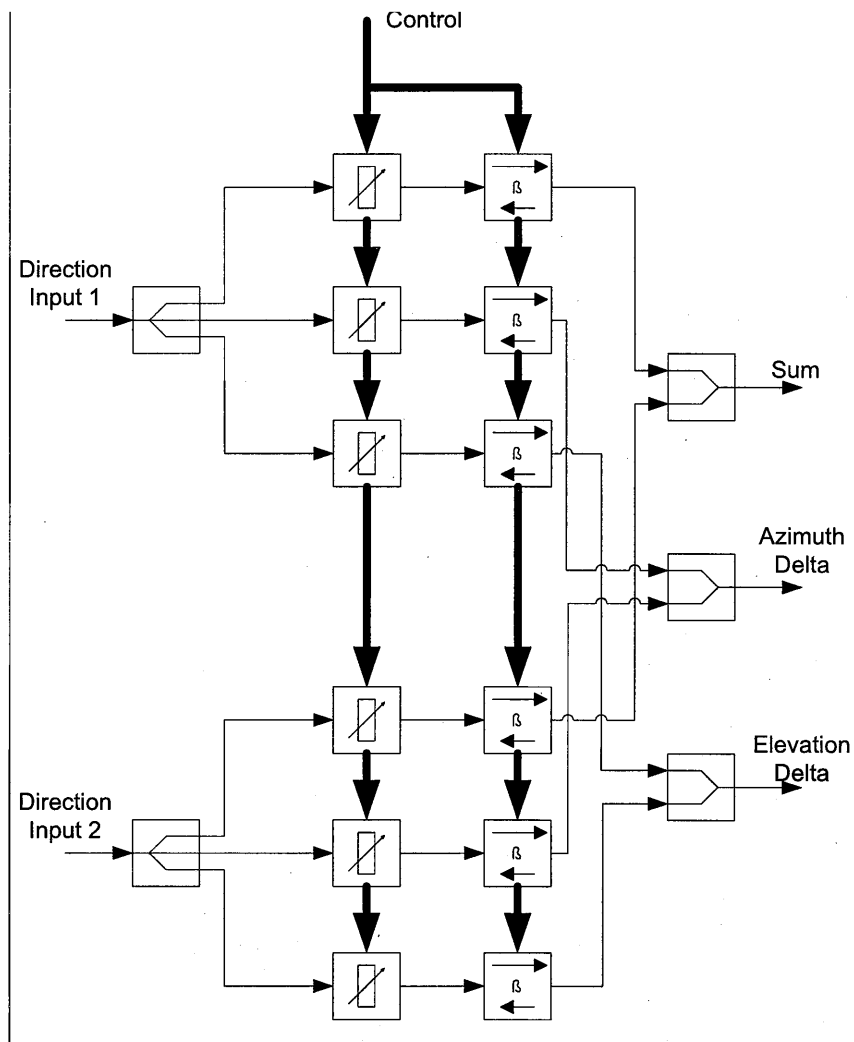


Figure 4 Simplified block diagram of an antenna simulator

If the antenna cannot easily be removed, or the radar does not supply the antenna-pointing angle, it is not possible to use an antenna simulator. This is often the case when evaluation tests have to be performed on a radar installed in an aircraft, where minimal information is available about the detailed radar operation and configuration. For example, when countries acquire a complete fighter aircraft with integrated radar and the operation of the radar under different conditions needs to be evaluated so as to improve the application of the fighter.

In this case it would be very useful to have an external simulator that can simulate the direction of arrival (DOA) of the signal from the target. There are several ways in which this can be achieved.

In the simplest case use can be made of a single antenna that is mechanically moved over a large area in front of the radar antenna. The disadvantage of this is that the speed and accelerations that the antenna must be moved for highly manoeuvrable targets can become excessive. Such a system will either be very expensive or will be limited in the dynamics of the target profiles which it can generate. Another problem is that flexible cables must be used between the antenna and the rest of the HIL system, which will add to the cost of the system as well as introducing signal distortion during movement. To move the HIL system with the antenna is not really an option because of the size and weight that must be moved, as well as the necessity of supplying power to the system still means a form of cable, even if the control can be done via wireless link.

A second approach would be to make use of a large number of fixed antennas, and the RF is switched from the HIL system to a specific antenna. By using fast switches this can be done at high rates. The number of antennas, and thus switches needed for this makes this solution impractical.

The solution suggested in this paper utilizes a very sparse array of antennas to illuminate the radar antenna under test. By varying the relative amplitude and phase of the antennas in the array, the apparent direction of arrival (DOA) of the simulator can be changed. From a cost perspective it is important to minimize the number of antenna elements as this determines the cost. Ideally only four elements should be used at any one time. If it is necessary to simulate large angles, more elements can be used, and the four appropriate elements selected. If this is done using switches after the amplitude and phase selection, care will have to be taken to ensure that the amplitude and phase selected is preserved. This should be possible with careful calibration.

2. Simulation scenario

To prove the concept a specific scenario was selected for the simulation study. The radar antenna chosen is a 1.2 m monopulse antenna operating at 9.5 GHz. The antenna was simulated as a square array consisting of omnidirectional elements and element spacing such that the antenna can have a scan angle up to 90°. A \cos^2 aperture taper was applied to the array for the sum pattern. An extra cos type correction was applied for the difference patterns in the middle of the aperture so as not to have the abrupt change in magnitude that would otherwise happen. This setup was chosen to give results that are close to what could be expected with a multi-mode monopulse horn feed. Figure 5, Figure 6 and Figure 7 gives the aperture distribution for the sum, azimuth difference and elevation difference patterns respectively. Figure 8, Figure 9 and Figure 10 shows the close in antenna patterns of the simulated antenna. Figure 11 and Figure 12 show the error function of the simulated antenna for the azimuth and elevation channels

respectively. Figure 13, Figure 14 and Figure 15 show the antenna patterns over a wider angular range.

The simulator array is a set of four horn antennas (similar to the AEL type pinwall wideband (2-18 GHz) horns) mounted at the four corners of a square, orthogonal to the radiation direction of the monopulse antenna. The array is at distance of 30 m from the radar antenna. For this scenario where the radar antenna and simulation array are symmetrical, the weights chosen for the simulation array antennas were chosen as real weights (no phase control) and with the weights selected by two independent variables W_x and W_y . Each weight is allowed to vary between 0 and 1. The actual weights of the four horns are then combination of the product of W_x , W_y , $(1 - W_x)$ and $(1 - W_y)$. Figure 16 shows the geometry and the amplitude weights of each horn.

The simulations were conducted for different element spacings so as to determine the maximum practical spacing could be obtained while still produce good results.

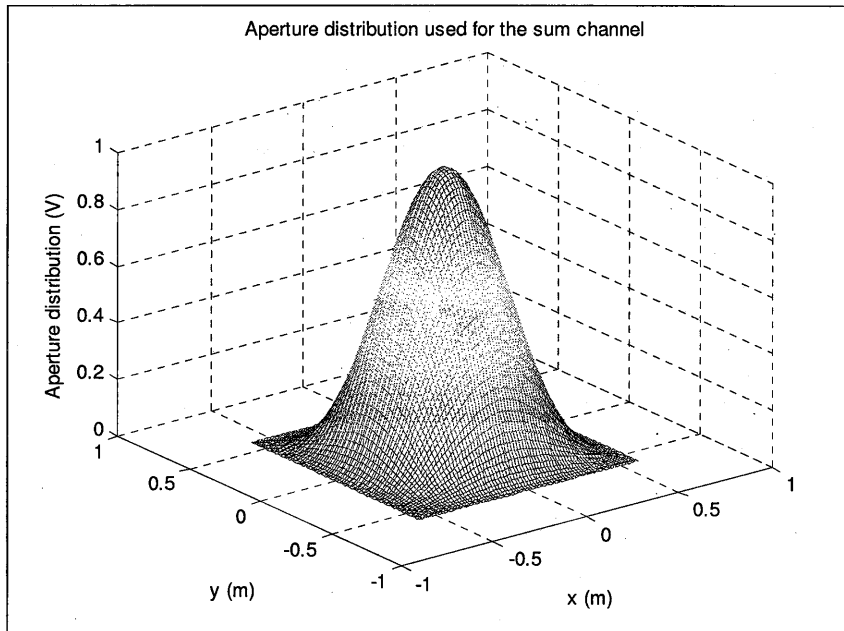


Figure 5 Aperture distribution used for the Sum pattern.

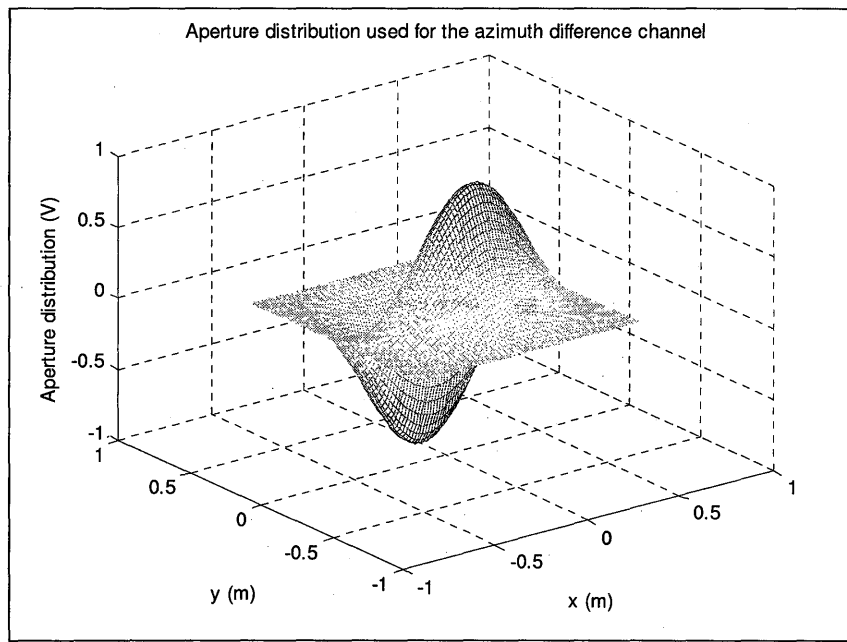


Figure 6 Aperture distribution used for the Azimuth difference pattern.

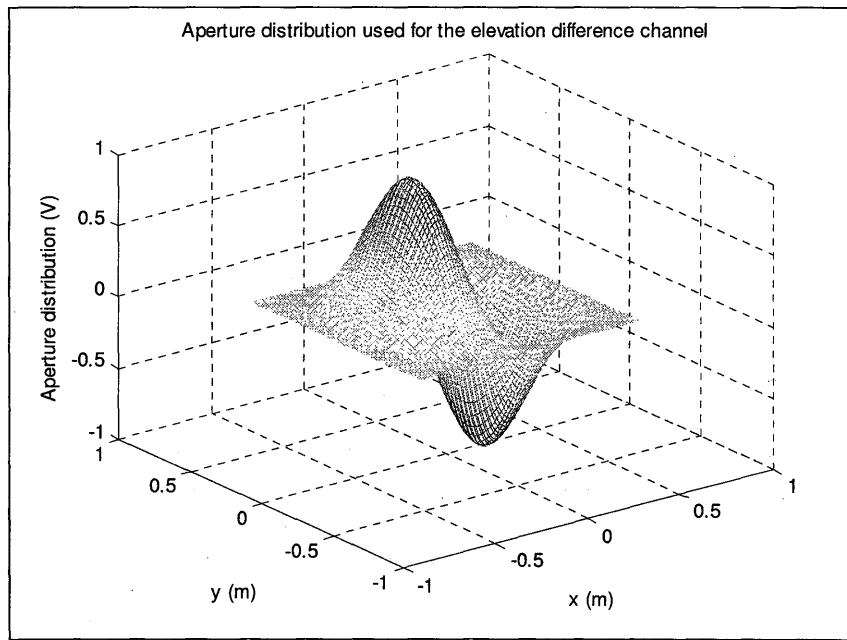


Figure 7 Aperture distribution used for the Elevation difference pattern.

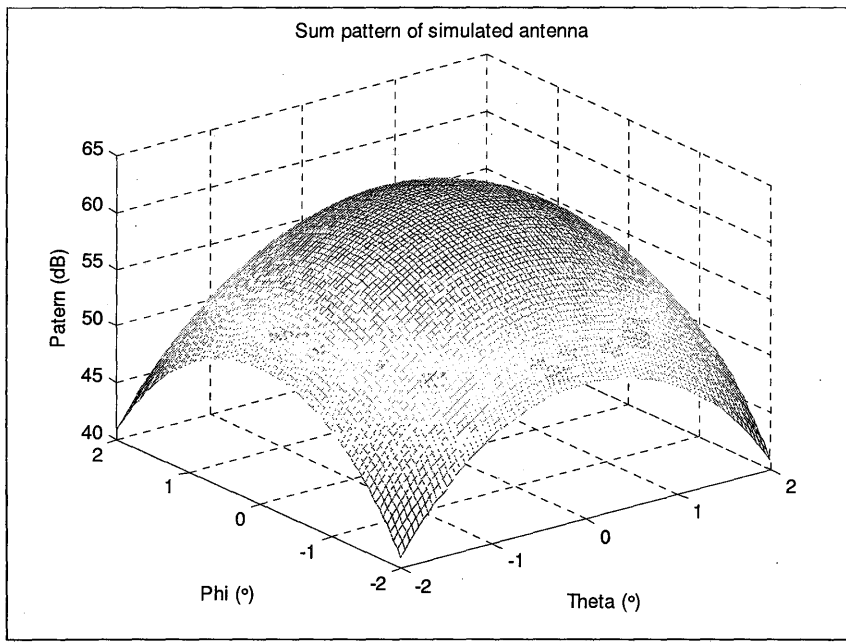


Figure 8 Sum pattern of simulated antenna.

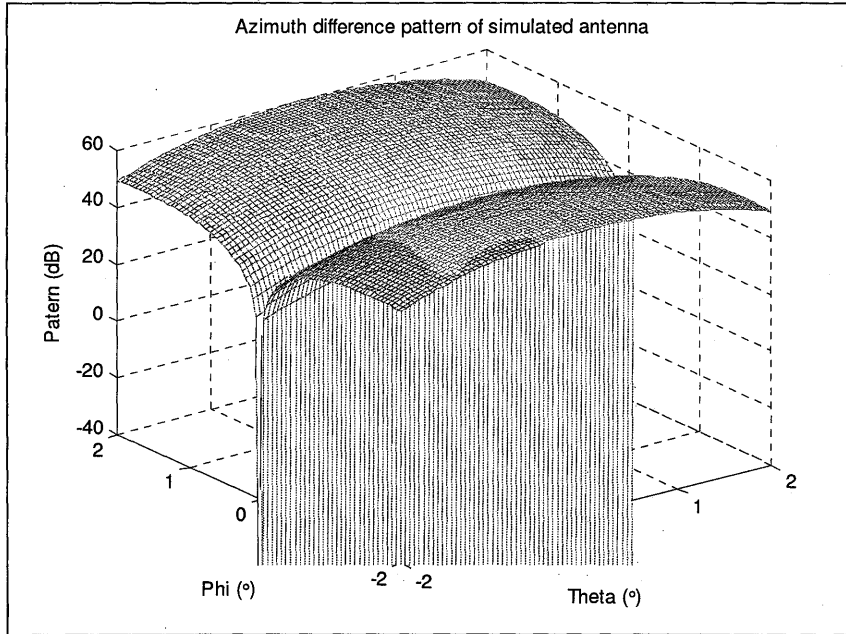


Figure 9 Azimuth difference pattern of simulated antenna.

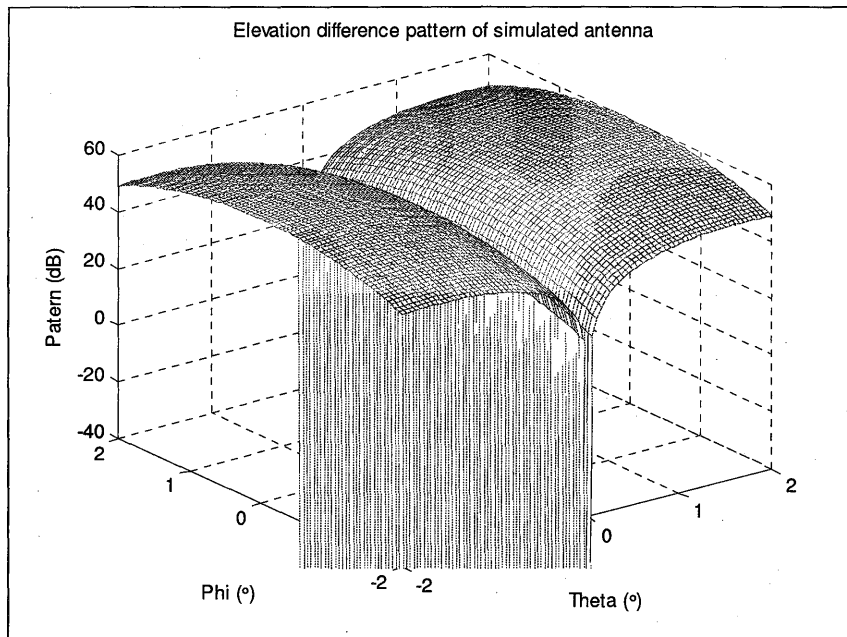


Figure 10 Elevation difference pattern of simulated antenna.

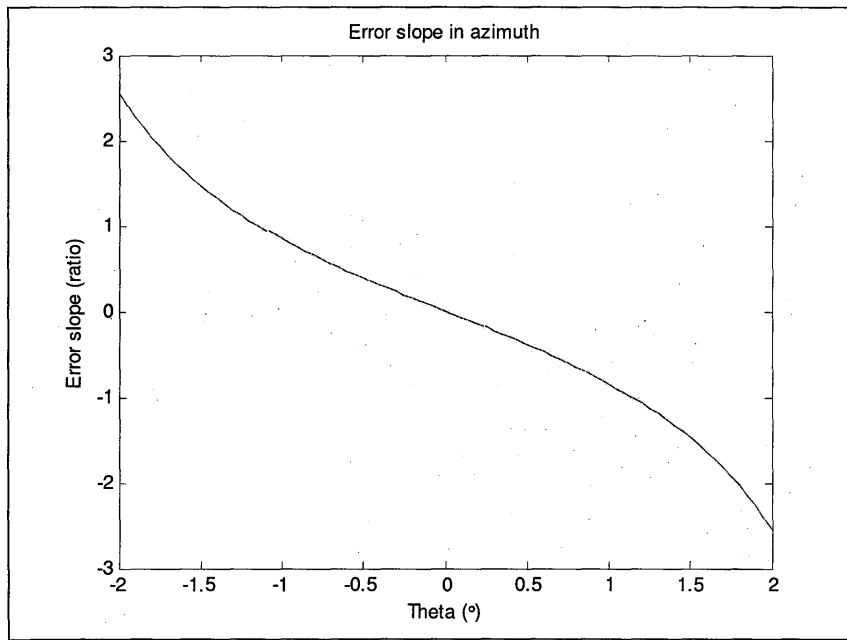


Figure 11 Error slope in the azimuth principle plane.

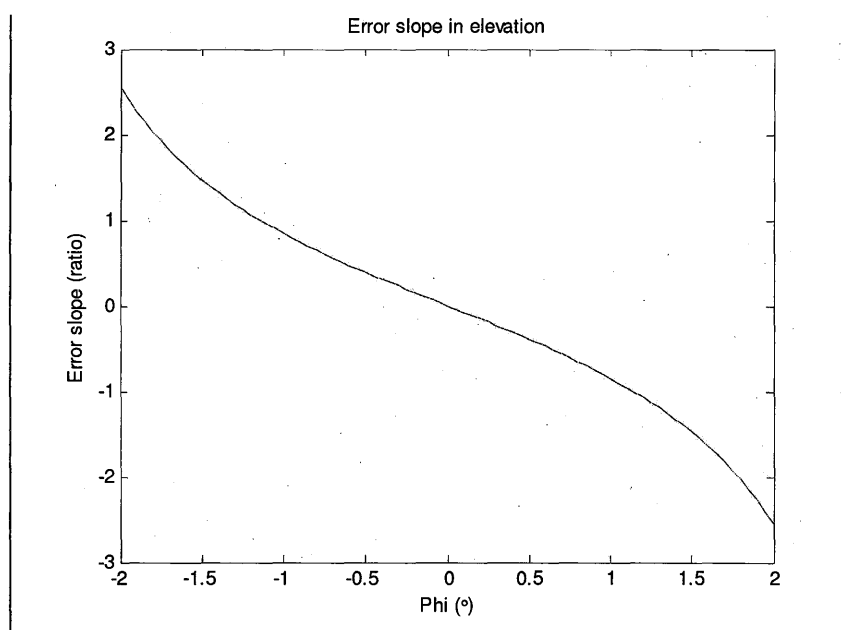


Figure 12 Error slope in the elevation principle plane.

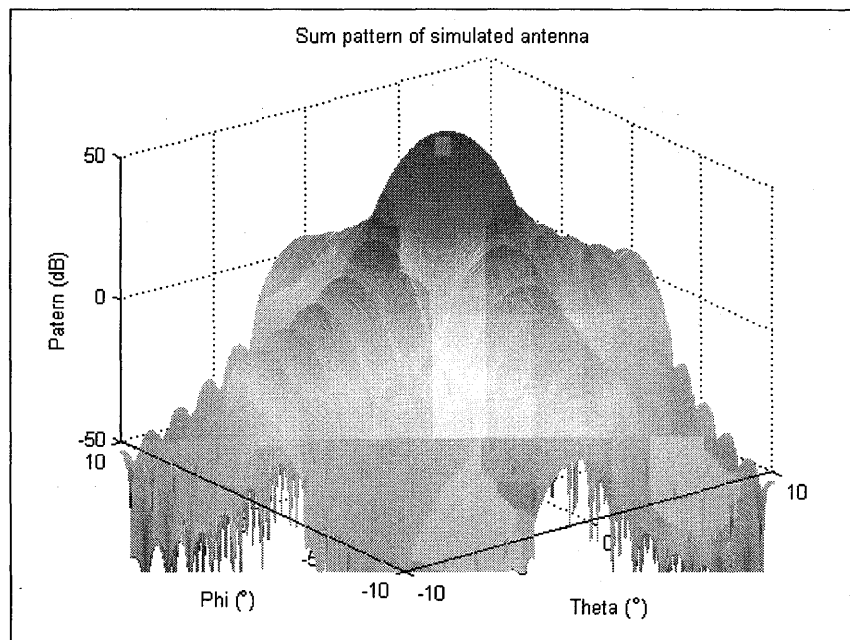


Figure 13 Sum pattern of simulated antenna (central 20°).

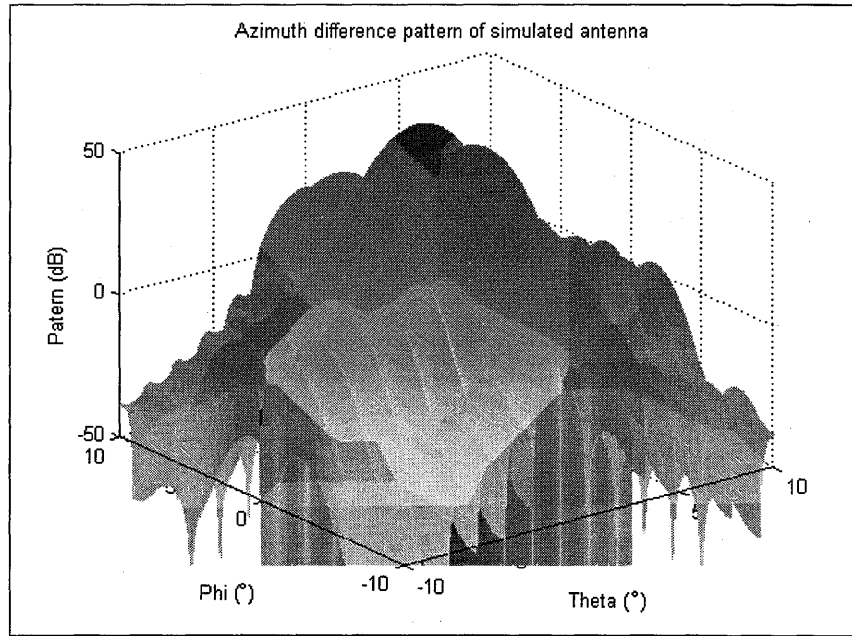


Figure 14 Azimuth difference pattern of simulated antenna (central 20°).

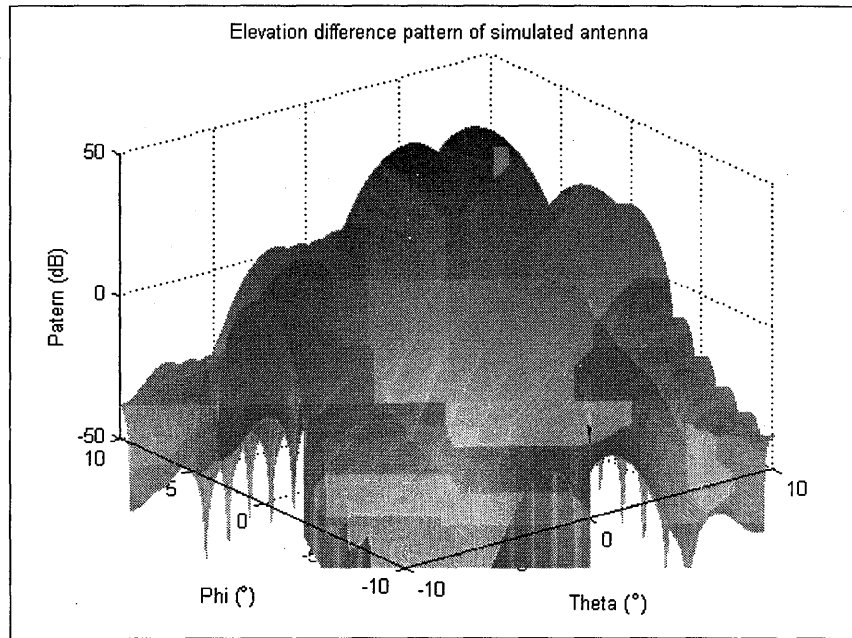


Figure 15 Elevation difference pattern of simulated antenna (central 20°).

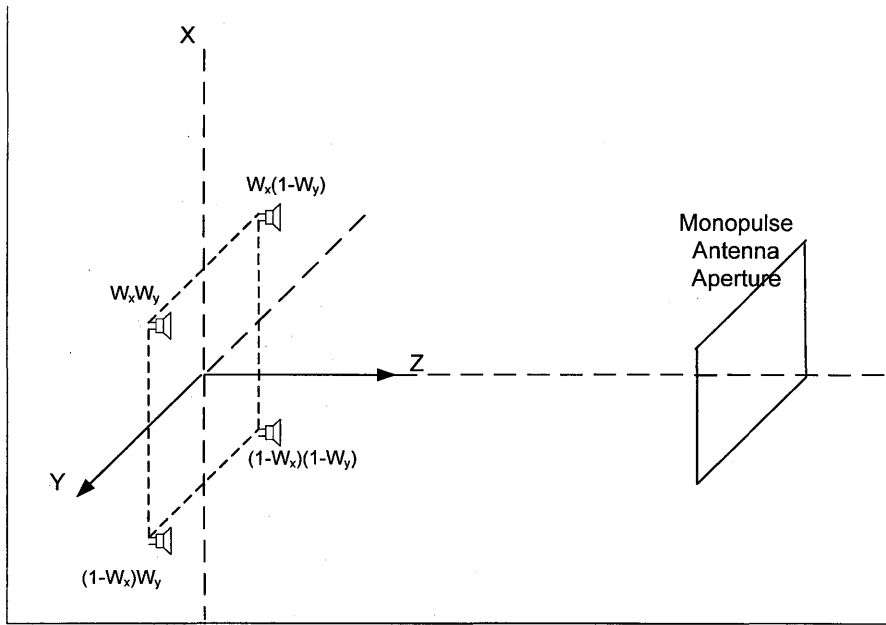


Figure 16 Geometry of the problem.

Simulation results

Figure 17 and Figure 18 show the perceived angle of arrivals as a function of the amplitude weights of the antennas for an antenna spacing of 2m. Figure 19, Figure 20 and Figure 21 show the magnitude of the received signal in the three antenna ports as a function of the simulated angles. It can be seen that this resembles the antenna patterns of the antenna as seen in Figure 8, Figure 9 and Figure 10. One difference is that there is no amplitude variation in the main beam for the sum direction. Because this variation is missing in all the antenna ports, this introduces no error in the direction of arrival.

Figure 22 and Figure 23 show the perceived angle of arrivals as a function of the amplitude weights of the antennas for an antenna spacing of 4m. Figure 24, Figure 25 and Figure 26 show the magnitude of the received signal in the three antenna ports as a function of the simulated angles. Again a good resemblance to the antenna patterns is seen. The magnitude variations on the antennas are now smaller for coverage of the full main beam of the antenna under test.

Figure 27 and Figure 28 show the perceived angle of arrivals as a function of the amplitude weights of the antennas for an antenna spacing of 6m. From the plots it can be

seen that only a very small portion of the main beam is covered and the technique fails for this spacing.

A spacing of 4m for this antenna size means that only a limited number of antennas are needed to cover an area large enough for experiments.

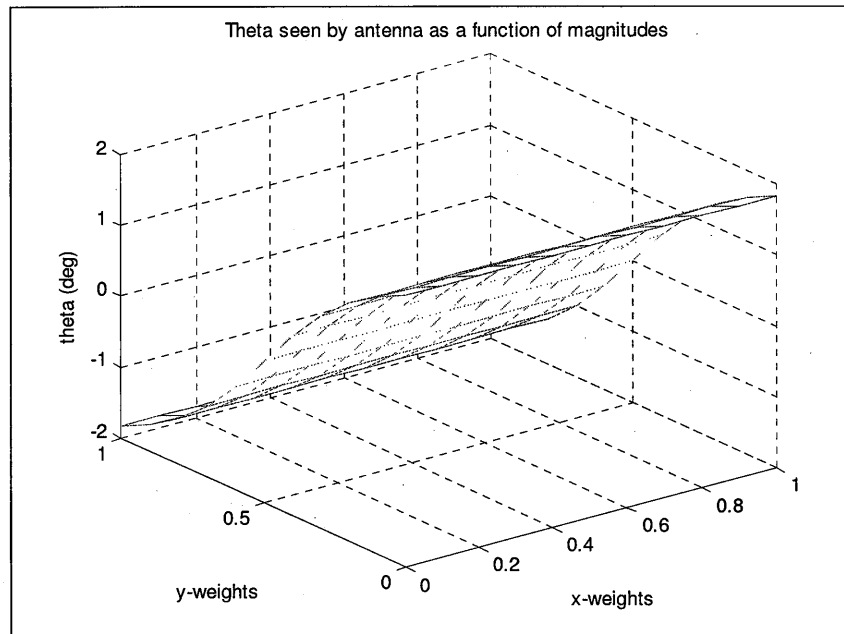


Figure 17 Theta angle seen by the radar as a function of the element weights for an element spacing of 2m.

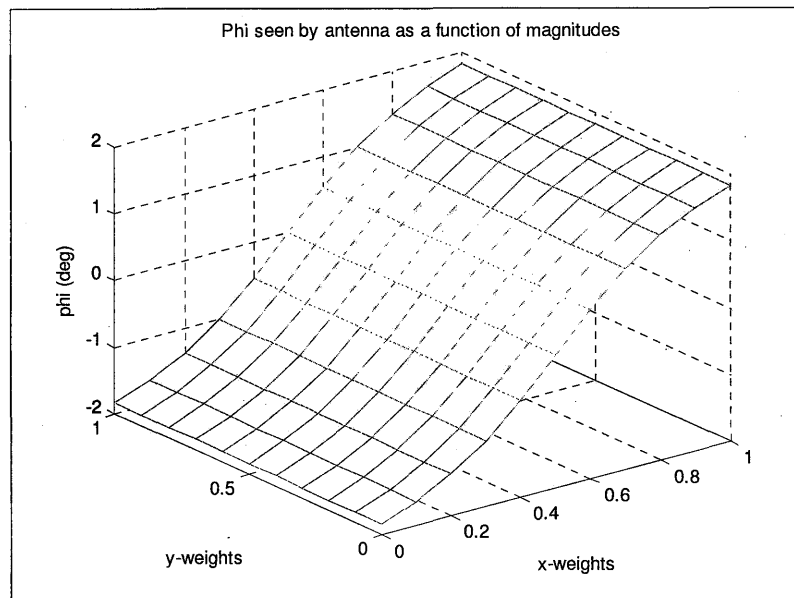


Figure 18 Phi angle seen by the radar as a function of the element weights for an element spacing of 2m.

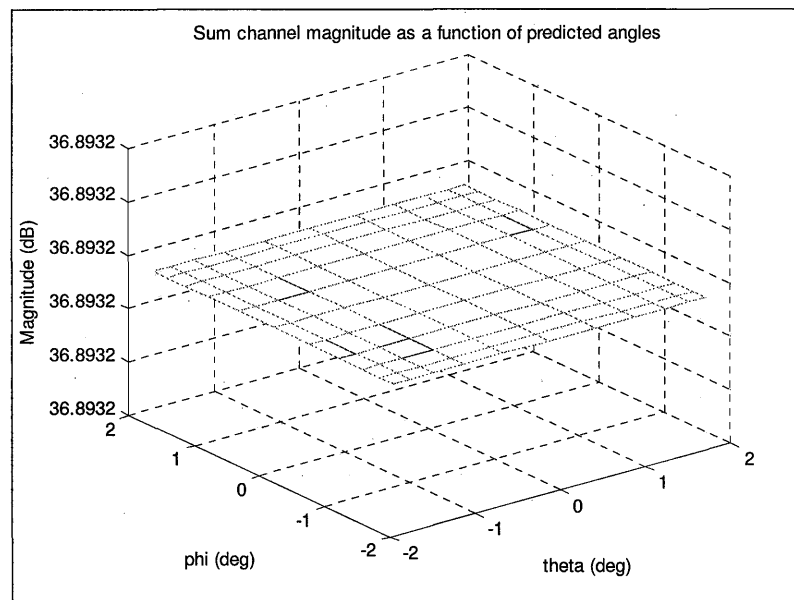


Figure 19 Sum channel magnitude seen by the radar as a function of simulated angles for an element spacing of 2m.

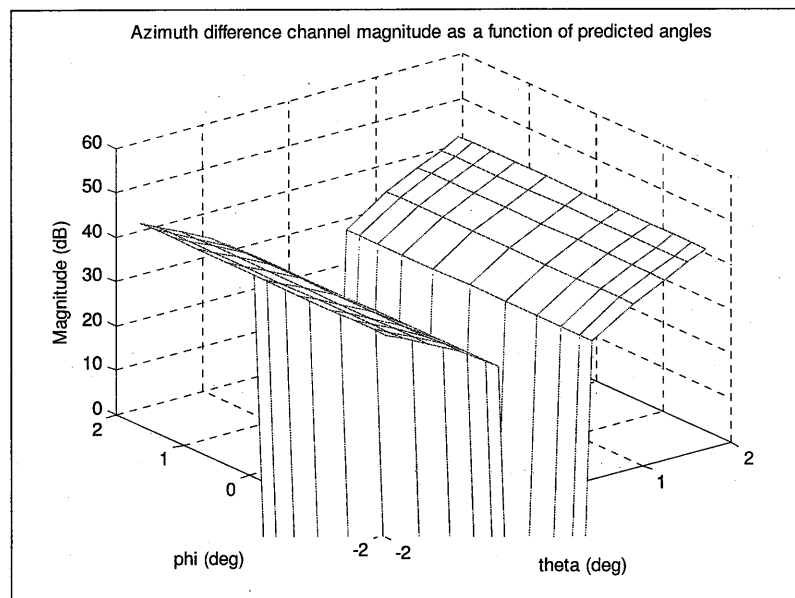


Figure 20 Azimuth difference channel magnitude seen by the radar as a function of simulated angles for an element spacing of 2m.

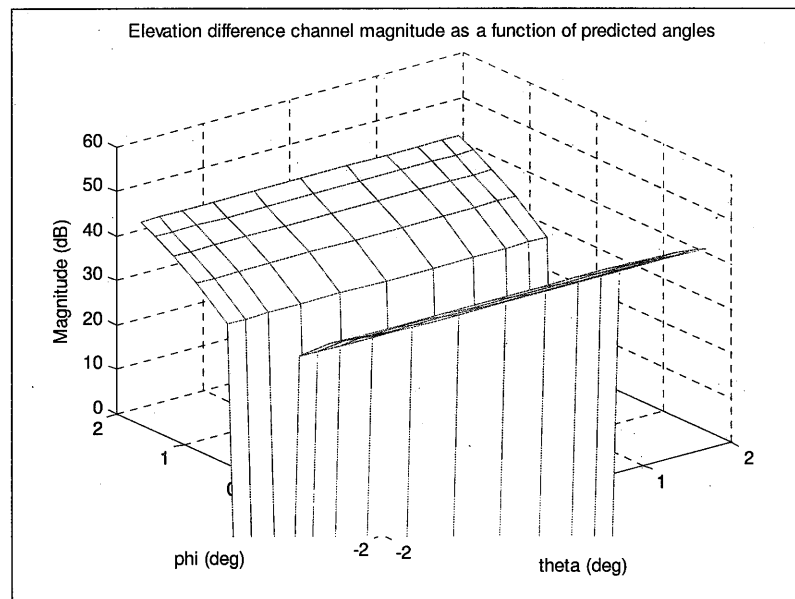


Figure 21 Elevation difference channel magnitude seen by the radar as a function of simulated angles for an element spacing of 2m.

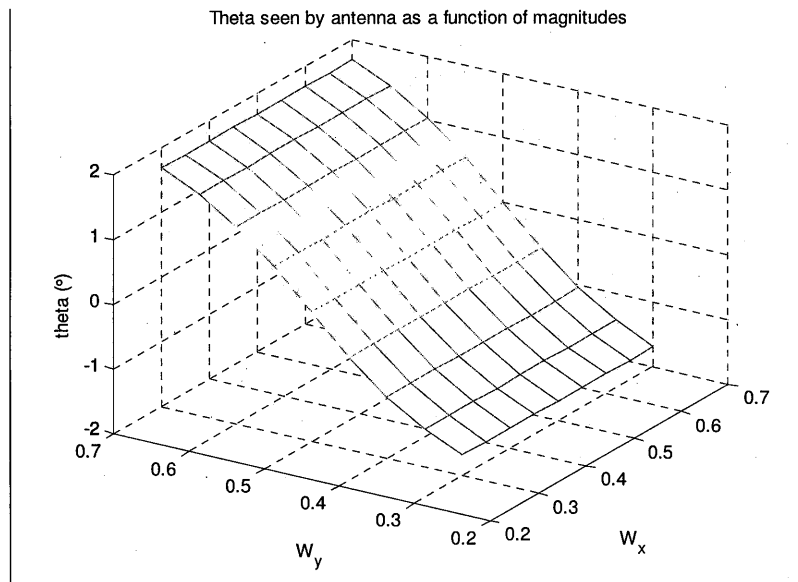


Figure 22 Theta angle seen by the radar as a function of the element weights for an element spacing of 4m.

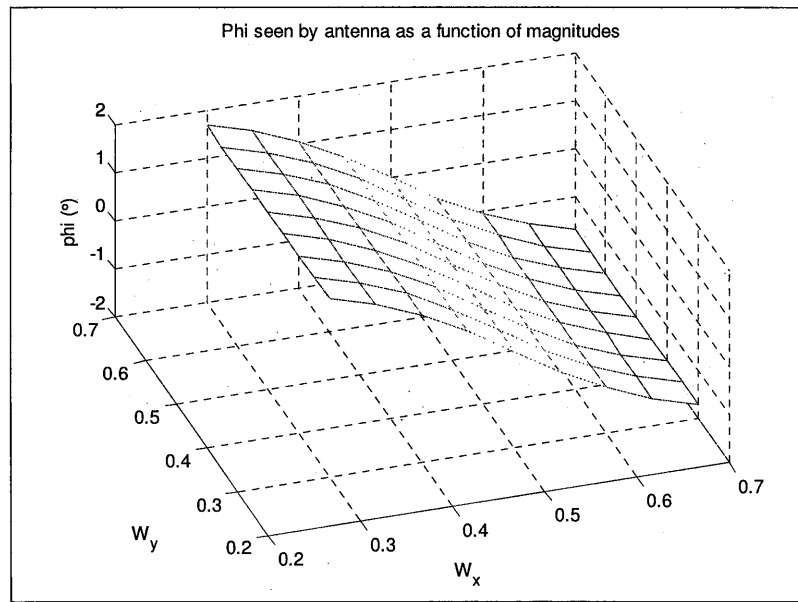


Figure 23 Phi angle seen by the radar as a function of the element weights for an element spacing of 4m.

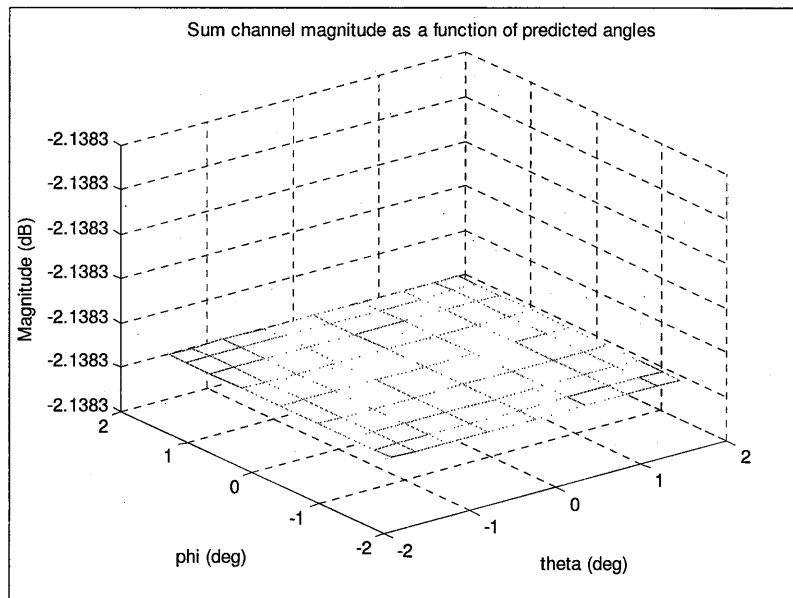


Figure 24 Sum channel magnitude seen by the radar as a function of simulated angles for an element spacing of 4m.

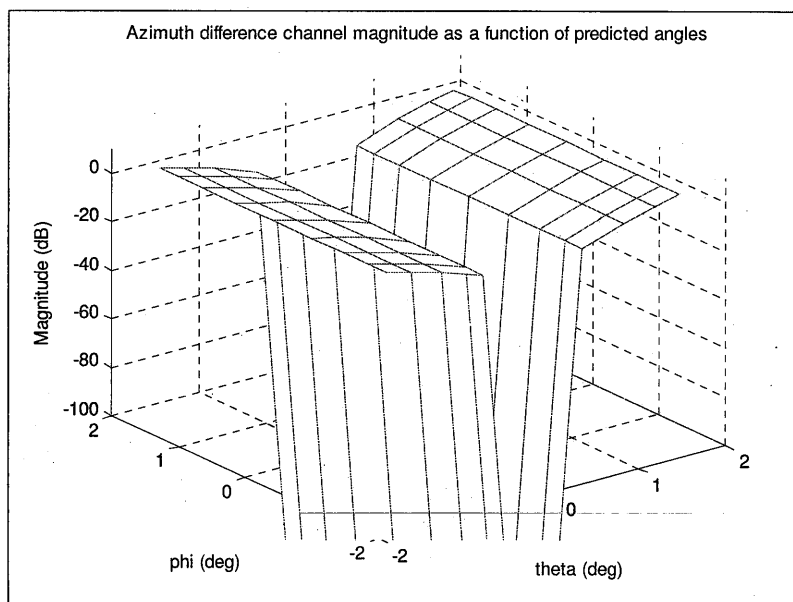


Figure 25 Azimuth difference channel magnitude seen by the radar as a function of simulated angles for an element spacing of 4m.

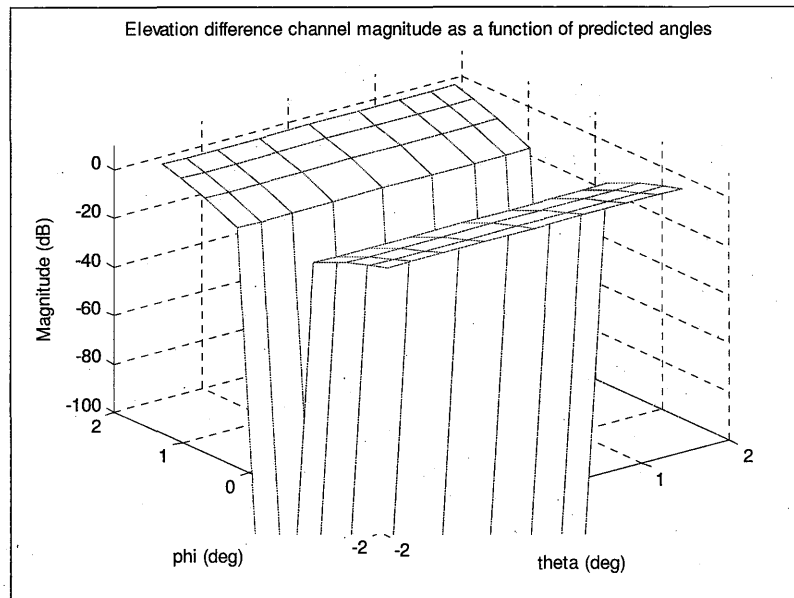


Figure 26 Elevation difference channel magnitude seen by the radar as a function of simulated angles for an element spacing of 4m.

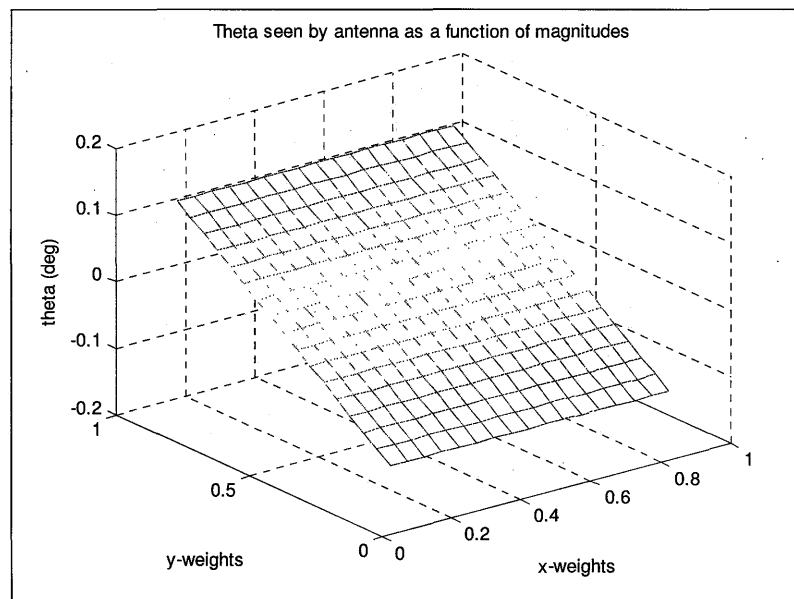


Figure 27 Theta angle seen by the radar as a function of the element weights for an element spacing of 6m.

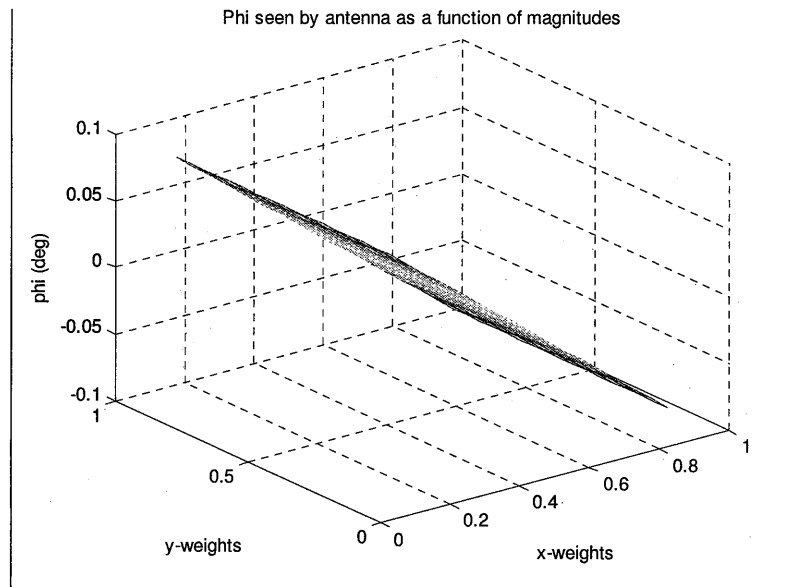


Figure 28 Phi angle seen by the radar as a function of the element weights for an element spacing of 6m.

4. Conclusions

Using only these four antennas spaced four meters apart, the complete tracking volume of the monopulse antenna was covered. This means that about 48 by 24 antennas are needed for a full spherical coverage around the antenna.

This technique appears to have merits and further investigation is planned.

WIDEBAND FOLDED HORN ANTENNA ARRAY FOR 20kV IMPULSE

Jin-Seong Lee^{1*}, Jin-Woo Park¹, Byungwoon Jung¹, Frances J. Harackiewicz², and
Byungje Lee¹

¹RFIC Research and Education Center, Kwangwoon University

447-1, Wolgye-Dong, Nowon-Gu, Seoul, 139-701, Korea

* Currently a Ph. D. Candidate at Kwangwoon University, Seoul, Korea

²Department of Electrical and Computer Engineering

Southern Illinois University

Carbondale, Illinois 62901-6603

Abstract: A wideband folded horn antenna (FHA) array, which can handle a 20 kV impulse input signal, is proposed. To reduce the overall dimension of a conventional TEM horn antenna, the radiating element of the proposed antenna is folded twice parallel to the direction of the electric field. The proposed antenna can operate as a combination three TEM horn antennas of different lengths. Folding the radiator twice to effectively cover the wide frequency band, the proposed antenna gives one main horn and six sub-horn elements (four smaller horns and two larger horns). A 20kV impulse input signal is divided into the 1 x 4 FHA elements. The divider has a stripline structure and is designed as the transformer. The proposed folded horn antenna array consists of a radiator with folded horn structure and a stripline structure power divider, and air breakdown is also considered. Overall size is 1790 mm x 1050 mm x 360 mm and its impedance bandwidth (VSWR<3) is 1349 MHz (131 ~ 1480 MHz).

1. Introduction

Recently, as the technology of electronic communication grows, the effect and precaution of high power electromagnetic waves on communication devices have been studied. Also, generating the strong electromagnetic wave using the high power microwave (HPM)

system and then testing its effect on the targeted devices has been performed and studied. In the HPM system, the high power signal is required to transmit the desired signal level to the targets. The power capacity of the HPM system can be limited by a breakdown. If a breakdown occurs by the high power, an efficiency of the power transmission is decreased. Also the high power signal can be reflected to its source due to a short, and then it may break the source. A breakdown has been studied with various materials, but in this paper it is only considered in the air. In general, it is well-known that air breakdown occurs at 30 kV/cm [1]. To prevent a breakdown in a HPM system, the antenna array and the power divider are also designed carefully since an air breakdown may occur at both the radiating elements and the divider. For a HPM system which uses a high power short impulse as its input signal, in general, an antenna must operate at the ultra wide band (UWB) in the frequency domain. Although the TEM horn antennas have been widely used to radiate impulse signals [2], in this paper, a FHA is proposed to reduce the dimension of the conventional TEM horn antenna, and it can be used for the HPM system which uses 20kV of impulse with 500ps of rising time as the input signal.

2. Design of the Folded Horn Array Elements

A conventional TEM horn antenna is very useful to transmit the pulse signal since it transmits a TEM wave, but it also has a disadvantage of large size in the low frequency band, that is, its size goes up as the frequency becomes lower [3]. The proposed FHA can reduce the size of a conventional TEM horn antenna by still maintaining the structural and electrical advantages of a TEM horn antenna. The performance of a conventional TEM horn antenna is determined by the antenna length, the conducting plate spacing, and the angle between the antenna radiators [4]. Figure 1 shows a conventional TEM horn antenna and the proposed FHA which is a TEM horn antenna folded once. For a conventional TEM horn antenna, one can easily see the relation among the antenna length, the conducting plate spacing, and the angle between radiators:

$$\tan(\theta/2) = A/2l \quad (1)$$

where θ is the angle between two radiating plates of the TEM horn antenna, l is the antenna length, and A indicates the conducting plate spacing. The conducting plate

spacing (A) at the “mouth” should be at least half wavelength ($\lambda/2$) long. The FHA is W-shape shown as the solid line along the segment ***g-b-e-c-i*** in Figure 1. The segment ***g-a-i*** displays a conventional structure of the TEM horn antenna. For higher mode mutual suppression of the FHA, the length C is optimized [5]. Then, at the half length (P_0 level) of B, the antenna is folded once parallel to the direction of electric field. Now, a FHA consists of three horn antennas: two smaller horns and one larger horn. Two small horn antennas (two ①s) include the segments ***d-b-e*** and ***e-c-f***, and one main horn antenna (②) is formed along the segment ***g-b-e-c-i***. Repeating the same procedure, the numbers (N) of horn antennas and the level of the antenna aperture (P_m) to be needed for the FHA can be easily calculated by

$$N = 2^m - 1. \quad (2)$$

Figure 2 shows the FHA which is folded twice (on the axis of P_1 , P_0) parallel to the direction of the electric field. Now, the proposed FHA has the 1×4 elements of an array, and the length of the TEM horn antenna is reduced by folding it twice. Figure 3 shows the structure of the proposed antenna used for EM simulation of CST [6]. The antenna is designed by three levels of P_1 , P_2 , and P_3 . The largest horn antenna (③) operates at the lowest frequency band. Two horn antennas (②) and four horn antennas (①) operate at the middle frequency and at the highest frequency band, respectively. In other words, the proposed antenna consists of three different sizes of the TEM horn antennas. Figure 4 and 5 show the dimension of the proposed antenna in x-y plane and y-z plane, respectively. The distance of the gap (gap_a , gap_b , gap_c , and gap_d) between the conducting plates as shown in Figure 5 is maintained by 18.5 mm, in this work, to avoid the air breakdown for a 20 kV impulse.

3. Design of the Power Divider

The proposed antenna consists of four TEM horn antennas between P_0 and P_1 levels. Then, the 4 way power divider is required to feed each radiating element. In the HPM system, the waveguide structure is widely used to transmit the high power energy to the antenna. However, it is limited to use the waveguide for the UWB HPM system since each waveguide has the cut-off frequency. In this paper, a high power ultra wide band

power divider, which has a strip structure, is designed to simultaneously feed four small horn antennas as shown in Figure 5. Figure 6 shows the detailed drawing of the designed power divider. The input impedance of the power divider is 50 ohms, and a strip structure using transformer is constructed to obtain wide bandwidth. The impedance at each term of the power divider is 150 ohms, and they are constructed as the four way structure so that they excite four horn antennas (①) with the uniform amplitude and the phase between the P_0 and P_1 level as shown in Figure 3. Also, to avoid the air breakdown at the power divider, the distance between the stripline and ground plane in the strip structure is maintained at 9.5mm. The size of the power divider is 1350 mm x 150 mm x 24 mm.

4. Proposed Folded Horn Antenna Array

Figure 7 shows the photograph of the proposed FHA array. The antenna mainly consists of the folded horn structure radiators and the stripline power divider. The ground of the power divider is formed by Duralumin (thickness=2 mm), and a copper (thickness=1 mm) is used for the stripline. At the input port of the power divider, 50 ohms of the DIN type-connector is used. Maintaining the uniform height between the stripline and the ground of the stripline type of the power divider by the Polyethylene ($\epsilon_r = 2.25$) supporters and the screw bolts, the performance variation of the power divider is minimized. Also, the firm electrical contact between the power divider and the radiator maintained by the support-3 (Polyethylene: $\epsilon_r = 2.25$). The support-3 not only keeps the good electrical contact but also aids in avoiding the air breakdown between the stripline feed and the radiating element. The support-4 (Polyethylene: $\epsilon_r = 2.25$) maintains good electrical contact between the DIN type-connector and the input part of 4 way power divider, and it also aids in preventing the air breakdown. Figure 8 shows the proposed FHA which is set up for the radiation pattern measurement in an anechoic chamber. The Duralumin (thickness=2 mm) is used for the radiating elements since it is very light and has high conductivity. To maintain the antenna elements firmly, the support-1 (Poly carbonate: $\epsilon_r = 3.1$) and support-2 (Acrylic: $\epsilon_r = 2.5$) are also used.

5. Simulation and Experimental Results

Figure 9 shows the simulated dB magnitude of S_{11} of the proposed antenna. The solid line indicates the results of the antenna structure without the dielectric supporters as

shown in Figure 3, and the dashed line shows the result with the various dielectric supports (support-1, 2, 3 and 4). It is noticed that the proposed antenna has a wide bandwidth (about 200 to 1200 MHz except the frequency band “a” between 470 and 560MHz) when $VSWR < 3$. Figure 10 shows the measured dB magnitude of S_{11} of the proposed FHA. The measured antenna bandwidth is 1349 MHz (131~1480 MHz, $VSWR<3$). It is noticed that there is a small difference between the measured and simulated result. Figure 11 shows the simulated and measured radiation patterns in the y-z plane. Table 1 shows the simulated and measured gains and HPBWs of the proposed FHA from 400 MHz to 1100 MHz.

6. Conclusion

The FHA array which has a folded TEM horn radiating elements and the power divider is proposed to reduce the length of the conventional TEM horn antenna. The proposed FHA array has a wide bandwidth (131~1480 MHz, $VSWR<3$), and its length is reduced up to about 73% of the length of a conventional TEM horn antenna in the same frequency band. The proposed antenna is designed to resist against 20kV impulse in the air. In the future, the proposed antenna will be studied and improved for broader band operation, higher gain, and higher power application up to 100kV impulse.

7. Acknowledgments

This work is financially supported by the Ministry of Education and Human Resources Development (MOE), the Ministry of Commerce, Industry and Energy (MOCIE) and the Ministry of Labor (MOLAB) through the fostering project of the Lab of Excellency, and supported in part by the post BK21.

8. References

- [1] K. Chang, RF and Microwave Wireless Systems, pp. 44, New York: John Wiley & Sons, 2000.
- [2] J. D. Taylor, Introduction to Ultra-Wideband Rader Systems, pp. 176-183, Florida: CRC Press, Inc., 1995.

[3] D. A. Kolokotronis, Y. Hung, and J. T. Zhang, "Design of TEM Horn Antennas for Impulse Radar", IEEE High-Freq. Postgrad. Student Colloq., pp. 120-126, 17 September 1999.

[4] A. S. Turk and B. Sen, "Ultra Wide Band Antenna Designs for Ground Penetrating Impulse Radar Systems", IEEE Electromagnetic Compatibility, Int'l Symp., vol2, pp. 888-891, 11-16 May, 2003.

[5] V. B. Braude, S. B. Sukhovetskaya, and B. J. Sukhovetsky, "Wide-band Folding Horn Type Microwave Antennas", Antennas and Propagation for Wireless Communications, IEEE-APS Conf., pp. 143-146, 2000.

[6] CST Microwave Studio, Version X, CST GmbH, Darmstadt, Germany.

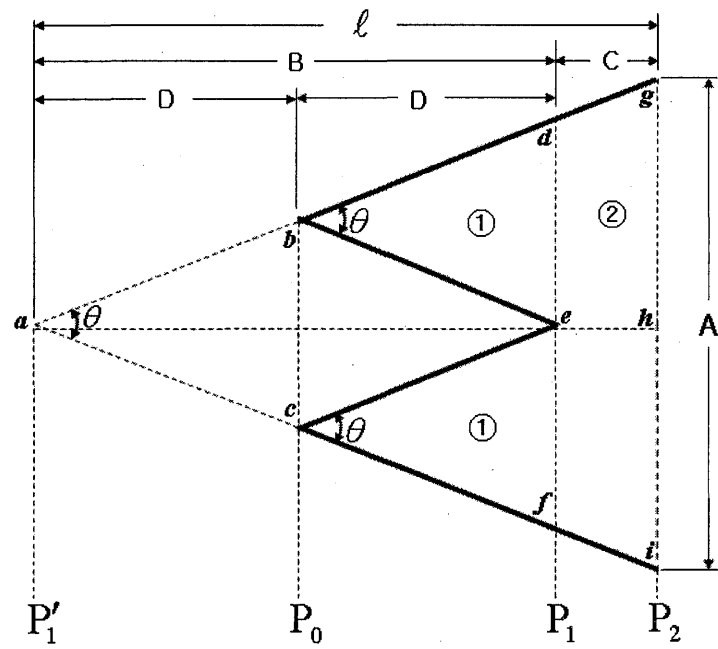


Figure 1. Folded horn antenna structure folded once parallel to the direction of electric field

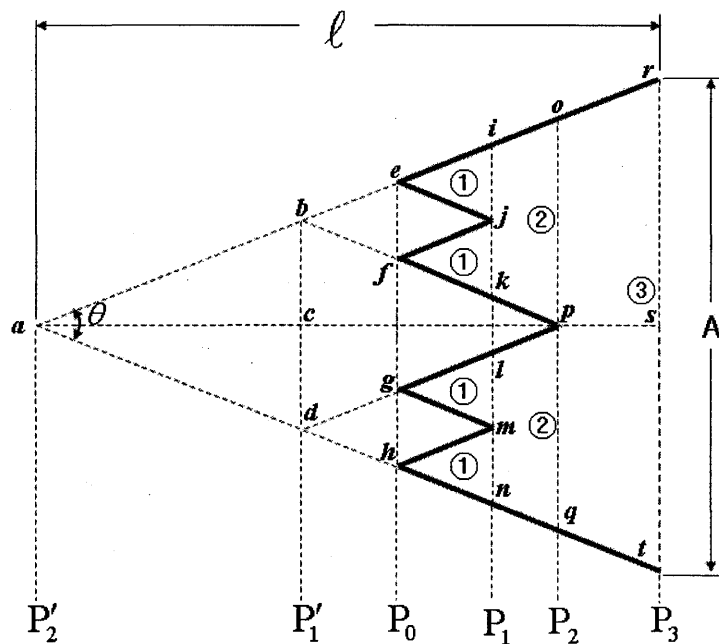


Figure 2. Folded horn antenna structure folded twice parallel to the direction of electric field

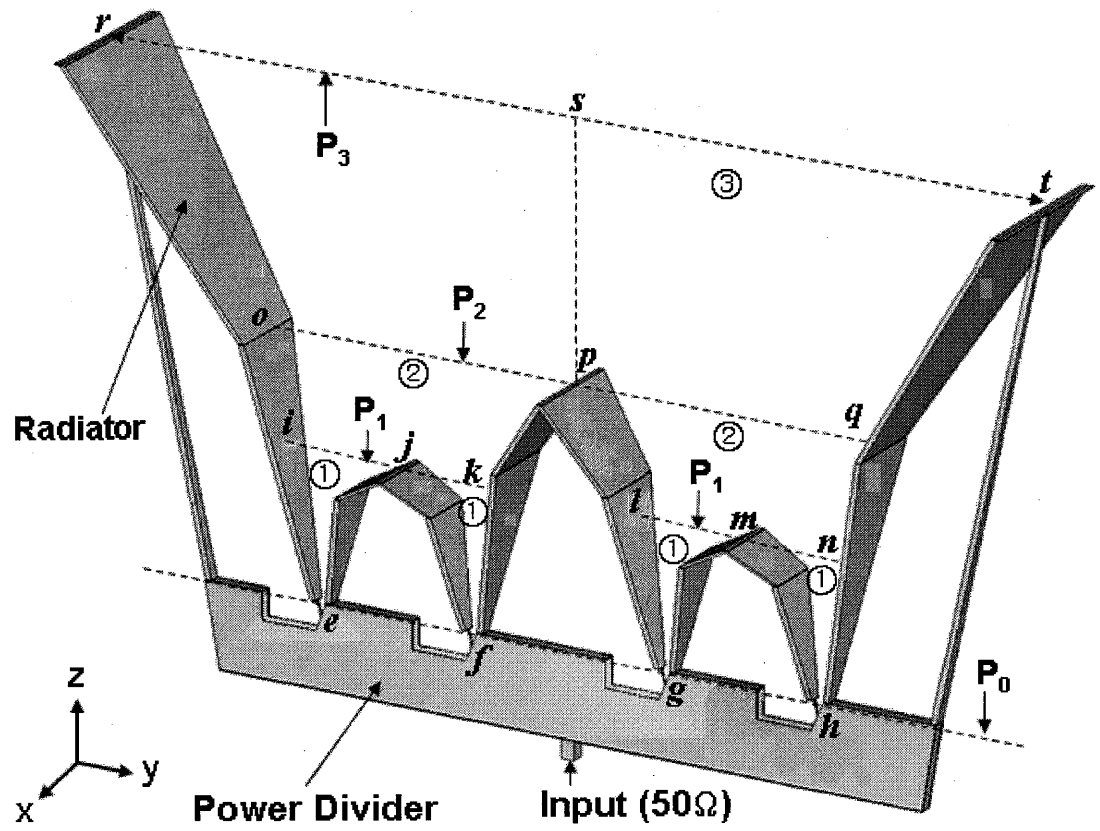


Figure 3. Antenna structure for simulation by CST (unit: mm)

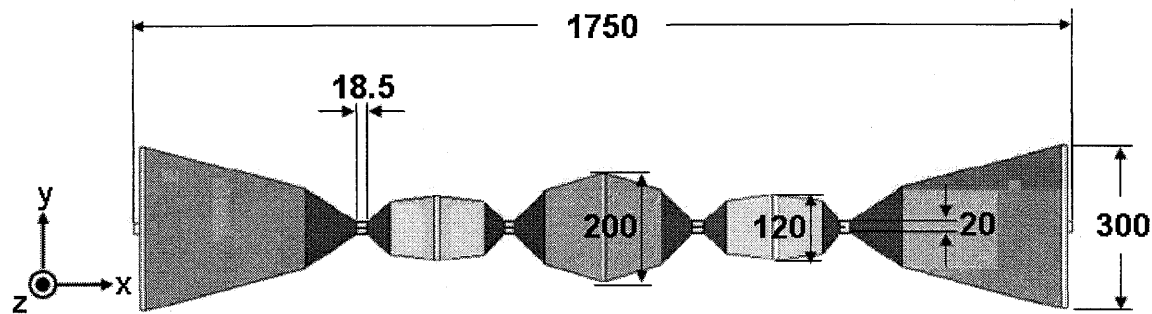


Figure 4. Dimension of the antenna in the x-y plane (unit: mm)

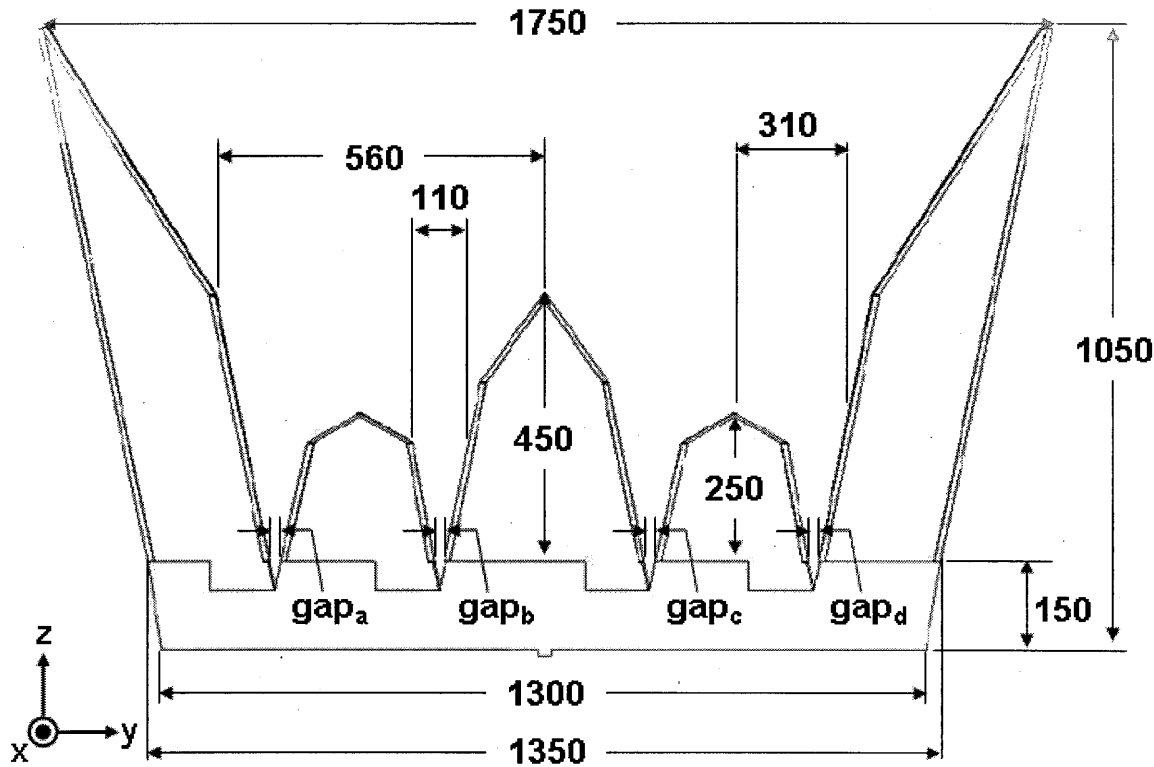


Figure 5. Dimension of the antenna in the y-z plane (unit: mm)

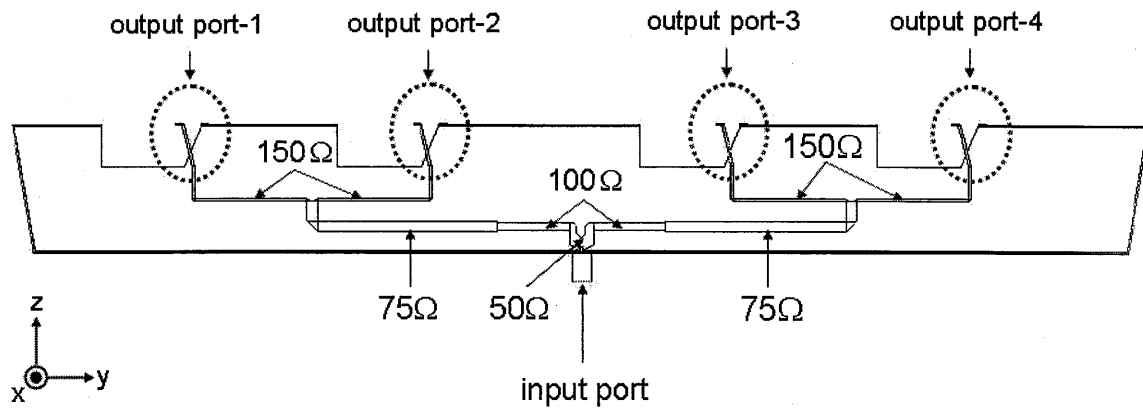


Figure 6. Impedance at each port of the power divider for simulation

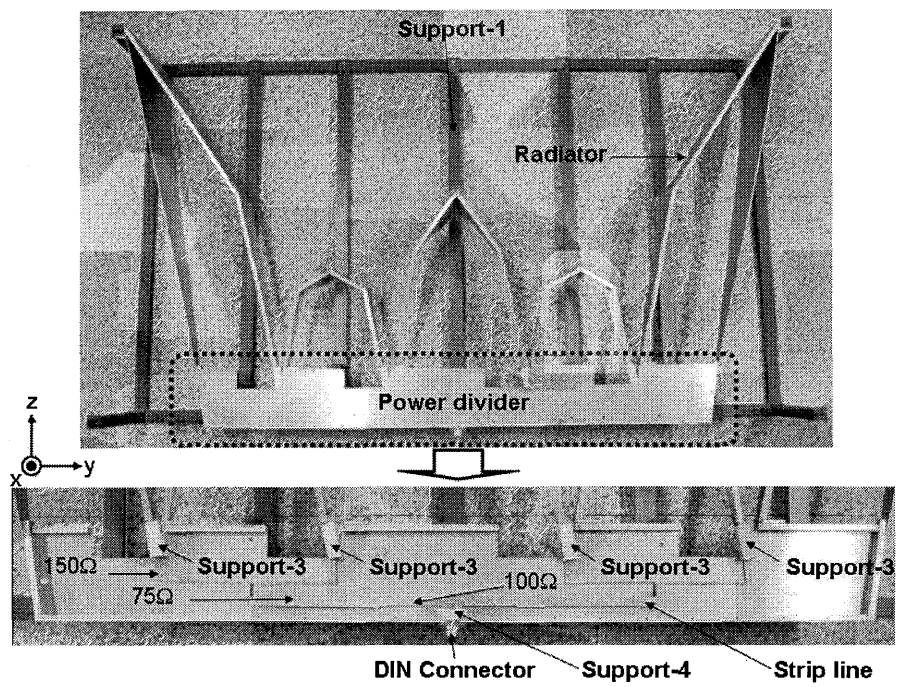


Figure 7. Structure of the proposed antenna in the y-z plane

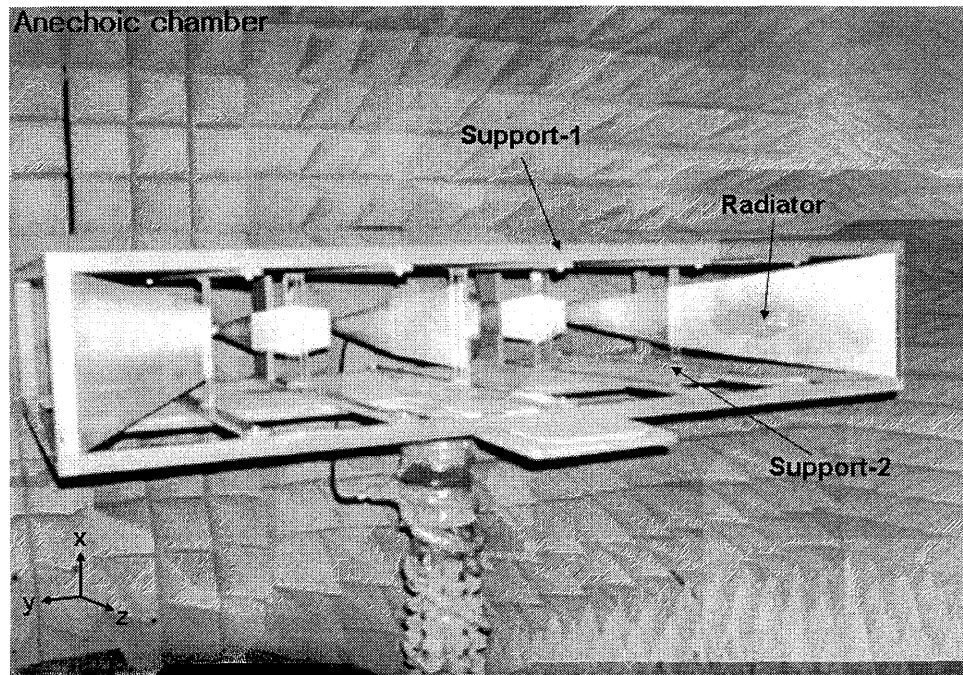


Figure 8. Photograph of the proposed antenna

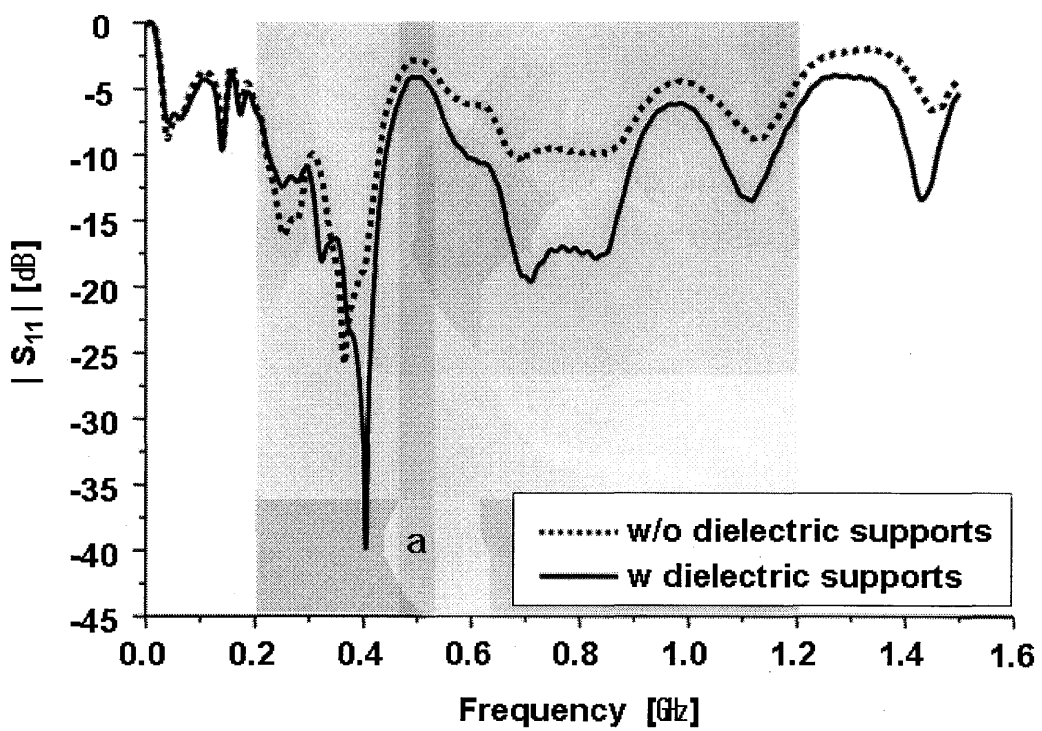


Figure 9. Simulated dB magnitude of S_{11} of the proposed antenna

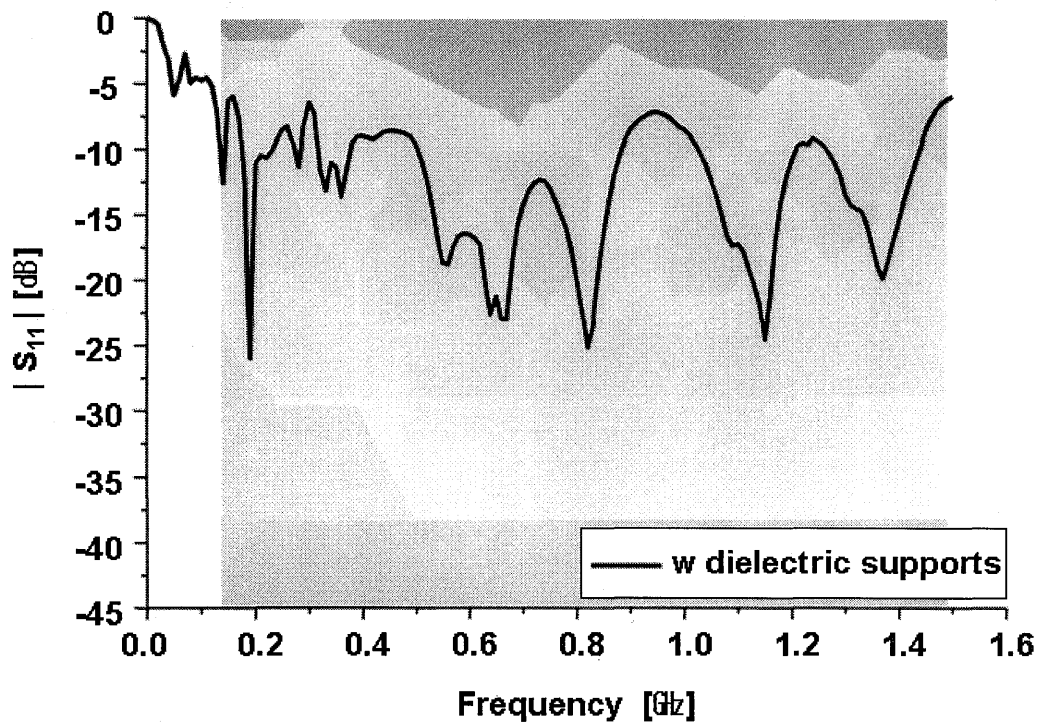
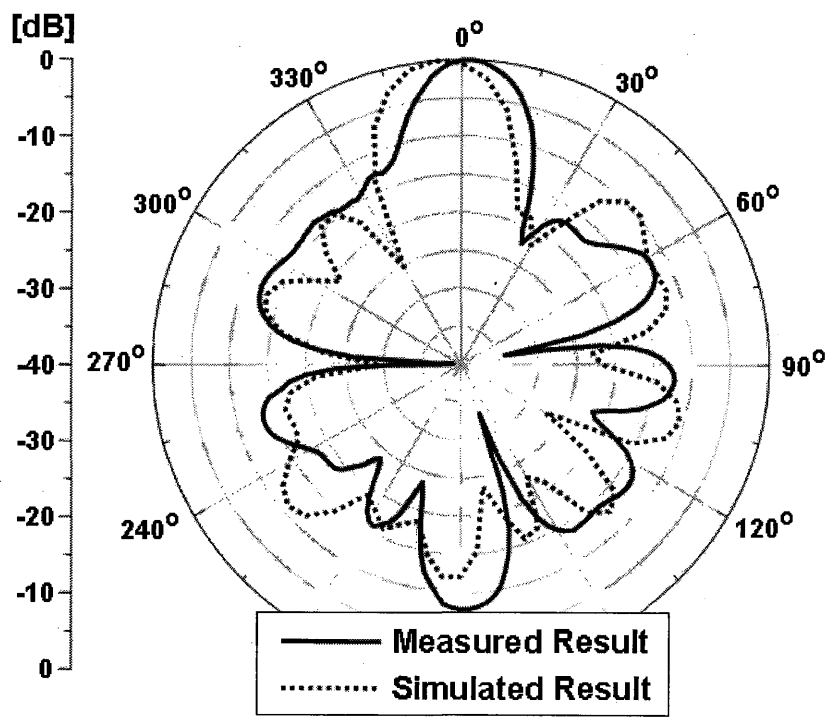
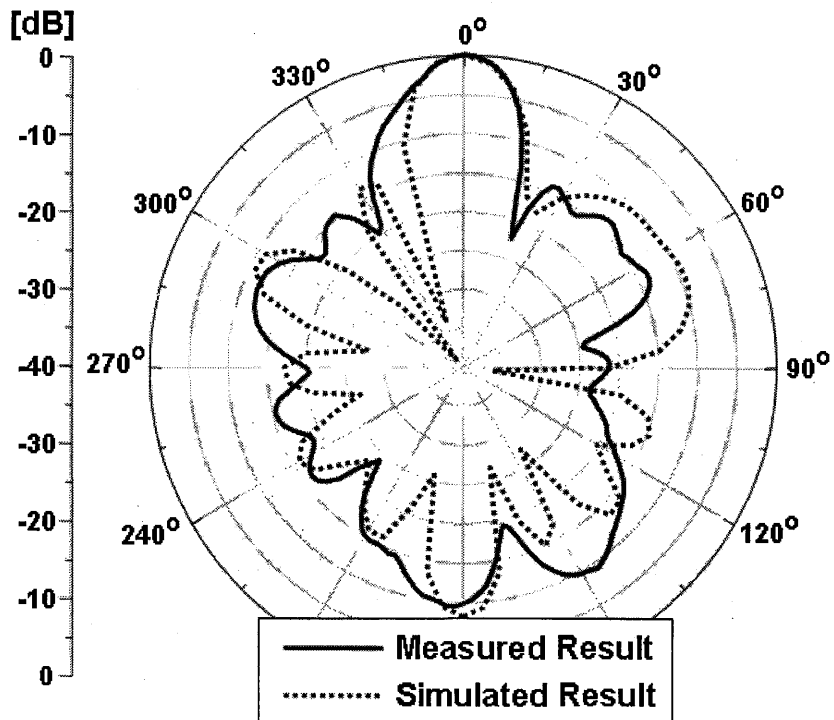


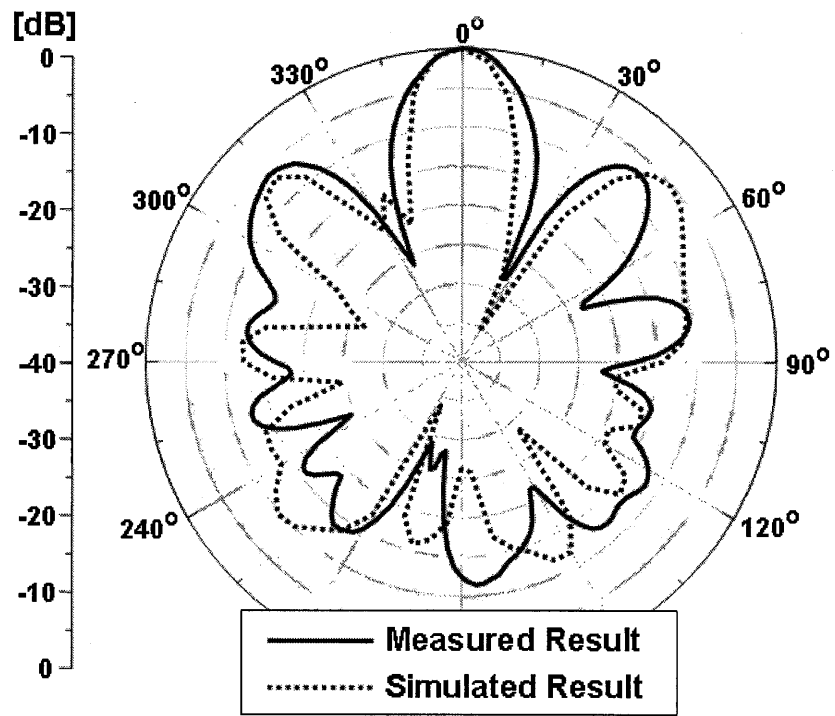
Figure 10. Measured dB magnitude of S_{11} of the proposed antenna



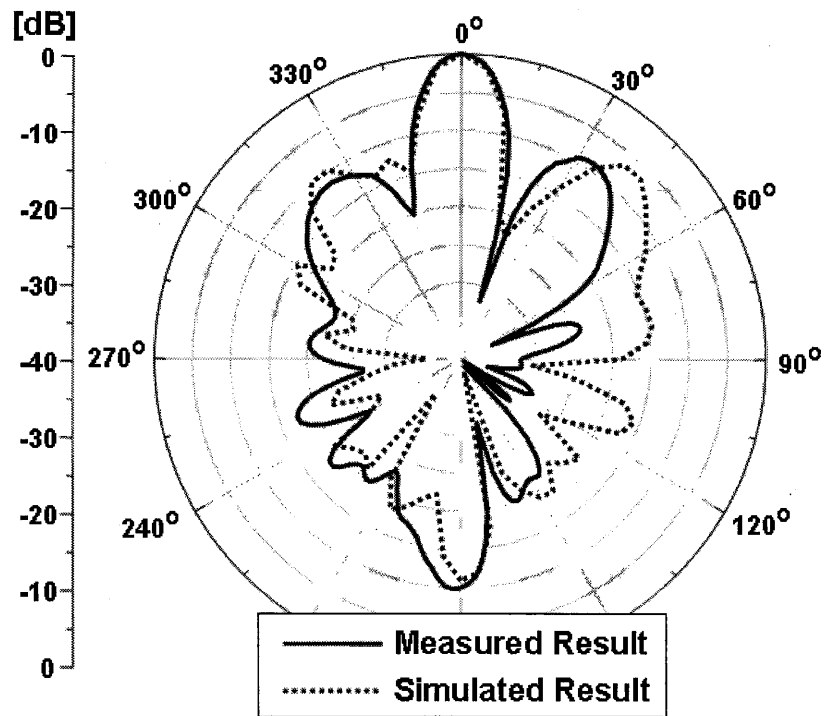
a) 400 MHz



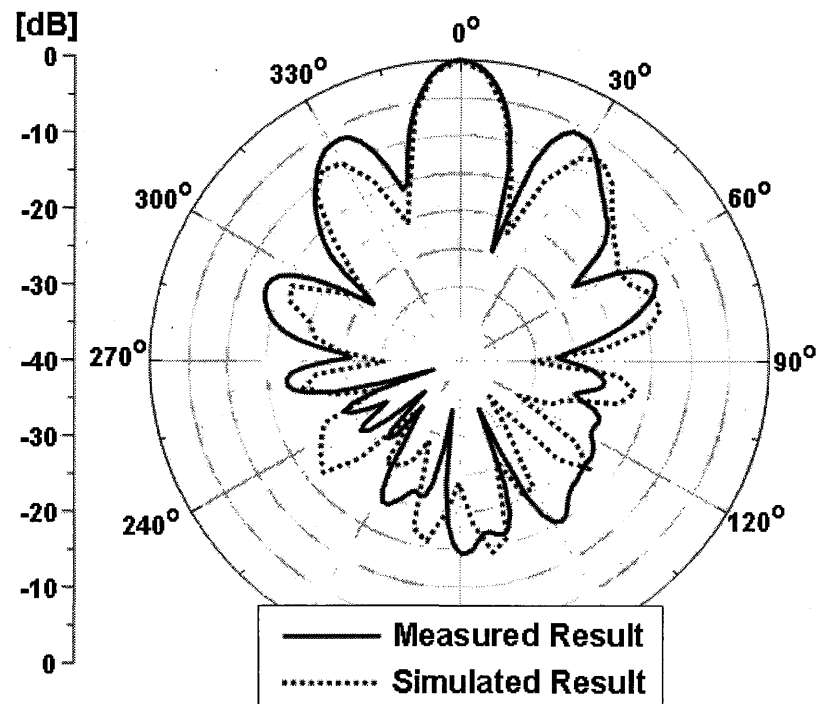
b) 500 MHz



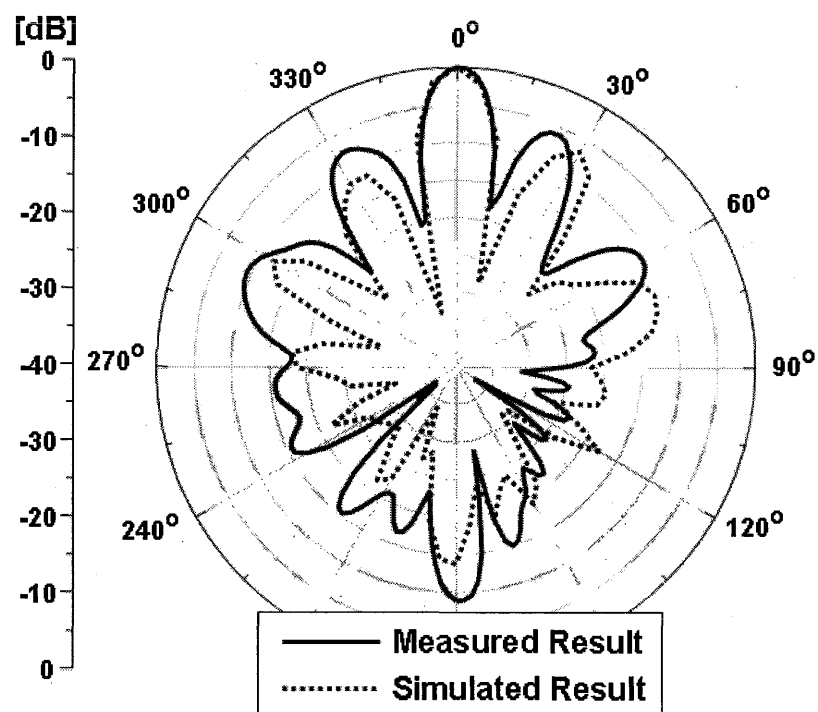
c) 600 MHz



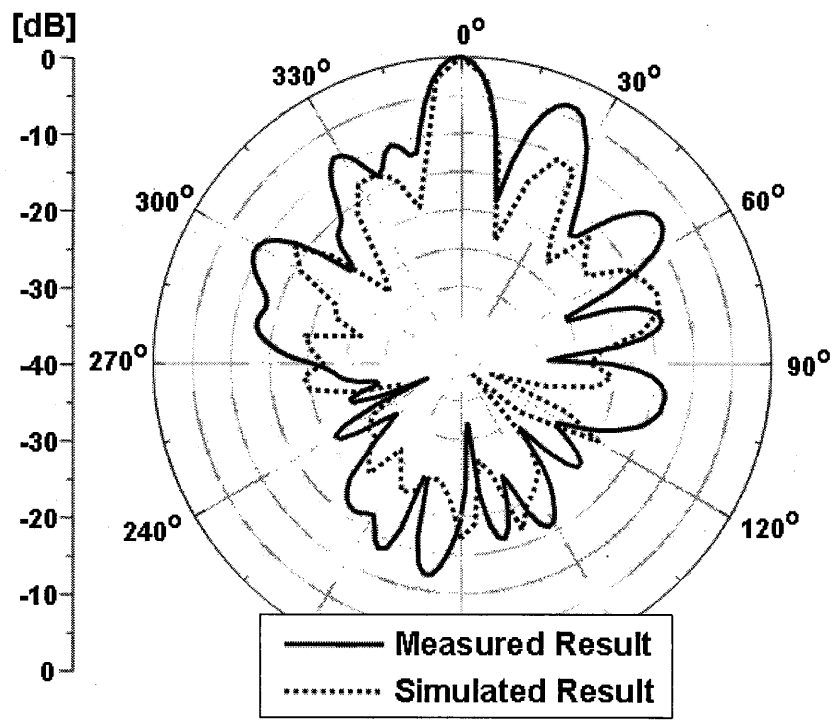
d) 700 MHz



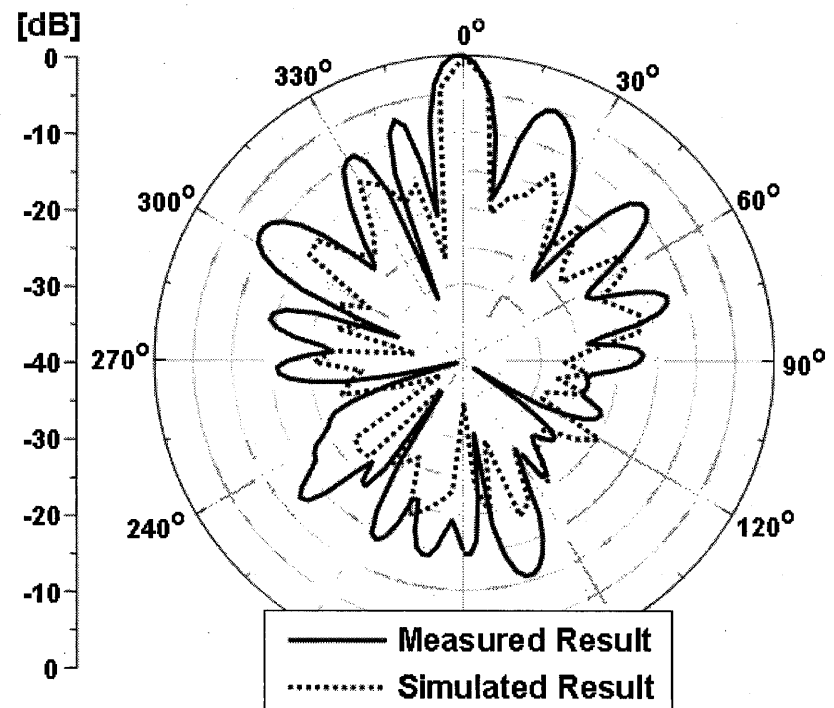
e) 800 MHz



f) 900 MHz



g) 1000 MHz



h) 1100 MHz

Figure 11. Simulated and measured radiation patterns at z-x plane.

Table 1 Compared result of measured and simulation

Frequency (MHz)	Simulation		Measurement	
	y-z plane		y-z plane	
	G _{max} (dBi)	HPBW (Degree)	G _{max} (dBi)	HPBW (Degree)
400	8.8	20.5	8.6	18.0
500	10.0	17.4	8.9	17.9
600	10.3	14.4	11.0	17.4
700	11.2	12.3	12.4	13.5
800	11.8	13.0	10.8	14.1
900	12.6	11.3	12.4	11.1
1000	13.8	10.3	13.0	10.6
1100	14.0	9.4	13.7	9.7

Development of Conformal Antenna Materials Technology to Enable “Paint-On” Antenna Arrays for Air Force Aerospace Applications

Thomas G. Campbell and C. J. Reddy

Applied EM, Inc., 144 Research Drive, Hampton, VA 23666

Robert C. Boyd

Unitech, LLC, 228-B Patterson Avenue, Hampton, VA 23669

ABSTRACT

Conformal antenna materials technology is being developed that enables new designs using “painted-on” robotic manufacturing methods. This research [1] is addressing the need for new and novel antenna manufacturing techniques for future aerospace applications. Antenna arrays on composite aircraft structures are usually flush-mounted to provide size and weight reductions to the extent possible without affecting aerodynamic performance. Unfortunately, conventional design methods are difficult to apply to complex geometries such as high performance aircraft i.e. UCAV’s and advanced Sensorcraft designs. These design methods are typically used on singly curved surfaces with large radii of curvature but difficult to apply when surfaces with small radii of curvature, doubly curved objects, or multi-layer configurations are encountered. Therefore, new technologies are being developed that will enable robotic applications of polymer dielectric layers and conductive coatings to form radiating antenna arrays with feed manifolds directly onto complex structures. This paper describes the progress of materials research with experimental results on characteristics of newly developed unique and patented dielectric and conductive coatings.

1. *Introduction*

New innovative concepts are needed for designing conformal antennas for a full spectrum of military, aerospace, and civilian applications. Conventional conformal antennas are designed to be ‘flush-mounted’ to the shape of the aircraft, spacecraft or ground vehicles. Design considerations for conformal antennas include requirements such as: reduce aerodynamic drag and heating effects, provide specific radiation pattern characteristics, achieve stealth capabilities, achieve improved mobility, and security communication requirements. In the past, designing antennas to ‘conform’ to complex shapes and geometries as depicted in Figure 1, as well as to thin film membrane materials and fabrics is indeed challenging. Therefore, the purpose of this research proposal is to address this opportunity and to provide a class of new conformal antenna materials (and designs) for military and aerospace applications. On August 31, 2004, Applied EM, Inc. (AEM) was awarded a Phase II SBIR to continue the research and to apply this technology to design an end-fire phased array antenna for an aircraft wing configuration.

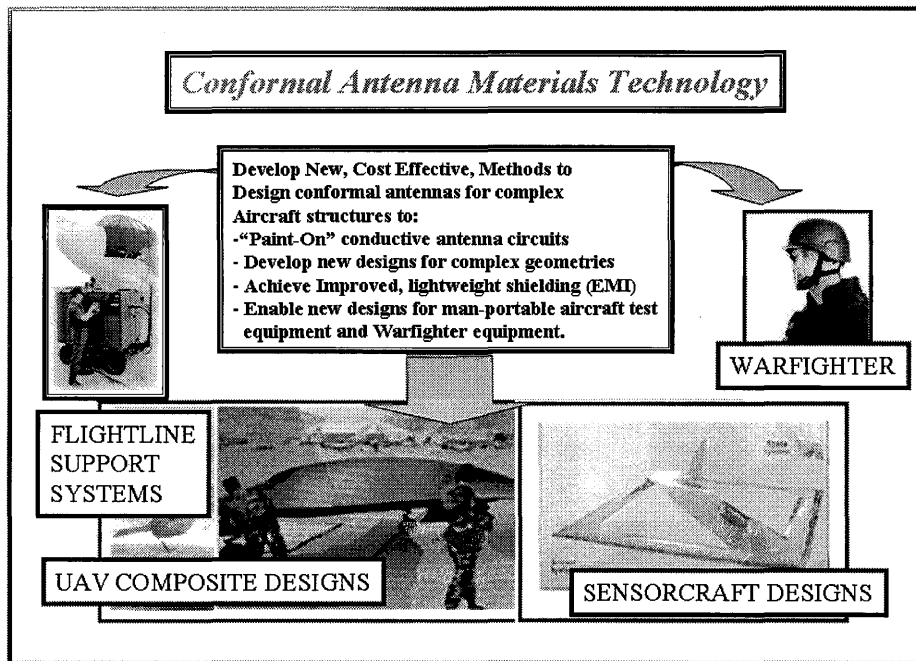


Figure 1 – Conformal Antenna Materials Technology research program goals and potential applications of the technology.

During Phase I, AEM teamed with Unitech, LLC to develop the basic elements of conformal antenna materials, and these accomplishments provided the foundation for the Phase II research activities. Major accomplishments during Phase I are listed below:

- Developed several polymer-based dielectric coatings that are compatible with robotic spray applications and achieved layer thickness capability from 0.020 – 0.100 inches which are suitable for building multiple layers.
- Developed polymer-based dielectric coatings that exhibit dielectric constants from 2.1 to 3.0 with loss tangent in the range of 0.04-0.08 at X-Band.
- Developed methodology for using laser-cut, pressure sensitive adhesive templates for applying “paint-on” circuits of microstrip antennas and microstrip transmission lines.
- Applied EM software analysis tools were demonstrated (and verified with measurements) for various microstrip element configurations.
- Developed EM properties characterizations of dielectric and conductive material coatings using NASA Langley’s Electromagnetic Properties Measurement Laboratory (EPML).
- Developed antenna experiments to demonstrate and verify the concept for “paint-on” conformal antenna designs.
- Formulated an experimental concept for integrated wing array design experiments.
- Developed “spray-on” techniques that enable manufacturing methods for “paint-on” conformal antenna designs.

- Investigated (and tested) EM compatible coatings for sand/rain erosion protection for the conformal antenna designs.

During Phase II, AEM added Composite Optics-ATK and Pratt and Whitney to the team to expand and develop the experimental wing phased array that simulates the application of “paint-on” antennas to a specific aircraft structure. The details regarding the phased array wing design and development are presented in reference [2] and will not be discussed in this paper. The basic goals of the Phase II program are to expand the development of the technology and, as depicted in Figure 2, investigate robotic manufacturing methods for “paint-on” conformal antenna designs.

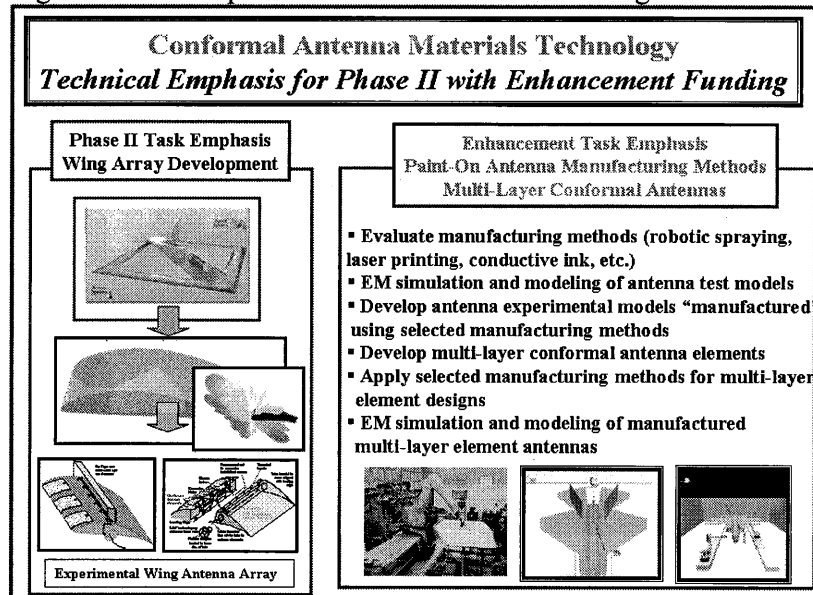


Figure 2 – Technical emphasis for Phase II with the Enhancement funding award.

The research goals for the Enhancement Award activities have been integrated with the existing Phase II tasks to demonstrate manufacturing methods for conformal “paint-on” antenna technology.

2. *Research Requirements*

Research requirements were established early in the program in polymer materials, antenna designs, EM analysis, and experimental array designs. The Air Force Research Laboratory (AFRL) personnel suggested a possible demonstration of the technology by designing an end-fire phased array antenna that could be integrated with a scaled wing profile of a high performance aircraft. This ‘focused design’ application provided a clear direction for the Conformal Antenna Materials technology program and a means to evaluate the readiness level of this technology. A “focus mission” concept has not only provided an operational goal for the SBIR, it defined many of the tasks for the Phase II work plan.

Classification of Material Coatings: New polymer-based dielectric materials were required that exhibited the rheology to produce relatively thick coatings with low dielectric constants and with low loss tangents. Therefore, several developmental categories were identified for Unitech's material coatings which includes Unishield® [3] and these are listed below. Category (1) was the emphasis for this SBIR whereas categories (2) and (3) are considered to be "spin-off" technologies that could be pursued through possible commercialization efforts after the completion of the SBIR research.

(1) "Paint-On" Antenna Designs

- (a) Dielectric Layers: Epoxy-based dielectrics to include quartz filler and no-filler resin designs along with casting and spraying application methods.
Estimated Range of Dielectric Constant: $\epsilon = 2.0$ to 4.0 ; will determine tolerance variations of dielectric constant. The epoxy-based coatings enable thicker substrate layers and compounding to produce lower losses.
Layer Thickness: The range of substrate thickness shall be 0.0625 - 0.100 inches.
- (b) Unishield Conductive Layer; Weight – 0.0217 lbs./sq. ft.; with high ranges of conductivities.
- (c) Unishield Layer Thickness: 2-3 mils of dry film thickness (DFT) (3 mils per layer).

(2) "Flex" Substrate Designs

- (a) Dielectric Substrates:
 - Urethane Foam material
 - Urethane Elastomer material
 - Moldable dielectric (Refractory Sheet)
Layer Thickness: 0.158 , 0.133 -inches.
Dielectric Constant: (Range of dielectric constants to be determined)
- (b) Conductive Layer: 'Super' Flex Unishield with high range of conductivity.

(3) Laminated Antenna Designs

- (a) Quartz-Honeycomb core materials
- (b) RP-46 Composite Resin (Dielectric)
Dielectric Constant: $\epsilon = 2.9$; $\epsilon^{11} = 0.001$ @ 10 GHz.
- (c) Conductive Unishield/RP-50 coating resin (600° F Curing Temp.)

Film Thickness Control Methods: Film thickness control methods are required for all spray-on coatings using polymer-based materials. Initially, water-based emulsion type systems were desired to achieve the dielectric film build layer. Emulsion systems do not provide the film-build capabilities that are necessary to achieve the range of layer thicknesses for conformal antennas. Even though various fillers can be used with these emulsion polymers, it is still difficult to achieve high film build and thick substrate layers using these formulations. So, initially, the development of polymer epoxy-based coatings were selected so that higher film builds could be achieved.

Dielectric and conductive coatings were sprayed to determine and repeatable film thickness and then evaluated for accuracy. Based on the results of the various trial runs, a final film thickness control procedure was selected.

Selection of EM Analysis Methods: AEM uses commercially available EM software such as FEKO [4]. Specifically, FEKO software code was used to predict EM performance of two classes of microstrip antennas; (1) monopole pattern configuration and (2) slot radiation pattern-configuration. The impedance, bandwidth and radiation patterns of the microstrip antennas were predicted and compared with the painted-on antenna experiments with good agreement. These results are discussed later in this paper.

Test Requirements for EM Properties of Material Specimen: Test requirements were established for precision network analyzers to measure the EM properties of all material specimens that were developed. A plan for all of the SBIR material property EM tests emphasized C-Band and X-Band frequencies.

Conformal Antenna Design Requirements – “Focused Mission Array Design”: The overall goal of this research project is to demonstrate the design capability for “paint-on” conformal antennas and to focus this research to enable potential applications of the technology. Therefore, the “Focused Mission” concept established the technology requirements for the Phase-II task activities. The technical results could, possibly, provide contributions to on-going flight programs such as the SensorCraft Technology Program, Uninhabited Airborne Vehicle (UAV), or, possibly, the Joined-Wing Air Force Project. Related to these missions are performance specifications that could be useful to determine the integration and environmental requirements for conformal antennas required for these missions. A phased end-fire antenna array concept was selected that will be integrated with wing cross sections shown in Figure 3. The wing cross-section data was provided by Air Force Research Laboratory personnel.

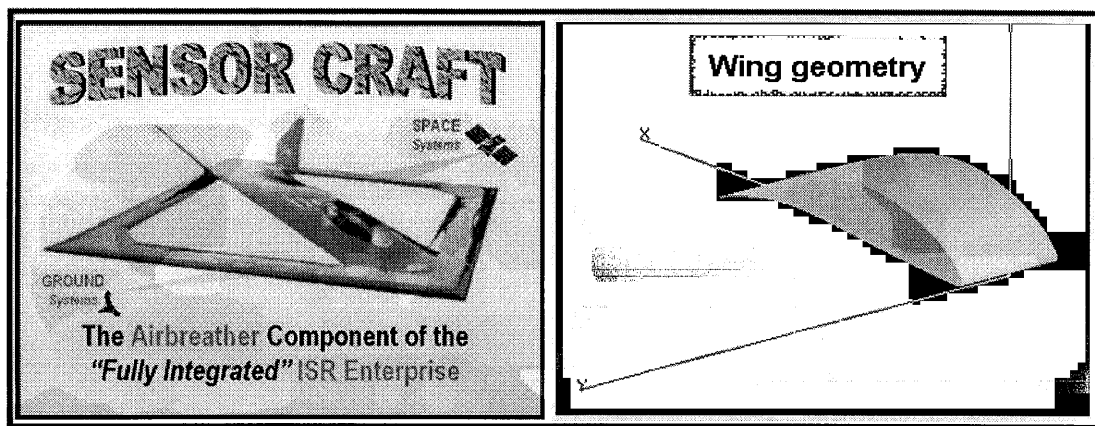


Figure 3 – Wing configuration selected for the end-fire phased array antenna design.

Also, AFRL personnel emphasized wide bandwidth (5-10%) designs, but it is important that the basic capabilities for “paint-on” antenna technology be developed first and then wider bandwidth designs can be developed. If the initial emphasis was placed on

achieving wide bandwidths (say 10% or greater), then the basic technology for "paint-on" antennas could have been reduced. For reference purposes, the data from [5] Bailey and Parks and Bailey and Desphande [6] provides basic relationships for square and circular microstrip patch antennas.

An intermediate bandwidth goal of (5-7%) was established and the basic square patch microstrip element design was selected using parameters for that purpose. In addition, the selection of square patch element designs will be compatible with subsequent array designs for end-fire aircraft (Sensorcraft) wing configurations. Since numerous microstrip elements designs for wide band operation are available in the literature, these designs will be studied later using the technology that has been developed.

3. Development of Polymer-Based Material Coatings for Conformal Antenna Design Applications

In the development of the dielectric materials for conformal antennas, three parameters were of particular interest: 1) polymer film thickness, 2) low dielectric constant and 3) low loss tangent. Since most standard commercial substrate materials include a basic thickness of 0.062," this thickness was selected as the initial goal for the spray-on polymer-based materials. This was accomplished by using a controlled amount of material, fixed spray pressure and flow rate. Once the thickness of each spray application was determined, we were able to achieve our goal thickness by layering. This procedure was repeated over three different applications and achieved the same results.

The next goal was to develop material coatings that exhibit low dielectric constants and low RF losses. Several additional polymer options were considered initially which affects the electrical properties (dielectric constant and dissipation factor) as polymers react with the epoxy. An Amidopolyamine was initially used as a crosslinker and the EM test results for these samples are discussed later in this report. In considering other polymers for example, a Triethylenetetramine exhibits a dielectric constant of 3.2 at 1 MHz and a dissipation factor of 0.031. For this material, as the frequency increases, the dielectric constant tends to decrease but the dissipation factor increases. Another possibility that was considered was Nadic Methyl Anhydride that has a dielectric constant of 3.1 @ 1 MHZ and a dissipation factor of .015.

A database on polymer-based dielectric formulations was reviewed and compared with preliminary selections and then final material selections were prepared for EM tests. The physical characteristics of these materials were investigated as well. After an 'optimum' list of materials was selected, formulations were fabricated on substrates (60-80 mil film thickness). Various epoxy base polymers were prepared using a variety of cross linking agents. Also, Urethane polymers were formulated with various cross linking agents applicable for urethane cross-linked dielectric materials. Cyanate Ester polymers were also considered as a coating and as a dielectric matrix. But, initial investigations found that most of the commercially available Cyanate Ester polymers are engineered for composite manufacturing and would not be compatible with the antenna coatings developments. Essentially, these systems are characterized by long cure cycles at

elevated temperatures, usually greater than 175° C or 347° F. and the use of pressure to form a laminate. Investigation were not continued regarding a suitable Cyanate Ester system because lower temperature cure coating system are required.

Formulations were developed for the epoxy /polyamidoamine, polysilazane, silane modified polyglycidyl ether / cycloaliphatic amine, and a polyester / urethane. In addition, the following filler formulations were developed; epoxy /polyamidoamine with ceramic filler, glass filler and boron nitride filler; polysilazane with ceramic filler; silane modified polyglycidyl ether /cycloaliphatic amine with ceramic filler and glass fill. The plan for materials development is presented in Figure 4.

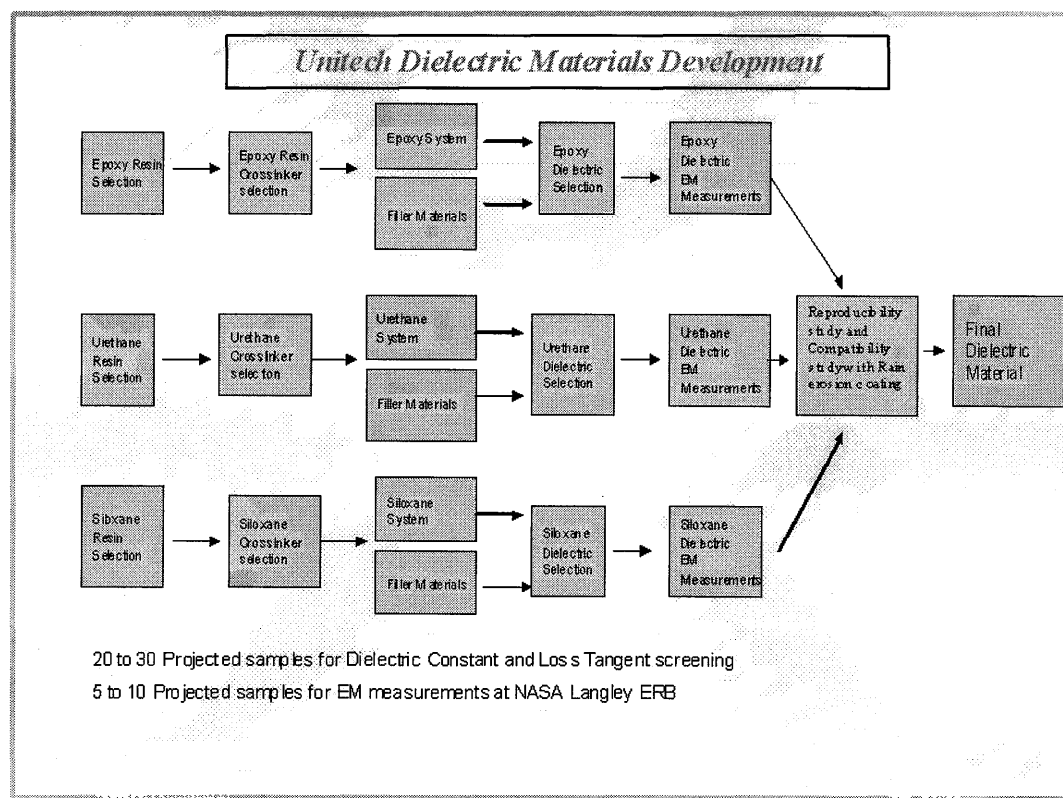


Figure 4 – Flow diagram for materials and process development.

Using this plan, candidate materials were formulated and prepared for EM tests and characterizations. A preliminary list of these materials is provided in table I showing the code number designation for each formula and the composition.

<u>Formula Code</u>	<u>Polymer Base</u>	<u>Filler Material</u>
LB-064	Epoxy / Polyamidoamine	Fumed Silica
LB-065	Epoxy / Polyamidoamine	Ceramic
LB-066	Polysilazane	None

LB-067	Polysilazane	Ceramic
LB-068	Epoxy / Polyamidoamine	Glass
LB-069	Silane / Polyglycidyl Ether	None
LB-070	Silane / Polyglycidyl Ether	Ceramic
LB-071	Silane / Polyglycidyl Ether	Glass
LB-072	Epoxy / Polyamidoamine	Boron Nitride
LB-073	Epoxy / Polyamidoamine	None
LB-074	Polyester / Urethane	None

Table I – Current listing of developed material formulations ready for EM screening tests.

Dielectric substrates were fabricated for each of these formulations and they consisted of filled and unfilled systems. Several sheets (approximately 8x12-inches, 0.0625-inch layer thickness) were fabricated by spraying the polymer based dielectrics onto a metallic ground plane. Individual coupons were machined from the dielectric sheets for waveguide (EM) testing and the remainder of the sheet was used for transmission line assembly testing. In addition, experimental trials with various application methods were performed to determine the most accurate method and equipment for the application of the selected materials to curved surface (such as the leading edge of the wing geometry).

Polymer Dielectric Testing:

EM tests and evaluations were conducted in accordance with the plan shown in Figure 5 and screening tests were conducted on the material samples using the precision airline method and later, samples were prepared for X-Band waveguide measurements. This setup provided measurements up to 6 GHz. Reproducibility of dielectric materials is very important and was addressed as selected formulations were repeated and measured during the EM coaxial screening measurements. The EM measurement procedures outlined were implemented with promising results as variations in dielectric constant and loss tangent properties for the various polymer-based coatings were obtained.

EM Measurements of Material Properties

Airline test specimens were prepared for each formulations listed in Table I and EM tests conducted to determine the dielectric constant and loss tangent. Two approaches were investigated initially to prepare the doughnut samples which included a die punch to form the airline “doughnut” and actual machining of the doughnut. The punch set was fabricated to fit into the airline tube. But, it was found that some of the polymers systems were too hard for the punch set and required machining. So, machining the doughnut samples from a “sheet” of coating material was the approach implemented for the EM measurements.

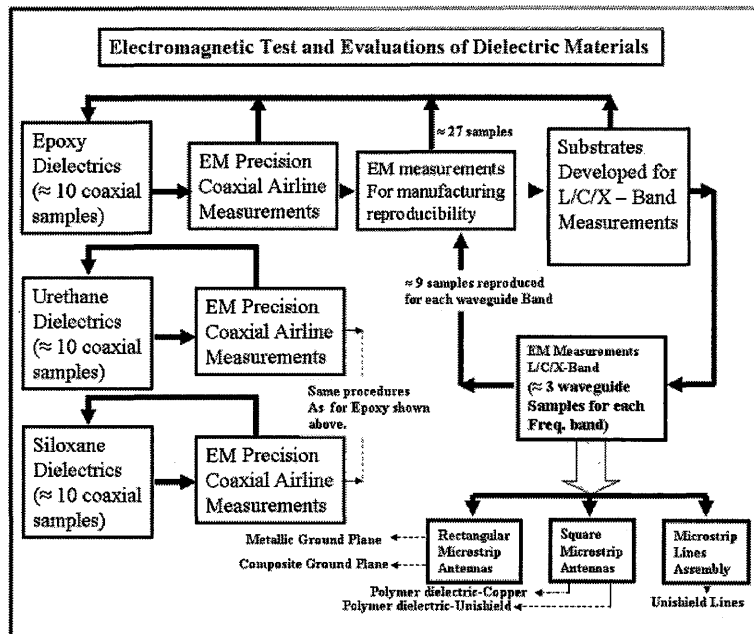


Figure 5 – Development and Test plan for polymer-based dielectric materials for conformal antenna designs.

Precision airline procedures were developed to test the material samples and the array of instruments used to measure the dielectric specimens are presented in Figure 6. Agilent software was used to calculate the dielectric constant and loss tangent for the individual dielectric “doughnuts” and MATLAB was used for plotting the final results. Material measurements were repeated so that systematic measurement errors can be determined. It is very important that we determine the variations in material properties due to: (1) variations in the material formulations, (2) variations in sample thickness, and (3) variations in the EM properties measurements. Preliminary results indicated slightly different values for dielectric constant for samples of different thickness of the same material lots but these effects were later attributed to measurement repeatability.

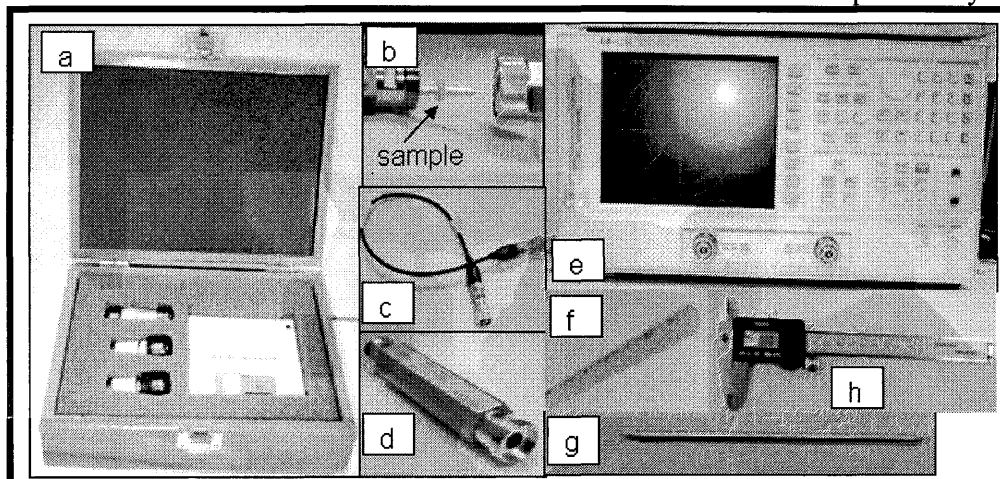


Figure 6 – Some of the instruments associated with the coaxial precision airline EM testing of dielectric materials. The instruments labeled are: (a) calibration kit, (b) sample

for testing, (c) coaxial cable with APC connectors, (d) 7 mm, 50 ohm Airline, (e) Network Analyzer, (f) material sample extractor/inserter, (g) center conductor for the Airline, and (h) precision measuring calipers for material thickness measurements.

The setup for calibrating and material measurements and the components used are shown in Figure 7. It was determined that approximately 100 dB of dynamic range is required for accurate and repeatable measurements.

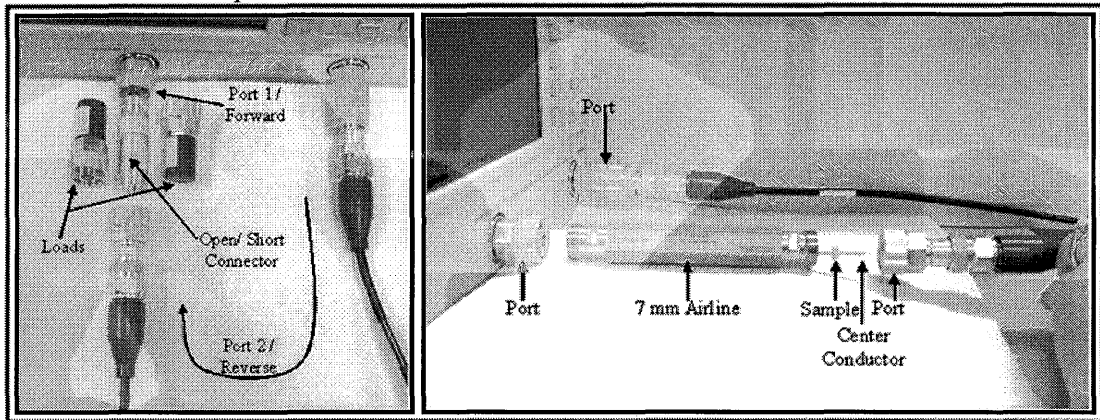


Figure 7 – Procedures for calibrating the network analyzer and photograph of the full setup for dielectric material sample measurements.

The lot numbers selected for re-measurements are LB-069, 070, and 082. These selected examples are for the Epoxy and Silane/Polyglycidyl Ether polymer-based systems and associated filler materials as listed in Table II. These systems have varying physical characteristics and these features along with the EM properties were evaluated.

For. Code	Polymer Base	Filler Material
LB-069	Silane / Polyglycidyl Ether	None
LB-070	Silane / Polyglycidyl Ether	Ceramic
LB-082	Silane / Polyglycidyl Ether	Boron Nitride

Table II – Preliminary “down-selection” of polymer dielectric materials having favorable EM characteristics.

Typical measurement results exhibited by these samples are presented in Figures 9 for the LB-070 formulation and similar trends were obtained for LB-069 and LB-082 but are not presented in this report. In Figure 8, it can be seen that the dielectric constant decreases with frequency as it should but effects due to specimen thickness were also observed. These effects were determined to be measurement errors going from one setup to another and slight variations in material formulations. Since the wing antenna array will be designed to operate at 5.5 GHz, that frequency range was of particular interest as the data on dielectric constant and loss tangent were reviewed. For the LB-069, material samples were measured and re-measured and the results indicated dielectric constant of 3.6 and 3.43. Also, the loss tangent was measured to be 0.055 and 0.054 for the two measurements.

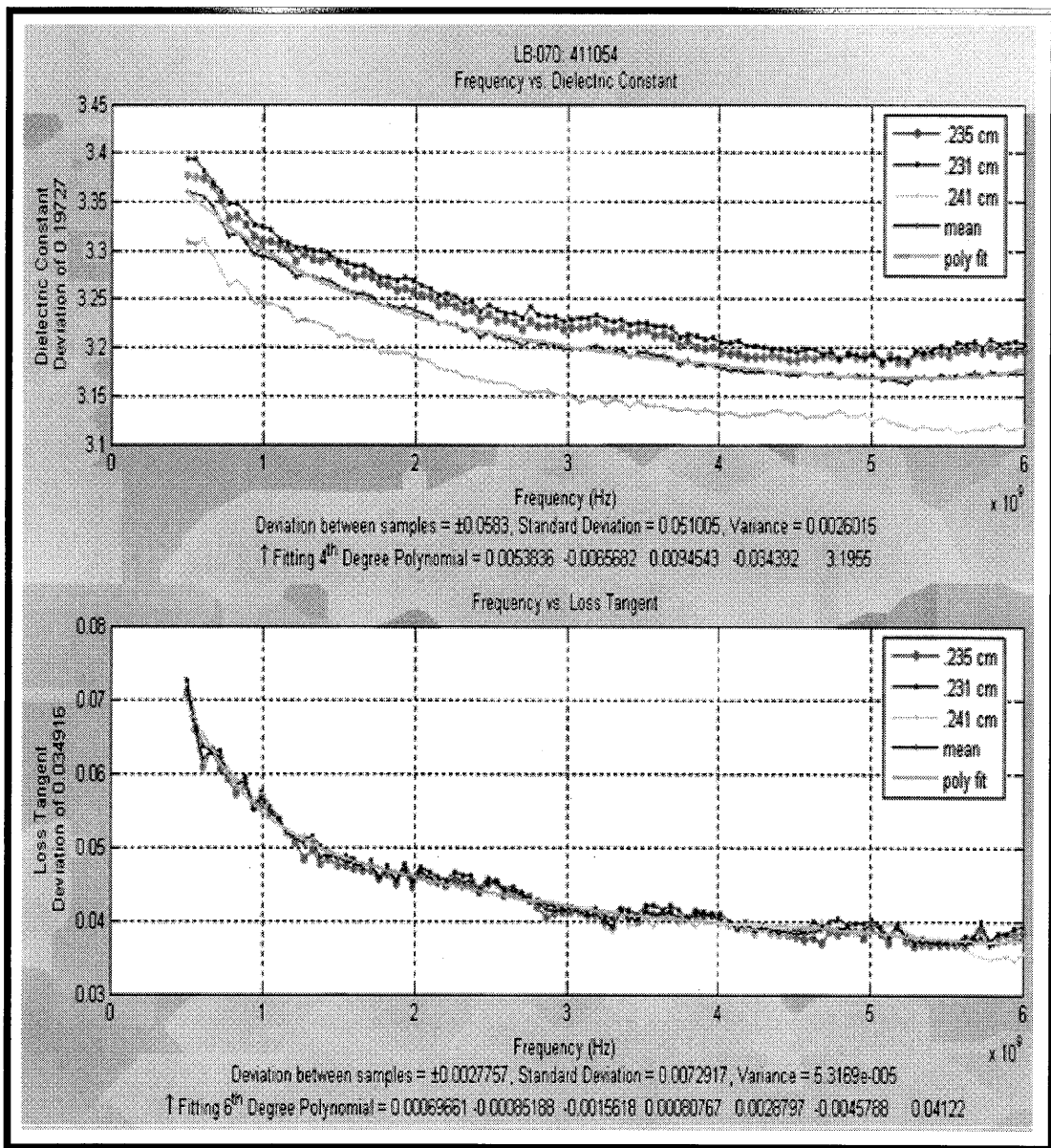


Figure 8 - Dielectric and loss tangent measurement results for LB-070 material.

The results for the LB-070 indicated less variation in loss tangent but noticeable variations in dielectric constant due to sample thickness. For instance, the 0.241-cm sample had a dielectric constant of 3.12 and 3.20 for the 0.231-cm sample. These variations indicated that the consistency in the formulations had to be improved so that the use of the material properties could be confidently used to design antennas.

EM measurements were conducted on all the samples and selected samples were re-measured to determine repeatability. These systems have varying physical characteristics and these features along with the EM properties were evaluated and a down-selection

process was initiated. Previous test results for the LB-070 indicated less variation in loss tangent but noticeable variations in dielectric constant due to sample thickness. For instance, the 0.241-cm sample had a dielectric constant of 3.12 and 3.20 for the 0.231-cm sample. These variations are not necessarily bad for the antenna design but consistency is required in all material formulations for antenna design applications

Of the three materials down selected, LB069, LB070 and LB082, they each had certain attributes. The LB069 had the lowest overall dielectric constant at an average of 2.765, but the loss tangent was averaged at 0.049. The LB082 had a good dielectric constant, average of 2.985 and a loss tangent average of 0.0391. The LB070 had a slightly higher dielectric constant, averaging 3.049, but the loss tangent averaged 0.0351. All three of these materials were made from the same Polyglycidyl Ether polymer. The differences found in the dielectric constant and loss tangent were due to the filler effects. Since all three materials were from the same polymer base, only slight differences in performance were expected with the three materials chosen. The final selection of the baseline material (LB-070) was then based on RF properties. Figure 9 shows the spread between the “down selected” formulations for the L-Band /C-Band (doughnut) airline measurements and the X-Band waveguide measurements. . The LB070 was chosen based on the lower loss tangent.

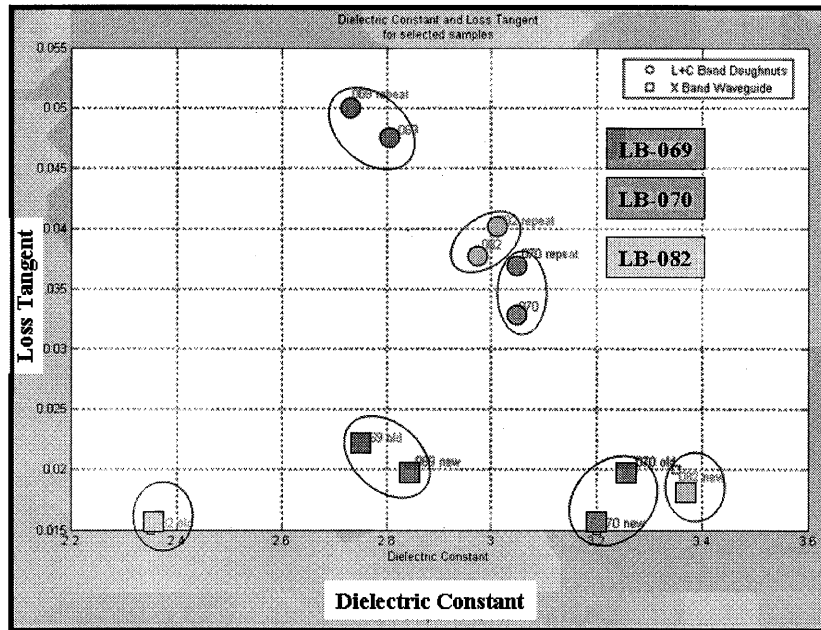


Figure 9 – Loss tangent versus dielectric constant data for the three down selected formulations (LB-069, LB-082, and LB-070).

In addition to the development and testing of dielectric coatings was the need to develop highly conductive coatings for antenna designs. This development is discussed next.

Advanced Conductive Coating Development (LB-088)

Based on earlier test results, the RF characteristics of baseline Unishield conductive coating was found to be inadequate for antenna feed circuits due to the high insertion loss characteristics. As a result, a new and improved conductive coating (LB-088) was

developed and preliminary RF tests (shown in Figure 10) indicated good results for antenna design applications. Additional tests were conducted to evaluate the quality of spray applications. In each test, the dry film thickness and resistance of the sprayed coatings were measured.

The results of test (#1) indicated a dry film thickness of 1.4-1.6 mils and conductivity (resistance) of 0.018 ohms per square. Results of the second test trial indicated a dry film thickness of 1.1 to 1.2 mils and better (resistance) conductivity of 0.009 ohms per square were achieved. LB-088 was selected for all subsequent antenna designs.

Development of Advanced Conductive Coatings for Conformal Antenna Designs

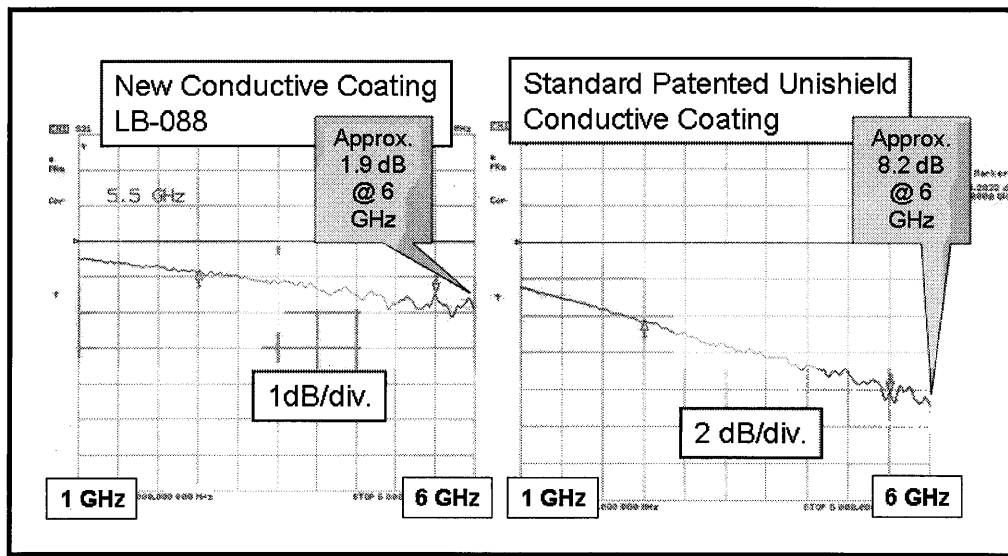


Figure 10 – Comparison of loss characteristics of the new conductive coating (LB-088) with standard Unishield coating.

During preliminary antenna tests, problems were encountered (during Phase I) when conductive coatings (not LB-088) were applied to graphite composite materials. Essentially, the antenna performance such as the resonant frequency and radiation pattern gain levels were affected by the poor conductivity with the ground plane coating. In Phase II, this problem was encountered again when conductive coatings on composite materials were measured. The problem was further analyzed by inspecting the condition of graphite composite materials before coating and when the resistance of the composite materials was measured. Initially, it appeared that the continuity of an antenna ground plane (using conductive coatings on the graphite composite structure) was degraded due to coating interactions. Since the composite materials used on the wing model will be coated with the painted-on array, this problem had to be solved. The resistance of the (uncoated) wing surface varied greatly depending on where the meter probes were placed and what pressure was applied. Also, differences were observed whether the composite surface was smooth or rough – which means resin “rich” or resin “starved.”

This problem became more evident when several types of conductive coatings with and without sealant coatings were applied to GFE materials. NASA measurement test results produced varying shielding effectiveness levels and were thereby inconclusive as to the effects of the conductive coatings on the graphite materials. As a minimum, these tests indicated that a pre-coated surface (before applying Unishield or LB-088 conductive coating) would not degrade the conductivity of the ground plane for the array. But this did not solve the problem. In the final analysis, a decision had to be made regarding the composite wing section and how to achieve a good conductive ground plane for the array.

As this problem was researched further, and especially in the design of low observable composite materials, it was determined that graphite composite surfaces had to be lightly “sanded” before applying the conductive ground plane coating. Sanding the composite surface removes the top resin coating and exposes graphite fibers and thereby produces better contact with the conductive coating. Subsequent tests on small coated samples of composite materials resulted in drastically improved conductivities. Therefore, that procedure was adopted and implemented to prepare the wing for painting the array. A sealer coat will not be applied to the wing surface prior to applying the LB-088 conductive ground plane.

4. Conformal Material Paint Parameter Tolerance Study

In order to better understand the RF performances of “painted-on” antenna elements, a paint parameter tolerance study was conducted by McNaul [7] and highlights of that study are presented in this paper. The materials tolerance study is used to determine the allowable variations in various paint formulations that will affect painted-on antenna performance. So, the objective of this study was to identify and quantify cause and effect relationships between special paint material characteristics and RF antenna performance. McNaul’s approach was to use a “simple” 3-D model in HFSS for a generic planar microstrip antenna element. The antenna element that was modeled is shown in Figure 11. The initial parametric analysis task has been completed and will be updated once the final array has been developed and tested. A single element parametric model provides the capability to “dial-in” strategic parameters and observe RF performance changes in tuning, impedance, pattern, gain, and bandwidth.

Key paint tolerances were identified such as registry, slump, undercut, dielectric constant, loss tangent, conductivity, thickness, etc. The model will be useful to run parametric simulations and feeder lines can be added during the next phase of the task. The first list of parameters include variations in dielectric thickness, dimensional accuracies of the patch antenna, EM properties as measured of the dielectric and conductive coatings, feed positions, type of ground plane and variations in conductivity of ground plane (metal and composite).

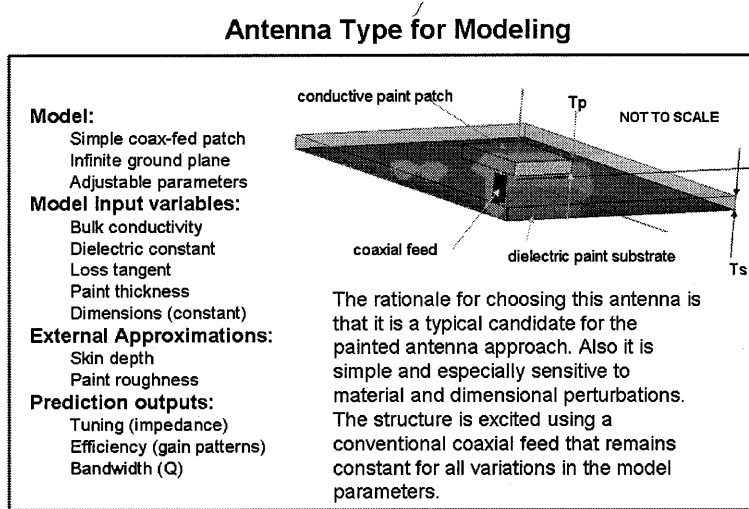


Figure 11 – Antenna patch configuration used in parametric tolerance modeling task.

Various polymer-based dielectric material formulations were developed and applied to several antenna element designs (that are painted-on) to predict resonant frequency and bandwidth characteristics. Using the EM characteristics for these polymer-based dielectric materials, the resonant frequencies and bandwidth characteristics were predicted. It is important to understand the variations in the EM characteristics (dielectric constant and loss tangent versus frequency) so that accurate antenna element designs could be developed. The variations in dielectric constant and loss tangent are due to variations in the fabrication process as well as to systematic measurement errors. Element designs were limited to single layer dielectric configurations (at this stage of the conformal antenna materials program), and the bandwidth design goal is approximately 5% for the element. Variations in the material properties (dielectric constant and thickness) demonstrated in Figure 12 shows the resonant frequency of the square element design for the wing array.

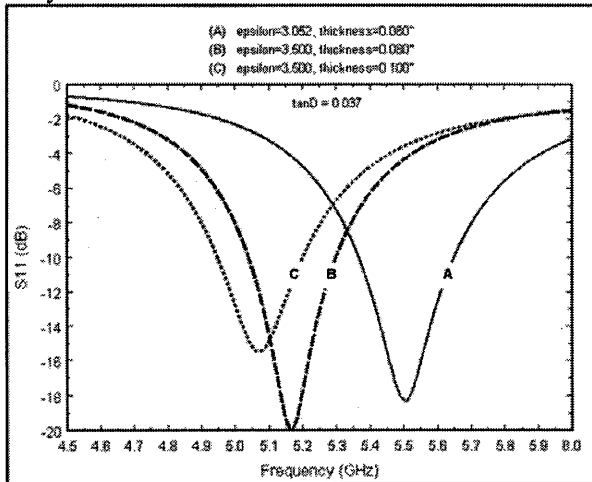


Figure 12 – Effect of material variations on the resonant frequency of the square microstrip antenna.

This study employed preliminary “back of the envelope” analysis followed by a full-wave parametric model of a specific antenna type that addresses the most significant paint material contributions. The basic objectives for this parametric tolerance study are listed below:

- ✓ Identify paint material properties most likely to cause changes in antenna RF performance
- ✓ Establish an expected range of the paint material property values.
- ✓ Identify antenna RF performance parameters that can be used as effect indicators.
- ✓ Perform general “back-of-envelope” analysis of paint material properties and their RF contributions.
- ✓ Select antenna type for full-wave parametric modeling.
- ✓ Construct the antenna model that parameterizes all the significant material properties.
- Using the antenna model simulate the selected antenna RF performance while varying the paint material properties.
- Summarize the results of the trade study analysis.

The antenna RF performance parameters are listed in Table III along with the paint material properties and how these properties could affect antenna performance. These performance parameters that are affected by the paint properties are discussed briefly below.

Pattern – This is the shape and magnitude (dBi) of the radiated field of the antenna. It is directly related to the currents flowing on the antenna. The currents are effected by the conductivity and losses in the paint.

Resonance – For very narrow band antennas such as the microstrip patch antenna the antenna structure will resonate at a particular frequency. The location of the resonance is affected by the electrical length of the antenna dimensions. The dielectric constant of the paint directly effects electrical length.

Efficiency – Some of the RF energy that flows into the terminals of an antenna will be absorbed in the losses in the materials and not be radiated. These losses are dictated by loss tangent and bulk resistivity of the paint.

Bandwidth – Losses in the paint also alter the Q of the resonant antenna thereby increasing or decreasing the band width. For antennas such as the microstrip patch the dielectric paint thickness also affects the bandwidth.

Antenna RF Performance Parameters				
Paint Material Property	Patterns	Resonance	Efficiency	Bandwidth
Dielectric constant	✓	✓		✓
Dielectric Loss Tangent			✓	
Bulk Resistivity			✓	
Thickness	✓			✓
Protective Paint Flash Coating 1\	✓	✓	✓	✓

1\ Protective paint variation has replaced roughness in this study

Table III – Antenna performance parameters that are affected by paint material properties.

In order to start the tolerance study, paint material properties of conductive and dielectric coatings were provided and examples of this data have been previously discussed in this report. These data were used in parametric studies for the design of individual elements and this study will be updated after the wing array is fabricated and tested. The resulting tolerance data for the paint material properties are presented in Table IV and categorized as minimum, baseline, and maximum variations.

Paint Material Property	Tolerance		
	Minimum	Baseline	Maximum
Dielectric constant	2.08	3.04	3.1
Dielectric Loss Tangent	.030	.0375	.045
Surface Resistivity [Bulk Conductivity]	.02 Ω/sq \1 [54.3x10 ⁶ Siemens/m]	.02 Ω/sq [54.3x10 ⁶ S/m]	0.2 Ω/sq \1 [.54x10 ⁶ Siemens/m]
Conductive Paint Thickness	3 mils	6.5 mils	10 mils
Dielectric Paint Thickness	.070" [.075"]	.080"	.090" [.085"]
Protective Paint Flash Coating	4 mil Er 3.5 Er"=.04	7 mil Er 4.2	10 mil Er=5.0 Er"=.15

Table IV – Tolerances for the paint material properties for conformal antenna designs.

The range of conductor thickness selected for the study is considered sufficient to support five skin depths required for proper electrical operations. This justified the use of the sheet resistivity numbers provided at 5.5 GHz for two values of bulk conductivity (0.54 x

10^6 S/m) and (54×10^6 S/m). The corresponding sheet resistance values (for the conductive paint) would be 0.20 ohms/square to 0.02 ohms/square respectively. These results are shown in Figure 13.

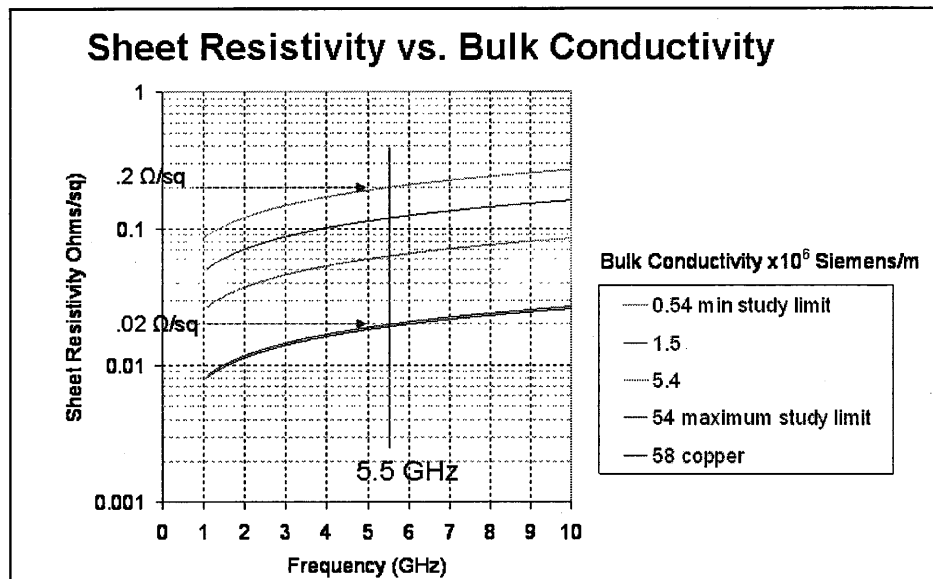


Figure 13 – Sheet resistivity versus bulk conductivity.

The skin depth of the conductive coatings varies as a function of frequency as shown in Figure 14. Information presented in this figure is based on the assumption that the conductor paint thickness is greater than five skin depths. It also shows that sheet resistivity can be deceptive depending on how it is measured. This study assumes that sheet resistivity is measured at 5.5 GHz.

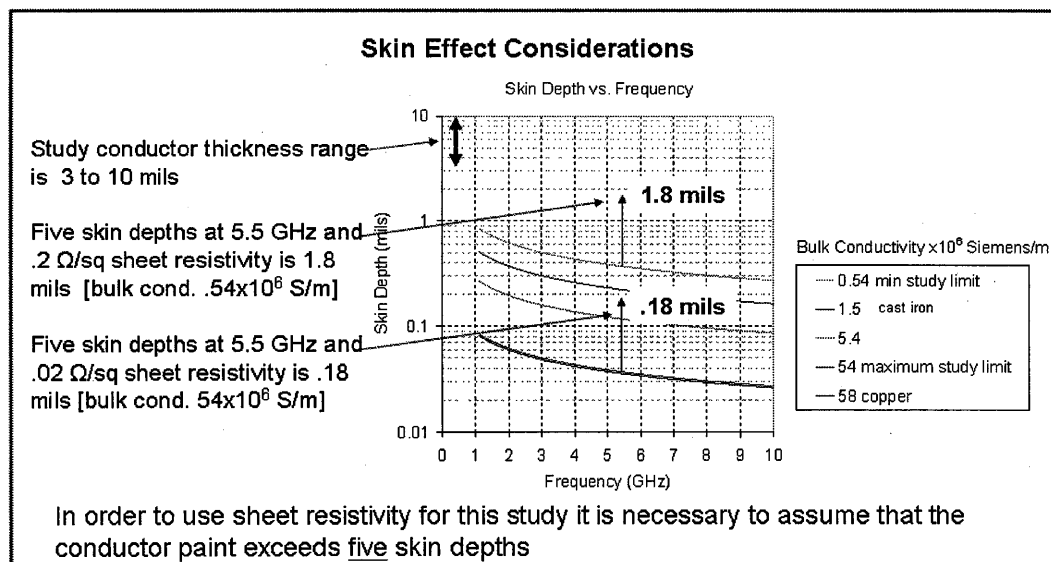


Figure 14 – Skin depth versus frequency as a function of bulk conductivity (sheet resistance) for conductive coatings.

Essentially, the following relationships are important to consider regarding conductive paint coatings:

- Skin depth is a function of bulk resistivity and frequency.
- Conductors require thicknesses of >5 skin depths to realize 99% of the maximum conductivity possible.
- Model assumes that the conductive paint thickness satisfies the 5 skin depth criteria. (i.e. range = 0.1 to 50 mils)
- Sheet resistivity (Ω/sq) is a function of frequency and skin depth when the paint is $>5 \times$ skin depth.
- Simulation must include resistivity in the predictions.
- Higher resistivity implies higher loss paint.

For this study, various ranges for tolerance values were established for RF performance studies and examples were selected from Table V for conductive paint, dielectric paint, and protective paint coatings. The patch element dimensions were held constant for the examples selected.

File name	Conductive Paint		Dielectric Paint			Protective Paint		Patch	
	Bulk Conductivity	Thickness (mils)	Thickness (mils)	Dielectric constant	loss tangent	Thickness/ ϵ_r	loss tangent	L	H
BASELINE_PATCH_065_800_304_0375_02	54.3 MS/m	6.5	80	3.04	.0375	7 mils/4.2	.023	.535	.395
PATCH_065_800_304_0375_00	22.0 MS/m	6.5	80	3.04	.0375	7 mils/4.2	.023	.535	.395
PATCH_065_800_304_0375_20	2.2 MS/m	6.5	80	3.04	.0375	7 mils/4.2	.023	.535	.395
PATCH_030_800_304_0375_02	54.3 MS/m	3	80	3.04	.0375	7 mils/4.2	.023	.535	.395
PATCH_100_800_304_0375_02	54.3 MS/m	10	80	3.04	.0375	7 mils/4.2	.023	.535	.395
PATCH_065_700_304_0375_02	54.3 MS/m	6.5	70	3.04	.0375	7 mils/4.2	.023	.535	.395
PATCH_065_900_304_0375_02	54.3 MS/m	6.5	90	3.04	.0375	7 mils/4.2	.023	.535	.395
PATCH_065_800_208_0375_02	54.3 MS/m	6.5	80	2.08	.0375	7 mils/4.2	.023	.535	.395
PATCH_065_800_310_0375_02	54.3 MS/m	6.5	80	3.10	.0375	7 mils/4.2	.023	.535	.395
PATCH_065_800_304_0300_02	54.3 MS/m	6.5	80	3.04	.0300	7 mils/4.2	.023	.535	.395
PATCH_065_800_304_0450_02	54.3 MS/m	6.5	80	3.04	.045	7 mils/4.2	.023	.535	.395
PATCH_065_800_304_0375_02_a	54.3 MS/m	6.5	80	3.04	.0375	4 mils/3.5	.023	.535	.395
PATCH_065_800_304_0375_02_b	54.3 MS/m	6.5	80	3.04	.0375	10 mils/5.0	.023	.535	.395
PATCH_065_800_304_0375_02_c	54.3 MS/m	6.5	80	3.04	.0375	7 mils/4.2	.011	.535	.395
PATCH_065_800_304_0375_02_d	54.3 MS/m	6.5	80	3.04	.0375	7 mils/4.2	.030	.535	.395
PATCH_065_900_208_0375_02	54.3 MS/m	6.5	90	2.08	.0375	7 mils/4.2	.023	.535	.395
PATCH_065_700_310_0375_02	54.3 MS/m	6.5	70	3.10	.0375	7 mils/4.2	.023	.535	.395

Table V – Range of tolerance variations for antenna performance analysis studies.

The analysis results on antenna performance due to tolerances in conductive paint are presented in Table VI. Also, analysis results on antenna performance due to tolerance variations in dielectric paint effects are presented in Table VII.

Conductive Paint Effects			
Paint Thickness		Paint Bulk Conductivity*	
	Min. 3 mils	Baseline 6.5 mils	Max. 10 mils
Resonance frequency (GHz)	5.59	5.51	5.44
Return loss @ resonance (dB)	-32.4	-38.2	-38.2
Bandwidth (MHz) @ 10 dB return loss	320	310	300
Peak Gain (dB)	6.24	6.42	6.44
Peak Directivity (dB)	4.01	4.02	4.19
Efficiency (%)	59.8	57.4	59.6
	Min. 2.2 MS/m	Baseline 54.3 MS/m	Max. 22.0 MS/m
Resonance frequency (GHz)	5.51	5.51	5.52
Return loss @ resonance (dB)	-48.5	-38.2	-37.9
Bandwidth (MHz) @ 10 dB return loss	310	310	300
Peak Gain (dB)	6.44	6.42	6.44
Peak Directivity (dB)	4.00	4.02	4.15
Efficiency (%)	57.0	57.4	59.0

* Bulk conductivities correspond to DC sheet resistivities of .2 Ω/sq (2.2 MS/m) and .02 Ω/sq (22.0 MS/m) measured on 6 mil thickness material.

Table VI – Conductive paint effects and tolerances studied for paint thickness and paint bulk conductivity.

These results indicate that the tolerance variations for the conductive paint do not adversely affect the gain performance of the patch element – assuming the proper skin depth and conductivity values are provided. The gain is slightly affected for the minimum, baseline, and maximum tolerance variations anticipated.

Dielectric Paint Effects			
Paint Thickness		Paint Loss Tangent	
	Min. 70 mils	Baseline 80 mils	Max. 90 mils
Resonance frequency (GHz)	5.56	5.51	5.47
Return loss @ resonance (dB)	-30.0	-38.2	-33.3
Bandwidth (MHz) @ 10 dB return loss	290	310	330
Peak Gain (dB)	6.61	6.42	6.34
Peak Directivity (dB)	3.90	4.02	4.31
Efficiency (%)	53.6	57.4	62.7
	Min. .030	Baseline .0375	Max. .045
Resonance frequency (GHz)	5.52	5.51	5.51
Return loss @ resonance (dB)	-26.3	-38.2	-31.7
Bandwidth (MHz) @ 10 dB return loss	290	310	320
Peak Gain (dB)	6.39	6.42	6.44
Peak Directivity (dB)	4.44	4.02	3.76
Efficiency (%)	63.8	57.4	54.0

Table VII – Dielectric paint effects and tolerances studied for paint thickness and paint loss tangent characteristics.

Also, it was noted that the paint thickness variations do not adversely affect antenna performance for the minimum, baseline, and maximum tolerance variations.

Dielectric Paint Effects (continued)			
Paint Dielectric Constant (Er)		Combined Effects (thickness/Er)*	
	Min. 2.08	Baseline 3.04	Max. 3.10
Resonance frequency (GHz)	5.42	5.51	5.47
Return loss @ resonance (dB)	-23.5	-38.2	-38.8
Bandwidth (MHz) @ 10 dB return loss	380	310	310
Peak Gain (dB)	7.37	6.42	6.34
Peak Directivity (dB)	5.61	4.02	3.94
Efficiency (%)	66.7	57.4	57.6
	Min. 90/2.08	Baseline 80/3.04	Max. 70/3.1
Resonance frequency (GHz)	6.42	5.51	5.52
Return loss @ resonance (dB)	-23.9	-38.2	-29.3
Bandwidth (MHz) @ 10 dB return loss	390	310	280
Peak Gain (dB)	7.37	6.42	6.43
Peak Directivity (dB)	5.66	4.02	3.80
Efficiency (%)	67.4	57.4	54.6

* Typically for the patch design, bandwidth broadens with increase in dielectric thickness and reduction of dielectric constant.

Table VII (Cont'd) – Dielectric paint effects and tolerances studied for paint dielectric constant and combined effects of thickness and dielectric constant.

Performance effects calculated for variations in dielectric constant and thickness of the paint coatings do have major effects on antenna performance as shown in Table V (cont'd). These results are presented in different formats for tuning and radiation patterns and shown in Figures 15 and 16 respectively.

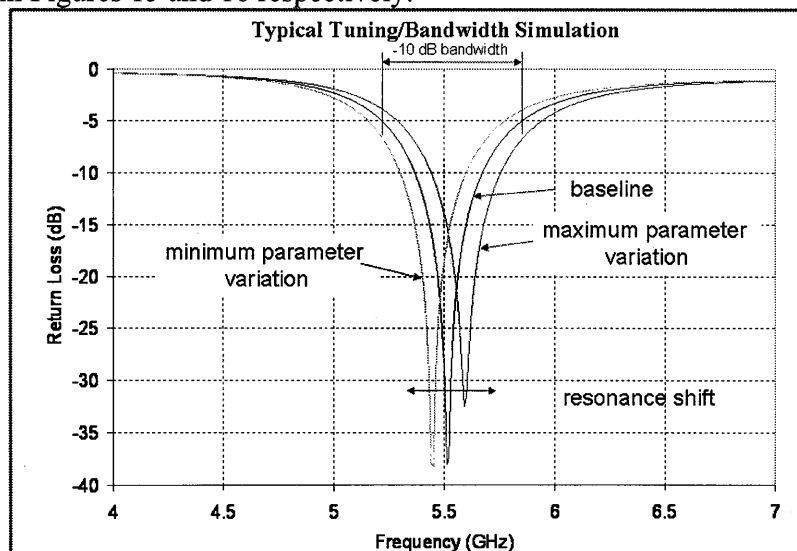


Figure 15 – Typical tuning and bandwidth simulation results for patch antenna element for minimum, baseline, and maximum parameter variations.

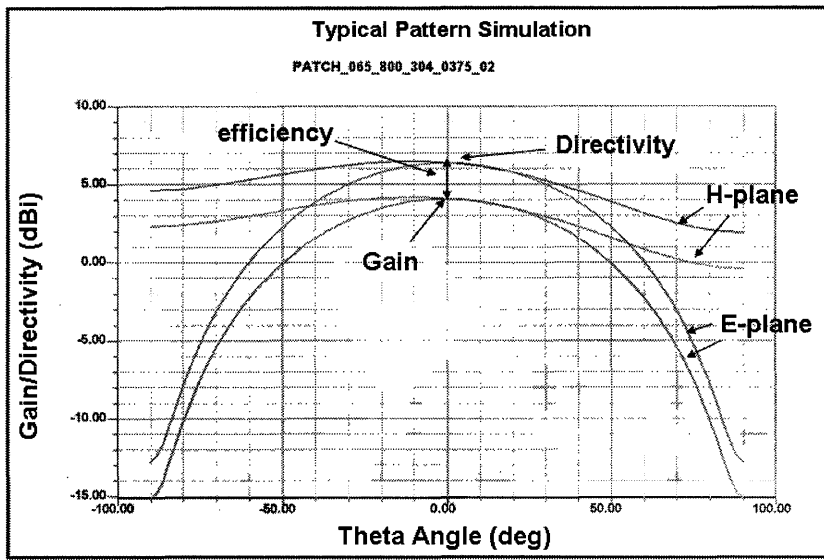


Figure 16 – Typical radiation pattern simulation results for patch antenna element for minimum, baseline, and maximum parameter variations.

Protective (rain erosion) type coatings were also considered in this tolerance study but those details will not be discussed in this report. It is anticipated that tolerance variations in the paint formulations will be predominant factors that will affect antenna performance. Therefore, strict manufacturing controls will be required in the application of conformal antenna ‘paint-on’ antenna fabrication methods.

5. Experimental Antenna Designs Using Conformal “Paint-On” Techniques

In order to fully evaluate antenna designs using the polymer-based materials, experimental antennas were developed. A transmission line test assembly was also fabricated using copper strips and conductive top coats to insure proper conductivity to the microstrip lines. This was important to learn because the method of feeding a painted microstrip antenna had to be determined and copper foil serving as a transition layer was a practical approach. The overall AEM system design capability provides the basis for developing functional breadboard antenna models that were to be tested and evaluated. Included in these evaluations, three rectangular microstrip antennas were fabricated and assembled on a flat metallic ground plane. The physical geometries and dimensions for the L-Band, C-Band, and X-Band rectangular elements were discussed previously (and shown in Figure 3). As described by Balanis [8] using the cavity model for rectangular microstrip antennas, if $L>W>h$, the dominant mode is the TM_{010} and the higher order mode is TM_{001} and if $L>L/2>W>h$; then the second order mode is TM_{020} instead of TM_{001} .

As noted in Figure 3, the dimensions of each experimental rectangular patch indicated that $L>W>h$. Therefore, the frequencies for the prominent resonator modes for each

antenna element were calculated using FEKO EM software and in the initial calculations, the dielectric constant for the NF dielectric measured early during the Phase I program was used. The results are presented in Figure 17 for the L-Band antenna and Figure 18 for the C-Band element. The calculated frequencies were off considerably from the measurements so we began to investigate the reasons for the disagreement. At that time, the dielectric material was not the same as the material measured months ago and the fumed silica was added to the formulation in order to improve the rheology of the final coating. Therefore, the dielectric constant for each antenna was varied in the calculations until a match with the return loss measurements was achieved across the frequency range for each antenna.

Rectangular microstrip antennas were fabricated using the laser-cut templates that defined the dimensions for each patch along with the feedpoint locations. The “paint-on” methods were used to spray-on the polymer –based dielectric layer (0.0625-inch) and the Unishield conductive layers. The antenna configurations included L-Band, C-Band, and X-Band element designs. In addition to the objective to correlate EM analysis and experimental measurements, these tests provide a method to determine the dielectric constant and loss tangent of the dielectric layer. The resonant frequencies for the various modes were determined and after the measurement results were obtained, parametric analysis was conducted to determine the dielectric constant and loss tangent of the dielectric material necessary to match the experimental results. The accuracy of the EM analysis capability is demonstrated in this experimental effort using the rectangular patch antennas.

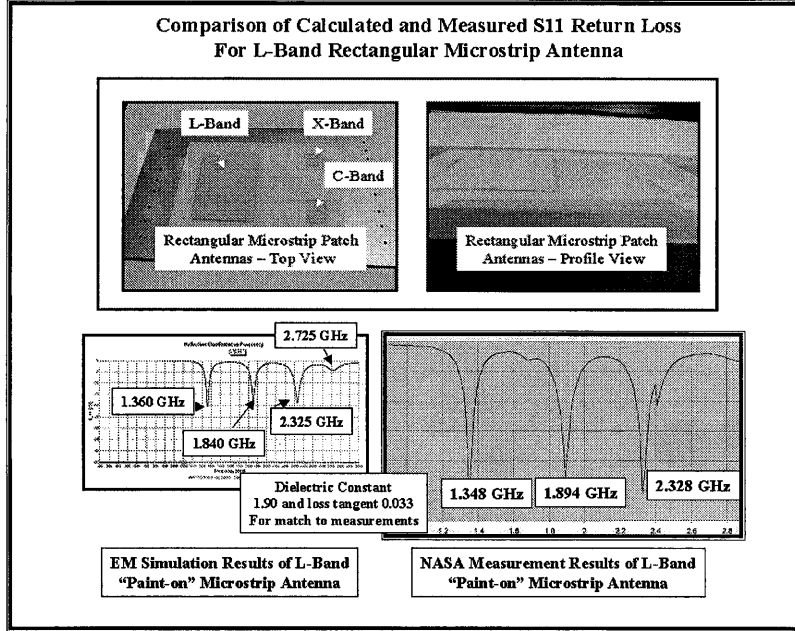


Figure 17 - Comparison of calculated and measured S11 Return Loss characteristics for the L-Band Rectangular “Paint-on” Microstrip Antenna.

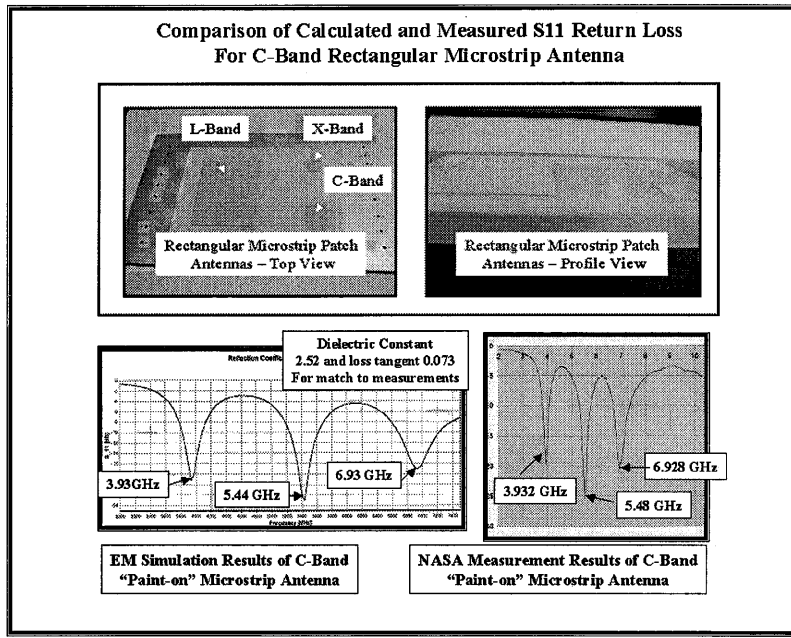


Figure 18 – Comparison of the calculated and measured S11 return loss characteristics for the C-Band Rectangular “Paint-on” Microstrip Antenna

The dielectric constant and the loss tangent properties of the dielectric layer were varied as indicated and it was found that different values of dielectric constant for each antenna were necessary to achieve a match. It was found that for the L-Band antenna, a dielectric constant of 1.90 and a loss tangent of 0.033 matched the measurements. For the C-Band antenna, the dielectric constant and loss tangent values were 2.52 and 0.073 respectively that were required to match the measured data. Calculated and measured radiation patterns for the L-Band antenna at the prominent resonant modes are presented in Figure 19.

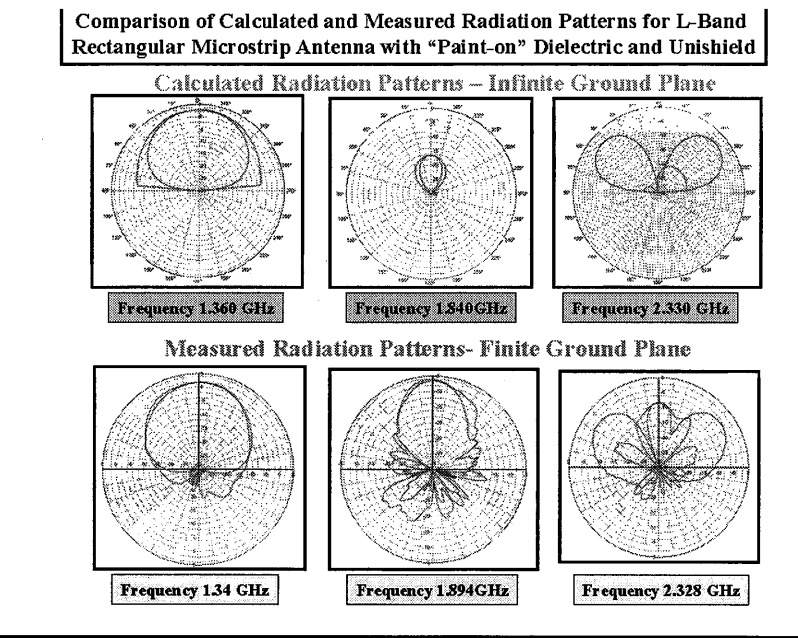


Figure 19 – Calculated and measured radiation patterns for the L-Band rectangular microstrip antenna assuming dielectric constant 1.90 and loss tangent of 0.033.

After these results were completed, similar calculations were made for the X-Band antenna element. It can be seen that for both the L-Band and the C-Band antennas, good agreement was achieved between the calculated and measured return loss characteristics not only in the resonant frequencies but also for the VSWR's for the respective modes.

In a similar manner, analysis was extended to the X-Band antenna element as shown in Figure 20 and it was necessary to vary the dielectric constant and loss tangent again to match the measured data. It can be seen in the measurements, the TM_{010} mode is distinct (with a good VSWR) but the TM_{001} mode is mismatched and the TM_{020} mode is more distinct than for the calculated TM_{020} mode. Also, in order to achieve a match to the measured data, the dielectric constant and loss tangent were determined to be 3.2 and 0.033 respectively. Using these assumed values for the dielectric constant and loss tangent, good agreement resulted in the calculated dominant mode frequency but significant differences were exhibited for the higher order modes. Obviously, these errors will be studied after the actual EM properties for the dielectric layer have been determined. Small specimens of the dielectric layer were removed from the rectangular plate so that X-Band measurements can be conducted to determine the dielectric constant.

To summarize the results of the rectangular patch antenna experiments, the following Table VIII lists the resonator frequencies both (measured and calculated) and the per cent errors associated with these comparisons. It can be noted that assuming the dielectric constants and loss tangents are as assumed, the errors are observed to increase significantly above 5.46 GHz (for the X-Band antenna element).

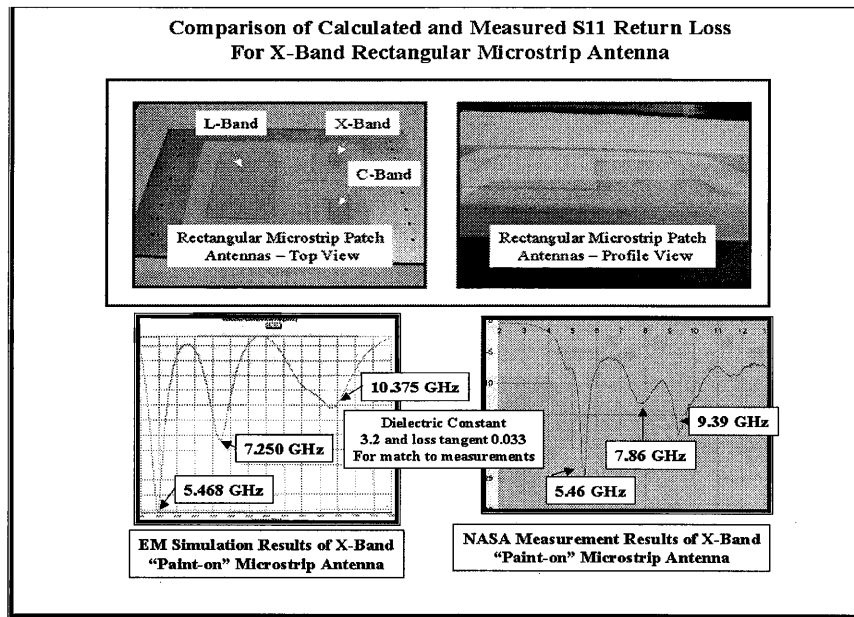


Figure 20 - Comparison of the calculated frequencies for the prominent resonator modes for the X-Band antenna and the resulting dielectric constant required to match the measured results.

Comparing the measurement results with the calculated return loss characteristics for the L-Band rectangular microstrip patch again shows the accuracy of the EM simulation capability using FEKO. It can be seen that not only are the three major resonances predicted but the fourth “dip” at 2.725 GHz is predicted and verified in the measurement results. In addition, the measurement results indicate a higher VSWR for the second mode at 1.84 GHz but the calculated performance shows essentially the same VSWR for all three modes.

Table VIII – Summary of measured and calculated resonant frequencies for the rectangular microstrip “paint-on” antenna elements.

1.0 Antenna L-Band	Dielectric Constant/Loss Tangent	Measured TM_{01}	Calculated, TM_{01} % Error	Measured TM_{001}	Calculated, TM_{001} % Error	Measured TM_{020}	Calculated, TM_{010} % Error
	1.90/0.033	1.348	1.360 0.9%	1.894	1.840 2.85%	2.328	2.325 0.12%
C-Band X-Band	2.52/0.073	3.932	3.930 0.05%	5.480	5.440 0.72 %	6.928	6.930 0.028%
	3.20/0.033	5.460	5.468 0.146%	7.860	7.250 7.7%	9.390	10.375 10.4%

All of this data and comparisons with theory validated the performance of antennas designed using polymer-based materials.

7. Evaluation of Robotic Manufacturing Methods for Conformal “Paint-On” Antenna Design Applications

As stated in the goals and objectives for the Phase II/Enhanced SBIR research project, one of the major objectives is to investigate the potential for using robotic manufacturing methods for conformal ‘paint-on’ antenna materials technology. So, in that regard, a subcontract was awarded to Pratt and Whitney Automation, Inc. to evaluate their capability for robotic manufacturing methods.

Before actual test antennas could be fabricated, Unitech and Pratt and Whitney personnel had to work with the polymer coating materials and establish the proper robotic spraying procedures so that the repeatability and accuracy of the process could be determined. So, trial runs were conducted adjusting spray settings and mixtures for both the LB-070 dielectric coating materials and the LB-088 conductive coating materials. Not only was the LB-088 evaluated but the dielectric coating (LB-070) was also tested and found to be acceptable using P & W robotic spraying methods. The setup at P & W for the LB-088 test cases and typical results spraying onto glass specimens are shown in Figure 21.

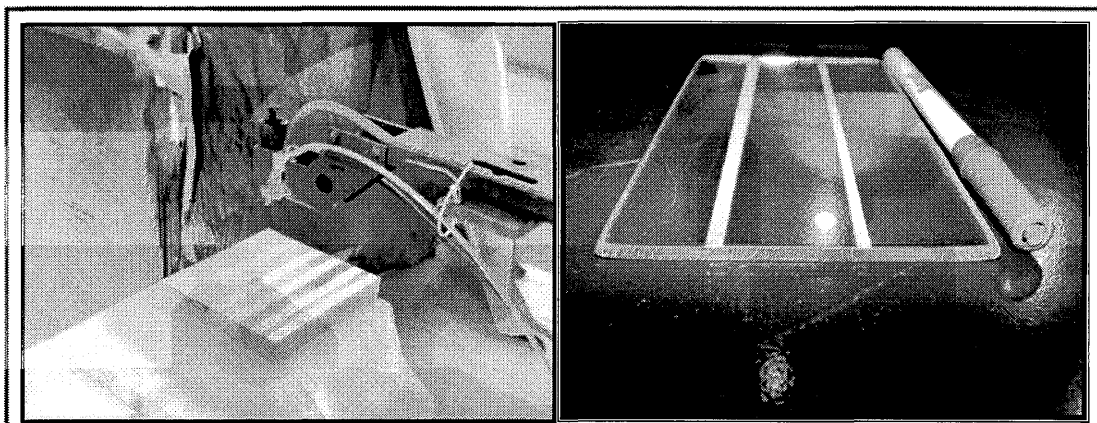


Figure 21 – Photographs of robotic spray setup at Pratt & Whitney along with sprayed lines using LB-088 conductive coating materials.

The antenna test circuits (on the commercial substrates) have been tested and the results are extremely encouraging regarding the capability to robotically apply conformal antenna designs using polymer-based materials. Additional tests are currently underway as well as a computer simulation modeling of the robotic manufacturing methods as applied to conformal antenna materials.

8. Summary

Significant progress has been made developing conformal antenna materials technology which includes using “painted-on” robotic manufacturing methods. This research addressed the need for new and novel antenna manufacturing techniques and has demonstrated several examples as to how this technology can be applied. One of these experimental antenna designs that has been described in a complimentary paper during this symposium is the 64-

element phased array that was ‘painted onto’ a scaled model of a composite wing. Steps are currently underway to commercialize this technology for future aerospace applications.

9. Acknowledgements

The outstanding support by Madiha Jafri at Applied EM for her expert analysis and measurements of the EM properties of the various dielectric materials is greatly appreciated. Also, the technical support and measurements by Mr. Kenneth Dudley of NASA Langley Research Center and Mr. Hunter Walden, Lockheed Martin Corporation, for antenna pattern measurements of the various test antennas.

10. References

- [1] Michelle Champion, SBIR-AF03-206, Contract No. FA8718-04-C-0046 for Air Force Research Laboratory, Hanscom Air Force Base, SBIR Phase II.
- [2] M. C. Bailey, C. B. Ravipati, T. G. Campbell, and C. J. Reddy, “Design, Analysis and Experimental Test Results of a Conformal Phased Array Antenna Painted on a Composite Wing,” 30th Antenna Applications Symposium, Robert Allerton Park, Illinois, Sept. 20-22, 2006.
- [3] Unishield®, Patented Conductive Coating, Unitech, LLC
- [4] FEKO, Comprehensive Electromagnetic Solutions, www.feko.info
- [5] M. C. Bailey and F. G. Parks, “Design of Microstrip Disk Antenna Array,” NASA Technical Memorandum 78631, February 1978.
- [6] M. C. Bailey and M. D. Desphande, “Analysis of Rectangular Microstrip Antennas,” NASA Technical Paper 2276, March 1987.
- [7] W. McNaul, “Conformal Antenna Materials – Paint Parameter Tolerance Study,” Study conducted in fulfillment of subcontract with Applied EM, December, 2005.
- [8] Constantine A. Balanis, “Antenna Theory, Analysis, and Design,” John Wiley and Sons, 1997.

Design, Analysis, and Experimental Test Results of a Conformal Phased Array Antenna Painted on a Composite Wing

M. C. Bailey, C. Babu Ravipati, Thomas G. Campbell and C. J. Reddy
Applied EM, Inc., 144 Research Drive, Hampton, VA 23666

ABSTRACT

A major element of the Conformal Antenna Materials Technology research program by Applied EM, Inc. is the design and development of an experimental phased array on a simulated Sensorcraft wing profile section. The antenna design utilized polymer dielectric materials and conductive coatings that were developed during the SBIR AF03-206 research program and electromagnetic test results indicate the overall readiness level of this technology. This paper describes the stages of the array design with performance predictions using CAD/Solid Works and FEKO electromagnetic modeling and simulation methods. The antenna design consists of a 64-element C-Band array that is phased for end-fire radiation pattern. The array is “sprayed-on” the wing using the polymer dielectric and conductive coatings. Technical details regarding these material and array design are discussed. The next stage for this research program is to develop robotic manufacturing methods and demonstrate applications for conformal antenna designs.

1. Introduction

There is a need for new innovative concepts for designing conformal antennas for a full spectrum of military, aerospace, and civilian applications. Conventional conformal antennas are designed to be ‘flush-mounted’ to the shape of the aircraft, spacecraft or ground vehicles in order to reduce aerodynamic drag and heating effects, to satisfy radiation pattern requirements, to achieve stealth capabilities, to achieve improved mobility, or to satisfy security communication requirements. Designing antennas to ‘conform’ to (more than just being flush-mounted) complex shapes and geometries as well as to a thin film membrane is indeed challenging. This research addresses that need to provide design alternatives for new conformal antennas materials for military and aerospace applications.

On August 31, 2004, Applied EM, Inc. (AEM) was awarded an SBIR [1] research project and is continuing to develop conformal antenna “paint-on” materials technology, and significant accomplishments are being made to raise the readiness level of this technology. Now, the current task is to demonstrate some of these accomplishments through the design and development of an end-fire phased array antenna that is painted onto a composite experimental wing section. This research is also being extended to evaluate robotic manufacturing methods for this technology and there is the potential to

demonstrate the cost effectiveness of this technology. For not only can robotic manufacturing methods be used to paint aircraft sections, and/or apply stealth coatings, it may now be possible to add sophisticated antenna designs and circuits during the fabrication process of the entire structure. Figure 1 depicts the application of this technology to a meaningful antenna design but possible to robotic manufacturing.

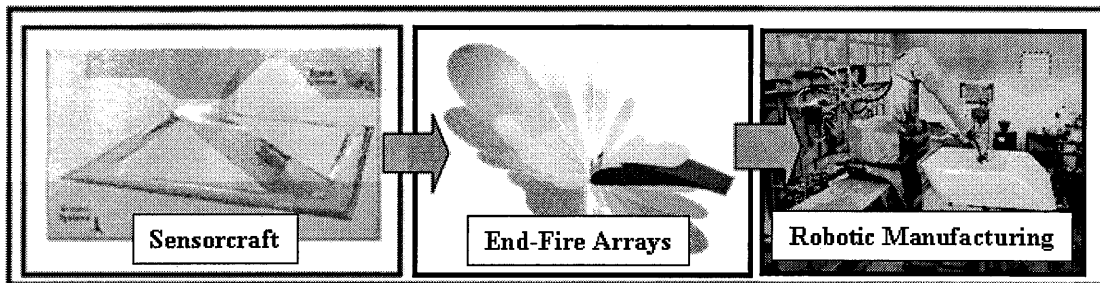


Figure 1 – Potential application of conformal “paint-on” antenna materials technology to end-fire array designs and to robotic manufacturing methods.

AEM’s research team includes Unitech, LLC, Composite Optics-ATK, and Pratt and Whitney Automation Technologies. A critical element of this research is the development and optimization of polymer-based dielectric layers and conductive coatings and Unitech, LLC has supported AEM in the development of these materials.

Since designing antennas using this technology is the primary goal for the Air Force Research Laboratory, the overall capability and effectiveness of conformal antenna “paint-on” technology is being demonstrated through the design and testing of a meaningful phased array antenna which is integrated on a composite experimental wing section. The purpose of this paper is to describe the design and development of this phased array. Information pertaining to the development of the materials is described in [2] and presented in this symposium.

2.0 EM Research Requirements

Requirements for an antenna (focused design) were established with AFRL personnel and the overall design approach was selected that would best demonstrate advancements of the conformal antenna materials technology program. An end-fire type phased array design operating at C-Band frequencies was selected as a “focus mission” that serves to guide the technology development and this array will conform to the top surface of a scaled section of a graphite composite wing.

This experimental antenna design effort identified the technology tasks required to support this design and the resulting EM performance characteristics could support AFRL’s interest in digital beam forming arrays for conceptual Sensorcraft platforms. A rendering of the experimental wing concept is shown in Figure 2 along with the goals and objectives for the Phase II/Enhanced project which includes the additional emphasis to investigate robotic manufacturing methods for conformal paint-on antenna materials technology.

Preliminary EM requirements that were established included azimuth scan limits, elevation scan limits, bandwidth, polarization, gain, and environmental requirements. More details on the EM design requirements are presented later in this report. EM analysis and simulation methods were developed to predict the performance of the wing phased array prior to actual experimental tests of the array. This was considered to be critical to the overall capability to fully understand tolerance effects associated with “paint-on” antenna materials that especially affect antenna performance.

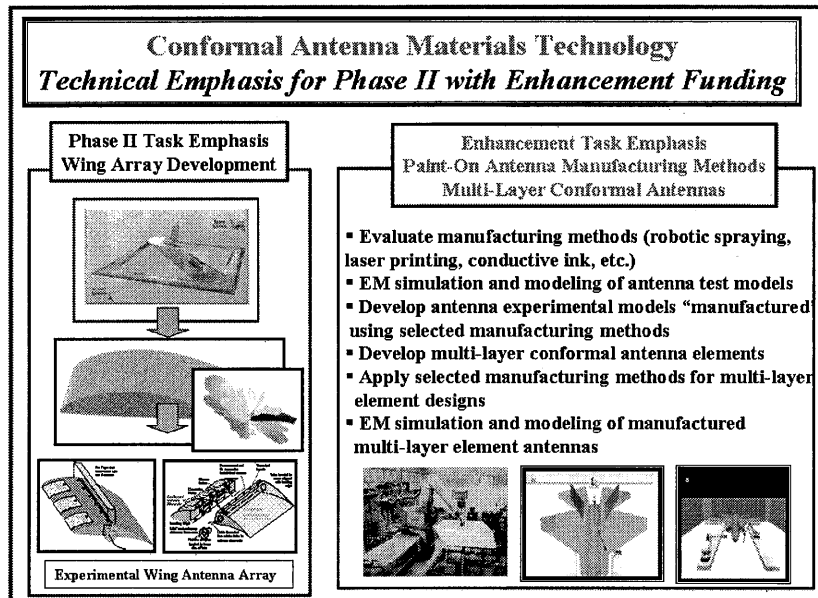


Figure 2 – Technical emphasis for the SBIR Phase II/Enhancement Award showing the wing array development and the emphasis on robotic manufacturing methods.

3.0 Notional Design Approach for the End-Fire Phased Array Antenna

Early in the research program AFRL personnel provided the wing profile for the array design consideration; so, a notional design was formulated as shown in figure 3. This study was initiated using computational simulations analysis for the curved array and to assess the potential for forming a beam off the leading edge of the wing profile. The two dimensional wing array simulations were conducted for 8-element and 16-element array configurations and for positions of 0-degree, + 20-degree, and - 20-degree scans. Initially, radiation patterns were calculated for a single row of elements to determine the amount of beam tilt that may be required to position the beam off the leading edge of the wing. The simulations also identified the element excitations for elevation and azimuth scanning simulations (using 2-dimensional wing configurations).

The element design considered for these simulations was a rectangular microstrip patch at each of the locations on the top surface of the wing. All array radiation pattern calculations were performed at 5.5GHz.

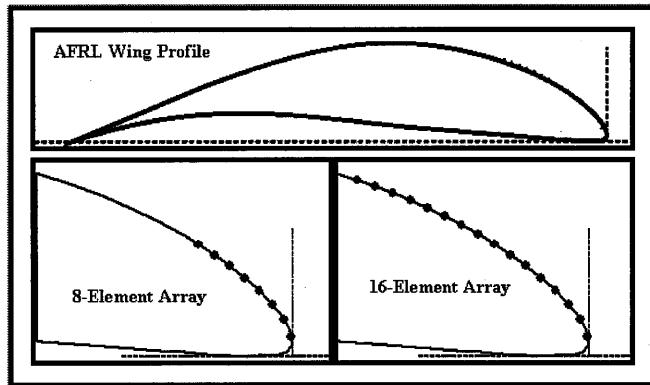


Figure 3-Cross-sectional geometry of wing and array elements near the leading edge.

A center-to-center element spacing along the curved surface of 1.0 inch was determined to be reasonable for minimizing grating lobe effects and allowing sufficient space for resonant rectangular patches on the surface. The array excitation was selected as uniform amplitude with a phase distribution to compensate for the array curvature while also scanning the beam in the desired elevation direction. The calculated radiation pattern in the elevation plane for the beam pointing off the leading edge is shown in figure 4. Figures 5 shows the calculated radiation patterns for the beam scanned + 20 degrees in elevation.

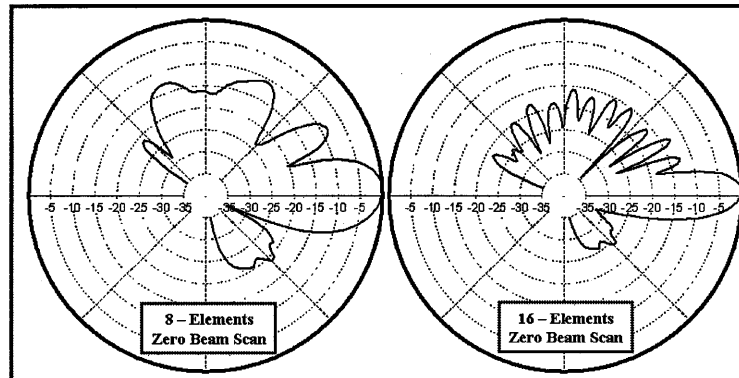


Figure 4 -Elevation pattern for curved array with excitation for pattern off leading edge.

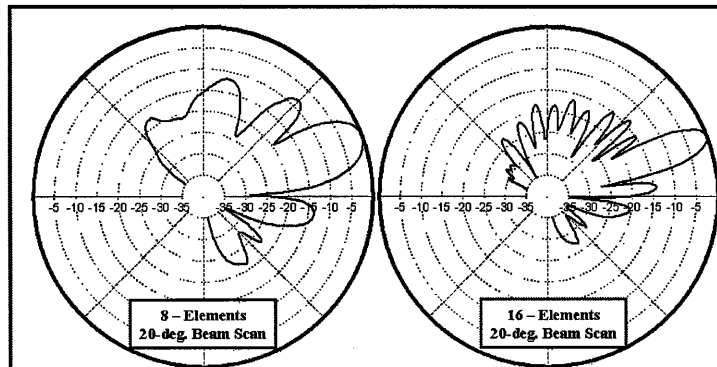


Figure 5 - Elevation pattern for curved array with beam scanned 20 degrees up.

These initial array analyses indicated that a reasonable beam can be formed off the leading edge and that some limited elevation phase scanning can be achieved by an array located on the top curved surface of the wing. Better beam formation and elevation scanning may be possible by wrapping the array around the leading edge and onto the bottom surface; however, this approach was has not modeled. The potential exists for elevation pattern sidelobe reduction with optimized amplitude excitation distributions using this array concept.

4.0 Wing Phased Array – Development of Polymer-Based Materials for the Array Design

Development of Dielectric Coatings

Based on the SBIR Phase I technology results, the polymer-based dielectric and conductive coatings were selected for the array design. The dielectric constant and loss tangent values are in the range of 2.97 – 3.6 and 0.037 – 0.055, respectively. Several variations of these materials were developed to further improve the overall EM properties of the selected materials. In the meantime, EM sensitivity analyses are conducted to determine variations in EM performance for the range of characteristics for the polymer-based dielectric coatings for the array design. The ‘optimum’ formulations were selected for further substrate fabrication and EM tests. Based on the EM measurements of the polymer-based dielectric coatings, these parameters were used in the design and computational simulations for all components of the integrated wing array – element, feed and beam-forming network, and the complete array.

Material coatings were applied to test substrates with film thicknesses from 60-mil to 80-mil and then tested at AEM and NASA. Substrates were machined to coaxial (and subsequent waveguide) dimensions for analysis and testing. Based on all of the subsequent substrate test results, dielectric materials were down-selected for antenna design tasks.

The following tasks were accomplished:

- Unitech fabricated specimen (“doughnuts”) for a 7-mm precision airline which included approximately 22 categories of polymer-based dielectrics with and without various filler materials for EM measurements and characterizations.
- Applied EM (AEM) conducted EM measurements/characterizations (up to 6 GHz) on approximately 30 dielectric material specimens of the 22 categories of polymer-based dielectric materials developed by Unitech.
- AEM developed laboratory measurement procedures for EM measurements (screening materials based on EM properties) and resolved calibration issues (specimens (“doughnuts”) for 7-mm precision airline) required for accurate material measurements.

Based on the results of all of the EM material property measurements, the down selection process resulted with LB-070 as the dielectric coating material for the wing phased array. The resulting dielectric constant and loss tangent characteristics for the “down-selected”

coatings are presented in Figure 6 and the resulting dielectric constant and loss tangent for LB-070 values are approximately 3.05 and 0.0325. All of the primary candidate materials are polymer-based Silane/Polyglycidyl Ether systems with ceramic and boron nitride fillers.

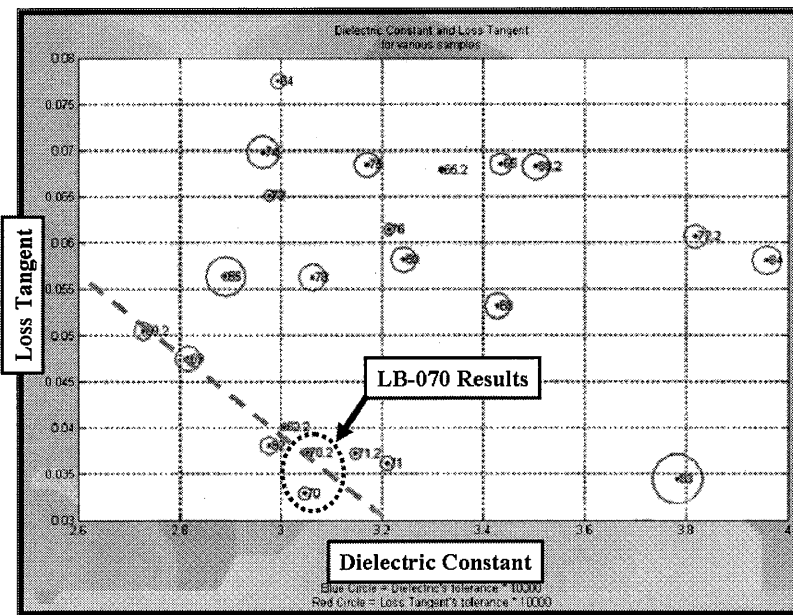


Figure 6 – EM measurement results for the polymer dielectric materials and selection of LB-070 as the baseline material.

The test results for the LB-070 indicated less variation in loss tangent and dielectric constant but variations did occur in some of the measurements that were attributed to measurement error especially in handling small specimens with varying thicknesses.

Development of Improved Conductive Coatings

In addition to the development and testing of dielectric coatings, highly conductive coatings were also developed to provide the necessary material coatings for antenna designs. Unitech, LLC conducted tests on selected materials that included; evaluation of Inter-coat compatibility and adhesion per ASTM D 3359, Standard Test Method for Measuring Adhesion by Tape Test, and/or ASTM D 4541, Standard Test Method for Pull-Off Strength of Coatings Using Portable Adhesion Tester. Impact resistance, per ASTM D 2794, Standard Test Method For Resistance of Organic Coatings to the Effects of Rapid Deformation (Impact). The results of these tests are being prepared by Unitech.

The RF characteristics of the baseline Unishield conductive coatings were found to be inferior for antenna feed circuits based on insertion loss measurements. As a result, a new and improved conductive coating (LB-088) was developed and RF tests indicated low insertion loss characteristics as compared to the original Unishield formulations. Two

tests were conducted to evaluate the quality of spray applications and dry film thickness and resistance characteristics.

The results of test (#1) indicated a dry film thickness of 1.4-1.6 mils and conductivity (resistance) of 0.018 ohms per square. Results of the second test trial produced a dry film thickness of 1.1 to 1.2 mils and better (resistance) conductivity of 0.009 ohms per square were achieved. Therefore LB-088 was selected for all subsequent antennas designs and steps were implemented to test these coatings for Pratt & Whitney's robotic spraying applications. These investigations will be discussed later in this report.

Unishield Conductive Coatings on Graphite Composite Panels

Antenna design problems were encountered during Phase I when Unishield conductive coatings (not LB-088) were applied to graphite composite materials especially the radiation gain levels. In Phase II, this problem was encountered again and the problem was further analyzed by inspecting the condition of the graphite composite materials before coating and measuring the surface resistance of the composite materials. Initially, it appeared that the continuity of an antenna ground plane (using conductive coatings on the graphite composite structure) was degraded due to material interactions. Since the wing model for the array is graphite composite materials, this problem had to be solved. The surface resistance of the (uncoated) wing surface was found to vary greatly depending on where the meter probes were placed and what pressure was applied. Also, variations in resistance were observed whether the composite surface was smooth or rough – which means either resin “rich” or resin “starved.”

This problem became more evident when several types of Unishield conductive coatings with and without sealant coatings were applied to graphite composite materials. Material samples were provided to NASA for measurements and those test results produced even more varying shielding effectiveness levels; so, no conclusions could be made as to the proper coating procedures.

This problem was researched further and experiences involved in the design of low observable materials indicated that the graphite composite surfaces should be lightly “sanded” before applying the conductive ground plane coating. Sanding the composite surface removes the top resin coating and exposes graphite fibers and thereby provides better conductivity with the ground plane coating. Subsequently, tests were conducted on small GFE coated samples and found improved overall conductivities. This procedure has been adopted and implemented to prepare the wing for painting the array. Therefore, a sealer coat will not be applied to the wing surface prior to applying the LB-088 conductive ground plane.

Thermal cycling during applications of the dielectric and conductive coatings is required and one cycle consists of the following; subjecting the material layer to a temperature of -65° F for a period of 1 hour, then moving the specimen directly to a 180° F oven for a period of one hour, then allowing the specimen to remain at ambient temperature for a period of one hour. Trial runs using the materials selected consisted of coating on

composite and aluminum panels to achieve the desired film thickness. Then, the panels were tested through a minimum of 20 cycles and evaluated for cracking, loss of adhesion, and other possible defects.

5.0 Wing Phased Array – Probe-Fed Element Design

Several element designs were considered for the end-fire array and finally, a probe-fed square microstrip element was selected for the end-fire, integrated wing design. The probe-fed configuration was selected because of the need to know the effect of paint tolerances on EM performance on each element and, subsequently, on the total array. Having probe-fed elements will allow measurements on each element of the array and, then, differences in performance could be attributed to variations in the EM properties of the paint coatings at various locations in the array. So, probe-fed elements will enable diagnostics in the event ‘trouble-shooting’ will be required after the array EM performance has been determined.

During this stage of the design, the dielectric layer was limited to a single layer dielectric configuration (at this stage of the conformal antenna materials program). Therefore, the bandwidth anticipated for the element design would be approximately 5%. The radiation patterns were calculated for representative element locations to determine if the element design needed to be refined depending upon location on the curved wing cross section. Array element excitations were calculated to form a beam broadside to the wing leading edge. The microstrip element dimensional parameters were determined for resonance at the desired test frequency (5.50 GHz).

As the various polymer-based dielectric material formulations were developed, the resulting EM performance of the square element was calculated in regard to resonant frequency characteristics and bandwidth. It is important to understand the variations in the EM characteristics (dielectric constant and loss tangent versus frequency) so that accurate antenna element designs could be formulated. The variations in dielectric constant and loss tangent are primarily due to variations in the fabrication process and lesser extent to systematic measurement errors. These variations were studied and, subsequently, the element design was finalized. In the meantime, it was important that ‘trial’ designs be conducted using the latest EM data on the materials to track the process especially in regard to resonant frequency, bandwidth, and gain. The element design configuration of the element design is presented in Figure 7

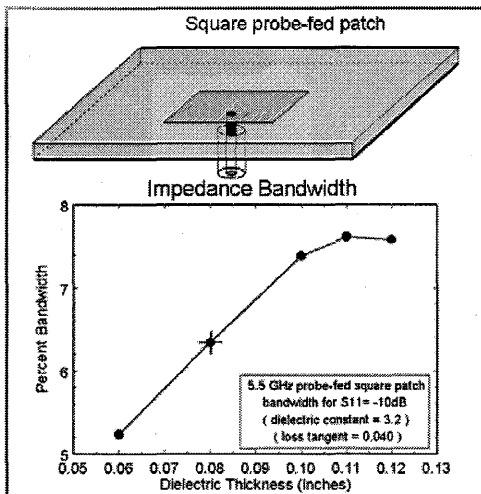


Figure 7 – Element design configuration along with predicted bandwidth characteristics using EM characteristics for dielectric materials.

Effects of Curvature on Conformal Antennas

In addition to the substrate characteristics that will affect the bandwidth and resonant frequency of the conformal antenna, the shape of the substructure will also affect the resonant frequency (and bandwidth) of the antenna. The effects of curvature on the fabrication of conformal antennas are discussed are discussed, for example in [3], [4]. This effect was analyzed and correlated with previous results of experimental tests. It is important to note that many of the design parameters of conformal antennas are being considered in this research phase and these results will be applied during Phase II tasks to demonstrate the design of phased array antennas integrated on aircraft wing geometries.

Microstrip (square patch) antennas on finite curved ground planes were analyzed using the Method of Moments based software FEKO. The dielectric constant of the substrate was assumed to be 2.7 and substrate thickness 0.090-inches. The geometry of the structure and mesh of the dielectric and metal regions, used in FEKO simulations, with varying radii of curvature (3.75, 0.75, 0.52, and 0.37-inches respectively) are shown in the Figure 8.

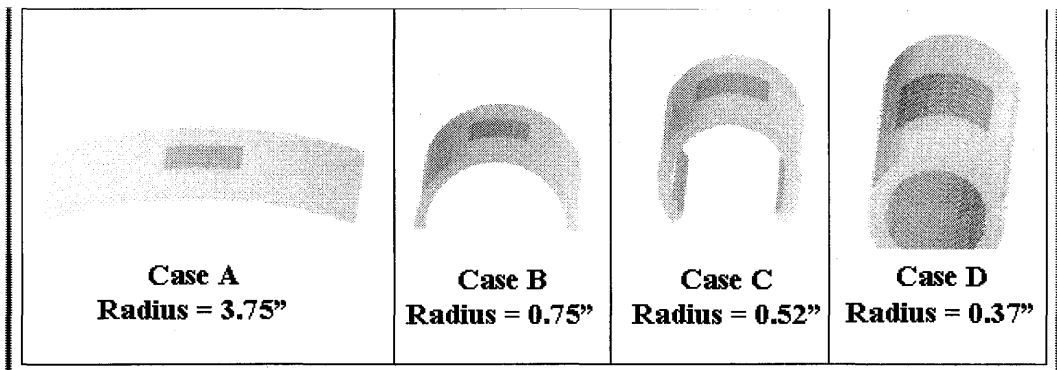


Figure 8 – FEKO simulations of microstrip patch antenna on curved substrate and ground plane configurations for several radii of curvature.

The computed return loss for these cases is shown in the Figure 9 below. As seen from these results, the resonance frequency of the microstrip antenna shifts towards higher values (approximately 1%) with decreasing radius of curvature and the return loss is reduced from -36 dB to -17.5 dB.

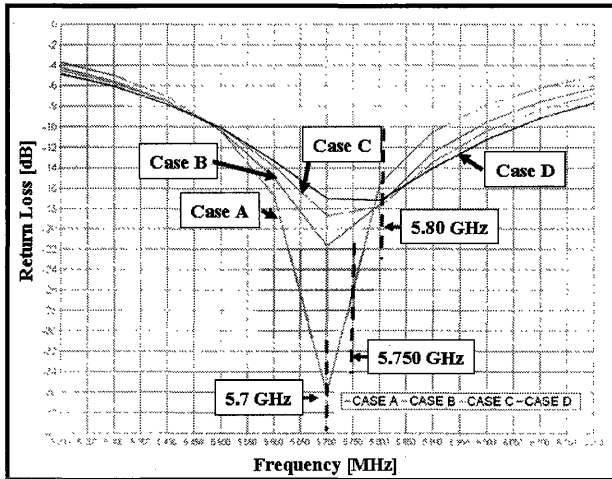


Figure 9 - Computed return loss of microstrip antenna on curved surface.

Additional experiments were conducted to determine the effects of dielectric and uniformity on microstrip antennas using a Teflon-Ceramic (Epsilam-10) dielectric substrate material. This dielectric substrate was selected for this investigation since it can be bent to conform to a substructure. In this investigation, several L-Band rectangular microstrip patch antennas were fabricated and they were bent around metal cylinders of different radii to determine the changes in frequency, VSWR, and bandwidth due to bending. The results of these experiments are as follows:

- Resonant frequency always increases (approx. 1% or less) with decreasing radius of curvature of the substrate and ground plane.
- The useable bandwidth tends to increase with decreasing radius of curvature.
- The VSWR increases significantly with decreasing radius of curvature.

- The copper cladding of the substrate begins to wrinkle as the radius of curvature approaches 0.50-wavelengths in the dielectric.

Element design analysis was extended to investigate performance on the wing structure as shown in Figure 10.

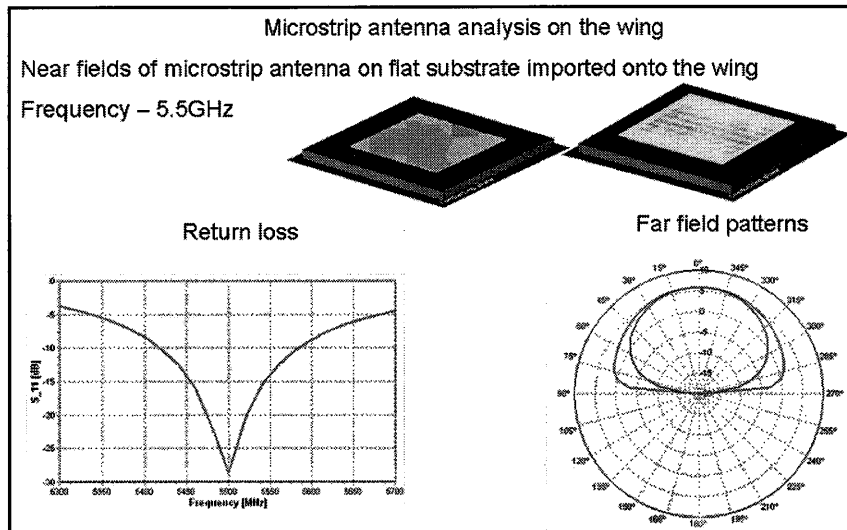


Figure 10 – Microstrip antenna analysis by analyzing the near fields of the individual elements on a flat substrate and imported onto the wing geometry.

The microstrip analysis of the element on the wing was continued for the near fields of the element on a flat substrate imported onto the wing required 21120 triangles and 31472 unknowns at the design frequency of 5.5 GHz. A chart outlining these steps of the analysis is presented in Figure 11.

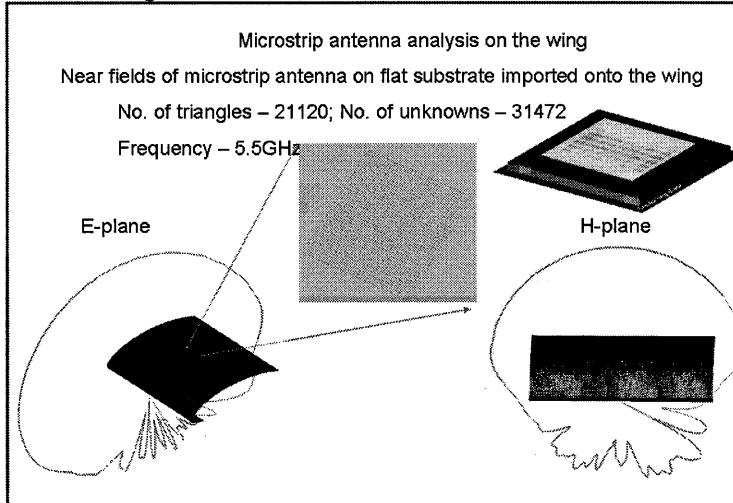


Figure 11 – Chart outlining the number of triangles and unknowns for analyzing the near fields on individual antenna elements of the array.

The near fields of the microstrip antenna element designs were imported onto the wing configuration. As indicated above, 21,120 triangles with 31,472 unknowns were

formulated in the FEKO EM simulations. After the individual elements were analyzed and imported onto the wing geometry, a 16-element linear array (one row of elements of the 64-element array) was analyzed to determine the elevation plane pattern. The first radiation pattern was calculated for a partial wing configuration and a comparison with the full wing configuration is shown in Figure 12.

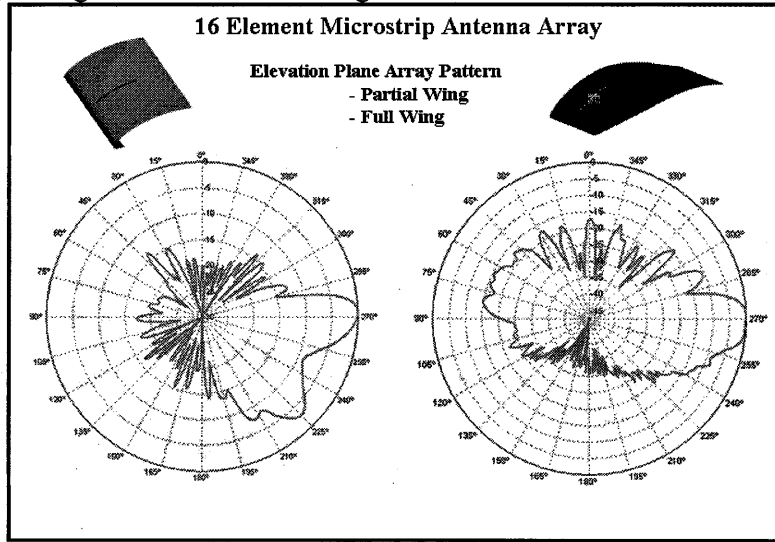


Figure 12 – Comparison of radiation pattern calculations of a 16-element array on partial and full wing configurations – elevation plane radiation patterns.

In addition to the element configuration, mutual coupling effects were analyzed to determine if the element impedance was adversely affected by the adjacent element. These results are presented in Figure 13 and it can be noted that the mutual coupling is approximately 22.5 dB for the element spacing designed for the array.

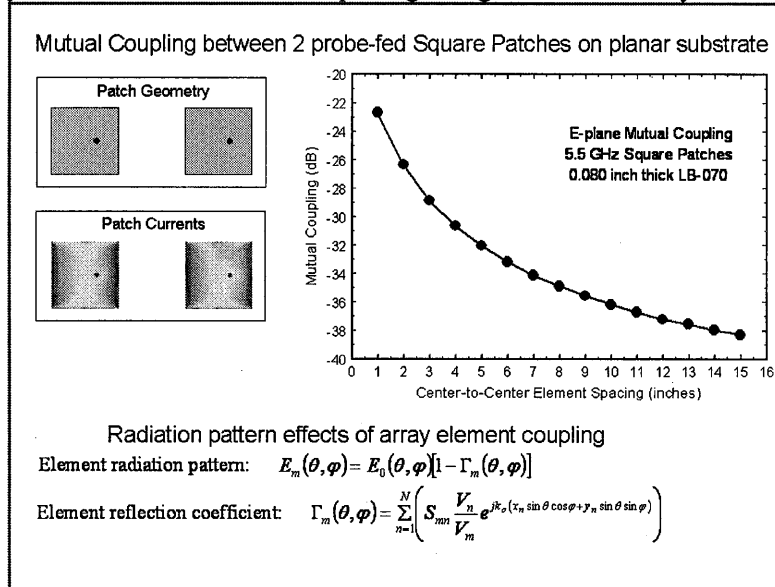


Figure 13 – Mutual coupling between two probe-fed square patch elements on a planar substrate.

As this analysis was conducted for two probe-fed patch elements on a planar substrate, it is anticipated that the element mutual coupling will decrease further when the elements are placed on curved ground planes.

As stated previously, the use of probe-fed elements enables the opportunity for further comparisons between calculated and measured element patterns in the array for possible diagnostic purposes. The radiation patterns will be calculated for each array element location on the wing cross-section as well as the impedance for each array element location on wing cross-section.

6.0 Wing Phased Array – Computational Simulations

EM computational simulations were developed for the 3-dimensional wing array for the 64-element array configuration and these simulations were used to predict the performance of the array and also provide a means to correlate the EM results with the tolerance effects studies for the “paint-on” conformal material coatings. The location of the array on the wing is shown in Figure 14. The computational simulations will also identify the need for adjustments to individual element design details to improve the radiation pattern characteristics as required.

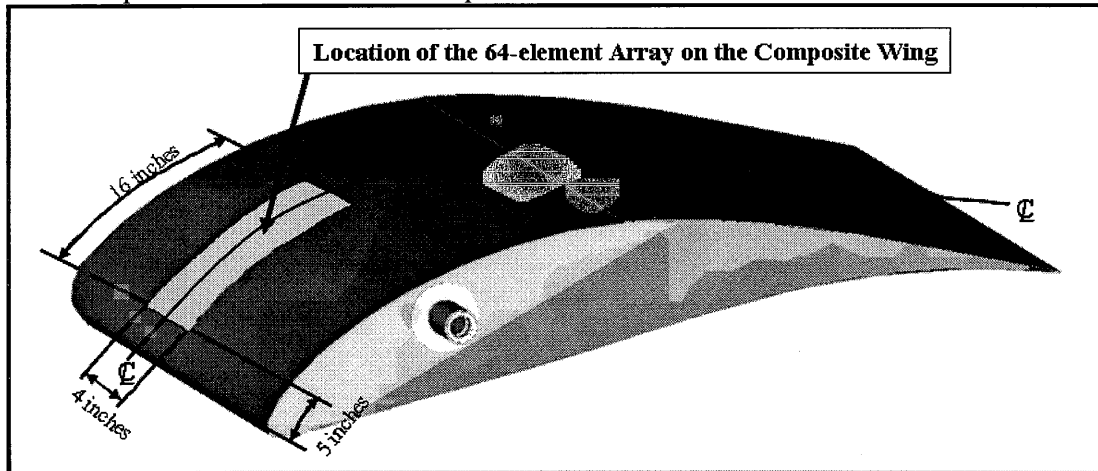


Figure 14 – Location of the 64-element phased array on the composite experimental wing profile.

The 64-element array is positioned approximately 5-inches from the leading edge of the wing and this location was a compromise between the effect on the radiation pattern and the physical limitations anticipated for installing the array and associated power dividers and cables for the array. This compromise was necessary in view of the fact that probe-fed elements compose the array and cable connections are required to each element. A center-to-center element spacing along the curved surface of 1.0 inch was determined to be reasonable for minimizing grating lobe effects. The array excitation was selected as uniform amplitude with a phase distribution to compensate for the array curvature while also scanning the beam in the desired elevation direction. The 64-element array configuration is shown in Figure 14 and FEKO EM analysis methods were selected for

array performance predictions. The analysis features associated with the FEKO software include the following:

- Solution Techniques – MoM, Physical Optics, UTD, Planar Green's functions, Hybrid MoM/PO and MoM/UTD
- Fast Solutions – Multi-Level Fast Multipole Method
- Model Import Formats – Nastran, Patran, AutoCAD, FEMAP

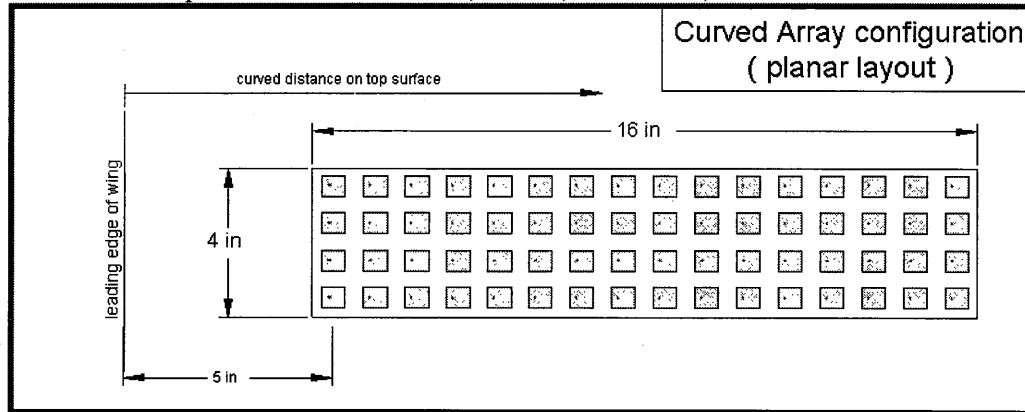


Figure 15 – Diagram of the 64-element array for the experimental composite wing.

Previous array patterns were calculated using Physical Optics analysis and comparisons with the FEKO results are presented in Figure 16.

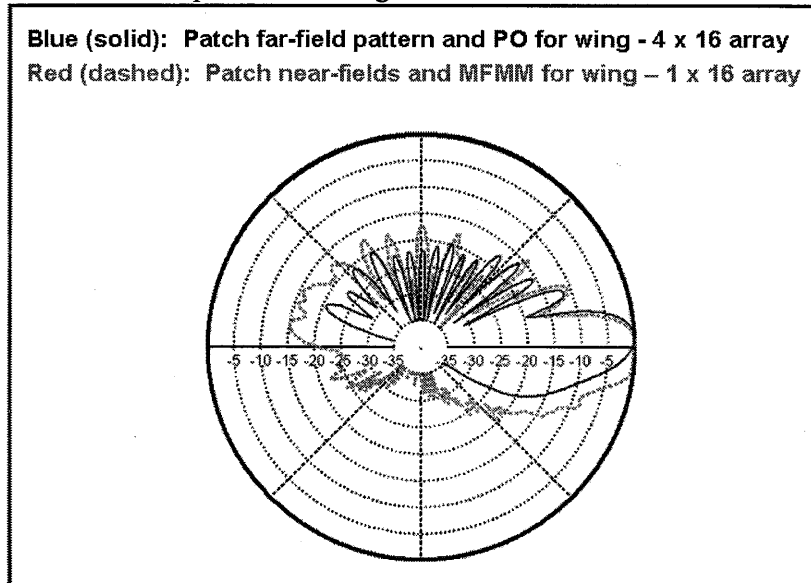


Figure 16 – Comparison of FEKO 1x16 array pattern with the 4x16 PO calculations.

These initial array analyses indicate that a reasonable beam can be formed off the leading edge and that some limited elevation phase scanning can be achieved by an array located on the top curved surface of the wing. Better beam formation and elevation scanning may be possible by wrapping the array around the leading edge and onto the bottom surface; but, this was not considered necessary for this experiment demonstration.

Preliminary results using FEKO (shown in Figure 17) indicates the overall capability of that EM software to provide accurate performance predictions for the 64-element array as the development continues. Eventually, a total 3-D radiation pattern simulation will include all of the constitutive materials of the array.

CAD-FEKO (Parametric Analysis Model Development):

The purpose of this task was to develop an integrated mechanical CAD and EM software model of the experimental wing with the “paint-on” phased array so that parametric studies can be performed as well as performance predictions of the array prior to radiation pattern measurements at NASA Langley. The capability to simulate the wing array geometries (of all painted layers) is critical to the understanding of the as-measured characteristics of the conformal painted array. Therefore, it was important to work out all of the issues associated with the merging of the CAD mechanical models with the FEKO EM software. The first step was to develop a CAD mechanical model of the as-built experimental wing model. Using a mechanical scanning device, data was collected and a CAD geometry model of the experimental wing was developed. Photographs of the scanning equipment used to measure the experimental wing are shown in Figure 18.

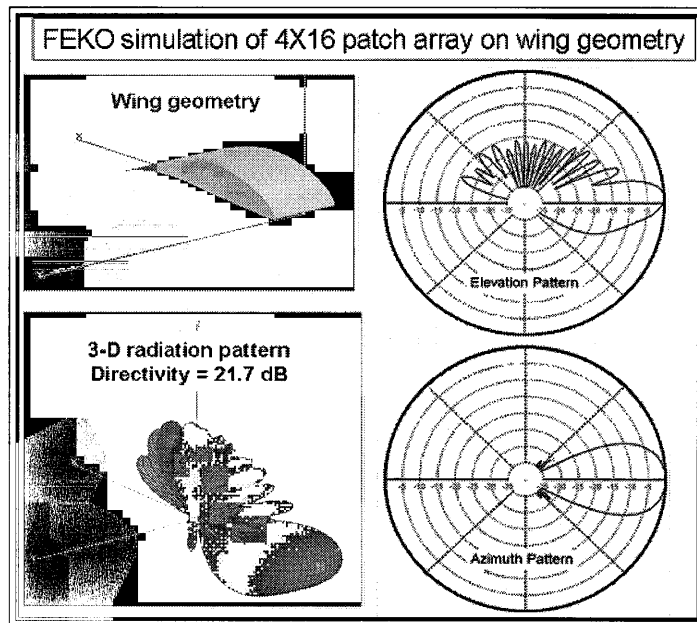


Figure 17 – FEKO simulations of 4x16 patch array on the composite wing geometry.

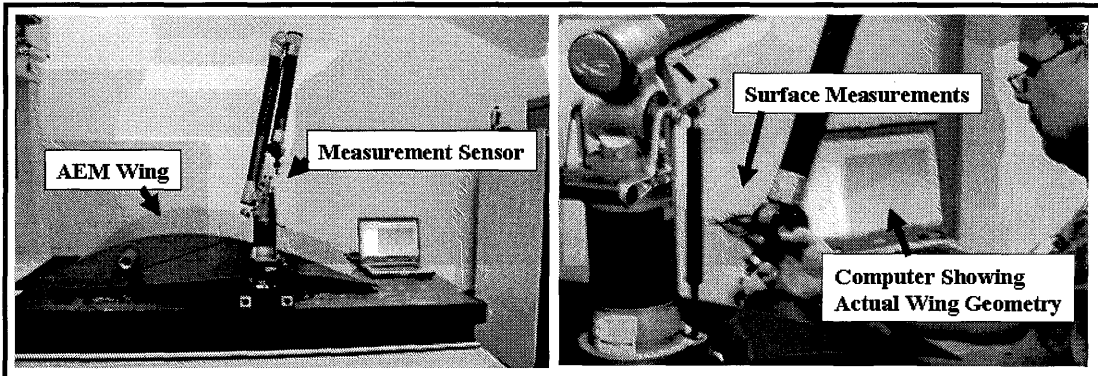


Figure 18 – Photographs of measurement setup to mechanically scan the surface of AEM's experimental wing.

Preliminary surface measurements indicated surface accuracy deformations as much as 0.030-inches existed on the wing surface, and in the area where the array will be located, surface undulations on the order of 0.010-inches were measured. Based on these results, it appears these deformations could be due to the tooling used to fabricate the wing. In regard to the surface errors (0.010-in.) in the area of the array, the effect of these errors on electrical performance can be determined since these errors can be located and characterized (in respect to specific antenna locations).

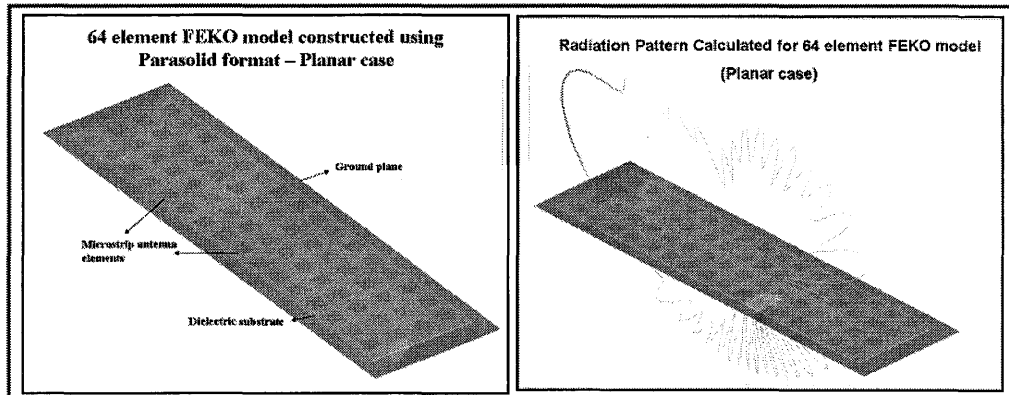
The CAD geometry information was integrated with the CAD-FEKO model of the wing phased array and dimensions provided for substrate dielectric layer thickness, conductive coating, microstrip element dimensions, and RF connector and offset dimensions. Essentially, two CAD models were developed for the phased array on the wing. One mechanical model has the necessary detail that shows the entire array component layers, and RF connector locations. The second CAD model provides mechanical detail information that is needed to “union” the array geometry with the CAD-FEKO EM software. The CAD-FEKO model is used by AEM personnel to conduct various EM simulations of the wing array and to provide EM performance predictions prior to radiation pattern tests at NASA Langley.

Experimental tests will measure element impedances and coupling levels for the sub-array. Mutual coupling effects will be considered which normally cause (1) a distortion of the radiation pattern, (2) an element-driving impedance that varies as the array is phased to point the beam in different directions, and (3) a polarization variation with scan angle in an array with elements that can support more than one sense of polarization. The degree to which the mutual coupling affects the performance of the array will depend upon the element type, the polarization and excitation of each element, the geometry of the array, and the surrounding environment. To accurately model the effects of mutual coupling in the design of array antenna, the analysis must include all these factors.

The microstrip elements of the array are designed for a center frequency of 5.5 GHz. The development plan for testing and evaluating the antenna element designs for the wing phased array has been discussed in previous reports and will not be repeated herein.

Development of the mechanical CAD models enabled AEM to develop a FEKO model of the wing array which is constructed using Parasolid format. The element dimensions (0.564-inch square) and probe-fed pin location (0.110-inch) from center of the patch were provided to EATI for modeling.

Preliminary EM simulations have been conducted using a flat plate 64-element configuration and the CAD-FEKO model (for this configuration) used for simulations is presented in Figure 19 (a). A center-to-center element spacing along the curved surface of 1.0 inch was acceptable to minimize grating lobe effects. The array excitation was selected as uniform amplitude with a phase distribution to compensate for the array curvature while also scanning the beam in the desired elevation direction. The results (shown in Figure 19(b)) show computational simulations for the elevation plane. These results signify that progress has been made to develop the capability for EM simulations that will be important to fully understand the parametric effects for “painted” antenna designs. The FEKO simulation software will be used on the actual wing geometry to provide accurate performance predictions for the 64-element array.



(a) 64-element FEKO model. (b) Radiation pattern for 64-element FEKO model.
Figure 19 – 64 element FEKO model constructed using Parasolid format – planar case.
Elevation pattern shown for information purposes.

Further modifications were made in the CAD mechanical model of the curved wing configuration to improve ‘merging’ with FEKO and, soon, radiation patterns will be calculated for the actual curved wing array configuration. Since the array is probe-fed, individual element characteristics will be calculated as well as array patterns as a function of frequency. The results of these simulations will be compared with experimental test results obtained by NASA Langley. Hence, the technology of the Conformal “Paint-On” Antenna Materials research will be evaluated based on the overall EM performance of the antenna design applications --- ranging from individual elements to the radiation pattern performance of the 64-element phased array.

7.0 Wing Phased Array – Design of Phase Distribution Circuit for End-Fire Radiation

The beam-forming network provides the phase distribution circuit for progressive phase shifts to achieve end-fire radiation and the circuit schematic is shown in Figure 20.

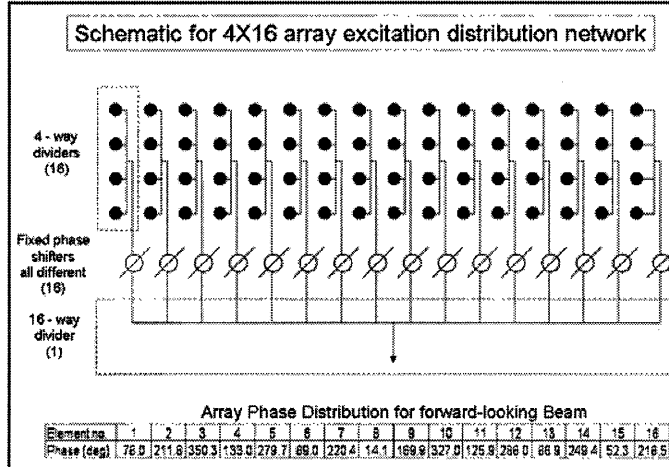


Figure 20 – Phase distribution circuit proposed for the End-Fire Phased Array Antenna.

Phase distributions will be required to scan the beam toward the horizon by compensating for the curvature of the wing and the necessary phase to scan the beam. Based on the results of these simulations, the phase distribution circuit for the array has been developed using relatively low loss coaxial cables, (16) 1 x 4 way power dividers, and (1) 16 x 1 power divider. Adjustable phase shifters are also used in each line to compensate as required for slight variations in the phase delay associated with each cable.

Table I lists the design and measured values for the array excitation distribution network. The excitation phase delay is given in degrees with respect to the trailing element. The first column is the calculated design values for the composite wing array. The second column is the difference or phase delay with respect to the previous element. The third column is the the measured phase. Phase adjustable SMA adapters were employed to improve the resulting measured phase distribution. The final column lists the error between the design and measured phase distributions. The worse case error is about 6.8 electrical degrees for PD_03. The overall phase characteristics for the circuit are acceptable for testing the wing phase array.

Φ_{PHASE_LAG}	$\Delta\Phi_{DESIGN}$	$\Phi_{MEASURED}$	$\Delta\Phi_{MEASURED}$	$\varepsilon = \left \frac{\Delta\Phi_M - \Delta\Phi_D}{\Delta\Phi_D} \right $
PD_16	0.00	0.00	174	-
PD_15	164.22	164.22	10	0.1
PD_14	327.17	162.95	-158	3.1
PD_13	129.67	162.50	37	1.5
PD_12	290.56	160.89	-125	0.7
PD_11	90.65	160.09	79	2.6
PD_10	249.53	158.88	-80	0.1
PD_09	46.60	157.07	122	0.6
PD_08	202.46	155.86	-31	1.8

PD_07	356.13	153.67	175	154	0.2
PD_06	147.53	151.40	21	154	1.7
PD_05	296.84	149.31	-129	150	0.5
PD_04	83.52	146.68	78	153	4.3
PD_03	226.24	142.72	-55	133	6.8
PD_02	4.74	138.50	161	136	1.8
PD_01	138.55	133.81	32	129	3.6

Table I - Array Phase Distribution for forward-looking Beam.

The current tuned phase distribution circuit has an average element error of less than two percent. PD_03 and PD_04 may require further refinement before the standard deviation of the element errors can be reduced ($\sigma_{\epsilon} \approx 1.87$).

8.0 Wing Phased Array – Development of Array Elements (using polymer-based dielectric materials)

Single layer substrate elements (square patch) were developed using the selected (LB-070 and LB-088) polymer-based dielectric materials. A 13-element microstrip patch configuration, shown in Figure 22, was fabricated which represented different locations in the array environment in the wing geometry. The purpose for this test was to verify the precise element dimensions and the location of the feedpoint of the element, the input impedance, and the mutual coupling effects for the 64-element array. This microstrip patch assembly included a 3x3 sub-array of square elements in the center of the plate and this test configuration was extremely useful in determining mutual coupling effects and verifying element RF performance before fabrication had begun on the wing array. The composite ground plane was fabricated and the surface was prepared (as previously discussed) by lightly “sanding” the graphite composite material surfaces before applying the conductive coating.

There has always been a design issue regarding how to provide a good RF ground connection when antennas are “painted onto” non-metallic structures; so, it was necessary to modify SMA connectors by soldering a copper sleeve to the connector flange and then spreading the copper sleeve into a “flower” shaped leaves on top of the painted ground plane (after the connector is inserted through the clearance hole). EM tests were conducted on all of the element positions on the composite (13-element) assembly and evaluations were made as to the individual element performance (resonant frequency, pattern and gain characteristics). These connector installations are shown in Figure 21.

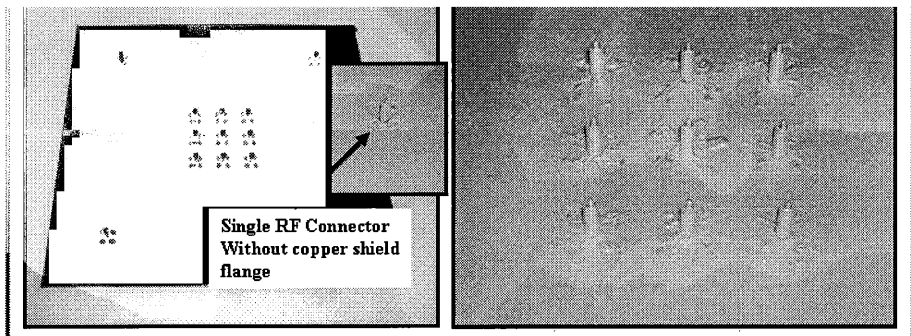


Figure 21 – 13-element board assembly on a graphite composite board showing application of LB-088 conductive ground plane coating.

After the LB-088 conductive ground plane is applied to the graphite composite board, LB-070 dielectric coating is sprayed onto the top surface (as shown in Figure 22) and the board in preparation of the antenna elements are painted next.

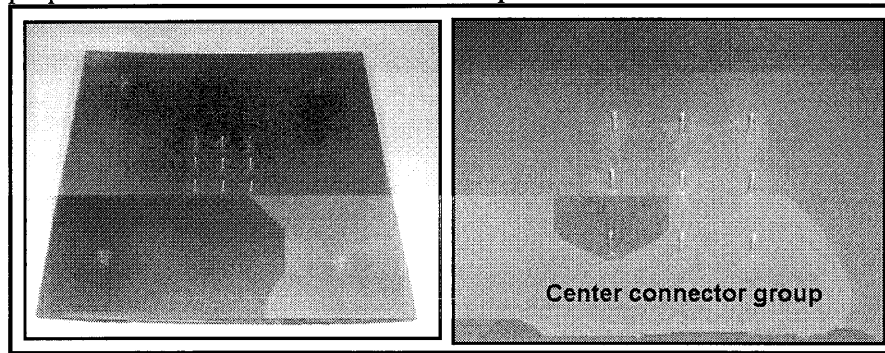


Figure 22 – Photographs of the 13-element graphite composite board after the LB-070 dielectric coating has been applied.

Tests Using Commercial (Dielectric) Substrate

Using a similar 13-element template, a commercial laminate was assembled with similar microstrip patch antenna elements. The dielectric constant of the commercial substrates was 3.0 which is the same as the LB-070 painted dielectric layer. So, the purpose of this test was to experimentally verify analysis predictions of resonant frequency and element mutual coupling effects. It is important that the mutual coupling effects for the 64-element array are experimentally verified. The configuration for the commercial substrate boards and element dimensions were identical to the template (shown in Figure 23). The measurement results indicated the individual resonant frequencies for each element in the center 9-element cluster. RF connectors were soldered to the individual elements and ground plane on the back surface of the substrates. Several iterations (installing the connectors) were required because any inconsistency in the symmetry of the connector center pin to the antenna element affects the residual feed reactance which results in detuned resonant frequency for the element. It can be seen that each element has essentially the same resonant frequency and good repetitive procedures have been developed for element RF connections. These results verified that the element design

will perform satisfactorily in the wing array configuration especially in regard to element spacing, mutual coupling performance predictions. The mutual coupling levels between the center element and the eight adjacent elements were measured and observed to be 20 dB which is as predicted.

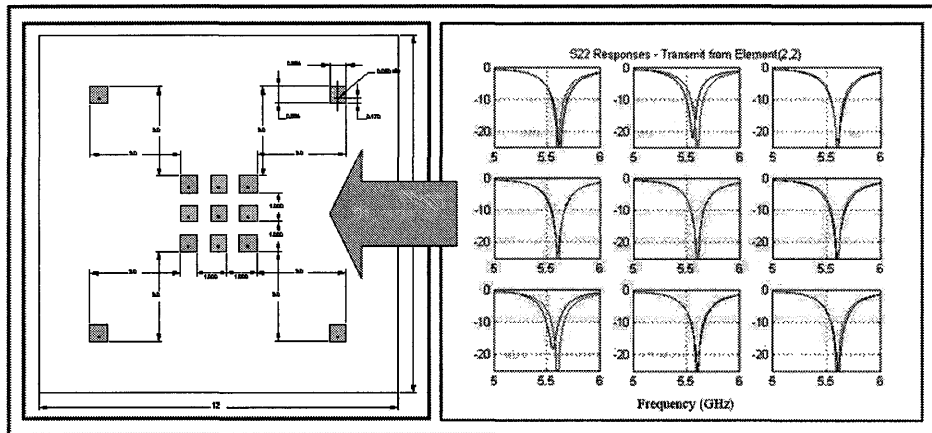


Figure 23 – Experimental results (*Commerical Board*) to verify resonant frequencies for each patch element in the 9-element center cluster configuration.

After the RF tests on the commercial board assembly were completed, the composite board assembly was developed and individual elements (on the 13-element board) were tested. This configuration closely represented the type of elements that are designed for the wing phased array. Figure 24 shows the orientation of the elements on the composite board and the numbering of each element location for testing and performance comparisons. When the composite board assembly was received at AEM, it was observed that cracking of the dielectric layer had occurred due a rapid high temperature curing cycle imposed by Unitech. Some of the antenna elements failed the EM tests because of cracks in the dielectric layer as well as some cracks in the element. Several elements were found to be acceptable and RF connectors were prepared on these elements for testing. These test results proved to be a valuable exercise as the preparations were being made to develop the wing phased array.

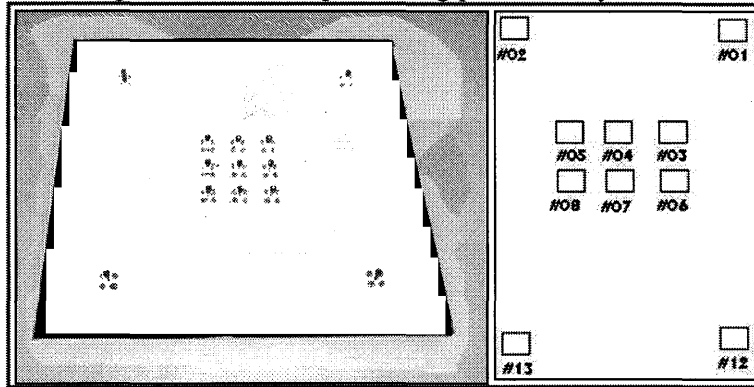


Figure 24 – Composite antenna assembly board showing numbering system for the individual elements.

Return loss measurements were conducted on each element of the 13-assembly and the effects of high temperature curing were very evident. Figure 25 shows return loss measurement results for elements 3, 4, and 5. The cure/heat cycle cracked elements #02 and #13. Element #01 was fabricated with no copper shield and this approach was found to be unacceptable as the ground connection was unreliable. ***Elements #3 and #5 of the second row fabricated (06/15/06) had cracks in the dielectric and antenna element conductive surfaces.***

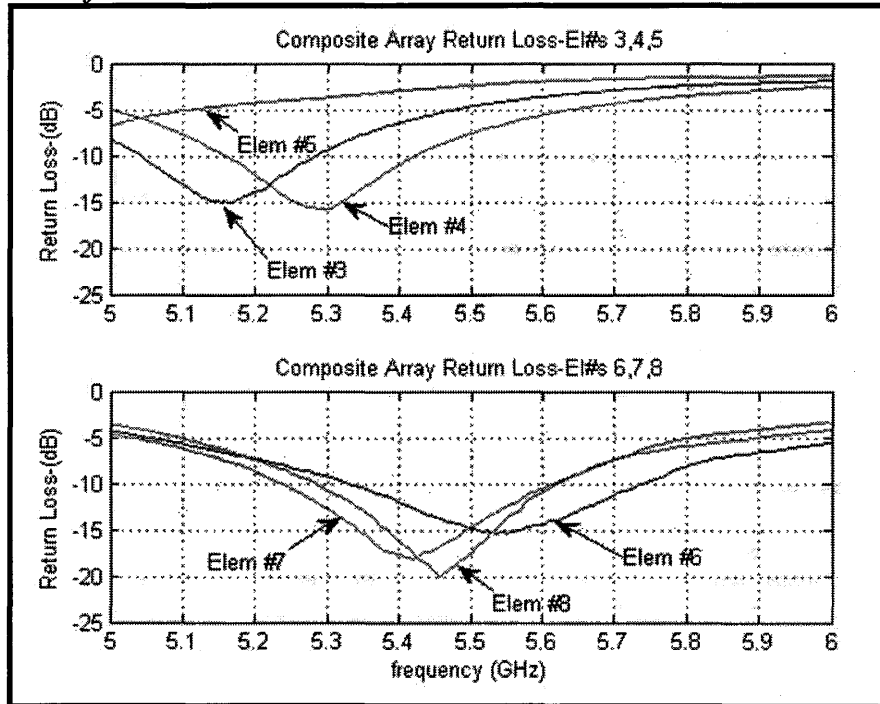


Figure 25 - Return Loss Responses for Composite Array Test Board Elements.

A second application of conductive paint was applied to element numbers 3, 4, and 5. The objective was to correct or improve the contact between the probe pad and the conductive patch. Substantial cracks in the dielectric exist in element numbers 3 and 5. The curing process for the application of the dielectric layer has since been modified to reduce the potential for discontinuities in the dielectric medium. The repainting procedure proved to be counterproductive for element numbers 3 and 5 as shown in the following figure. Figure 26 compares the original Return Loss responses to the repainted patch responses. Element 5 was severely detuned. Element 4 exhibited no significant change in impedance.

One likely explanation for the failure of Elements 3 and 5 would be conductive paint/material filled in the dielectric cracks during the repainting procedure.

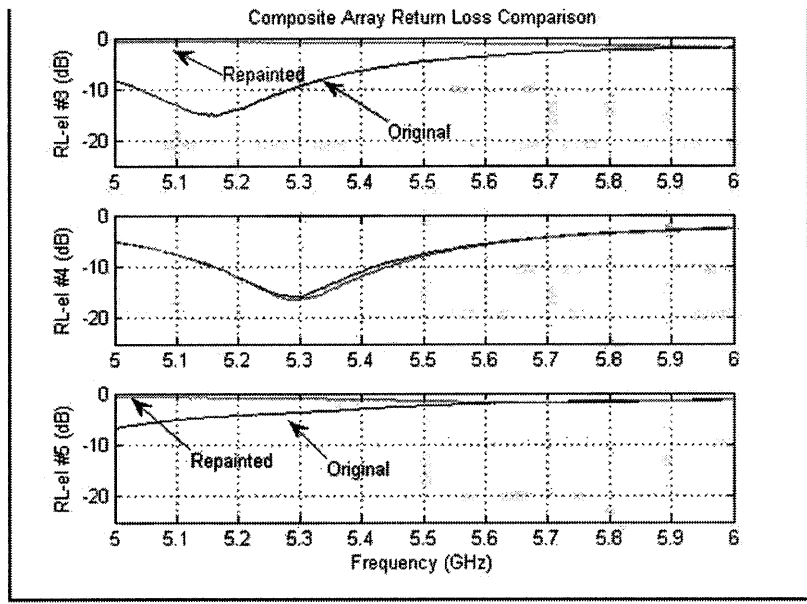


Figure 26 - Comparison of patch element Return Loss responses for a row chosen for Re-painting. Substantial curing cycle cracks existed in Elements 3 and 5.

Mutual coupling tests were conducted using the remaining good elements (#6, #7, and #8). Element #7 was used as the transmitting element and coupling to elements #6 and #8 was measured. The coupling levels measured were approximately 20 dB is similar to the results using the commercial substrate board assembly.

Bandwidth Comparisons of Microstrip Test Arrays on Commercial and Composite Boards

A similar test array constructed of commercial microstrip was measured earlier to refine fabrication methods and to establish a base line for future measurements. Return Loss responses for all nine elements of the commercial board were similar, and Element(1,1) was chosen for the following preliminary comparison to the optimum Return Loss response from the composite board (Element #8). The characteristics for these elements are presented in Figure 27. It can be seen that Element #8, the best of the composite board assembly, exhibits a bandwidth of approximately 6.2% and the resonant frequency is 5.4 GHz. The bandwidth is very close to the goal established throughout this research program and is superior to the commercial substrate (microstrip) antenna probably due to the higher losses in the painted dielectric.

A summary of the element RF tuning characteristics of the composite board assembly is provided in Table I. It can be seen that elements #6, #7, and #8 provide a trend on resonant frequency, bandwidth, and impedance match. Therefore, the design parameters associated with these elements (feed soldering method, element dimensions, etc.) were selected and is being fabricated in the 64-element phased array.

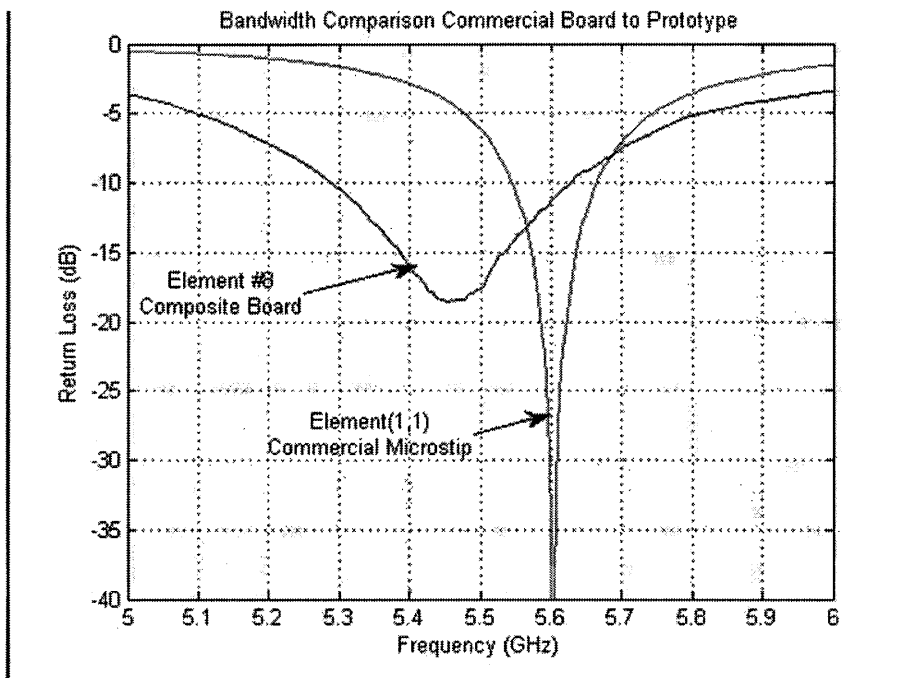


Figure 27 - Return Loss and Bandwidth comparison of commercial microstrip array
To the composite test array.

Bandwidth and Center frequency data is enclosed in Table II. The frequency limits for the bandwidth calculations were based on a RL>10dB.

	$f_{LOW}(\text{GHz})$	$f_C(\text{GHz})$	$f_H(\text{GHz})$	BW(%)
Elem(1,1)	5.55	5.60	5.66	2.0
Elem#03	5.04	5.16	5.29	4.8
Elem#04	5.16	5.30	5.42	4.9
Elem#05	N/A	N/A	N/A	N/A
Elem#06	5.33	5.55	5.74	7.4
Elem#07	5.24	5.42	5.62	7.0
Elem#08	5.29	5.46	5.63	6.2

Table II - Summary of Measured Bandwidth for Composite Test Array

9.0 Wing Phased Array – Fabrication

Fabrication of the Experimental Wing Section

Through a subcontract with Composite Optics-ATK the experimental wing section was designed and developed. The purpose of the experimental wing section was primarily to demonstrate “paint-on” antenna designs and was not designed for any other structural or wind tunnel type tests. The wing was designed to readily adapt to an antenna test model tower that is used in the anechoic test chamber at NASA Langley Research Center. The airfoil structure (shown in Figure 28) was built in two parts, a leading edge and the trailing edge to allow for easy connection and checkout of antenna cables. For each

section, a foam core was machined, or “hot-wired,” to an offset of the airfoil contour that accommodates the composite skin thickness. A .080” thick carbon epoxy skin was laid up on the foam and cured in place. The carbon epoxy material has similar electrical conductivity to the materials used for military aircraft (such as IM7, M55J, AS4). For the trailing edge, a tube was bonded into the core that is used for supporting the test body and to provide a path for running cables. For the leading edge, the foam was removed from sections where connectors are required for the antenna elements. Through-holes could be drilled into the skin as required to connect the elements to their cables. The flange of the leading edge was reinforced to accept shallow countersink fasteners. Their mating threaded fittings were bonded in the trailing edge section. Once the wing has been connected and the test body assembled, thin metal tape can be applied over the seams and fastener heads. The antenna cables extend out the hollow of the rotator adapter for connection to the transmitter electronics. Photographs of the fabrication process are presented in Figure 33 along with a photograph of the completed wing.

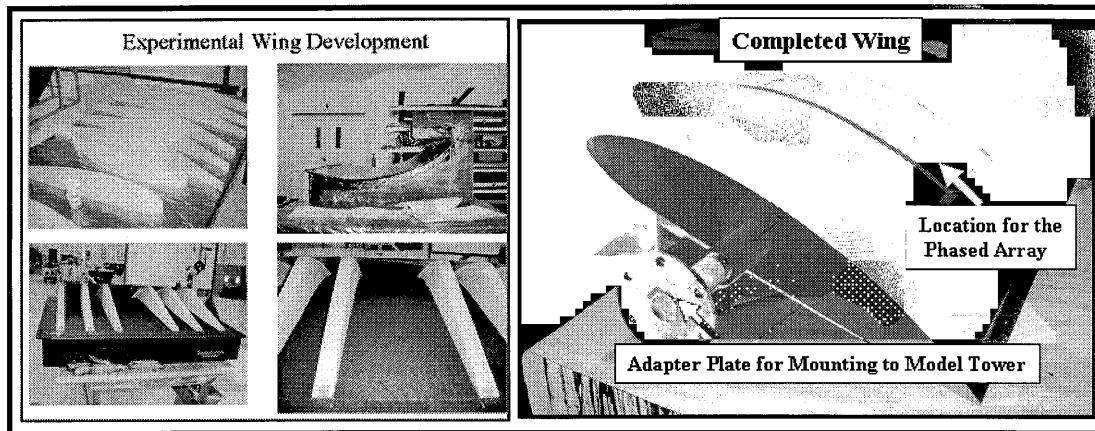


Figure 28 – Photographs of the fabrication stages in the development of the composite experimental wing for the phased array antenna

“Painting” the Phased Array on the Wing

Before the (LB-088) conductive coating and the (LB-070) polymer-based dielectric coating could be sprayed onto the wing for the array, the holes for the 64 RF had to be drilled into the wing surface. The detailed mechanical (IGES) model was then used to interface with a CNC machine and 64 holes were drilled in the graphite composite wing surface to accommodate all of the RF connectors for the array elements. Photographs of the wing after drilling and after applying the conductive coating (LB-088) for ground plane of the array are presented in Figure 29.

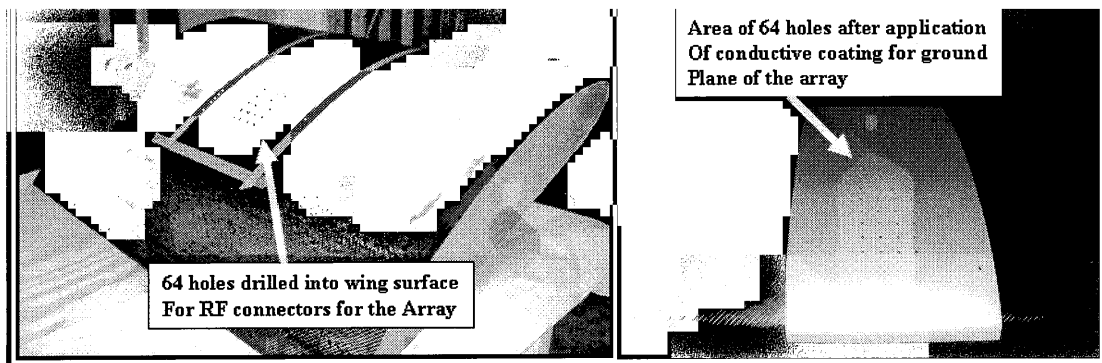


Figure 29 – Photographs of the wing after holes drilled for RF connectors, before and after application of LB-088 conductive ground plane.

After the LB-088 conductive coating was sprayed onto the wing surface and cured, the (64) RF connectors were bonded in place and the copper shields were folded down onto the ground plane coating. Then, another coat of LB-088 was applied to the areas around the connectors to assure good electrical contact from the connector shield to the antenna element ground planes. The results of this procedure are shown in the photographs in Figure 30 which also shows a test case using the vinyl templates that will be used in a later step to spray the antenna elements onto the dielectric coatings.

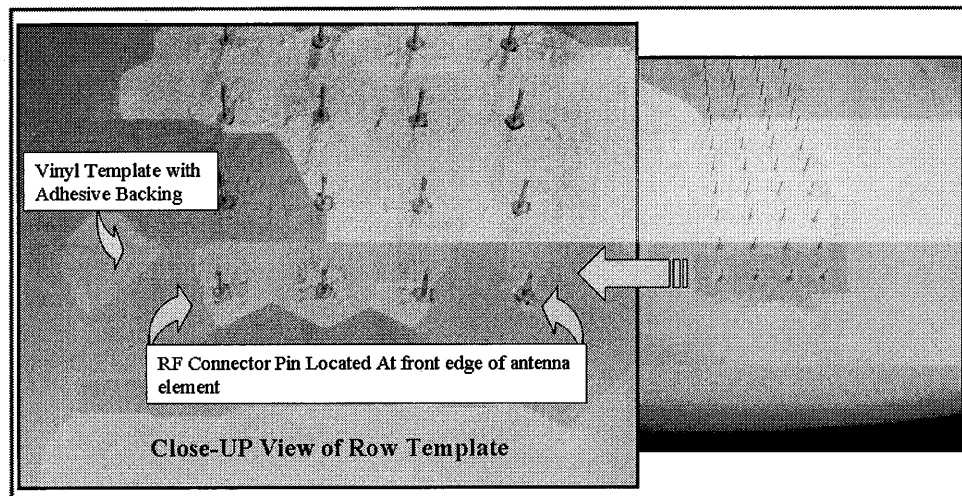


Figure 30 – Close-up photographs of the wing connectors after the copper tabs have been attached to the conductive ground plane and vinyl templates for painting the antenna elements.

Spraying the LB-070 dielectric coatings on the wing requires numerous coats and curing cycles to achieve the design goal of 0.080-inch overall film thickness for the array. The setup for curing the various coating applications is presented in Figure 31. IR lamps are positioned over the wing for curing and a sensor is shown hanging down close to the wing surface to provide accurate temperature control of the IR lamps. Feedback control for the IR

lamps is necessary to prevent overheating the wing surface which could cause cracks in the antenna surface.

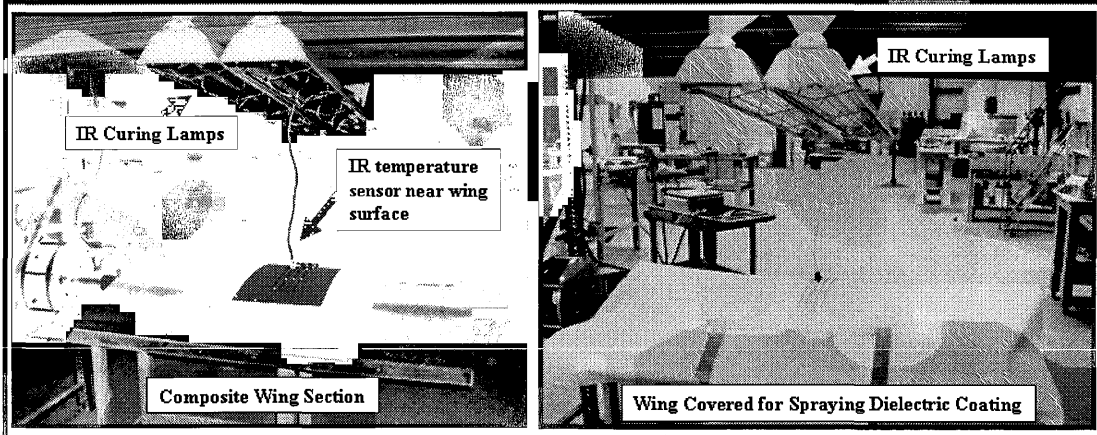


Figure 31 – Setup for applying and curing dielectric coatings for the wing phased array.

After numerous spraying of the LB-070 dielectric coatings, the buildup to 0.080-inch thickness is achieved and a closer view of the application is shown in Figure 32. After this stage of the fabrication process, flexible, laser-cut templates are used to provide the boundaries for the dielectric layer applications. After the dielectric layer(s) have cured, templates for the antenna circuits are used for spray applications of LB-088 conductive coatings to form the microstrip elements.

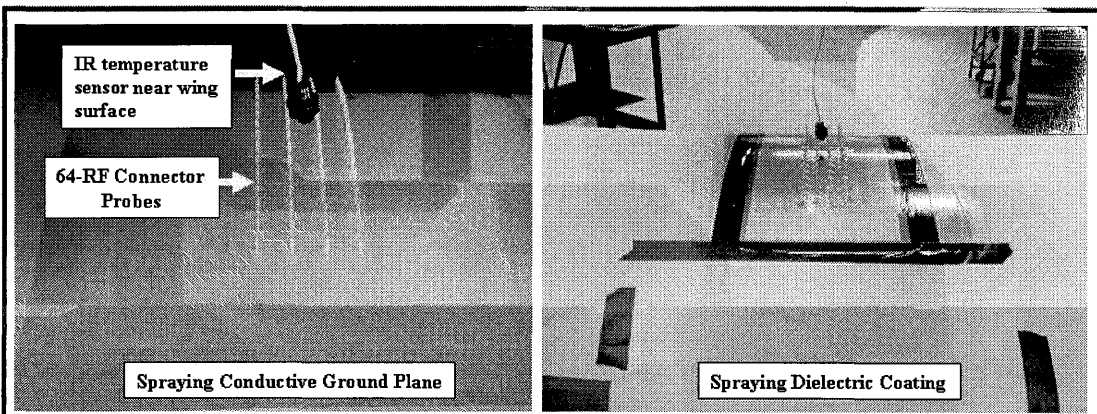


Figure 32 – Close-up photographs of the wing during applications and the curing cycle for the dielectric coatings.

10.0 Wing Phased Array – EM Test Results

EM tests of the wing phased array and comparisons with theory represent a summation of over three years of research and technology development and the results serve to demonstrate the overall readiness of Conformal Antenna Materials Technology. After the array was fabricated, the wing was tested initially at AEM to check the resonant frequencies of the 64-elements and the overall condition of the array. After completing the initial checkout, the phase distribution cables were attached to the array elements and

the wing was taken to NASA for radiation pattern tests. Figure 33 shows the wing installed in the Low Frequency Anechoic Chamber at NASA Langley.

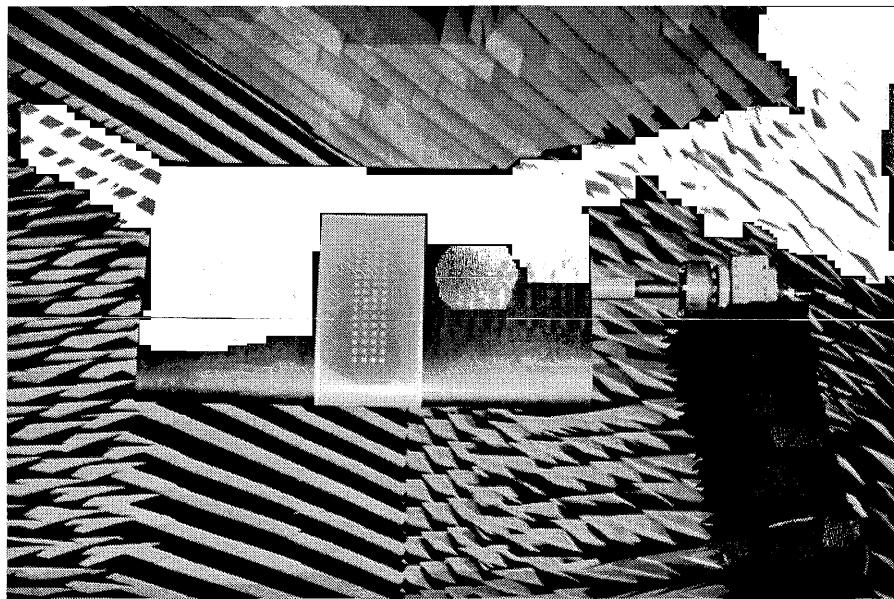


Figure 33 – Photograph of the wing array in the antenna test chamber at NASA.

Radiation pattern and gain tests were conducted at 5.3, 5.4, and 5.5 GHz and the results are presented in Figure 34. It can be noted that outstanding agreement is demonstrated between measured and calculated radiation patterns for both elevation and azimuth plane radiation patterns.

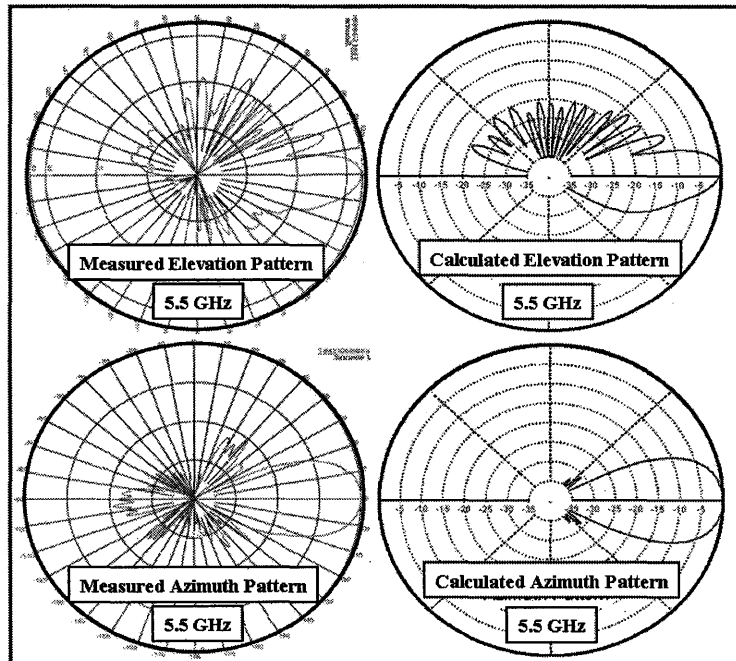


Figure 34 – Comparison of measured and calculated radiation patterns for the phased array “painted” on a composite wing section.

11.0 Future Plans – Total Robotic Manufacturing

In accordance with the goals and objectives for the SBIR Phase II/Enhanced program, robotic manufacturing methods were investigated to determine the potential for applications to conformal ‘paint-on’ antenna technology. Therefore, a subcontract was established with Pratt and Whitney (PW) and much progress was made to develop robotic manufacturing methods that can accommodate Unitech’s dielectric and conductive coatings. P&W successfully demonstrated robotically spraying both LB-070 (dielectric) and LB-088 (conductive) coating materials for developing antenna test circuits. P&W personnel also demonstrated success in spraying parallel lines on commercial substrates using the LB-088 as well as applying the LB-070 for complete “paint-on” antenna configurations. The accuracy of the lines was measured, width, parallelism, characteristic impedance of each line (and compared with theory), and the RF loss per length across wide frequency range. Potentially, a feed manifold design can be painted in future array configurations which would then provide a single RF connector for feeding the entire array.

These results indicated that P&W has the capability to robotically spray narrow line feed manifolds that are required for phased array antennas. For example, a feed manifold that has been designed for the wing phased array and that would replace all of the probe-fed elements would require 0.010-inch line widths. Based on P&W’s test results, it appears that it will be possible to spray conducting lines that accurately. In addition to the feasibility studies that were conducted by P&W, a computer simulation model was developed to present how robotic manufacturing methods can be used to paint-on antennas on aircraft wing section.

12. Acknowledgements

The outstanding support by Mr. Robert Boyd, Director of Technology at Unitech, LLC, is especially recognized for his expert designs of polymer-based materials and engineering support as well as to Sheila Bernal (Unitech, LLC) and Mr. Mick Hartzeim (AEM) for their dedicated and committed support to complete the fabrication of the wing phased array. In addition, the timely inputs and engineering support from Mr. Bruce Bailey at Eagle Aviation Technologies, Inc., is greatly appreciated. Also, the contributions of Mr. Christian Hearn of Applied EM, Inc. are acknowledged for his support designing and testing the phase distribution circuits for the array.

13. References

- [1] Michelle Champion, SBIR-AF03-206, Contract No. FA8718-04-C-0046 for Air Force Research Laboratory, Hanscom Air Force Base, SBIR Phase II.
- [2] T. G. Campbell, C. J. Reddy, and Robert Boyd, “Development of Conformal Antenna Materials Technology to Enable “Paint-On” Antenna Arrays for Air

Force Aerospace Applications," 30th Antenna Applications Symposium, Robert Allerton Park, Illinois, Sept. 20-22, 2006.

[3] W. Thomas, R. C. Hall, and D. I. Wu, "Effect of Curvature on the Fabrication of Wraparound Antennas," IEEE APS, Published March, 1997.

[4] D. Loffler, E. Gschwendtner, and W. Wiesbeck, "Design and Measurements for Conformal Antennas on Cylindrical and Spherical Geometries," 1999 IEEE 5th African Conference in Cape Town, South Africa, Sept. 28 – Oct. 1, 1999.

Impedance Bandwidth of a Wire Dipole with the Split-Coaxial Balun

Sergey N. Makarov and Reinholt Ludwig

IEEE ECE Dept., Worcester Polytechnic Institute, Worcester, MA 01609-2280 USA
(makarov@wpi.edu/ludwig.wpi.edu).

Abstract: In this study, a simple analytical transmission line model of a split-coaxial balun is proposed and tested. It is based on the coupled symmetric transmission line approach. The model leads to a closed-form analytical expression for the termination impedance/transfer function of the complete antenna system that includes a dipole, balun, and a non-splitted coaxial line of certain length. It accepts the impedance of a center-fed dipole as input parameter. The model is in excellent agreement with full wave simulations and enables us to optimize the impedance bandwidth of the dipole antenna. The model predicts a 12% 10 dB return loss bandwidth for the resonant dipole-balun configuration and a greater than 20% bandwidth for the combined dipole, balun and non-splitted line configuration. Finally, the model is confirmed by prototype measurements.

1. INTRODUCTION

A motivation for this work was a necessity to design a low cost mast-conformal linear 20%-wideband UHF wire dipole (400-500 MHz) with the controllable complex antenna factor (CAF) and the controllable *phase* characteristics. Some commercially available dipole antennas are either narrowband (cover the desired band in steps of 20-25MHz) or have a sufficient bandwidth (300-1000 MHz - TV dipoles or EMI dipoles) but an unknown phase transfer function. The most involved part of the design becomes a balun that simultaneously plays the role of a lossless impedance matching network and an antenna support (a mast).

Conventional baluns for symmetric wire dipole antennas are reviewed in several scholar sources - see for example [1]-[6]. Our attention is concentrated on the split-tube or split-coaxial balun (a "split coax" balun in Fig. 5-42 of Ref. [4] or type 10a balun in Fig. 43-24 of Ref. [6]). The balun is to be connected to an unfolded straight-wire dipole. This balun, in contrast to some other balun types, has a very convenient conformal geometry; it is easy to manufacture with commercial off-the-shelf tubing. It is used in both linear and circular polarization (turnstile) dipole configurations intended for communications systems [5],[7].

The balun itself is shown in Fig. 1, together with appropriate dimensions. Two dipole currents should exactly cancel each other on the outer conductor surface of the coaxial line after the split point, due to anticipated excitation symmetry [2]. On the other hand, the antenna is not shorted at the dipole feeding point due to the $\lambda/4$ short-to-open circuit transformation. According to [6], this type of balun "will give almost perfect balance over a wide frequency range if the slot width is kept small and symmetry is maintained at the strap end." In particular, Ref. [7] reports on an 8% bandwidth for the split-coaxial balun supporting the dipole with a reflector.

A non-conformal variation of the split-coaxial balun is known as the quarter-wave balun [1], [2], [8], that is referred to as a " $\lambda/4$ coaxial balun 1:1" in Ref. [1] - Fig. 9.25c, and as a "folded balun" in Ref. [2] - Fig. 5-26. For the quarter-wave balun, the slots are missing, but one wing of the dipole, which is connected to the inner conductor of the coaxial line, is simultaneously connected to the outer conductor at the distance of $\lambda/4$ from the feed by a straight rod. It is stated in [2] that this balun is "of course, not broadband because of the quarter wavelength involved in its construction". Ground plane may be present [8] or not [1], [2] at a distance of $\lambda/4$ from the feed. Yet another variation is a three-wire balun [6], [8] that completely replaces the $\lambda/4$ section of the coaxial line by three wires, two of which are connected to the ground plane at $\lambda/4$ and one - to the inner conductor of the coaxial feed at the same distance.

Despite a significant amount of research efforts on the split-coaxial balun outlined above, two fundamental questions remain unanswered. First, there is no simple quantitative estimate of the impedance bandwidth of the half-wave dipole with the split-coaxial balun versus the bandwidth of the equivalent center-fed dipole. Second, impedance matching and transfer function properties of the split-coaxial balun loaded with the wire dipole have not yet been investigated quantitatively. Note that return loss improvement provided by a matching network (balun) to the dipole antenna(s) may exceed 100-150% of the initial bandwidth both in theory [9],[10] and experiment [11].

Fig. 1 suggests that quantitative theory of the split-coaxial balun may be based on the three-conductor transmission line model. Such a model has been discussed independently in two papers [8], [12]. In both references, three independent conductors and a separate ground have been considered, which initially leads to a six-port transmission line network with the associated static capacitance matrix [8]. Though a general expression for the antenna admittance has been obtained in both [8] and [12], it was not quantified in terms of the parameters of the balun such as slot length, width, and thickness.

The three-conductor transmission line with no extra ground may be also described in terms of two independent propagating modes. Collin [14] first described two modes that can propagate along the split-coaxial line; one of them is the perturbed TEM fundamental mode (coaxial or bifilar mode according to terminology used in [15],[16]) and another is the slot mode that also extends into the surrounding space (monofilar mode according to the same references). This analysis, and an analysis reported in [17], was performed for the infinitely thin coaxial tubes only. On the other hand, Milligan [4] classified the two modes in the splitted line as TEM and TE₁₁; the latter notation is somewhat questionable due to anticipated cutoff of the coaxial TE₁₁ mode.

Our approach to the split-coaxial balun is based on separation of the balun into two coupled symmetric transmission lines. Coupled transmission line theory - see [13], [18]-[22] - introduces even and odd modes of propagation; with the even mode being independent of the mutual coupling parameters. For the symmetric case of a two-line network, the transmission equations for even and odd modes are decoupled, and every mode is described by the familiar two-port network equation and has its own characteristic impedance [18], [20]-[22]. Such an approach will lead to a simple closed-form solution for the transformed antenna impedance, which appears to be in excellent agreement with the full-wave simulations and experiment. The analytical solution allows us to rapidly estimate and optimize dipole performance over a wide range of balun parameters.

This paper is organized as follows: Section 2 describes the line and the load model, and the impedance transformation results. Section 3 discusses bandwidth of the half-wave dipole with a quarter-wave split-coaxial transformer. Section 4 gives a method of bandwidth enhancement, using two closely spaced resonances. Section 5 presents the corresponding experimental results and Section 6 concludes the paper.

2. COUPLED TRANSMISSION LINE MODEL OF THE BALUN

Separation into Two Coupled Lines

In Fig. 2 we suggest a way of separating the splitted coaxial line into two coupled symmetric transmission lines TL1 and TL2. The central conductor plays the role of ground common to both lines. This designation of "ground" has no special relevance beyond the fact that it is a convenient reference designation for maintaining symmetry. Two coupled lines are characterized by static self-capacitances C_{11} and C_{22} , and mutual capacitance C_{12} schematically shown in Fig. 2 - bottom.

The following assumptions are made that are based on the physical dimensions for the manufactured dipoles - see Fig. 1:

- i. the coaxial tube has a significant thickness $c - b$ so that the slot width is smaller than or equal to this value: $d \leq c - b$;
- ii. slot width d is small compared to the inner radius of coaxial tube b ;
- iii. radius of the inner rod a is on the order of the inner radius of the coaxial tube b ; in other words, the inner conductor is considered "thick".

Following these assumptions, the self-capacitances C_{11} and C_{22} are approximately equal to half of the static capacitance of the non-slotted coaxial line each [13]. Mutual capacitance C_{12} is that of two narrow slots (dominant part) plus the capacitance between two curved conductors (secondary contribution). Each of the slots is modeled by a parallel-plate capacitor. The same model is applied to the curved conductors. They are replaced by parallel plates of the same projection area $2b$, with an effective separation distance b_{eff} .

One thus has

$$C_{11} \approx \pi \frac{\epsilon_0}{\ln(b/a)}, \quad C_{22} \approx \pi \frac{\epsilon_0}{\ln(b/a)}, \quad C_{12} \approx 2 \frac{\epsilon_0(c-b)}{d} + \frac{\epsilon_0 2b}{b_{\text{eff}}} \quad (1)$$

where ϵ_0 is the dielectric constant of vacuum for the air-filled line. We have chosen the effective separation distance to be $b_{\text{eff}} = 0.5b$. It is evident that the capacitance expressions in Eq. (1) represent simple approximations that can be replaced by more accurate static capacitance expressions if desired. The implication of Eq. (1) suggests that the slot mode described in the introduction mostly concentrates within the slot and less in the surrounding space.

Coupled Symmetric Transmission Line Model

Fig. 3 shows the coupled TL model that utilizes the capacitance values established above. The characteristic inductances for the air-filled coupled line are given by [21]

$$L_{11}C_{11} = \mu_0\epsilon_0, \quad L_{22}C_{22} = \mu_0\epsilon_0, \quad L_{12} = L_{11} \frac{C_{11}}{C_{12} + C_{22}} \quad (2)$$

where μ_0 is magnetic permeability of vacuum. The characteristic impedances and propagation constants for the even (equal line voltages) and odd (opposite line voltages) modes read [13],[21],[22]

$$Z_e = \frac{1}{c_0 C_{11}} = \frac{1}{c_0 C_{22}}, \quad Z_o = \frac{1}{c_0 C_o} = \frac{1}{c_0 (C_{11} + 2C_{12})}, \quad \gamma_o = \gamma_e = \gamma_0 = jk_0 \quad (3)$$

where index 0 indicates free-space speed of light, wave number, and a propagation constant. With reference to Fig. 3, one obtains the chain, or ABCD matrixes, for the even and odd mode of the coupled line of length l in the form [18]

$$\begin{bmatrix} \frac{1}{2}(V_1 + V_2) \\ \frac{1}{2}(I_1 + I_2) \end{bmatrix} = A_e \begin{bmatrix} \frac{1}{2}(V_3 + V_4) \\ -\frac{1}{2}(I_3 + I_4) \end{bmatrix}, \quad A_e = \begin{bmatrix} \cos k_0 l & jZ_e \sin k_0 l \\ j/Z_e \sin k_0 l & \cos k_0 l \end{bmatrix} \quad (4)$$

$$\begin{bmatrix} \frac{1}{2}(V_1 - V_2) \\ \frac{1}{2}(I_1 - I_2) \end{bmatrix} = A_o \begin{bmatrix} \frac{1}{2}(V_4 - V_3) \\ -\frac{1}{2}(I_3 - I_4) \end{bmatrix}, \quad A_o = \begin{bmatrix} \cos k_0 l & jZ_o \sin k_0 l \\ j/Z_o \sin k_0 l & \cos k_0 l \end{bmatrix} \quad (5)$$

where $V_{1,2,3,4}$ are termination voltages and $I_{1,2,3,4}$ are termination currents. Both matrixes A_e and A_o are equivalent to the ABCD matrix for a single transmission line with the corresponding characteristic impedances Z_e and Z_o , respectively.

Termination

Fig. 4a) shows the termination setup for the dipole, balun, and the continued coaxial line. TL1 is shorted at the input - one dipole wing shorts this line. TL2 is connected to the equivalent antenna circuit - an ideal voltage source in series with the dipole (self) impedance Z_D . On the opposite end, two line conductors are connected in shunt at l (since the slot disappears) and form the outer conductor of a continued coaxial line. Ground (center conductor of the coupled line) becomes the inner conductor of the continued coaxial line.

The arrangement shown in Fig. 4a) allows us to establish the S-parameters of the balun [23], [24] and the related complex antenna factor (CAF) [24], or the reciprocal antenna transfer function. This step is necessary when the phase distortion characteristics of the dipole are evaluated as a function of frequency. In the present study, we are only interested in the impedance transformation of the split-coaxial balun. Therefore, the equivalent circuit has the form shown in Fig. 4b). It includes the dipole with impedance Z_D connected to a balun of length l and a non-splitted coaxial TL section of length L . The transformed impedance is given by

$$Z_s = \frac{V_s}{I_s} \quad (6)$$

where V_s is a voltage source applied to the terminals of the transmission line and I_s is the computed current. Straightforward calculations of the transformed antenna termination impedance are based on chain matrixes (4) and (5), and are given in the next subsection.

Transformed Antenna Impedance

With reference to Fig. 4b), the chain matrix for the transmission line section of length L yields

$$\begin{bmatrix} V_{\text{coax}} \\ -I_{\text{coax}} \end{bmatrix} = A_{\text{coax}} \begin{bmatrix} V_s \\ -I_s \end{bmatrix}, A_{\text{coax}} = \begin{bmatrix} \cos k_0 L & jZ_{\text{coax}} \sin k_0 L \\ j/Z_{\text{coax}} \sin k_0 L & \cos k_0 L \end{bmatrix} \quad (7)$$

where Z_{coax} is the characteristic impedance of the non-splitted line. The termination conditions on the antenna side and on the opposite side read

$$V_1 = 0, \quad V_2 = -Z_D I_2, \quad V_3 = V_4 = -V_{\text{coax}}, \quad I_3 + I_4 = I_{\text{coax}} \quad (8)$$

in terms of termination voltages $V_{1,2,3,4}$ and termination currents $I_{1,2,3,4}$.

Substitution of Eq. (8) into Eq. (4) for the even mode and using Eq. (7) gives

$$\begin{bmatrix} -\frac{1}{2}Z_D I_2 \\ \frac{1}{2}(I_1 + I_2) \end{bmatrix} = A_e \begin{bmatrix} -V_{\text{coax}} \\ +\frac{1}{2}I_{\text{coax}} \end{bmatrix} = A_e \begin{bmatrix} -1 & 0 \\ 0 & -1/2 \end{bmatrix} \begin{bmatrix} V_{\text{coax}} \\ -I_{\text{coax}} \end{bmatrix} = A_e \begin{bmatrix} -1 & 0 \\ 0 & -1/2 \end{bmatrix} A_{\text{coax}} \begin{bmatrix} V_s \\ -I_s \end{bmatrix} \quad (9)$$

Substitution of Eq. (8) into Eq. (5) for the odd mode allows us to find a relation between I_1 and I_2

$$\begin{aligned} \begin{bmatrix} +\frac{1}{2}Z_D I_2 \\ \frac{1}{2}(I_1 - I_2) \end{bmatrix} &= A_o \begin{bmatrix} 0 \\ -\frac{1}{2}(I_3 - I_4) \end{bmatrix}, \quad A_o^{-1} \begin{bmatrix} +\frac{1}{2}Z_D I_2 \\ \frac{1}{2}(I_1 - I_2) \end{bmatrix} = \begin{bmatrix} 0 \\ -\frac{1}{2}(I_3 - I_4) \end{bmatrix} \\ \Rightarrow \left[+\frac{1}{2}Z_D I_2 \right] a_o^{-1}_{11} + \left[\frac{1}{2}(I_1 - I_2) \right] a_o^{-1}_{12} &= 0 \Rightarrow I_1 = (1+K)I_2, \quad K = -\frac{Z_D a_o^{-1}_{11}}{a_o^{-1}_{12}} \end{aligned} \quad (10)$$

Substitution of this relation into Eq. (9) will express the termination current I_s in terms of the termination voltage V_s as follows

$$\begin{aligned} \begin{bmatrix} -Z_D I_2 \\ (2+K)I_2 \end{bmatrix} &= \underbrace{A_e \begin{bmatrix} -2 & 0 \\ 0 & -1 \end{bmatrix} A_{\text{coax}}}_{M} \begin{bmatrix} V_s \\ -I_s \end{bmatrix} = \begin{bmatrix} m_{11}V_s - m_{12}I_s \\ m_{21}V_s - m_{22}I_s \end{bmatrix} \\ \Rightarrow (2+K)m_{11}V_s - (2+K)m_{12}I_s + Z_D m_{21}V_s - Z_D m_{22}I_s &= 0 \Rightarrow V_s = \frac{(2+K)m_{12} + Z_D m_{22}}{(2+K)m_{11} + Z_D m_{21}} I_s \end{aligned} \quad (11)$$

Thus, the impedance Z_s is finally given by

$$\begin{aligned} Z_s &= \frac{(2+K)m_{12} + Z_D m_{22}}{(2+K)m_{11} + Z_D m_{21}}, \\ M &= \begin{bmatrix} \cos k_0 l & jZ_e \sin k_0 l \\ j/Z_e \sin k_0 l & \cos k_0 l \end{bmatrix} \begin{bmatrix} -2 \cos k_0 L & -2jZ_{\text{coax}} \sin k_0 L \\ j/Z_{\text{coax}} \sin k_0 L & \cos k_0 L \end{bmatrix} \end{aligned} \quad (12a)$$

where

$$\begin{aligned} K &= -\frac{Z_D a_o^{-1}_{11}}{a_o^{-1}_{12}}, \quad A_o^{-1} = \begin{bmatrix} \cos k_0 l & -jZ_o \sin k_0 l \\ -j/Z_o \sin k_0 l & \cos k_0 l \end{bmatrix}, \\ K &= -j \frac{Z_D}{Z_o} \cot(k_0 l) \end{aligned} \quad (12b)$$

If the balun is exactly a quarter wavelength ($K = 0$) and the additional coaxial line section of length L is absent, the termination impedance becomes that for the familiar quarter-wavelength transformer [8]

$$Z_s = \frac{Z_e Z_e}{Z_D} \quad (13)$$

For a coaxial line with $Z_{\text{coax}} = 50\Omega$, one finds $Z_e \approx 100\Omega$. Therefore, the split-coaxial balun will indeed behave as a 4:1 transformer for an idealized antenna load of $Z_D = 50\Omega$. Unfortunately, the load is now not properly matched. In order to achieve matching to a 50Ω , the characteristic impedance of the base non-split coaxial line should be considerably decreased.

It is interesting to note that for the folded dipole, whose input impedance is approximately four times the dipole impedance, Eq. (13) would give an almost ideal match to the balun section of the coaxial line with $Z_{\text{coax}} = 50\Omega$. Our attention is, however, concentrated on the unfolded dipole.

Comparison with Full-Wave Simulations (412 MHz Dipole)

In order to compare the results with a full-wave simulation software (ANSOFT HFSS v. 10.1) the following steps are done: first, the impedance Z_D of a center-fed dipole of interest is found numerically in ANSOFT and then tabulated. This impedance is then substituted in Eqs. (12) and the termination impedance Z_s is evaluated over a desired frequency band.

Simultaneously, another ANSOFT project was created that includes the complete antenna: the same dipole, balun connections, balun itself, and the additional coaxial line section of length L . The coaxial line is fed from the opposite end using a lumped port that defines the polarized TEM E -field across the cross-sectional ring of the coaxial line. Fine meshes with about 100,000 tetrahedra and discrete frequency sweeps are used to obtain accurate results.

Table I gives the physical parameters of a UHF dipole and a balun used for comparison. Both the slot and the dipole wings have the length of 170 mm, which approximately corresponds to the center frequency of 412 MHz. For convenience, here and in what follows we use standard off-the-shelf brass tubing/rod sizes available from McMaster Carr. The characteristic impedance of the non splitted coaxial line is still chosen to be as close as possible to $Z_{\text{coax}} = 50\Omega$. In that case Z_e is close to 100Ω and the split-coaxial balun is not expected to be matched properly, as discussed in the previous subsection.

Fig. 5 shows the surface current density distribution (logarithmic scale) for a dipole with the split-coaxial balun (left) and for the unbalanced dipole with the same parameters - right. Parameters for both dipoles are listed in Table I. For the dipole with the split-coaxial balun, the current density on the outer conductor beyond the balun is at least 120-140 times smaller than the maximum current density on the dipole wings. This value multiplied with the ratio of the radii gives us the ratio of the total currents inside and outside the

coaxial line as at least 40. Without the balun (Fig. 5-right), the ratio of total currents reduces to approximately 3. Thus, the balun performs its major function: the current cancellation on the outer side of the coaxial line (22 dB or better). The mode on the outer side of the conductor for the unbalanced dipole is a leaky traveling wave that may propagate along a single metal conductor (Sommerfeld wave) - see [25] and [1], pp. 549-555 - and may be reflected from the terminations. Therefore, one can see a well-developed standing wave pattern - see Fig. 5 - right.

Fig. 6a) shows impedance of the center-fed test dipole with 170 mm wing length. Fig. 6b gives the impedance of the same dipole but connected to the balun and a continued coaxial line with the characteristic impedance of 54Ω - see Table I. The resistance is shown by a solid curve and the reactance is depicted by a dashed curve. One can see that there is no impedance matching in the present case and multiple resonances do occur. The corresponding return loss is shown in Fig. 6c) and d). All these solutions have been found using ANSOFT HFSS for the complete antenna model. The corresponding results of the transmission line theory (Eqs. (12)) with the parameters listed in Table I are given by the thin-lined curves in Fig. 6b) and 6d), respectively. The agreement between the two solutions appears nearly excellent, especially in Fig. 6b) where these solutions almost coincide, despite a complicated multi-resonant behavior of the present non-matched balun.

3. RESONANT IMPEDANCE BANDWIDTH

Balun parameters

In order to match the split-coaxial balun to the dipole and to the 50Ω front-end termination network, the following steps are done: First, the impedance Z_D of a center-fed dipole is again found numerically via ANSOFT HFSS and then tabulated. The resonant frequency and the resonant dipole wavelength λ_{Dres} are found from the condition $\text{Im}(Z_D) = 0$. The slot length l is then defined as $\lambda_{Dres}/4$. The length of the additional transmission line section L is kept at a minimum, which is necessary to ensure mechanical stability of the antenna - we choose $L = 10\text{mm}$.

To match the dipole resonant resistance, the even-mode impedance is found from Eqs. (1) and (2). We have

$$Z_e = \frac{\ln(b/a)}{c_0 \pi \epsilon_0} \quad (14)$$

At the same time, Eq. (13) needs to be satisfied based on $Z_s = 50\Omega$, which gives

$$\frac{b}{a} = \exp(c_0 \pi \epsilon_0 \sqrt{50 Z_{Dres}}) \quad (15)$$

where Z_{Dres} is the dipole resistance at resonance. Either a or b in Eq. (15) can be varied so as to achieve impedance matching. We prefer to vary a - the radius of the inner conductor.

All other parameters remain fixed as specified in the previous section (Table I); only the dipole wing length is changed from 170 mm to 156 mm compared to the previous case. The dipole is now centered at about 440 MHz. Table II provides with the parameters of the balun that most closely satisfy the conditions listed above for standard brass tubing/rod sizes.

Resonant Antenna Bandwidth (440 MHz dipole)

Fig. 7a) shows the return loss of the center-fed dipole with 156 mm wing length and Fig. 7b) gives the return loss of the same dipole with the balun designed according to Table II. The thick curve corresponds to the ANSOFT HFSS solution whereas the thin curve is the transmission line model. The agreement between both solutions is good.

The main observation is that the bandwidth of the dipole with the splitted-coaxial balun is about 12% in Fig. 7b). This is larger than the bandwidth of the original center-fed dipole (i.e., 8%) by approximately a factor of 1.4. To explain this result we consider Eqs. (12) with L equal to zero. This yields

$$Z_s = \frac{(2+K)jZ_e \sin k_0 l + Z_D \cos k_0 l}{(2+K)2 \cos k_0 l + 2Z_D j / Z_e \sin k_0 l}, \quad K = -j \frac{Z_D}{Z_o} \frac{\cos k_0 l}{\sin k_0 l} \quad (16)$$

An asymptotic expansion with the following approximations

$$\begin{aligned} k_0 l &= \frac{\pi}{2} + \delta, \quad \delta \ll 1, \quad \cos k_0 l \approx -\delta, \\ \sin k_0 l &\approx 1 - \delta^2/2, \quad K \approx j \frac{Z_D}{Z_o} \delta \end{aligned} \quad (17)$$

results, to main order of approximation, in the expression

$$\begin{aligned} Z_s &\approx \frac{(2+K)jZ_e - Z_D \delta}{-2(2+K)\delta + 2Z_D j / Z_e} \approx \frac{2Z_e + j\delta Z_D \left(\frac{Z_e}{Z_o} + 1 \right)}{2Z_D / Z_e + j4\delta} \\ &\approx \frac{Z_e^2}{Z_D} \left(1 + \left[j\delta \left(\frac{Z_D}{2Z_o} + \frac{Z_D}{2Z_e} - 2 \frac{Z_e}{Z_D} \right) \right] \right) \end{aligned} \quad (18)$$

For the dipole from Table II, the reactance term in the square brackets in Eq. (18) is reasonably small and positive; so is the dipole reactance close to the resonance. One may therefore conclude that it is a better matching of $\text{Re}(Z_e Z_e / Z_{Dres})$ to 50Ω than matching of the original Z_{Dres} to 50Ω , which makes the bandwidth wider. In other words, the bandwidth increase for the resonant dipole with the split-coaxial balun is a familiar action of the quarter wavelength transformer on real impedances.

Effect of Uncertainty in Slot Width and Length

An important question from the viewpoint of hardware prototyping is the effect of inaccuracy in slot width. Fig. 7c) investigates the effect of varying the slot width from 1 to 2 mm and its behavior on the return loss obtained with the transmission line model. Ten curves that correspond to different slot widths between 1 and 2 mm almost coincide. Therefore, the inaccuracy in slot cutting has generally a minor influence on the antenna performance. Similar results have been obtained with ANSOFT HFSS.

Fig. 7d) shows the effect of varying the slot length about $\lambda_{Dres}/4$ by $\pm 10\%$ and its effect on the return loss; the thick curve corresponds to $\lambda_{Dres}/4 + 10\%$. One can see that the impedance bandwidth slightly increases (up to 15%) with increasing slot length above $\lambda_{Dres}/4$. Unfortunately, Eq. (18) is unable to describe this effect, which is on the second order of magnitude with regard to the small parameter δ in Eq. (17).

4. BANDWIDTH ENHANCEMENT

Two Closely Spaced Resonances

With the help of the transmission line model, it has been found that the bandwidth of the dipole with balun can further be improved using the method of two closely spaced resonances. One of them is the original dipole resonance at a lower frequency. Another is a resonance of the system that consists of the balun connected to a finite, but still relatively short, section L of the non-splitted coaxial line with the impedance different from 50Ω . This line always presents in the hardware prototype in order to ensure mechanical stability - see Fig. 1. It is therefore advisable to use this "free" network element for bandwidth enhancement.

Bandwidth of the Dipole Network with Two Closely Spaced Resonances

The system balun+non-splitted line operates as a distributed matching network/filter, presumably of the second order. It may be properly tuned to achieve the second resonance at a slightly higher frequency. The dipole wing length is now 152 mm, which will correspond to the center frequency of the composite band of approximately 460 MHz. This center frequency is our final goal. Fig. 8 shows typical analytical tuning results for the return loss of the complete network (dipole+balun+non-splitted line). These results involve two parameters: balun length l that varies from 150 to 188mm in 20 steps; and non-splitted line length L that attains the values of 10, 25, 50, and 75 mm. The development of the second resonance can be seen while the non-splitted line length increases. The largest impedance bandwidth is thus obtained with $L=50$ mm as seen in Fig. 8c). It is slightly higher than 20%. However, the return loss now has a maximum in the middle of the band that is approaching -11 dB. The corresponding full wave simulation is very close to this result but reduces the maximum of the return loss within the band to approximately -13 dB.

Effect of Shift of the Center Conductor

A slight asymmetry in the position of the center conductor of the splitted transmission line may severely degrade performance of the matching network with the dual resonances.

For a shift of 0.5mm from the center position, the corresponding ANSOFT HFSS simulation predicts increase in the return from -13 dB to -8 dB in the center of the band. Therefore, in contrast to the other dipole parameters tested above, the position of the center conductor appears to be critical for the balun prototyping.

5. MEASUREMENT RESULTS

Dipole prototypes (460 MHz center frequency)

Using the matching network with dual resonances, a series of UHF dipole prototypes was custom built and tested for the center frequency of the band equal to 460 MHz. The corresponding physical parameters are listed in Table III. Some dipole prototypes are shown in Fig. 9. One outer and two inner Teflon rings, with the height of 10mm each, have been used to provide system stability and to properly position the inner conductor of the slotted transmission line. An SMA connector is soldered to the non-split section of the brass transmission line at the feeding point. All other connections are made in a solderless way. The dipole prototypes are low-cost and are built with commercial off-the-shelf brass/Teflon tubing and brass rods - see Table III. The prototypes may be assembled into an array of dipoles. All prototypes passed the "drop off" test. The dipole prototypes are intended for the use in an indoor geolocation wireless link.

Measurement

Measurement results for the return loss of dipole prototypes are obtained with Agilent's 8722ET Network Analyzer and are given in Fig. 10 (thin curves) compared to the analytical model - Eqs. (12) - thick dashed curve. The agreement in the impedance bandwidth of the antenna (frequency band where return loss is less than -10 dB) is nearly excellent between the individual dipoles as well as between the measured and predicted values. The analytical network model also agrees well with the ANSOFT simulations, see Fig. 11. Note that the ANSOFT model of the complete antenna takes into account some fine antenna details such as feed assembly, construction nuts, inner/outer Teflon rings, etc. The measured impedance bandwidth for individual dipoles ranges from 23% to 26%.

However, within the band, the measured return loss of the individual dipoles indicates a rather random behavior, with the maximum return loss as high as -12 to -11 dB for a couple of dipole prototypes. This behavior is likely due to mechanical intolerances of the present prototypes such as a small error in the position of the center conductor, a slight asymmetry of the feed assembly, etc. Another experimental design (with closer resonances) may indeed have a better return loss within the band, but at the expense of decreasing the overall 10 dB bandwidth.

In order to reduce the effect of manufacturing intolerances, each dipole has been equipped with a thin sliding brass ring that is seen in Fig. 9. The brass ring allows us to cover a small portion of the slots (reduce the slot length) and thus change the balance between two resonances in Fig. 8. The latter circumstance allows us to adjust (decrease) the maximum value of the return loss within the band.

A less important but still visible point of concern is a disagreement between theoretical (both the lumped circuit model and the full wave model) and experimental results in the

lower UHF band at approximately 300 MHz in Fig. 10. It is believed that the experimentally observed RF leakage in Fig. 10 is due to limited bandwidth (limited to approximately 400 MHz) of the absorber material used in the present measurements and the associated antenna loading.

6. CONCLUSIONS

In this study we have presented and validated a simple closed-form analytical TL model of the wire dipole with the split-coaxial balun. The model accepts the input impedance of the center-fed dipole as an input parameter and outputs the antenna termination impedance or the antenna transfer function. The model indicated a very good agreement with the full-wave simulations obtained at three different center frequencies (412, 440, and 460 MHz) and for different geometry parameters (non-matched balun, matched resonant balun, and matched balun with two closely spaced resonances).

The model predicts the impedance bandwidth of 12% for the $\lambda/4$ resonant balun and the bandwidth in excess of 20% for the properly tuned complete antenna network (dipole+balun+supporting section of the non-split transmission line). UHF wire dipoles built in accordance with this model are compact and low-cost, and indicate good repeatability in the center frequency and in the impedance bandwidth; they exhibit good agreement with theoretical predictions. The measured impedance bandwidth of the UHF dipoles is approximately 23-26%. However, the return loss behavior within the band needs to be improved and controlled more precisely, by improving hardware tolerances.

The present model is equally applicable to other dipole-like standard antennas of interest: a broadband (bowtie) dipole, a droopy dipole intended for better azimuthal coverage, a turnstile crossed dipole intended for circular polarization [5], or to a quasi-folded assembly of two crossed dipoles also intended for circular polarization [26]. For those systems, only the input impedance of an equivalent center-fed antenna needs to be recalculated. In particular, a similar impedance tuning procedure applied to a 90° bowtie dipole has reached the bandwidth of about 30% vs. 16% bandwidth for the corresponding center-fed antenna.

7. ACKNOWLEDGMENT

Authors would like to thank Mr. Robert Boisse and Mr. Patrick Morrison of WPI for the hardware support and Dr. Steven R. Best of Mitre Corporation for useful remarks. This work was supported in part by the U.S. Department of Justice under Grant 2003-IJ-CX-K025.

REFERENCES

- [1] C. A. Balanis, *Antenna Theory. Analysis and Design*, Wiley, New York, 2005, third ed., pp. 538-542.
- [2] W. L. Stutzman and G. A. Thiele, *Antenna Theory and Design*, Wiley, New York, 1998, second ed., pp. 183-187.
- [3] R. A. Burberry, *VHF and UHF Antennas*, Peter Peregrinus Ltd., London, 1992, pp. 242-245.
- [4] T. A. Milligan, *Modern Antenna Design*, Wiley-IEEE Press, New York, 2005, second ed., pp. 255.
- [5] ibid, pp. 231-237.
- [6] R. C. Johnson, Ed., *Antenna Engineering Handbook*, McGraw Hill, New York, 1993, third ed., pp. 43-23 - 43-27.
- [7] M. S. Gatti and D. J. Nybakken, "A circularly polarized crossed drooping dipole antenna," *IEEE AP-S International Symposium*, May 1990, vol. 1, pp. 254-257.
- [8] M. du Plessis and J. H. Cloete, "Analysis of three-conductor baluns using the static capacitance matrix," *IEEE AP-S International Symposium*, May 1990, vol. 1, pp. 549-552.
- [9] R. C. Hansen, "Fano limits on matching bandwidth," *IEEE Antennas and Propagation Mag.*, vol. 47, no. 3, June. 2005, pp. 89-90.
- [10]A. R. Lopez, "Review of narrowband impedance-matching limitations," *IEEE Antennas and Propagation Mag.*, vol. 46, no. 4, Aug. 2004, pp. 88-90.
- [11]R. K. Zimmerman, "Crossed dipoles fed with a turnstile network," *IEEE Trans. Microwave Theory Techniques*, vol. 46, no. 12, Dec. 1998, pp. 2151-2156.
- [12]H. Kogo, "Analysis of split coaxial line type balun," *IEEE Trans. Microwave Theory Techniques*, vol. 8, March 1960, pp. 245-246.
- [13]D. M. Pozar, *Microwave Engineering*, Wiley, New Your, 2005, third ed.
- [14]R. E. Collin, "The characteristic impedance of a slotted coaxial line," *IRE Trans. Microwave Theory Techniques*, Jan. 1956, pp. 4-8.
- [15]P. P. Delonge and A. A. Laloux, "Theory of the slotted coaxial cable," *IEEE Trans. Microwave Theory Tech.*, vol. MTT-28, no. 10, Oct. 1980, pp. 1102 – 1107.
- [16]D. H. Kim and H. J. Eom, "Mode matching analysis of axially slotted coaxial cable," *IEEE Antennas and Wireless Propagation Letters*, vol. 4, 2005, pp. 169-171.
- [17]J. Smolarska, "Characteristic impedances of the slotted coaxial line," *IRE Trans. Microwave Theory Techniques*, April 1958, pp. 161-166.
- [18]G. I. Zysman and A.K. Johnson, "Coupled transmission line networks in an inhomogeneous dielectric medium," *IEEE Trans. Microwave Theory Tech.*, vol. MTT-17, no. 10, Oct. 1969, pp. 753 – 759.
- [19]V. K. Tripathi, "Asymmetric coupled transmission lines in an inhomogeneous medium," *IEEE Trans. Microwave Theory Tech.*, vol. MTT-23, no. 9, Sep. 1975, pp. 734 – 739.

- [20]B. Bhat and S. K. Koul, *Stripline-Like Transmission Lines for Microwave Integrated Circuits*, Wiley, New York, 1989.
- [21]O. Zinke und H. B. Brunswig, *Hochfrequenz Technik I*, 5 Auflage, Springer, Berlin, 1995, pp. 194-200.
- [22]R. E. Collin, *Foundations for Microwave Engineering*, IEEE Press, Piscataway, NJ, 2001, second ed.
- [23]T. Iwasaki and K. Tomizawa, "Measurement of S-parameters of balun and its application to determination of complex antenna factor," *2003 IEEE International Symposium on Electromagnetic Compatibility EMC '03*, May 2003, vol. 1, pp. 62-65.
- [24]T. Iwasaki and K. Tomizawa, "Systematic uncertainties of the complex antenna factor of a dipole antenna as determined by two methods," *IEEE Trans. Electromagnetic Compatibility*, vol. 46, no. 2, May 2004, pp. 234-245.
- [25]A. Sommerfeld, *Electrodynamics*, Academic Press, New York, 1952, pp. 177-190.
- [26]K. Maamria and T. Nakamura, "Simple antenna for circular polarization," *IEE Proceedings on Microwaves, Antennas and Propagation*, vol. 139, no. 2, April 1992, pp. 157-158.

TABLE I
PHYSICAL PARAMETERS OF THE DIPOLE AND THE BALUN - NON-MATCHED BALUN. CHARACTERISTIC IMPEDANCES OF THE COUPLED LINE ARE $Z_e = 108\Omega$, $Z_o = 24\Omega$; CHARACTERISTIC IMPEDANCE OF THE NON SPLITTED COAXIAL LINE IS $Z_{coax} = 54\Omega$.

Component	Outer D (2c)	Inner D (2c)	Total length ($l + L$)	McMaster Carr #
Outer coaxial tube	7/16" 11.1 mm	0.3075" 7.8mm	24" 609.6 mm	#8950K68
Inner rod	1/8" 3.2 mm	--	24" 609.6 mm	#8953K41
Free length of dipole wing, D	1/8" 3.2 mm	--	6.69" 170 mm	#8953K41
Slot length from top, l	--	--	6.69" 170 mm	--
Slot width, d	--	--	59 mils 1.5 mm	--
Dipole offset from top, Δ	--	--	0.24" 6 mm	--

TABLE II
PHYSICAL PARAMETERS OF THE DIPOLE AND THE RESONANT $\lambda/4$ BALUN. CHARACTERISTIC IMPEDANCES OF THE COUPLED LINE ARE $Z_e = 59\Omega$, $Z_o = 22.5\Omega$; CHARACTERISTIC IMPEDANCE OF THE NON SPLITTED COAXIAL LINE IS $Z_{coax} = 29.6\Omega$.

Component	Outer D (2c)	Inner D (2c)	Total length ($l + L$)	McMaster Carr #
Outer coaxial tube	7/16" 11.1 mm	0.3075" 7.8 mm	7.02" 178 mm	#8950K68
Inner rod	3/16" 4.8 mm	--	8.98" 228 mm	#8859K155
Free length of dipole wing, D	1/8" 3.2 mm	--	6.14" 156 mm	#8953K41
Slot length from top, l	--	--	6.61" 168 mm	--
Slot width, d	--	--	40-60 mils 1.0-1.5 mm	--
Dipole offset from top, Δ	--	--	0.24" 6 mm	--

TABLE III
PHYSICAL PARAMETERS OF THE DIPOLE AND THE BALUN OPTIMIZED FOR A WIDER BANDWIDTH. CHARACTERISTIC IMPEDANCES OF THE COUPLED LINE ARE THE SAME AS IN TABLE II.

Component	Outer D (2c)	Inner D (2c)	Total length ($l + L$)	McMaster Carr #
Outer coaxial tube	7/16" 11.1 mm	0.3075" 7.81mm	9.06" 230 mm	#8950K68
Inner rod	3/16" 4.8 mm	--	9.06" 230 mm	#8859K155
Free length of dipole wing, D	1/8" 3.2 mm	--	5.98" 152 mm	#8953K41
Slot length from top, l	--	--	7.09" 180 mm	--
Slot width, d	--	--	47 mil 1.2mm	--
Dipole offset from top, Δ	--	--	0.24" 6 mm	--
Teflon tube-inner	5/16"	3/16"	Two rings: 10mm height	#8547K24
Teflon tube-outer	9/16"	7/16"	One ring: 10 mm height	#5033K36

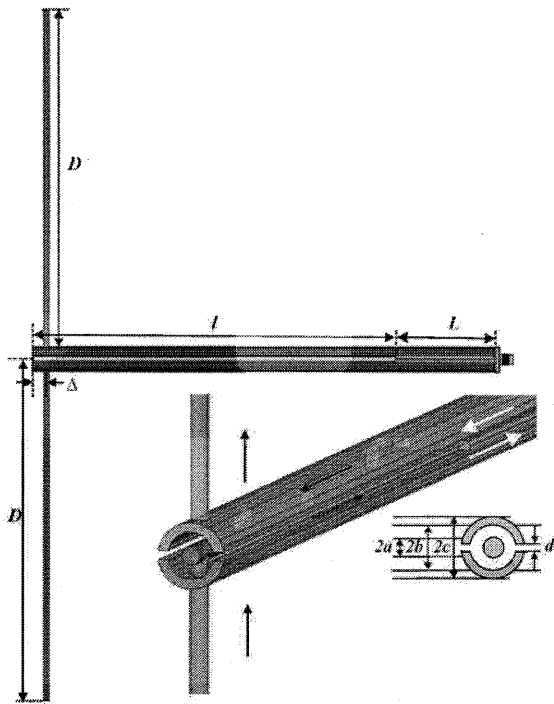


Fig. 1. Split-tube or split-coaxial balun geometry and associated dimensions.

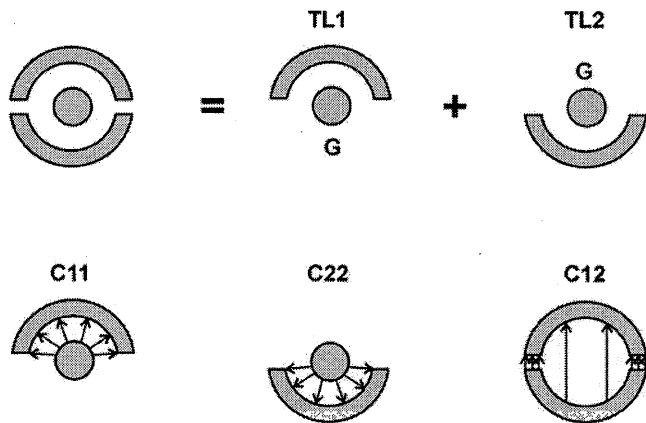


Fig. 2. Top - separation of the splitted coaxial line into two symmetric coupled lines; bottom - static capacitances: self capacitances C_{11} and C_{22} , and mutual capacitance C_{12} .

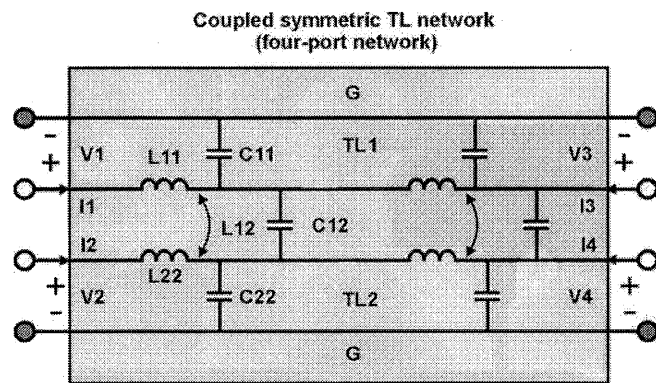


Fig. 3. Coupled symmetric transmission line model of the balun.

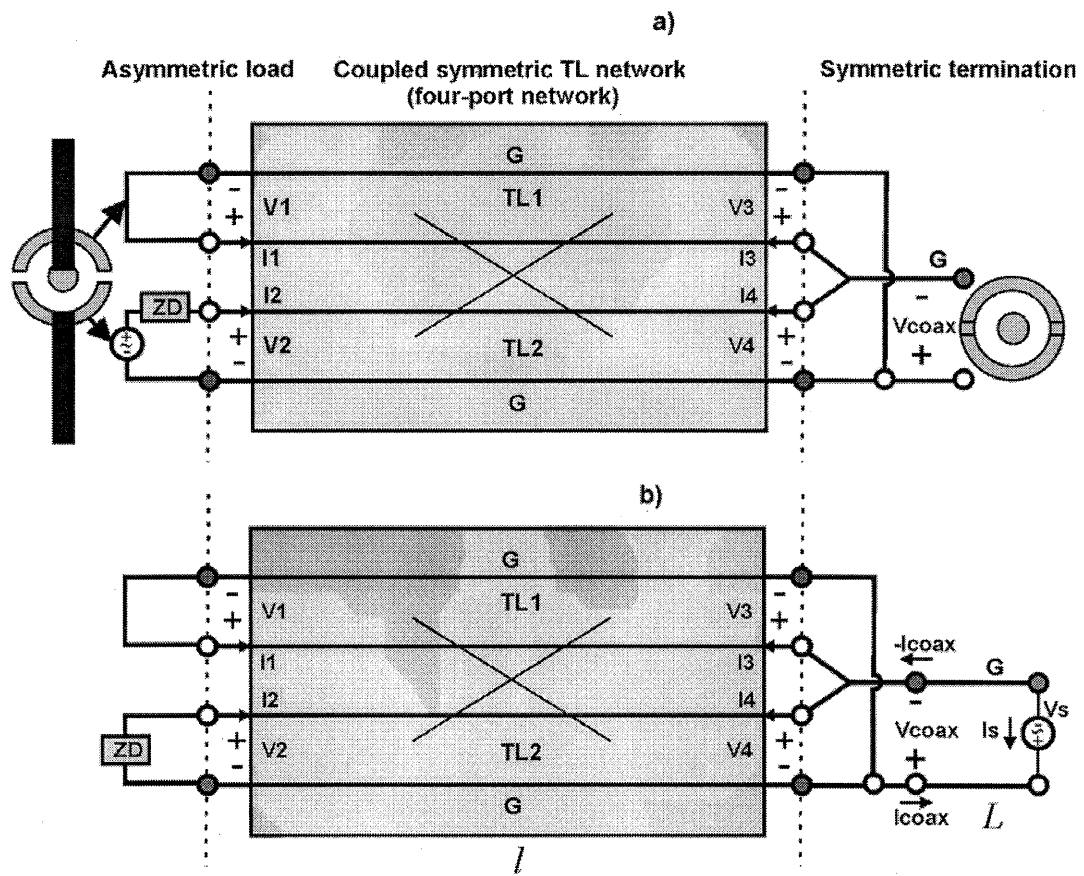


Fig. 4. Two termination schemes: a) - receiving dipole connected to the balun and a coaxial transmission line; b) - termination network used to find the transformed impedance $Z_s = V_s / I_s$ of the dipole with center-fed impedance Z_D connected to a balun of length l and a coaxial TL section of length L .

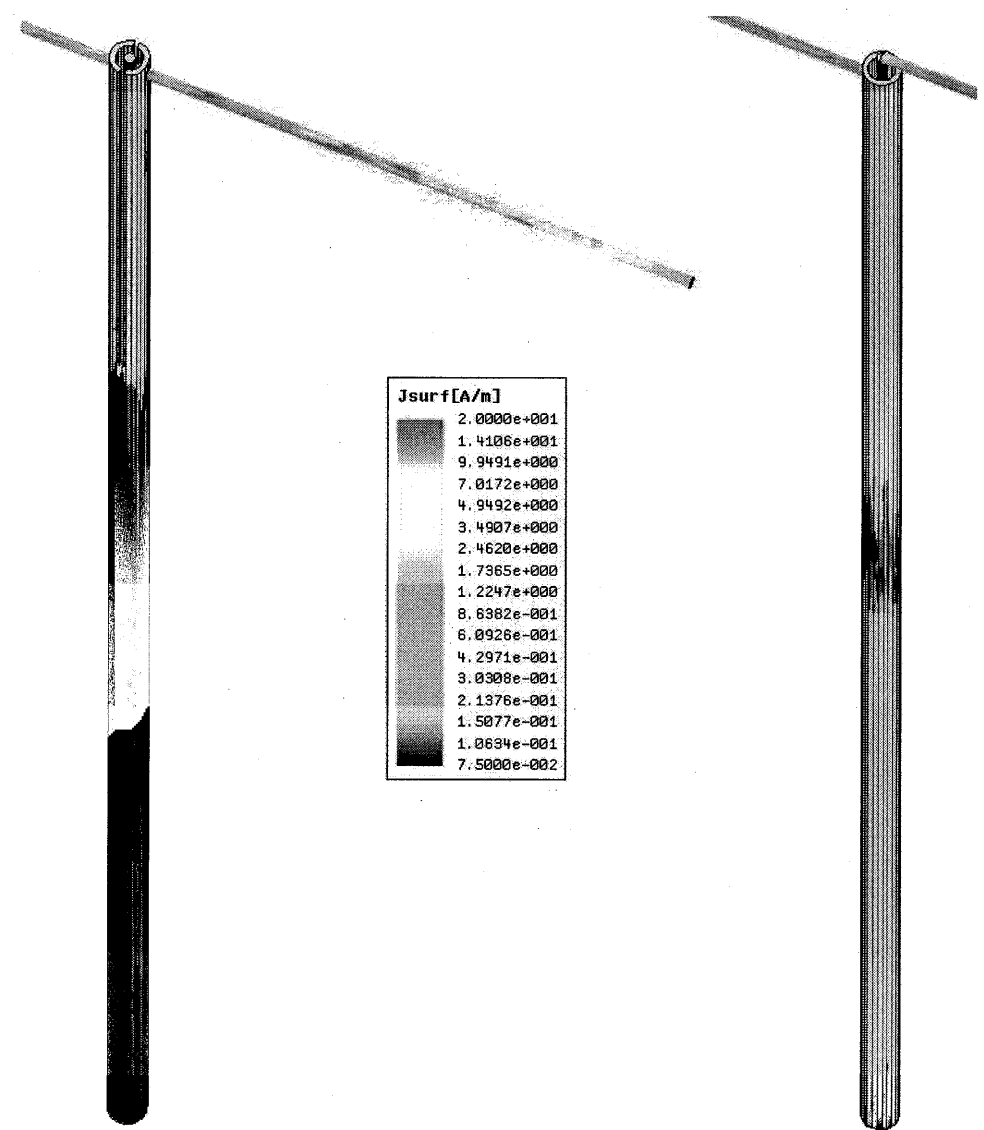


Fig. 5. Surface current density distribution (logarithmic scale) for a dipole with split-coaxial balun (left) and for the unbalanced dipole with the same parameters (Table I)-right.

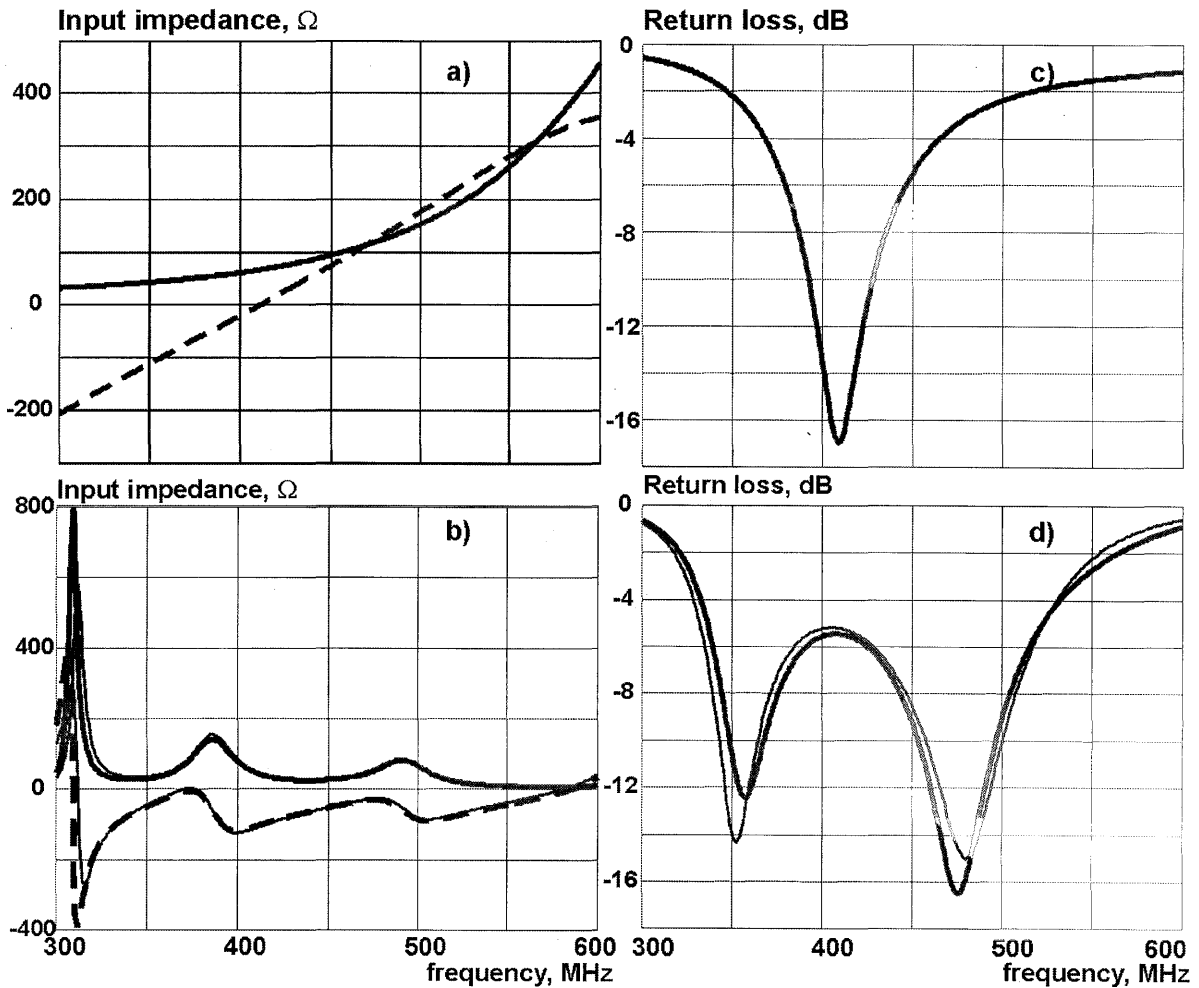


Fig. 6. a) - Impedance behavior of the center-fed test dipole with 170 mm wings; b) - impedance of the same dipole connected to the balun and a continued coaxial line with the characteristic impedance of 54Ω - see Table I. Resistance - solid curve, reactance - dashed curve. c), d) - Return loss for the cases a) and b), respectively. Solutions are obtained using ANSOFT HFSS. Transmission line theory is given by thin curves in Fig. 6b) and 6d).

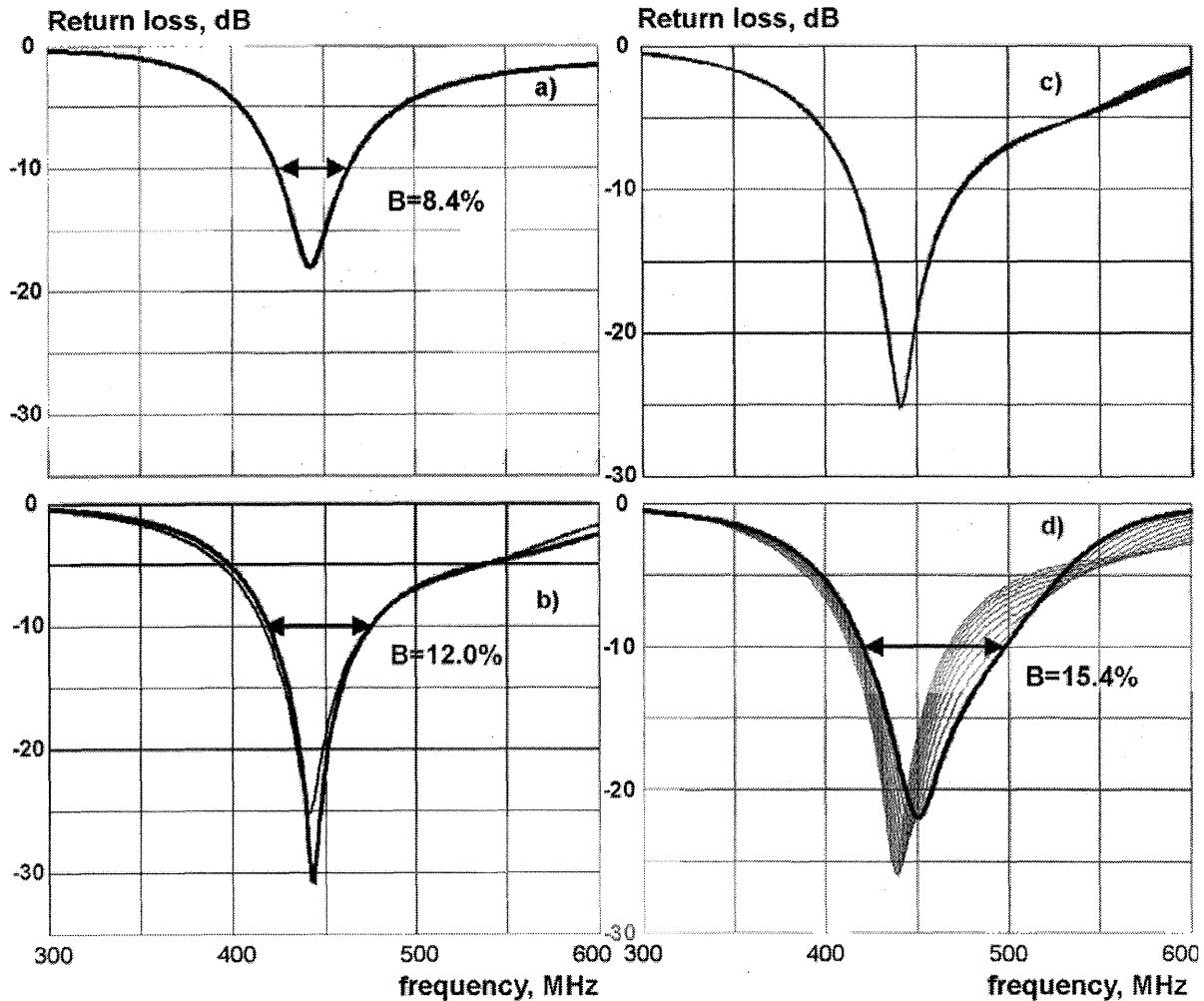


Fig. 7. a) - Return loss of the center-fed dipole with 156 mm wings; b) - return loss of the dipole with balun according to Table II. Thick curve - ANSOFT HFSS solution; thin curve - transmission line model. c) - effect of varying slot width from 1 to 2 mm on the return loss - transmission line model. d) - effect of varying slot length about $\lambda_{Dres} / 4$ by $\pm 10\%$ on the return loss; thick curve corresponds to $\lambda_{Dres} / 4 + 10\%$ - TL model.

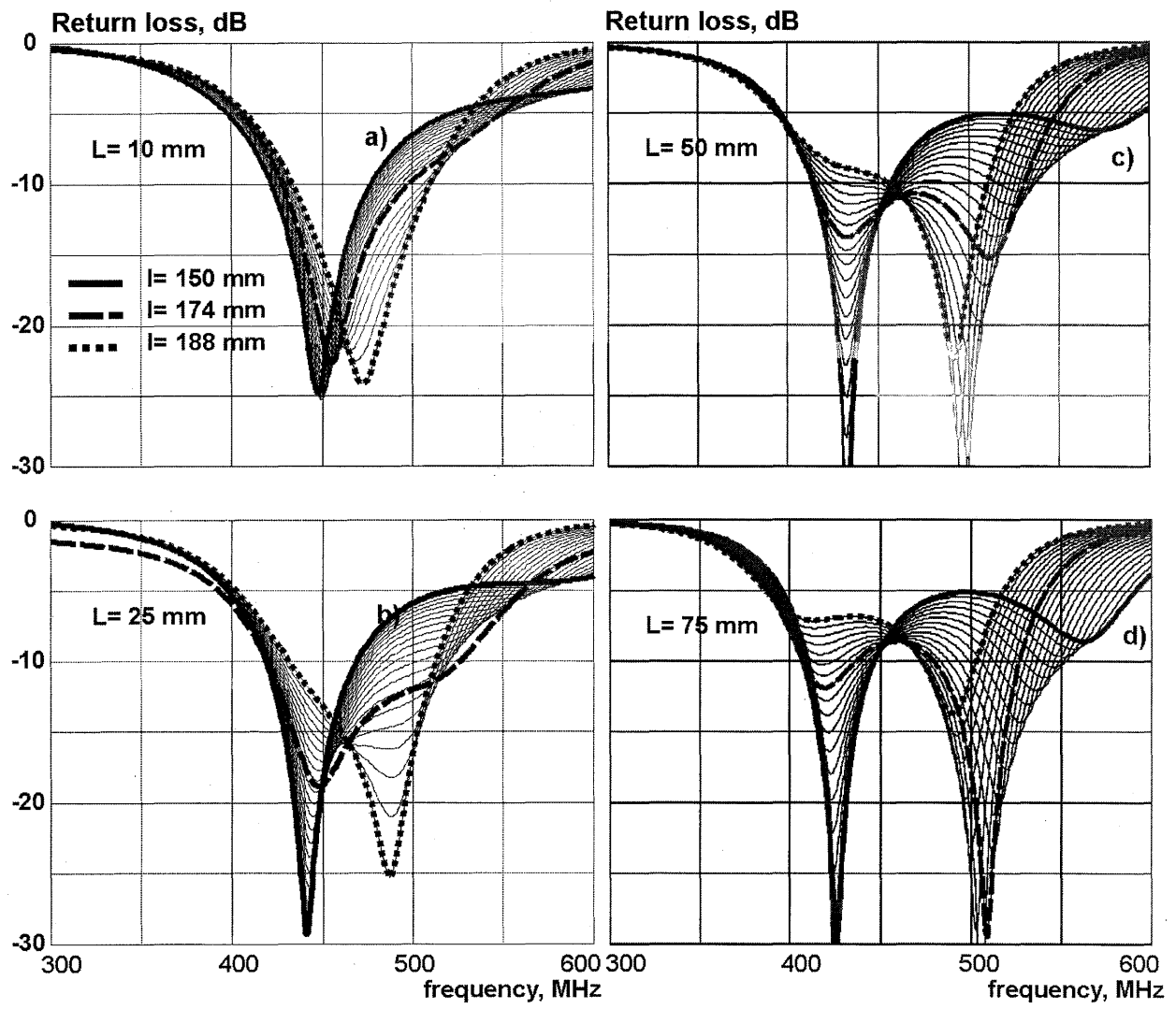


Fig. 8. Development of the second resonance with increasing the length of the non-split transmission line section. a) - $L=10\text{mm}$; b)- $L=25\text{mm}$; c) - $L=50\text{mm}$; d) - $L=75\text{mm}$. In every plot, a sweep is made over the balun length l that varies from 150 to 188mm in 20 uniform steps.

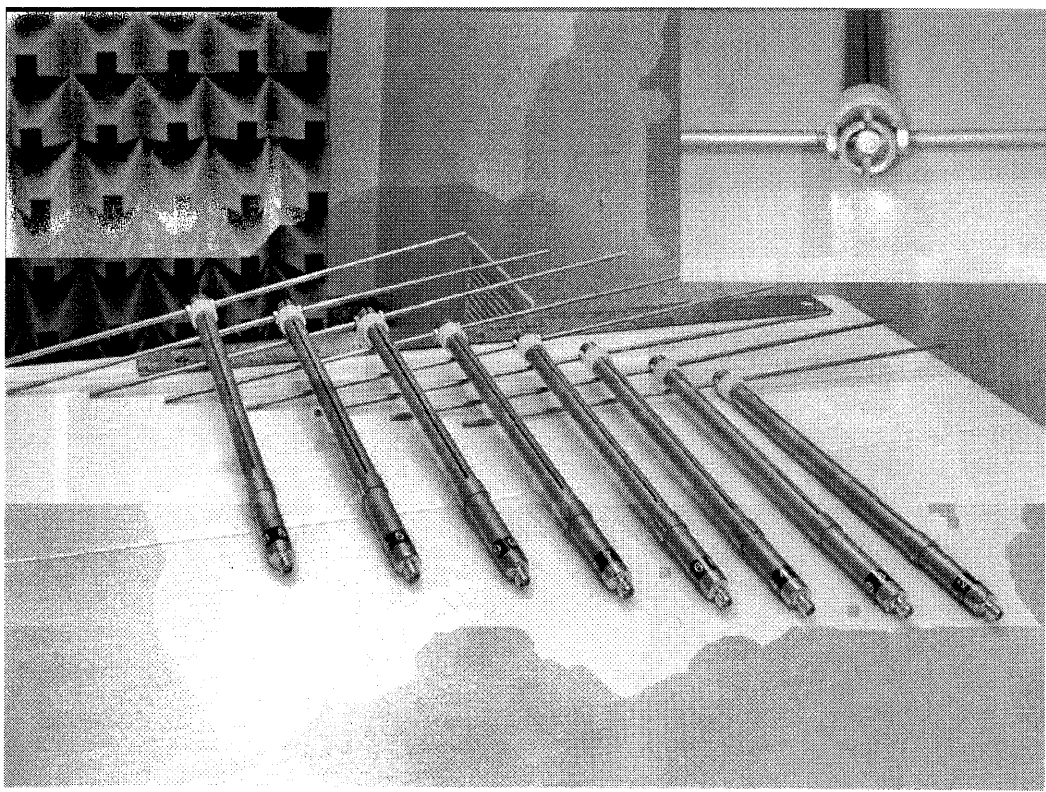


Fig. 9. A series of dipole prototypes built according to data from Table III.

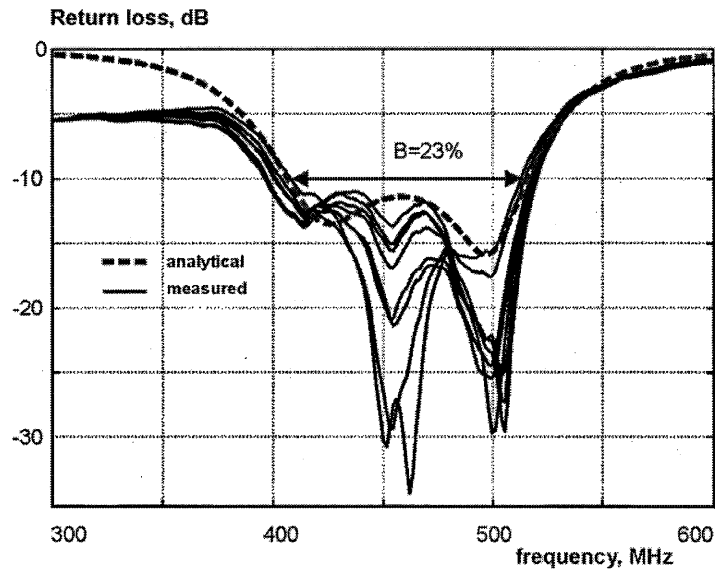


Fig. 10. Return loss measurements for eight 460 MHz dipole prototypes (thin curves) compared to the corresponding analytical TL solution - thick dashed curve. The minimum experimental 10 dB bandwidth is 23%.

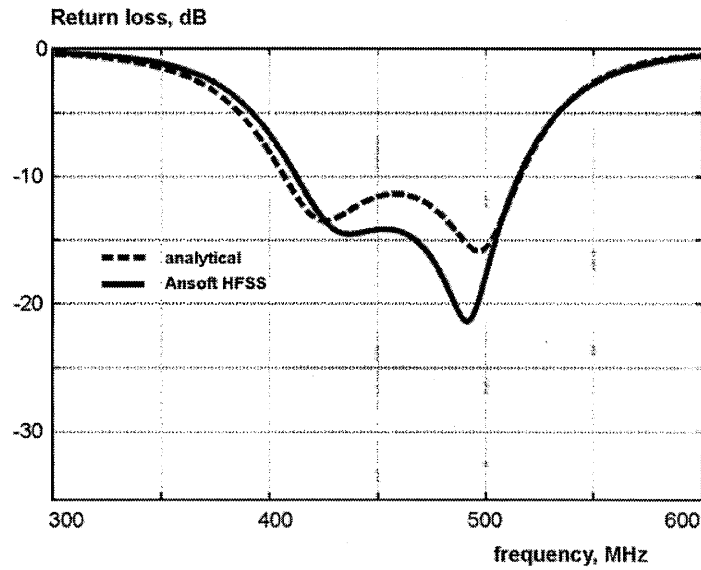


Fig. 11. Analytical TL solution for the dipole prototype vs. the corresponding full-wave ANSOFT HFSS simulation for the complete antenna model.

Progress in the Design of a Small Wideband Antenna

Steven R. Best
MITRE
M/S S230
202 Burlington Road
Bedford, MA 01730
sbest@mitre.org

Abstract: This paper presents the status of our ongoing work in the development of an efficient, broadband, small disk-loaded folded monopole. We first present a brief overview of our prior work in developing a small wideband antenna having a 2:1 VSWR (50Ω) over a 2.5:1 frequency bandwidth. Here, we present an improved design that exhibits a 2:1 VSWR encompassing a 3:1 frequency bandwidth. In addition to our consideration of the antenna's impedance bandwidth, we describe bandwidth limitations in terms of the antenna's radiation pattern characteristics. We also examine the relationship between the antenna's quality factor (Q) and matched VSWR bandwidth. We show that the Q of the antenna does not violate the lower bound on Q , often referred to as the Chu limit. However, we show that at some frequencies, the antenna's matched VSWR bandwidth is greater than would be expected from the inverse of Q , illustrating that the inverse relationship between bandwidth and Q does not hold over the entire bandwidth. As part of our work in small disk-loaded folded monopoles, we describe interim results on simulating the performance properties of the Goubau antenna. Finally, we describe improved feed structure arrangements designed with the objective of improving the antenna's radiation pattern properties at the upper regions of the operating band.

1. BACKGROUND

At the 2004 *Antenna Applications Symposium*, we presented a discussion of our initial work towards the development of a small disk-loaded folded monopole [1]. Our work in this area evolved from our design efforts in electrically small antennas and the study of antenna quality factor and bandwidth. One of the antennas commonly referenced as a low Q , wideband antenna is the multi-element monopole antenna developed by G. Goubau and F. Schwering [2] – [4]. The multi-element Goubau antenna is depicted in Figure 1. It operates with a maximum 2:1 VSWR (with respect to 50Ω) over a frequency range of approximately 470 – 890 MHz, a 1.9:1 frequency bandwidth.

Our design objective was, and remains the development of a small antenna providing a maximum 2:1 VSWR (with respect to 50Ω) over a 3:1 or greater frequency band. At the same time, the design is expected to exhibit high radiation efficiency (> 90%) and $\lambda/4$ monopole-like radiation patterns over the entire operating band. Our design approach has been to use the disk-loaded folded monopole antenna concept [5], which employs a disk (top-hat) for capacitive loading, decreasing the operating frequency of the antenna, and multiple connections between the disk and ground (the folding implementation), increasing the impedance of the antenna [6]. These design techniques were embodied within the Goubau antenna. Another objective was to

design a disk-loaded folded monopole having dimensions that do not exceed those of the Goubau antenna, which has a height of 4.3 cm and an overall disk diameter of 12.3 cm.

One design implementation [1], providing a 2.1 *VSWR* over a frequency range of 554 – 1400 MHz (a 2.52:1 bandwidth), is depicted in Figure 2. The antenna has a height of 4.3 cm and an overall disk diameter of 12.3 cm. The feed point *VSWR*, simulated using Microwave Studio [7] is presented in Figure 3. This represents all of performance data presented in the 2004 paper [1].

2. ADDITIONAL PERFORMANCE EVALUATION OF EXISTING DESIGN

Since the 2004 paper, the antenna depicted in Figure 2 was fabricated using thin brass shim-stock. The antenna was fabricated at full-scale and is depicted in Figure 4. The antenna was mounted on a 4-foot square ground plane and its impedance was measured using an HP-8510 vector network analyzer. A comparison of simulated and measured impedance is presented in Figure 5. As evident in Figure 5, there is excellent agreement between the simulated and measured results. No modification of initial fabrication of the antenna was required. The fabricated antenna exhibited a 2:1 *VSWR* over a frequency range of 539 – 1399 MHz, a 2.59:1 frequency bandwidth.

The important performance characteristics remaining to consider are the antenna's radiation patterns over the entire operating bandwidth. These radiation patterns were not presented in the 2004 paper and were subsequently simulated using Microwave Studio. Given the fact that the antenna structure is not symmetric about the feed point, we expected significant pattern degradation at the upper end of the operating band. The simulated radiation patterns at 500 MHz, 1000 MHz and 1400 MHz are presented in Figure 6. The radiation pattern at 500 MHz exhibits a variation of approximately 1.5 dB in azimuth at the horizon. The substantial pattern variation (degradation) at the upper frequencies is evident from the results presented in Figure 6.

3. DESIGN VARIATIONS: BANDWIDTH IMPROVEMENT

Although we recognized that the physical design approach limits the antenna performance in terms of the radiation pattern degradation at the upper portion of the frequency band, we decided to proceed with further design variations with the intent of increasing the operating bandwidth. This approach was taken as we were specifically interested in understanding the relationship between *Q* and bandwidth for small wideband antennas, particularly those exhibiting multiple impedance resonances within their operating band.

The significant design variables associated with this antenna are depicted in Figure 7. These design variables include the dimensions of the cut-outs in the feed-arm (Cut-Out A) and top-disk (Cut-Out B), [*note: the dimensions of both cut-outs determine the number and radius of the impedance loops on the Smith Chart for the impedance of the antenna*]; the width of the bottom of the feed-arm (*w*) and the distance between the ground plane and the bottom of the feed-arm (*d*) [*note: the dimensions w and d determine the effective parallel matching capacitance at the feed point*]; the height or length of the feed-slots, *h* [*note: the dimension h the determines the*

series matching inductance at the feed point]; and finally, the width of the single folding connection to ground (W) and the spacing between the folding connection and the feed-arm (s). The antenna's height and top-disk diameter are not considered as design variables since the overall size of the antenna is to remain fixed.

Adjusting these design variables can significantly affect the shape of the impedance curve, particularly the number and radius of the impedance loops on the Smith Chart. The number and location of these loops can be adjusted so as to set the number of resonances within the operating band. In many instances, these adjustments do little to impact the overall operating bandwidth of the antenna. The impedance and return-loss of one example configuration are presented in Figures 8 and 9, respectively. While the impedance behavior is substantially different than that presented in Figure 5, the operating bandwidth is remarkably similar. This configuration exhibits a 2:1 *VSWR* over a frequency range of 536 – 1366 MHz, a 2.55:1 frequency bandwidth.

With further adjustment of these design variables, a configuration was developed that exhibits a 2:1 *VSWR* over an approximate 3:1 frequency band. The impedance and *VSWR* of this configuration are presented in Figures 10 and 11, respectively. This configuration exhibits a 2:1 *VSWR* over a frequency range of 550 – 1632 MHz, a 2.97:1 frequency bandwidth.

4. QUALITY FACTOR AND BANDWIDTH¹

The study of the antenna configuration exhibiting an approximate 3:1 frequency bandwidth led to the study of the relationship between the antenna's Q and matched *VSWR* bandwidth. Much of this material was presented at the 2005 APS Symposium [8]-[9] and is summarized here as it is considered to be an important part of our work in the design and development of these antennas. We begin with a discussion of Q and bandwidth.

The exact quality factor of the tuned antenna, $Q(\omega_0)$, is defined in terms of the ratio of internal energy, $W(\omega_0)$, and accepted power, $P_A(\omega_0)$, as [10]

$$Q(\omega_0) = \frac{\omega_0 |W(\omega_0)|}{P_A(\omega_0)} \quad (1)$$

which has been shown to be approximately equal to [10]

$$Q(\omega_0) \approx Q_Z(\omega_0) = \frac{\omega_0}{2 R(\omega_0)} |Z'_0(\omega_0)| \quad (2)$$

where

¹ Much of this section is taken from work presented at the 2005 IEEE APS Symposium [8]-[9] and is presented here since it is an important part of the ongoing work in the development and study of these antennas.

$$|Z'_0(\omega_0)| = \sqrt{R'(\omega_0)^2 + \left(X'(\omega_0) + \frac{|X(\omega_0)|}{\omega_0} \right)^2} \quad (3)$$

where $R'(\omega)$ and $X'(\omega)$ are the frequency derivatives of the untuned antenna's resistance and reactance, respectively.

In most practical applications, we are generally interested in defining and characterizing the antenna's operating bandwidth. For this reason, we seek a definition of bandwidth that is related to Q over a wide range of frequencies. A suitable definition of bandwidth for this purpose is matched *VSWR* bandwidth, $FBW_V(\omega_0)$, where the *VSWR* (s) of the tuned antenna is determined under the condition that the characteristic impedance, Z_{CH} , of the transmission line connecting the antenna to the matched source is equal to the antenna's feed-point resistance at the tuned frequency: $Z_{CH} = R(\omega_0)$. Matched *VSWR* bandwidth is equal to

$$FBW_V(\omega_0) = \frac{\omega_+ - \omega_-}{\omega_0} \quad (4)$$

where ω_+ and ω_- are the frequencies above and below ω_0 , respectively, where the *VSWR* is equal to s . Matched *VSWR* bandwidth and Q are related as given in [3]

$$Q(\omega_0) \approx Q_B(\omega_0) = \frac{2\sqrt{\beta}}{FBW_V(\omega_0)} \quad (5)$$

where

$$\sqrt{\beta} = \frac{s-1}{2\sqrt{s}} \leq 1 \quad (6)$$

One of the significant points associated with antenna Q is that there exists a fundamental lower bound on Q defined in terms of the antenna's occupied volume and the operating frequency. Given that Q and matched *VSWR* bandwidth are inversely related, a lower bound on Q implies that there exists a corresponding upper bound on matched *VSWR* bandwidth that can be achieved as a function of antenna size. The lower bound on Q is given by [11]

$$Q_{lb} = \eta \left(\frac{1}{(ka)^3} + \frac{1}{ka} \right) \quad (7)$$

where η is the radiation efficiency of the antenna, k is the free space wave number, $2\pi/\lambda$, and a is the radius of an imaginary sphere circumscribing the maximum dimension of the antenna. The relationships in Equations (2) and (5) were derived in [10] under the assumptions that the $\frac{1}{2}$ -

power matched *VSWR* bandwidth ($s = 5.828:1$) is not too large and that the antenna exhibits a single resonance and *VSWR* minimum within its defined operating band.

If the electrically small tuned antenna exhibits closely spaced resonances or multiple *VSWR* minimums within its operating bandwidth, the relationships between Q , Q_Z and Q_B (derived from the inverse of exact matched *VSWR* bandwidth) expressed in Equation (2) and (5) may not hold [8]-[10] particularly for values of $s \gg 1$. In many instances, a value of $s \rightarrow 1$ in Equation 6 can be chosen such that the value of Q_Z closely approximates Q_B . However, this does not guarantee that the value of either Q_Z or Q_B closely approximates the value of Q given by Equation 1.

To illustrate some of these points here, we calculate the Q [approximated by Q_Z , Equation (2)] of the antenna configuration having the impedance presented in Figure 10 and we compare it to the lower bound. This comparison is presented in Figure 12. While the Q of the antenna, approximated by Q_Z , closely approaches the lower bound, there is no frequency over the operating band where it is less than the lower bound. Next, we approximate the Q of the using Q_B , defined in Equation (5). A comparison of Q_Z , Q_B and the lower bound on Q is presented in Figure 13.

From Figure 13, we see that in some frequency regions, particularly at the lower end of the operating band, there is very good agreement between Q_Z and Q_B for values of s close to 1 ($s = 1.5$ and 2). At the upper end of the operating band the very good agreement between Q_Z and Q_B no longer holds, even for the lower values of s . This illustrates that the inverse relation between Q and matched *VSWR* bandwidth in these frequency regions no longer holds, particularly for higher values of s . What is of most interest is the relationship between inverse bandwidth and the lower bound on Q . If the inverse relationship between Q and bandwidth does not hold, we are interested in exploring whether or not a bandwidth can be achieved that exceeds the bandwidth limit implied from the lower bound on Q .

5. MODELING THE GOUBAU ANTENNA

Another aspect of our work in the development of small wideband disk-loaded monopoles is our understanding the performance and design variables of the Goubaud antenna better. While we have done some preliminary work in this regard, we have not yet put substantial effort towards this objective. To date, we have constructed a preliminary model of the Goubaud antenna in Microwave Studio, as depicted in Figure 14. Preliminary VSWR calculations do not match the published measurements. Preliminary pattern calculations, presented in Figure 15, indicate good pattern behavior at the low end of the operating band (500 MHz) and some pattern degradation occurring near the upper end of the operating band (1000 MHz). Our modeling of the Goubaud antenna is in its preliminary phase and much work is expected in refining the model, allowing us to gain more confidence in our simulation results.

6. DESIGN VARIATIONS: RADIATION PATTERN IMPROVEMENT

In conjunction with our work on quality factor and bandwidth, and our modeling of the Goubau antenna, the other area where we recognize the substantial need for improvement is in the radiation pattern properties of these antennas in the upper regions of the operating band. All of the antennas designed to date exhibit pattern degradation at the upper ends of the band due to the asymmetry of the antenna structure relative to the feed point. To improve the radiation pattern properties of the antenna we are in the process of re-designing the antenna to first make it symmetric, and then, as necessary modify the structure to optimize the impedance bandwidth. This work is in its beginning stage and we have only very preliminary results to present at this time.

An example of a symmetric antenna that we are considering is depicted in Figure 16. This antenna is specifically designed so that the feed point is at the center of the antenna structure and that all components within the antenna design are implemented symmetrically about the feed point. The antenna height is 4.3 cm and the top disk diameter is 12.3 cm. The return-loss for this antenna is presented in Figure 17 and radiation patterns are presented in Figure 18. The antenna exhibits very reasonable pattern performance over the entire frequency range from 500 MHz through 1500 MHz. The antenna exhibits a 2:1 VSWR over a 2.18:1 frequency bandwidth and a 3:1 VSWR over a 2.47:1 frequency bandwidth. Work is underway to increase the operating bandwidth.

7. DISCUSSION

We have presented a brief overview of our progress in the development of a simple disk-loaded folded monopole antenna. Our physical design objectives are to maintain a maximum antenna height of 4.3 cm and a maximum overall diameter of 12.3 cm, matching the profile of the Goubau antenna. Our performance design objective is to achieve a 2:1 *VSWR* frequency bandwidth of 3:1 or greater, an efficiency in excess of 90% and monopole-like radiation patterns over the entire bandwidth. Here we discussed preliminary results in terms of achieving a 2:1 maximum *VSWR* over an approximate 3:1 frequency bandwidth. Due to the physical configuration of the antenna, the radiation patterns suffer severe degradation at the upper ends of the frequency bandwidth. We also discussed results associated with our study on the relationship between quality and bandwidth, illustrating that the inverse relationship between *Q* and matched *VSWR* bandwidth does not always hold. Finally, we very briefly discussed our ongoing work in modeling of the Goubau antenna and the fact that we are working to improve the radiation patterns of the antenna at higher frequencies. Preliminary results were presented for each of these efforts.

8. REFERENCES

- [1] S. R. Best, "Small broadband disk loaded folded monopole antennas," *Proceedings of the 2004 Antenna Applications Symposium*, September 2004.
- [2] G. Goubau, "Multi-element monopole antenna," *Proceedings of the ECOM-ARO Workshop on Electrically Small Antennas*, Fort Monmouth, NJ, pp. 63-67, October 1976.

- [3] G. Goubau, N. N. Puri and F. Schwering, "Diakoptic theory for multielement antennas," *IEEE Trans. Antennas Propag.*, Vol. 30, No. 1, pp. 15-26, January 1982.
- [4] C. H. Friedman, "Wide-band matching of a small disk-loaded monopole," *IEEE Trans. Antennas Propag.*, Vol. 33, No. 10, pp. 1142-1148, October 1985.
- [5] E. W. Seeley, "An experimental study of the disk loaded folded monopole," *IRE Trans. Antennas Propag.*, pp 27 – 28, January 1956.
- [6] R. Guertler, "Impedance transformation in folded dipoles," *Proceedings of the IRE*, Vol. 38, pp. 1042-1047, September 1950.
- [7] Microwave Studio simulation software, www.cst.de
- [8] S. R. Best, "Bandwidth and the lower bound on Q for small wideband antennas," *2006 IEEE APS International Symp.*, Albuquerque, NM, Paper 157.10, July 2006.
- [9] S. R. Best, "The inverse relationship between quality factor and bandwidth in multiple resonant antennas," *2006 IEEE APS International Symp.*, Albuquerque, NM, Paper 157.4, July 2006.
- [10] A. D. Yaghjian and S. R. Best, "Impedance, bandwidth and Q of antennas," *IEEE Trans. Antennas and Propagat.*, Vol. 53, No. 4, pp. 1298- 1324, Apr. 2005.
- [11] J. S. McLean, "A re-examination of the fundamental limits on the radiation Q of electrically small antennas," *IEEE Trans. Antennas Propagat.*, Vol. 44, pp. 672-676, May 1996.

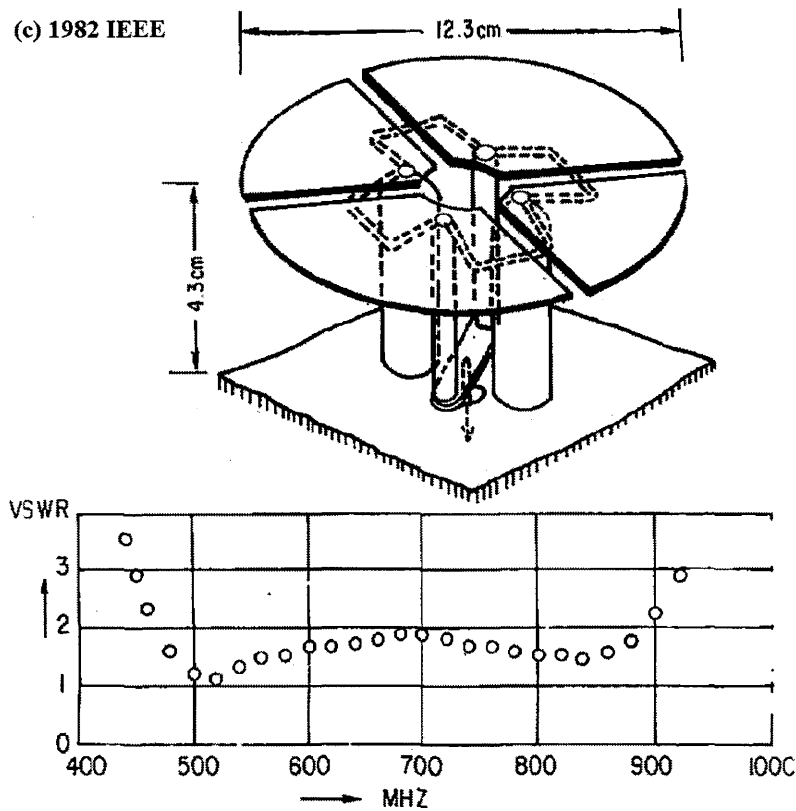


Figure 1. Depiction and measured *VSWR* of the Goubau multi-element monopole antenna [2]. The Goubau antenna exhibits a 2:1 *VSWR* over a 1.9:1 frequency bandwidth. The antenna has a height of 0.067λ at its lowest operating frequency.

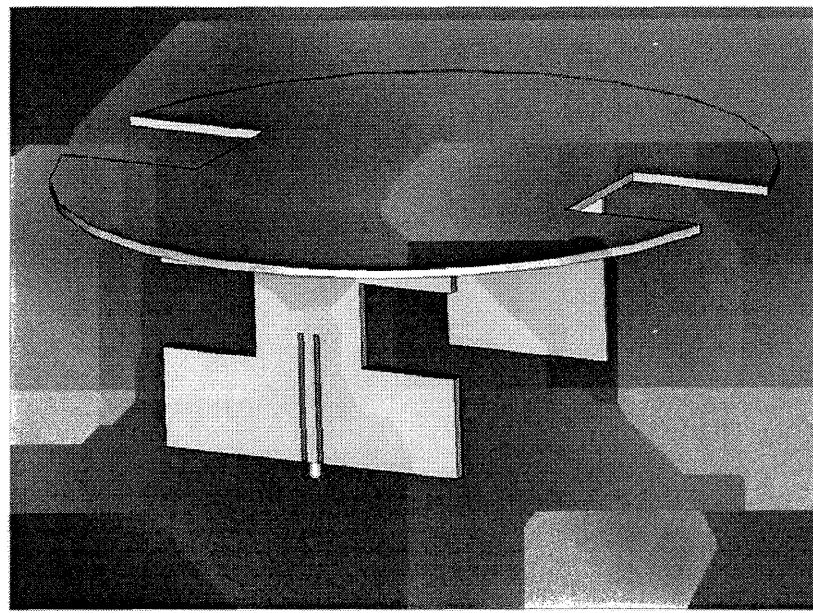


Figure 2. Depiction of the disk-loaded folded monopole design presented in the 2004 paper [1]. The antenna has a height of 4.3 cm and a disk diameter of 12.3 cm.

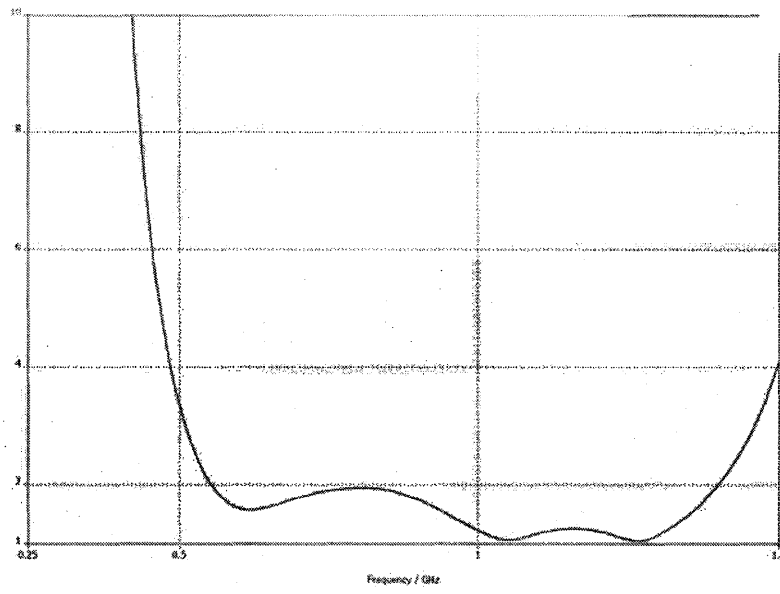


Figure 3. Simulated *VSWR* of the disk-loaded folded monopole design depicted in Figure 2. The antenna exhibits a 2:1 *VSWR* (simulated) over a frequency range of 554 – 1400 MHz, a 2.52:1 frequency bandwidth.

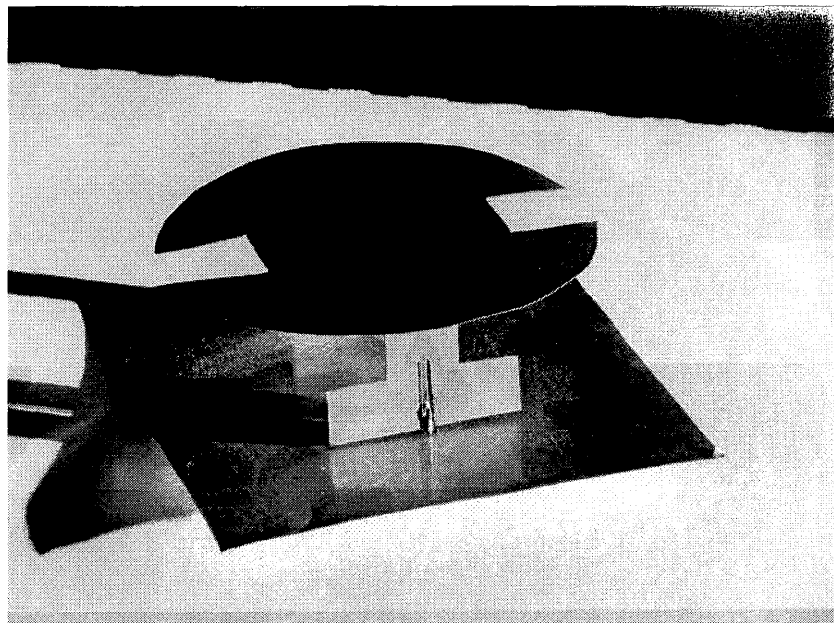


Figure 4. Photograph of the full-scale fabrication of the disk-loaded folded monopole antenna depicted in Figure 2.

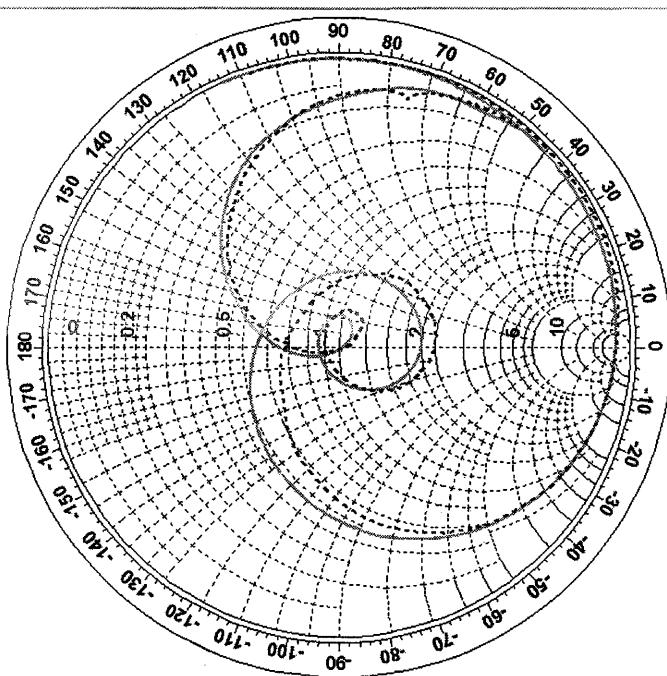


Figure 5. A Comparison of simulated and measured impedance for the disk-loaded folded monopole design depicted in Figure 4. The antenna exhibits a 2:1 VSWR (measured) over a frequency range of 539 – 1399 MHz, a 2.59:1 frequency bandwidth.

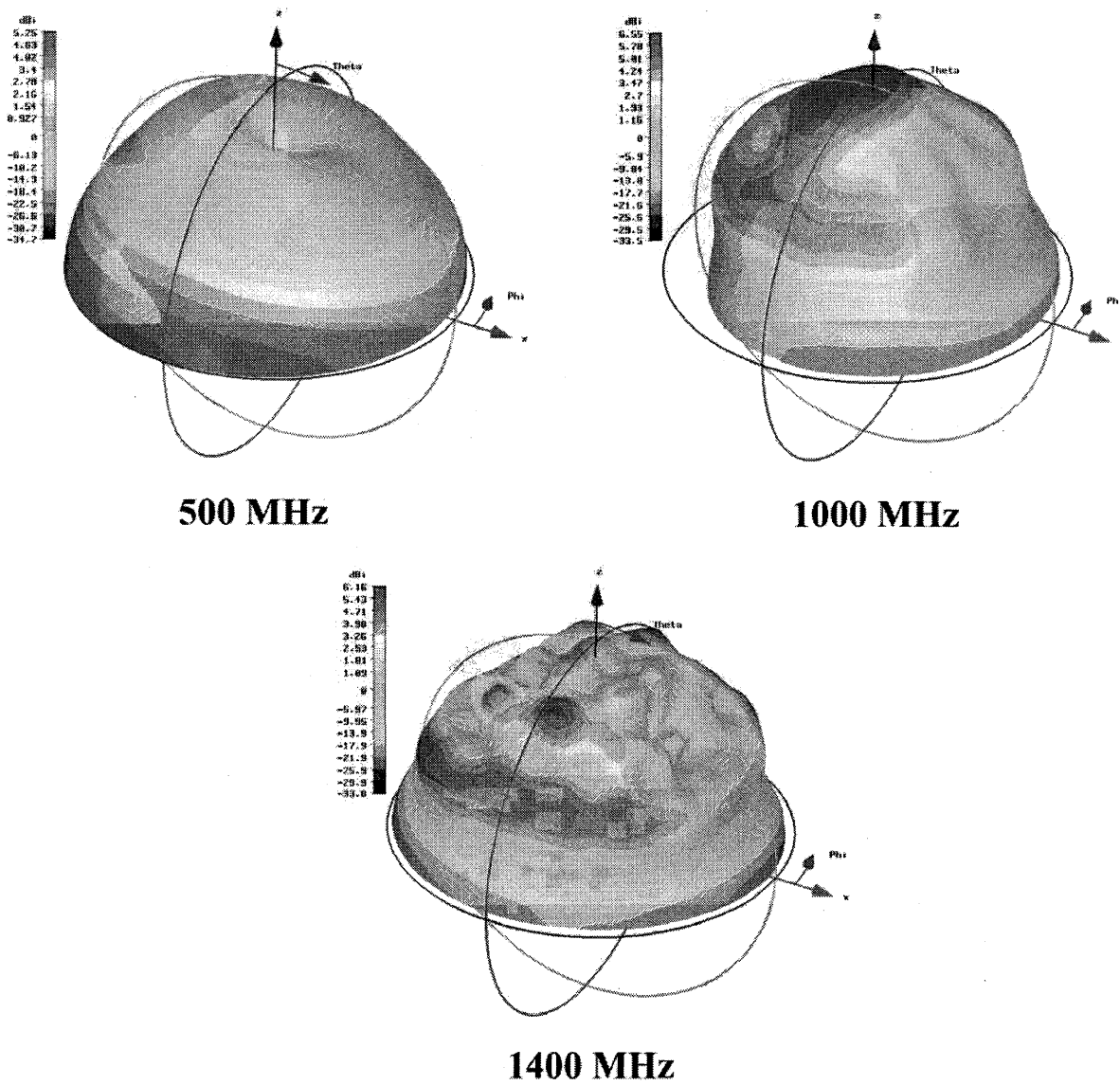


Figure 6. Simulated radiation patterns of the disk-loaded folded monopole antenna depicted in Figure 2 at 500 MHz, 1000 MHz and 1400 MHz.

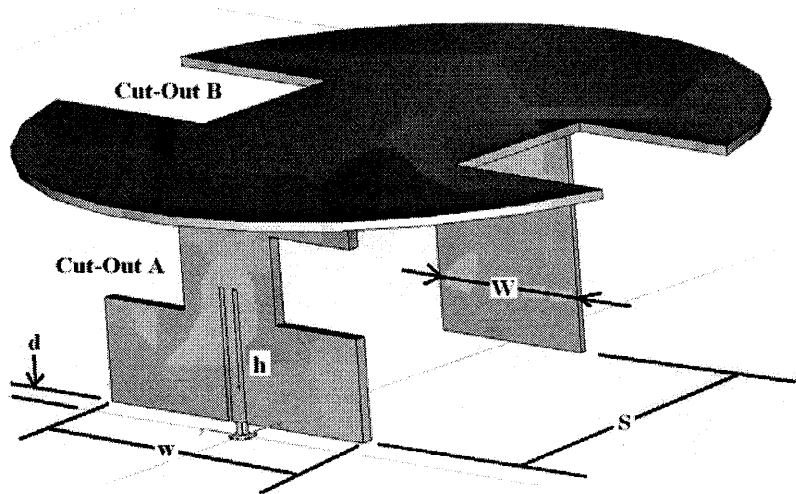


Figure 7. Depiction of the design variables for the disk-loaded folded monopole antenna.

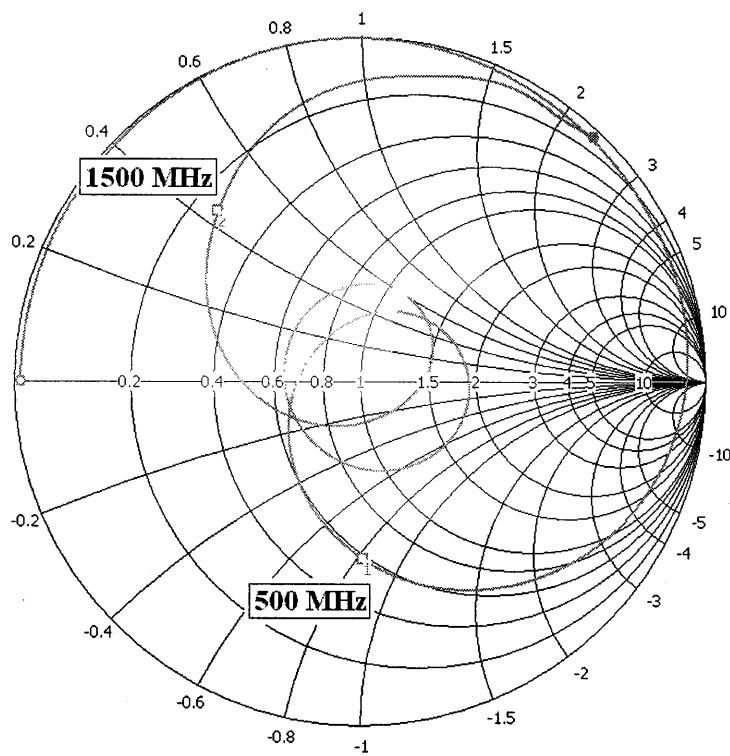


Figure 8. The impedance of one configuration shown to illustrate the difference in the shape of the impedance curve achievable by adjusting the dimensions of the design variables. This impedance plot should be compared to the impedance plot of Figure 5.

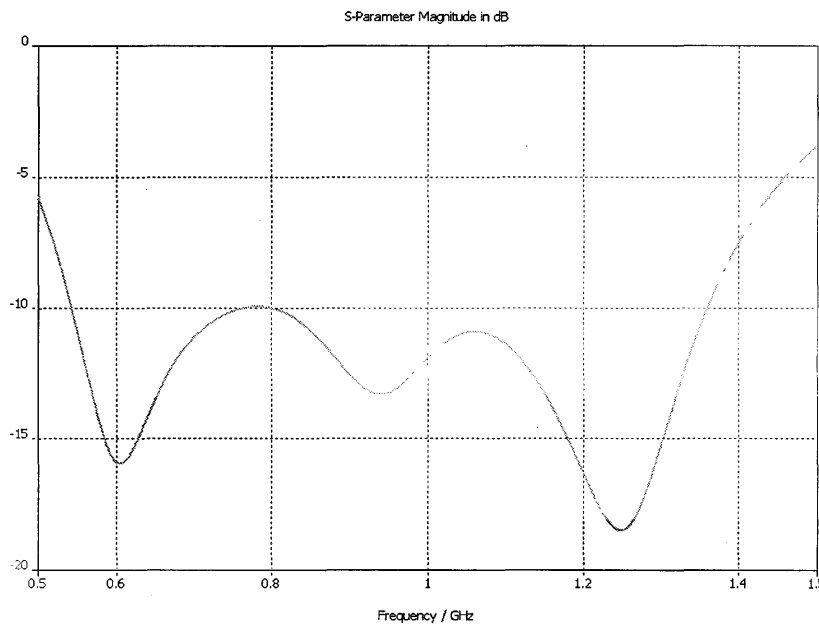


Figure 9. Return loss for the impedance data presented in Figure 8. This configuration exhibits a 2:1 *VSWR* over a frequency range of 536 – 1366 MHz, a 2.55:1 frequency bandwidth.

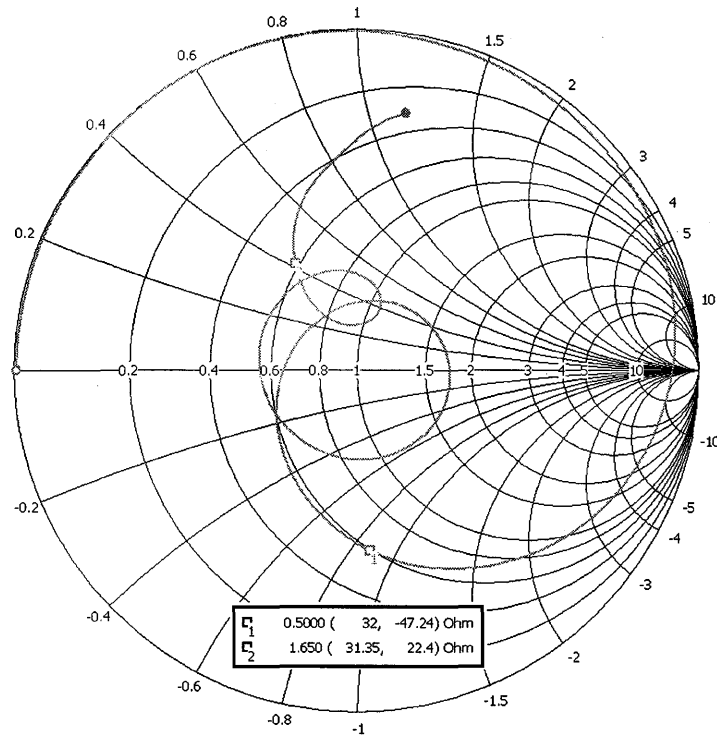


Figure 10. The impedance of the disk-loaded folded monopole configuration exhibiting an approximate 3:1 frequency bandwidth.

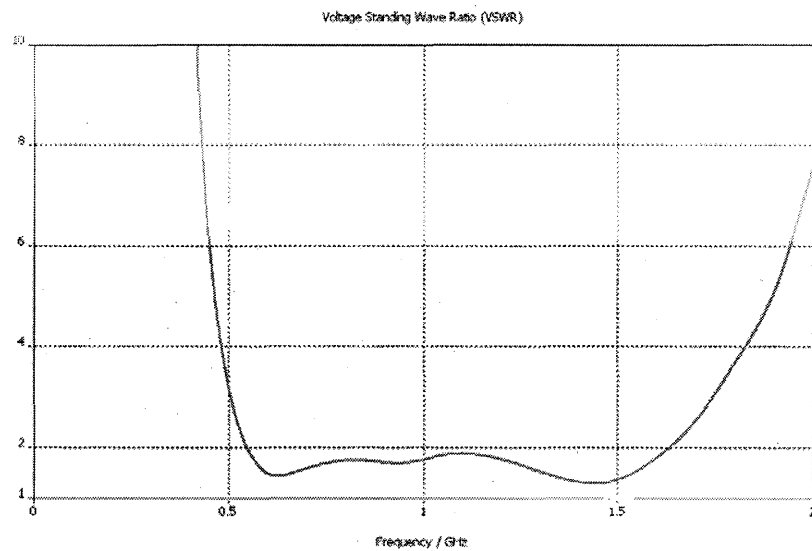


Figure 11. *VSWR* for the impedance data presented in Figure 10. This configuration exhibits a 2:1 *VSWR* over a frequency range of 550 – 1632 MHz, a 2.97:1 frequency bandwidth.

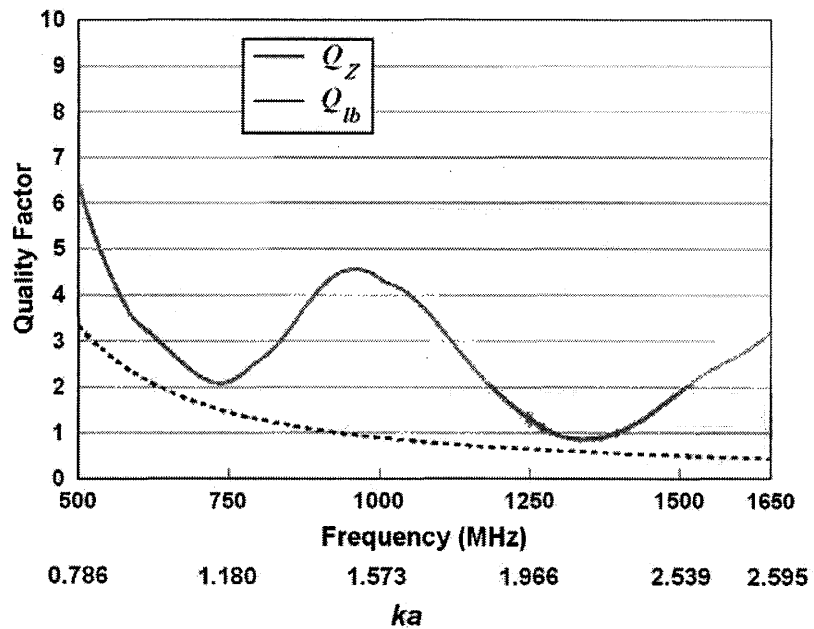


Figure 12, Comparison of Q_Z and the lower bound on Q for the disk-loaded folded monopole antenna exhibiting a frequency bandwidth of approximately 3:1. The impedance of the antenna is presented in Figure 10.

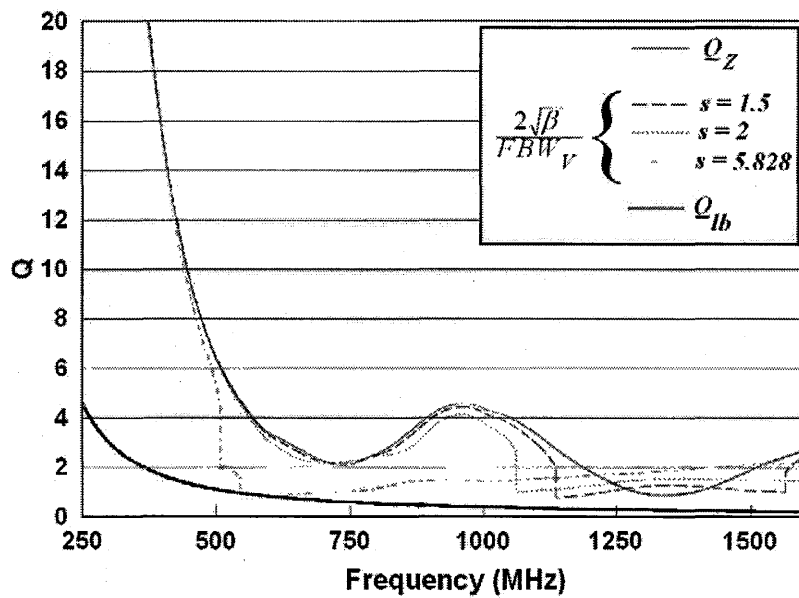


Figure 13, Comparison of Q_Z , Q_B and the lower bound on Q for the disk-loaded folded monopole antenna exhibiting a frequency bandwidth of approximately 3:1. The impedance of the antenna is presented in Figure 10.

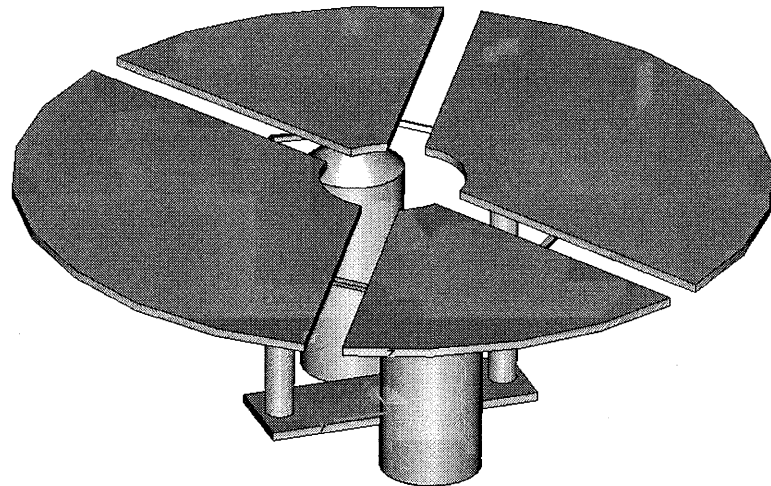
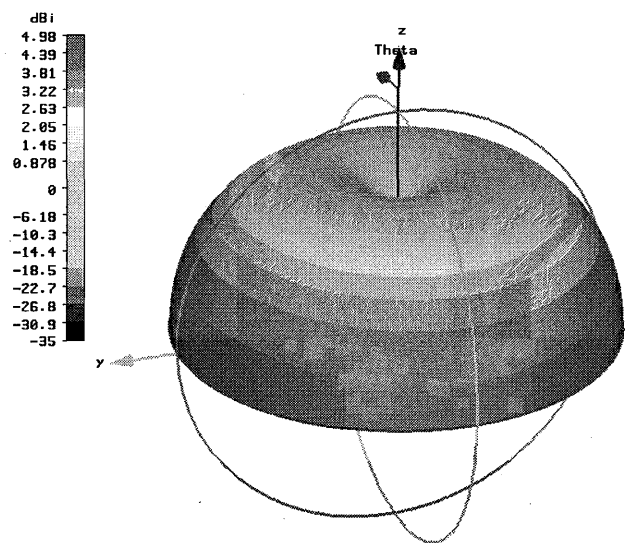
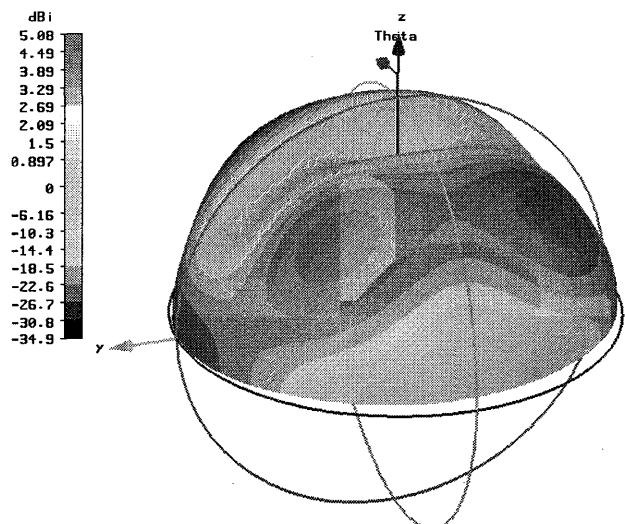


Figure 14. Depiction of the (one) Microwave Studio implementation of the Goubau antenna.



500 MHz



1000 MHz

Figure 15. Some preliminary pattern predictions for the Goubau antenna at 500 MHz and 1000 MHz. Further refinement of the Microwave Studio model is required before we have sufficient confidence in our model.

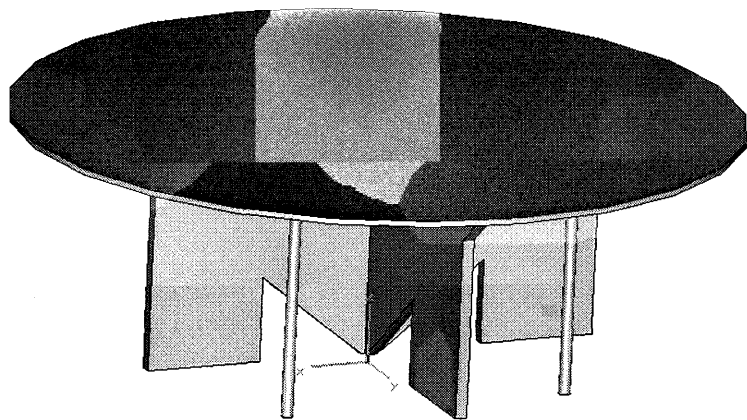


Figure 16. Preliminary disk-loaded folded antenna design having a symmetric structure.

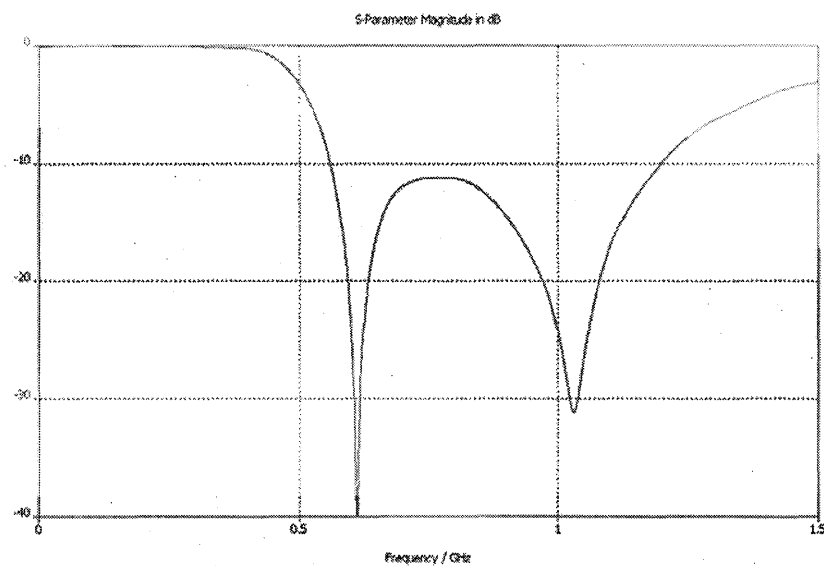
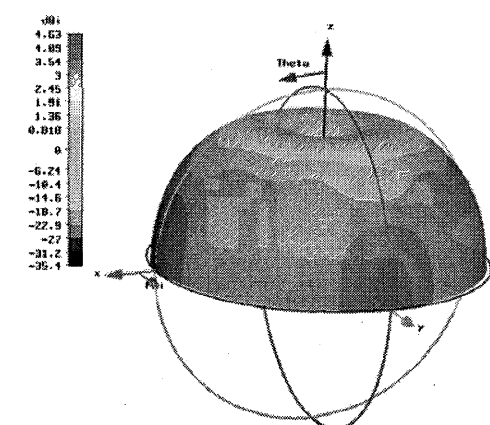
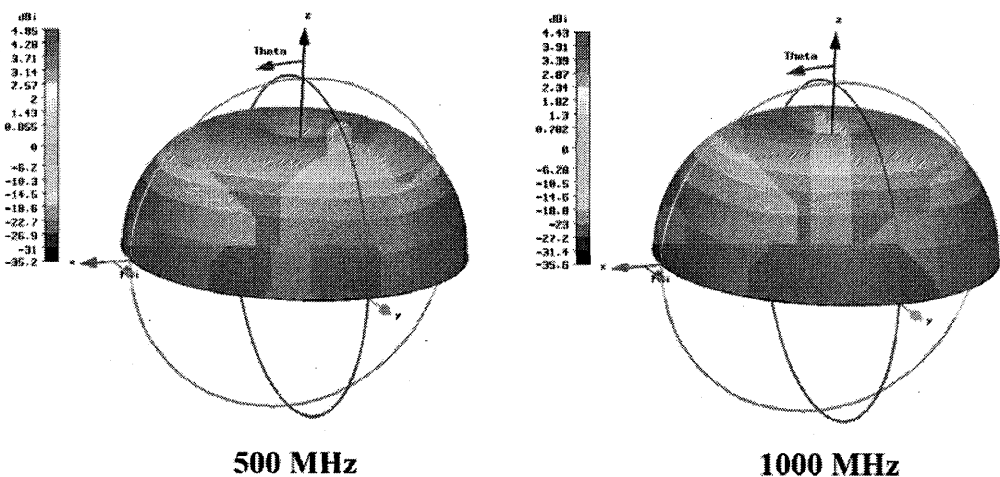


Figure 17. Return loss of the antenna depicted in Figure 16.



1500 MHz

Figure 17. Radiation patterns of the antenna depicted in Figure 16.

The Multi-Lens Array Architecture.

Danh Luu
AFRL/SNHA

Abstract: As communication and radar systems migrate toward wider bandwidths, the quantization lobes inherent in conventional phased array systems manifest as one of the foremost challenges for array designers who must consider not only the need for a large and inexpensive array with wideband requirements but also practical issues, such as the ease of transporting and realizing such an array. Large phased arrays based on conventional subarray architecture, with time delays at the subarray level, exhibit very high quantization lobes when scanned over a wide bandwidth. This paper describes a multi-lens (ML) array architecture that is suitable for very large arrays with wideband (bandwidth to center frequency ratio greater than 0.2) scanning requirements. In addition to having low quantization lobes, the ML array architecture is modular, scalable, and compact in volume. The proposed architecture approximates the ideal gradient time delay network with a combination of time delays at the subarray level, time delays of Rotman lenses, and small phase shifts. The basic idea behind the ML architecture is to concatenate multiple modified Rotman lenses together to form a large array with non-periodic phase settings across the large array to lessen the accumulation of quantization lobes at any specific angle.

1. INTRODUCTION

A. Quantization Lobes of Phased Array Systems.

Although wide-angle, high bandwidth, electronic scanning arrays are highly desirable, the present cost to build large arrays with such capabilities is prohibitive, since a time delay unit is required behind each element of an *ideal* wideband array. Subarraying to reduce the number of time delay units (and receivers) is a conventional approach to cut cost in a narrowband system. However, as we increase the bandwidth, the performance of the conventional subarray architecture degrades catastrophically due to the rising quantization (grating) lobes that have buried themselves beneath the sidelobes in the narrowband system but rise rapidly with increasing bandwidth. While we cannot live with these undesirable quantization lobes, we cannot live without them since they are natural companions of the various periodic aspects of the array, which enable us not only to reduce the fabrication cost and complexity of the array but also to simplify the array's analysis and controls.

B. Motivation behind the Multi-Lens (ML) architecture.

Under ideal assumptions (isotropic radiators, $\lambda/2$ spacing, uniform illumination, etc.), the far field antenna pattern is the Fourier transform of the aperture distribution across the surface of the array. The applied phase settings of the conventional subarray can be decomposed into two terms: the ideal phase term and the phase error term,

$$AF(\theta) = \sum_{n=0}^{N-1} e^{jn\pi \sin(\theta)} e^{-j\alpha_n} = \sum_{n=0}^{N-1} e^{jn\pi \sin(\theta)} e^{-j\beta_n} e^{-jE_n}, \quad (1)$$

where

$$\begin{aligned}\alpha_n &= \beta_n + E_n, \\ \beta_n &= n\pi \sin(\theta_0).\end{aligned}$$

E_n is the phase errors at the n^{th} elements, β_n is the ideal phase settings for scanning to θ_0 , and α_n is the applied phase.

From the modulation property of the Fourier transform and with $\exp(-j\beta_n)$ playing the role of the modulator, another way to compute the array pattern would be to take the error pattern, computed from the phase errors $\exp(-jE_n)$, and shift it to θ_0 .

When using conventional subarrays with narrowband systems (small array size and small bandwidth), the phase errors E_n are zero or nearly zero, and so the array pattern is simply a broadside beam shifted to θ_0 . However, when using a conventional subarray in a system with considerable bandwidth, the phase errors are not all zero and in general produce a plot similar to the phase errors plot shown in Figure 1.

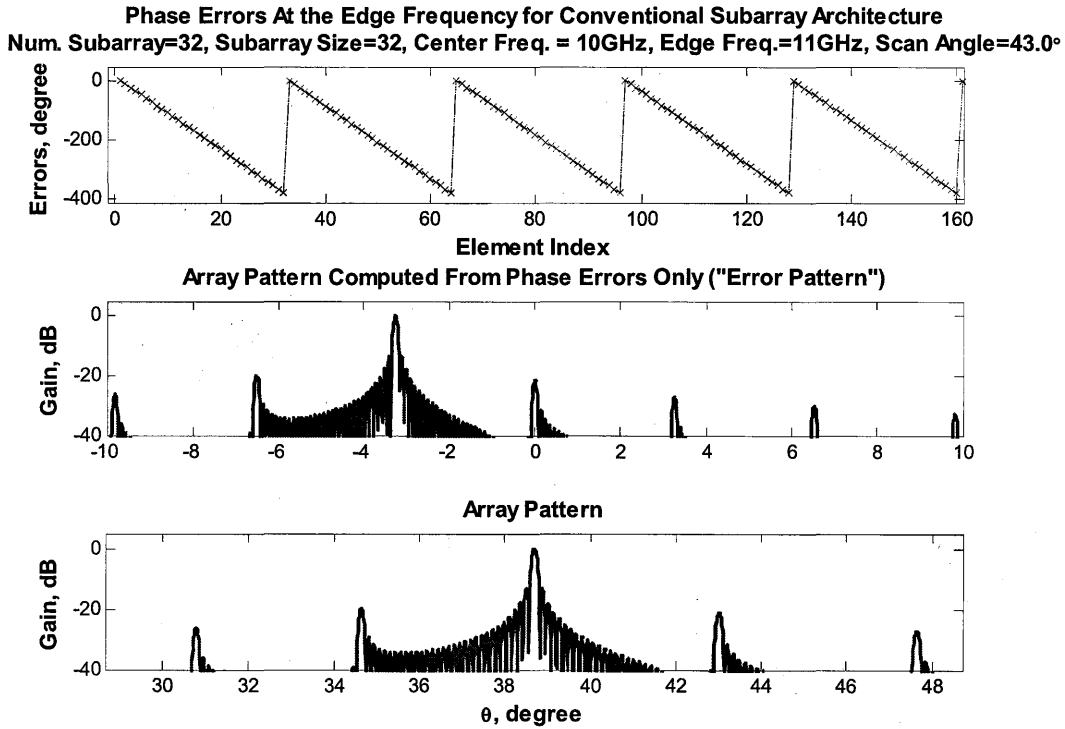


Figure 1. Phase errors and the array patterns corresponding to the applied phase. The phase errors and the array patterns were computed at the edge frequency for an array based on the conventional subarray architecture. The phase errors are shown for the first 160 elements of the array.

Unlike the zero bandwidth case, the error pattern of the edge frequency in the wideband case also has, in addition to the main beam at broadside, quantization lobes due to the periodic phase errors, E_n . The heights of these quantization lobes are generally related to the heights (maximum value) of the phase errors and the period of these quantization lobes is related inversely to the period of the phase errors. Since the phase error is a linear function of $\sin(\theta_0)$, at broadside scan ($\theta_0 = 0$) the phase errors are zero and as θ_0 increases the phase error also increases.

The ML array architecture to be discussed reduces the quantization lobes by reducing the phase scan angle, θ_0 . To smear out the grating lobe, the phase scan angle is set to different values from subarray to subarray so that looking across the array, the phase errors are non-periodic. Although there are many sources of phase and amplitude errors in the array that cause sidelobes to rise, only errors from phase shifters and array tapering are considered in this paper.

2. A SINGLE LENS.

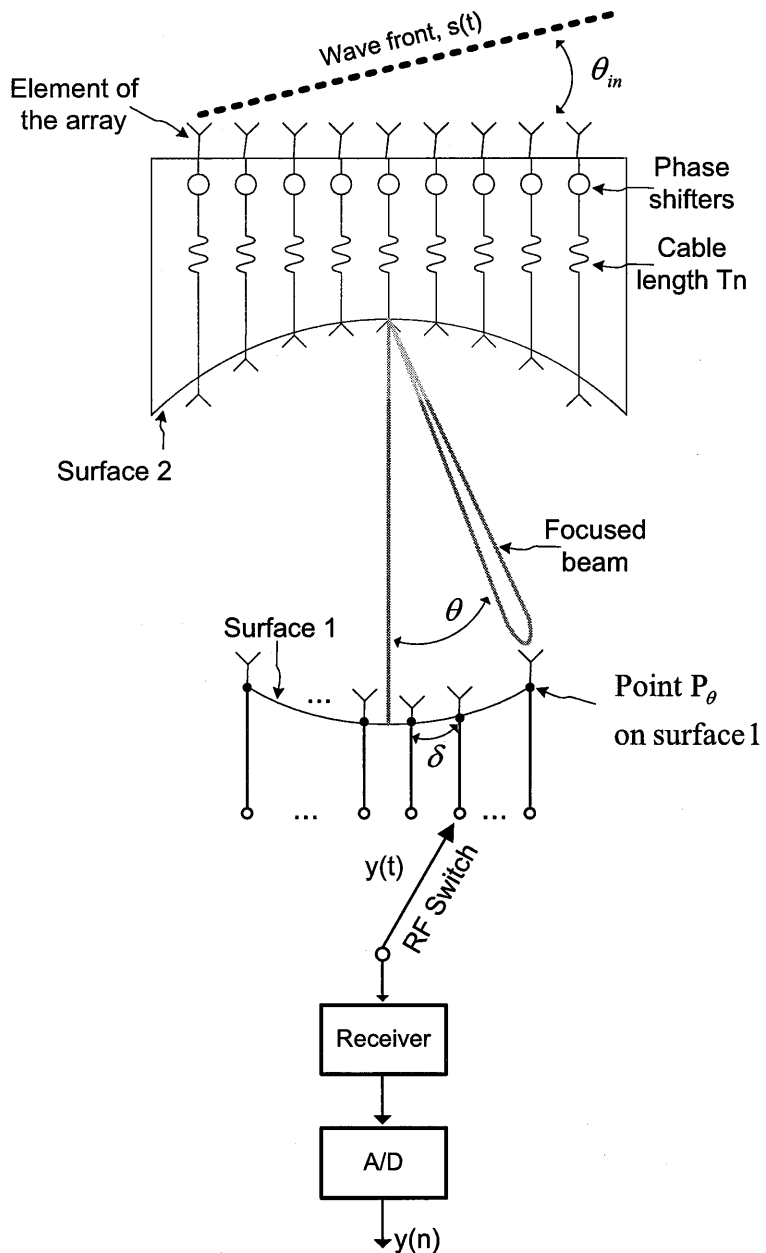


Figure 2. An illustration of a subarray of the Multi-Lens architecture.

A. Details of a Subarray.

The ML array architecture consists of M modified Rotman lenses with the detail of each lens, or “subarray”, shown in Figure 2 (the array is assumed to be used for receiving).

Connecting elements of the array to the ports on surface 2 are cables of variable lengths. The element spacing on surface 2 as well as the n^{th} cable length, T_n , are determined by three design equations derived in [4]. The constraints that lead to these design equations were written in terms of the three independent parameters in the lens: x_n , y_n (the coordinates of the n^{th} element on surface 2), and T_n (the time delay of the n^{th} cable that connects from the probe at (x_n, y_n) to the corresponding element in the linear array aperture). Details of the three constraints were discussed in [4] and can be summarized as follows: a) path lengths of the rays tracing from the incoming planar wave-front arriving at some angle θ_{in} to the focal point P_α on surface 1 are equal, i.e., a requirement of having a perfect focus at point P_α ; b) perfect focus at P_0 ; and c) perfect focus at point $P_{-\alpha}$. Although feed points along surface 1 between $P_{-\alpha}$ and P_α are imperfect foci, path length errors associated with these foci are small and insignificant compared to other sources of error in the array. Path length error is the difference between the maximum and the minimum lengths of the rays tracing from the incoming planar wavefront to a point on surface 1.

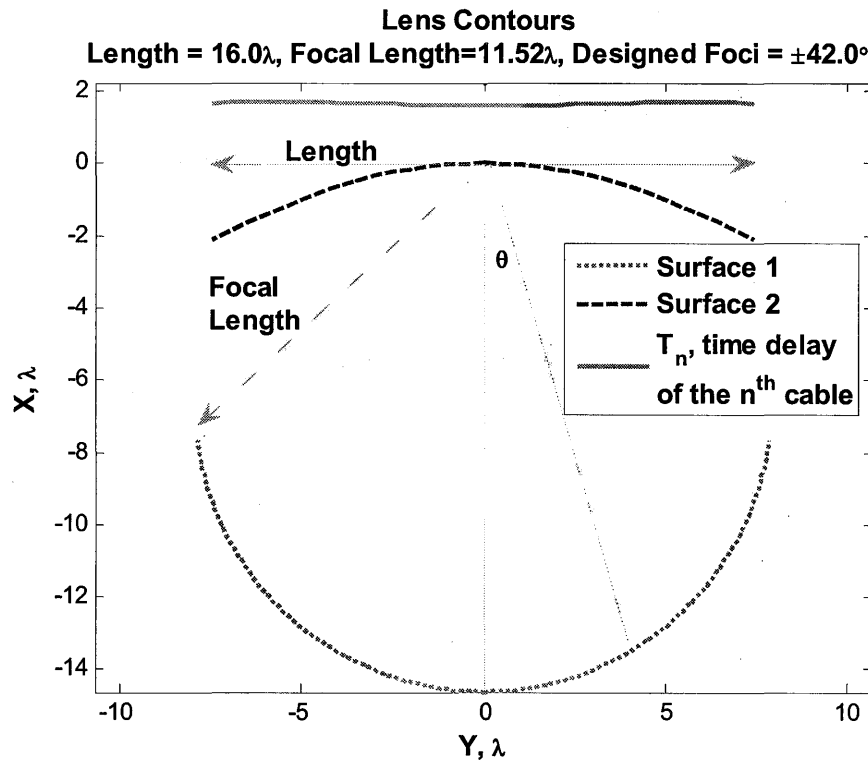


Figure 3. An illustration of the surfaces of a Rotman lens with length 16λ and foci at $\alpha = 0^\circ$ and $\alpha = \pm 42^\circ$.

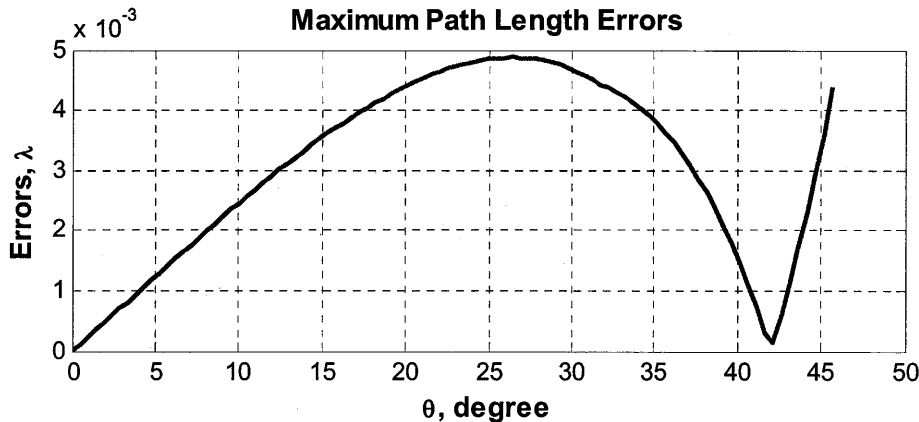


Figure 4. Path length errors for the foci on surface 1 of the lens in Figure 3.

For example, the two surfaces of a Rotman lens, designed with length 16λ and foci at 0 and $\alpha = \pm 42^\circ$ are shown in Figure 3. The path length errors, shown in Figure 4, at the designed foci are zero as expected whereas the path length errors at other points on surface 1 are small and can be considered as zero.

In the ML architecture to reduce the cost and complexity of the subarray, elements on surface 1 can be spaced sparsely at δ degree intervals. Hence the phase shifters are used to focus any incoming beam between $\pm\alpha$ to the center of an element on surface 1 as illustrated in Figure 5. Although one will attempt to set δ to be as large as possible to reduce the number of elements on surface 1, if δ is set too large, phase shifters will be required to scan to wide angles, which will cause beam squint at the subarray level, and elevated grating lobes at the array level. The strategy used in this paper is to initially choose δ , such that the beam squint at the edge frequency is less than half of the 3dB beamwidth of the subarray. After δ is determined, the array pattern is computed and the maximum grating lobe is compared against the desired level to determine whether δ needs to be decreased.

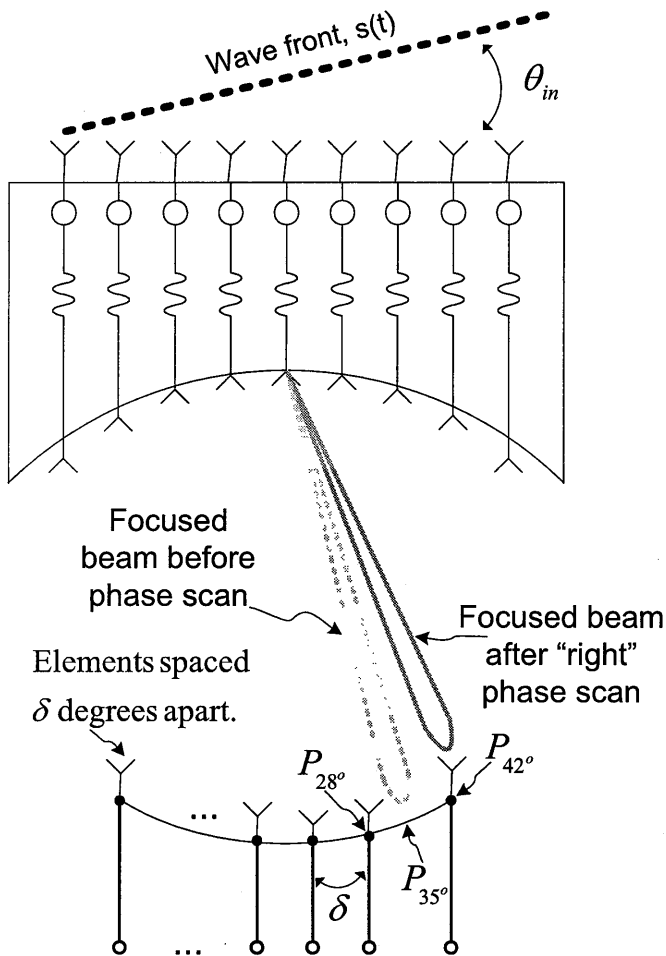


Figure 5. Phase scanning (focusing) a beam to the closest element on surface 1.

B. Computing the Far Field Subarray Pattern of a Single Lens

Suppose that the elements in the subarray lens are isotropic radiators and that a planar wavefront impinges on the array at θ_{in} . Assuming that the entire extent of surface 1 are in perfect focus, the received signal of the element located at point P_θ on surface 1 is,

$$y(t, \theta) = \sum_{n=0}^{N-1} s(t - \tau_n + w_n) e^{-j2\pi f_0 \tau_{phase}}, \quad (2)$$

where

$$\begin{aligned}\tau_n &= \frac{nd \sin(\theta_{in})}{c}, \\ w_n &= \frac{nd \sin(\theta)}{c}, \\ \tau_{phase} &= \frac{nd \sin(\theta_0)}{c}, \\ d &= \frac{\lambda_d}{2} = \frac{c}{2f_d}.\end{aligned}$$

$s(t)$ is the wavefront that impinges on the array, d is the distance between elements of the array, c is the speed of light, θ_0 is the phase scan angle, τ_{phase} is the phase scan, and f_0 is the center frequency.

Taking the Fourier transform of $y(t, \theta)$ with respect to time, t , yields

$$Y(f, \theta) = \sum_{n=0}^{N-1} S(f) e^{j2\pi f(-\tau_n + w_n)} e^{-j2\pi f_0 \tau_{phase}} = S(f) H(f), \quad (3)$$

where

$$H(f, \theta) = \frac{\sin(N\varphi/2)}{\sin(\varphi/2)} e^{\frac{jN-1}{2}\varphi},$$

$$\text{and } \varphi = \frac{\pi}{f_d} (f \sin \theta - f \sin \theta_{in} - f_0 \sin \theta_0).$$

$S(f)$ is the Fourier transform of $s(t)$ and has spectral content from f_{low} to f_{high} , N is the number of elements on surface 2, and f is frequency.

The received power at point P_θ can be computed using Eq. 3,

$$SAF(\theta) = \int_{f_{low}}^{f_{high}} |Y(f, \theta)|^2 df \quad (4)$$

If $s(t)$ is an ideal wideband signal, such that

$$\begin{aligned}S(f) &= 1, f_{low} \leq f \leq f_{high} \\ S(f) &= 0, \text{ otherwise}\end{aligned}$$

Eq. 4 simplifies to,

$$SAF(\theta) = \int_{f_{low}}^{f_{high}} |H(f, \theta)|^2 df = \int_{f_{low}}^{f_{high}} \left| \frac{\sin(N\varphi/2)}{\sin(\varphi/2)} \right|^2 df, \quad (5)$$

which is the *subarray power pattern* that has a peak when $\varphi = 0$ and $f = f_0$. For an incoming wavefront incident at θ_{in} , with phase shifters set to scan to θ_0 , the peak of the subarray pattern occurs whenever,

$$f(\sin \theta - \sin \theta_{in}) - f_0 \sin \theta_0 = 0 \quad (6)$$

or

$$\theta_{peak} = \arcsin(\sin \theta_0 + \sin \theta_{in})$$

For a wavefront arriving at θ_{in} and subarray phase setting set to scan to θ_0 , the peak of the focused beam on surface 1 is at $P_{\theta_{peak}}$. Eq. 6 computes the required phase setting to focus an incoming beam to a specified location, $P_{\theta_{peak}}$, on surface 1.

3. MULTIPLE LENSES.

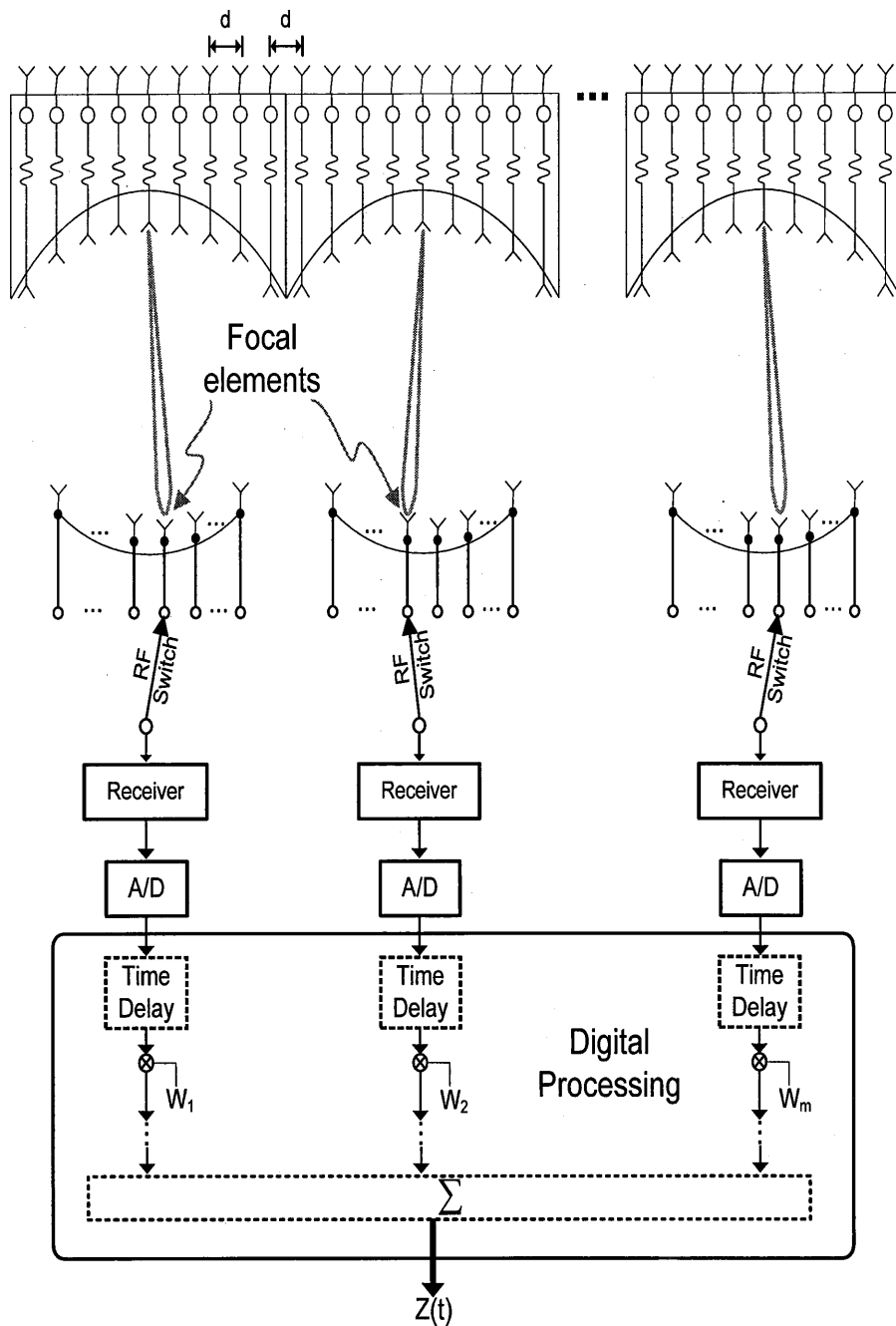


Figure 6. Block diagram of the Multi-Lens architecture.

The multi-lens (ML) array proposed in this paper consists of M subarray lenses placed adjacent to each other as shown in Figure 6. In the receive case, an incoming planar wavefront impinging on the array will be focused to an element on surface 1. RF switch

is used to connect the output of the element at the focal point to the input of the receiver. After the analog to digital conversion stage, the digital signal is weighed and time delayed using any of the techniques discussed in references [6] and [7].

A. Scattering Between Adjacent Lenses.

It is assumed that scattering between adjacent lenses is negligible in the receive case. To see why this assumption is valid, consider the lens in Figure 3 and suppose that there is a wavefront arriving at broadside. As seen in Figure 7, the separation angle, γ , between the two broadside focal points of two adjacent lenses is 48.1° . The energy that radiates from subarray 1 to subarray 2 is the sidelobe at $\gamma = 48.1^\circ$. It will be assumed that this energy is negligible as compared to the energy of the mainlobe. Although only a broadside case is considered here, the separation angles for other scan values are as wide as in the broadside case.

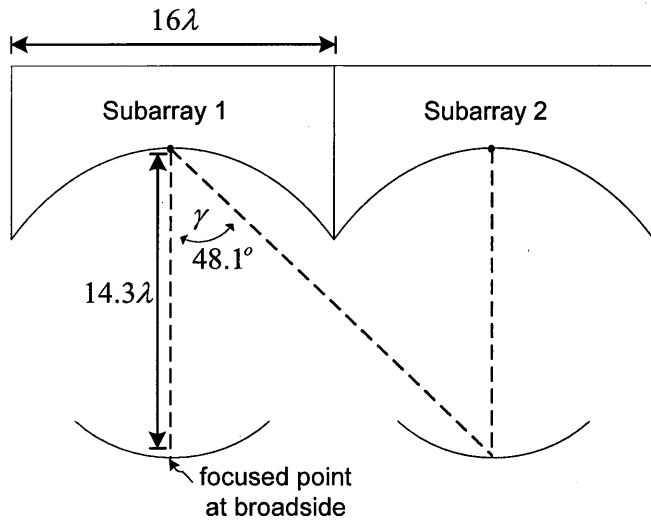


Figure 7. The separation angle γ between two focal points of two adjacent lenses.

B. Computing the Array Pattern of the Multi-Lens Architecture.

The ML array is steered using a combination of phase shifters and time delays. At the subarray level phase shifters are located between the lenses and the subarray apertures. Time delay units at the array level are located at the focal contour of each lens. As shown in Figure 6, the outputs of the M subarrays are summed, and the individual subarray's outputs $y_m(t)$ are time delayed by τ_m , then weighed with w_m . The time delay τ_m steers the subarray pattern to direction θ_{in} , while the weights w_m are used to lower the array's sidelobes to a desired level. The quantization lobe is not affected by w_m . The output signal after summing the M subarrays is,

$$z(t, \theta_{in}) = \sum_{m=0}^{M-1} w_m y_m(t + \tau_m - L_m), \quad (7)$$

where

$$\begin{aligned} D &= Nd, \\ L_m &= \frac{mD \sin(\theta_{in})}{C}, \\ \tau_m &= \frac{mD \sin(\theta_{in})}{C}. \end{aligned}$$

L_m is the difference in time delay between phase centers of subarray, τ_m is the digital time delay, and D is the distance between subarray.

Unless indicated otherwise, the set of digital weights, w_m , have been selected to produce a -32 dB Chebyshev window.

Taking the Fourier transform of $z(t, \theta_{in})$ with respect to t we have,

$$Z(f, \theta_{in}) = \sum_{m=0}^{M-1} w_m Y_m(f) e^{j2\pi f(\tau_m - L_m)}. \quad (8)$$

Eq. 3, expressed in terms of the scan angle of the m^{th} subarray, is given as

$$H(f, \theta_m) = \frac{\sin(N\varphi_m/2)}{\sin(\varphi_m/2)}, \quad (9)$$

where

$$\varphi_m = \frac{\pi}{f_d} (f \sin \theta^m - f \sin \theta_{in} - f_0 \sin \theta_0^m).$$

θ^m is the location of the focal element on surface 1 of the m^{th} subarray and θ_0^m is the phase scan angle at the m^{th} subarray.

Substituting Eq. 9 into Eq. 8 we have,

$$Z(f, \theta_{in}) = S(f) \sum_{m=0}^{M-1} w_m H(f, \theta_m) e^{j2\pi f(\tau_m - L_m)} \quad (10)$$

Suppose that $s(t)$ is an ideal wideband signal such that

$$S(f) = 1, f_{\text{low}} \leq f \leq f_{\text{high}}$$

$$S(f) = 0, \text{ otherwise}$$

The *wideband array power pattern*, $AF(\theta_{in})$, can be computed by integrating Eq. 10 over the desired frequency range,

$$\begin{aligned} AF(\theta_{in}) &= \int_{f_{low}}^{f_{high}} |Z(f, \theta_{in})|^2 df \\ &= \int_{f_{low}}^{f_{high}} \left| \sum_{m=0}^{M-1} w_m H(f, \theta_m) e^{j2\pi f(\tau_m - L_m)} \right|^2 df \\ &= \int_{f_{low}}^{f_{high}} g(f, \theta_{in}) df, \\ \text{where } g(f, \theta_{in}) &= \left| \sum_{m=0}^{M-1} w_m H(f, \theta_m) e^{j2\pi f(\tau_m - L_m)} \right|^2 \end{aligned} \quad (11)$$

There is no closed form solution for Eq. 11. However, since $g(f)$ varies slowly with respect to f , numerical integration using Simpson's 1/3 Rule is a convenient method to evaluate Eq. 11. It can be shown the result can be expressed as,

$$AF(\theta_{in}) = \int_{f_{low}}^{f_{high}} g(f, \theta_{in}) df \approx \frac{h}{3} \sum_{k=0}^{2K} l_k g(f_k, \theta_{in}), \quad (12)$$

where,

$$h = f_1 - f_0,$$

$$l_k = [1, 4, 2, 4, 2, \dots, 4, 1]$$

and the f_k are $2K+1$ equally spaced frequency points between f_{low} and f_{high} .

The wideband array patterns in Section 4 were computed using Eq. 12 with 33 frequency points. In narrowband system, Eq. 12 will produce the same array pattern as the classical phased array pattern. However, unlike the classical array pattern, which computes the power for a single frequency, Eq. 12 computes the power of the signal $s(t)$ at a given angle θ_{in} . So all frequencies in $s(t)$ contribute to the quantization lobe of the wideband power pattern.

4. EXAMPLES

The examples below demonstrate the wideband scanning feature of the ML array architecture. Although one would not normally use a conventional subarray for wideband scanning, the examples shown in Section 4A illustrate the severity of the quantization lobes associated with phase scanning in a large wideband conventional subarray.

A. Conventional Subarray

The array pattern for an array of 1024-elements based on the conventional subarray architecture is shown in Figure 8 at 43° scan. In this case, phase shifters are located behind each element, time delay units are located behind each of the 32 subarrays. The array in section 4A, 4B and 4C have an operating bandwidth of 2 GHz centered at 10 GHz and are assumed to have uniform tapering and ideal phase shifters with infinite accuracy. As expected, the peak quantization lobe is approximately 5 dB down from the main beam. The power pattern of the conventional subarray was computed using Eq. 11 with $\theta_0^m = 43^\circ$ for all subarrays.

**Power Pattern for a Conventional Subarray With 32 Subarrays Each With 32 Elements
ScanAngle = 43° , Operating Freq. = 9 to 11 GHz**

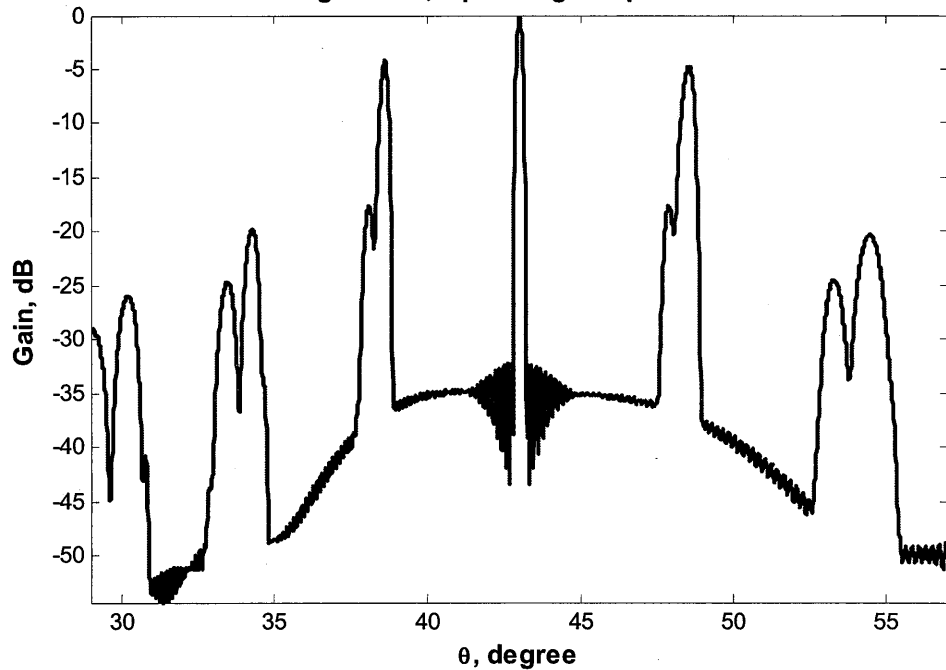


Figure 8. Wideband array pattern for an array of 32 subarrays, each with 32 elements, using a contiguous subarray architecture. The scan angle is 43° over a 2 GHz bandwidth, at a center frequency of 10 GHz.

B. An Array Based on Multi-Lens Array Architecture

The ML array architecture lowers quantization lobes by reducing and randomizing phase errors across the array. In addition to exhibiting low grating lobes, the ML architecture consists of M distinct and detachable subarray sections, which are modular and fairly compact in depth. For example, a 1024-element ML array with 32 subarrays has a focal length of $32 * (\lambda/2) * 0.72 = 11.52\lambda$, whereas an equivalent Rotman lens, would have a focal length of $1024 * (\lambda/2) * 0.72 = 368.64\lambda$, which is physically impractical.

In the cases shown in Figure 9, the ML array has 32 subarray lenses, each with 32 elements equally spaced ($d = \lambda/2$). The operating parameters are the same as in Section 4A. The desired sidelobe level is -29 dB for all scan angles between $\pm 45^\circ$. To achieve this low sidelobe level, elements on surface 1 of each subarray are placed at $\pm 42^\circ$, $\pm 28^\circ$, $\pm 14^\circ$ and 0 degrees so that phase shifters scan the beam to a maximum value of $\delta = 14^\circ$. In most cases, the phase scan angle will be less than $\delta/2 = 7^\circ$. The grating lobe level in the ML array increases or decreases with increases or decreases in the distance δ between adjacent elements on surface 1.

Unlike the conventional subarray architecture, where the maximum grating lobe occurs at the highest scan angle, the peak grating lobes in the ML architecture generally occur when the incoming planar wavefront is focused to a point P_θ that is in between any two elements on surface 1. For the current example, these points are $\pm 7^\circ$, $\pm 21^\circ$, and $\pm 35^\circ$ degrees. Suppose that the incoming wavefront is focused by the subarray lens to point P_{35° as shown in Figure 5. Using phase shifters, we have the option to scan the beam either to the element located at P_{42° (right scan) or to the element located at P_{28° (left scan). To make the phase errors non-periodic across the array which smears out the grating lobes, the decision to scan to the left or to scan to the right at each subarray is based on a randomly chosen binary string of length M . Details of a simple scheme that chooses the "random sequence" shown in Figure 9a are discussed in Appendix A. In this scheme, a '0' in the m^{th} position represents a left scan at subarray m and a '1' represents a right scan. With random scanning, the peak grating lobe at 35° scan is about -30.2dB, which is significantly lower than the -24.6 dB peak grating lobe that occurs in the non-random scanning case (not shown) with random sequence = "00...0".

Figure 9c shows the case where random scanning cannot be used. When the incoming beam is focused to point P_{45° , there is only one element next to the focal point and the only possible scan angle is the left scan to the element at 42° . Although the peak quantization lobe at -32.7 dB is not smeared out in this case, it is still very low since the phase scan angle is only 3° .

Array pattern of 1024-elements array (32 lenses) based on the ML architecture.
ScanAngle=35°, RandomSequence=00111000110011101101111100000101.

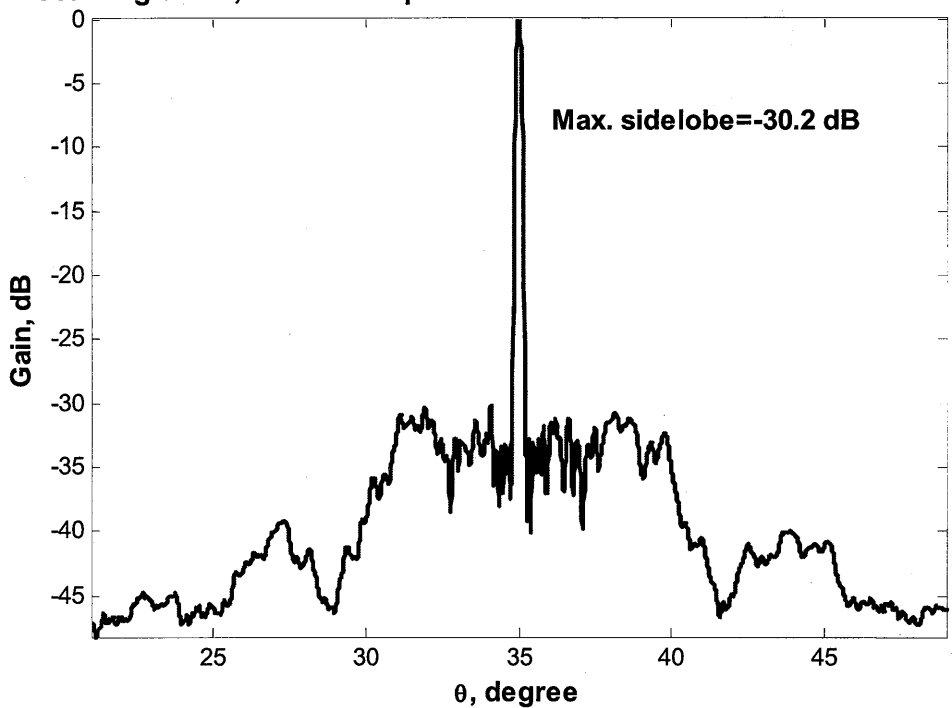


Figure 9a. Wideband array pattern of a 1024-element array based on the Multi-Lens architecture. The ML array consists of 32 subarray lenses which are scanned to different angles over a 2 GHz bandwidth centered at 10 GHz. The scan angles ($\theta = 35^\circ$, 7° , and 45°) were chosen to illustrate the worst cases quantization lobe level.

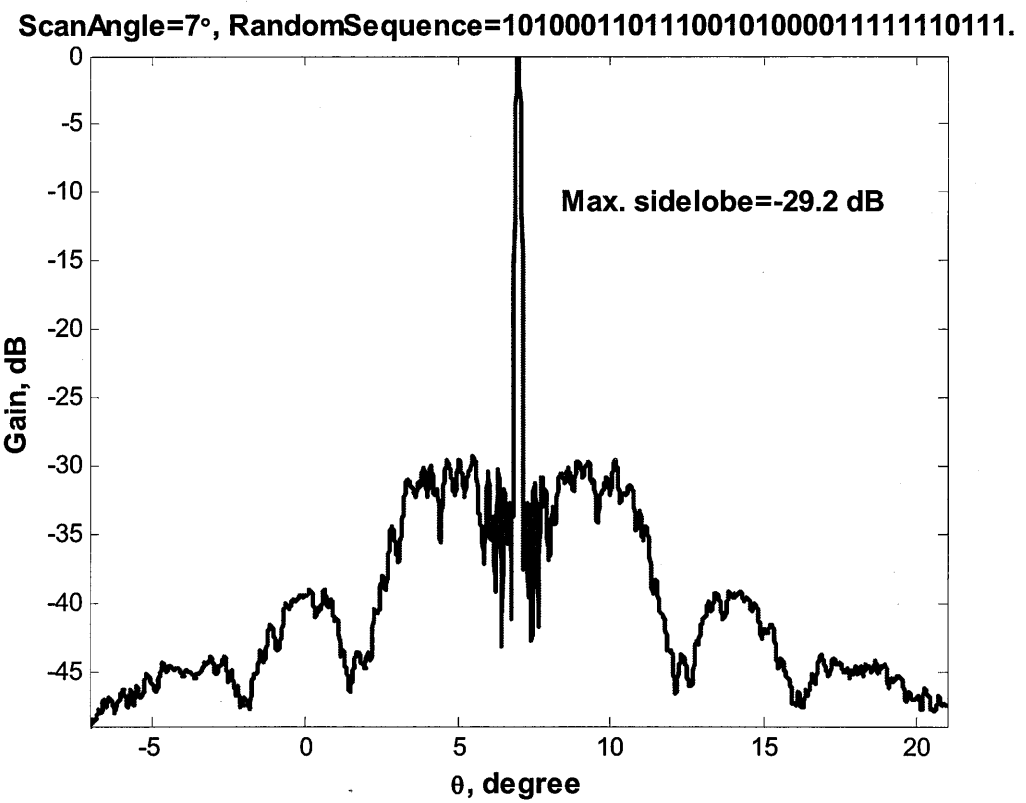


Figure 9b. Wideband array pattern for 7° degree scan.

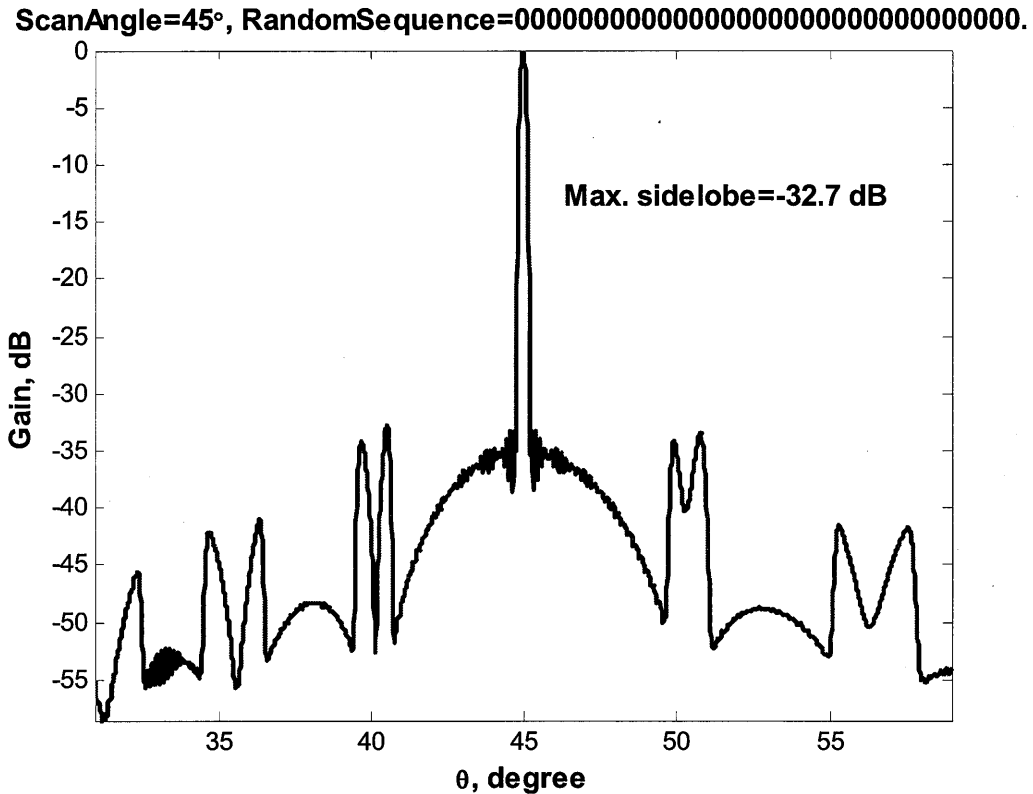


Figure 9c. Wideband array pattern for 45° degree scan. Random sequence equal to “00...0” means *left scan* at all subarrays.

C. Increasing the Size of an ML Array

Because the ML array architecture is scalable, an existing array can be enlarged by adding more lenses to the array, which suggests that the ML array architecture may be practical for large space-borne array systems. In addition to increasing the array’s size, adding more subarray lenses will also lower the peak grating lobes due to the reduction in width of grating lobes and the random phase scanning scheme, which smears out the grating lobes more evenly. To demonstrate this aspect of the ML architecture, the number of subarrays in Section 4B is doubled from 32 to 64. Even though the size of the array is increased from 512λ to 1024λ , the depth of the array remains unchanged at 11.5λ . As with convention subarray architecture, the reduction in height of the peak grating lobe occurs with increasing numbers of subarrays. However, in the ML architecture, the combination of smeared grating lobes that result from random phase scanning, and narrowed grating lobe widths, yield significantly better array patterns as shown in Figure 10.

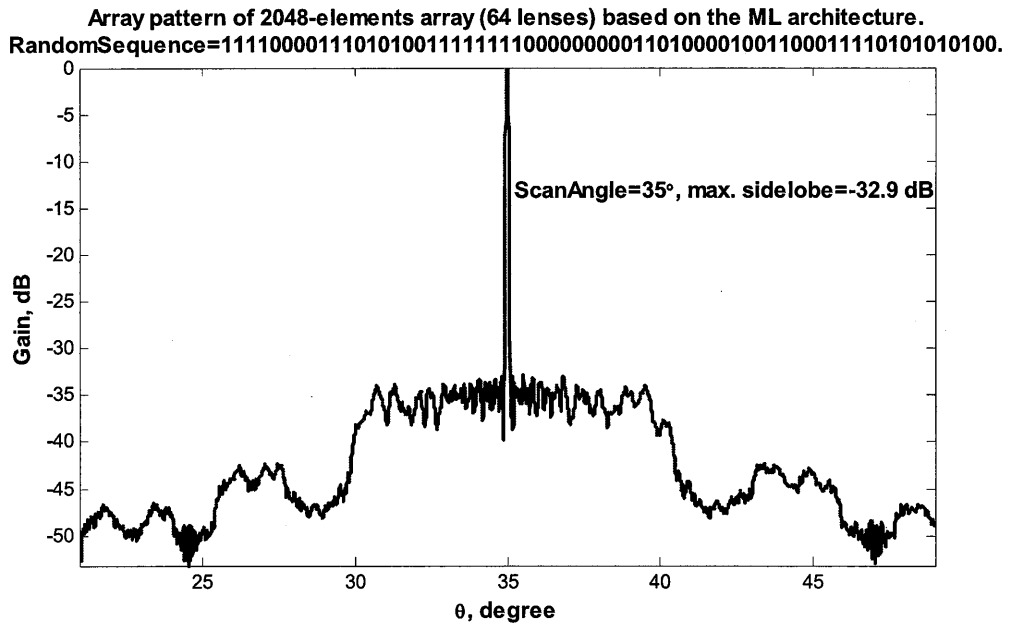


Figure 10a. Wideband array pattern of a 2048-element array based on the Multi-Lens architecture. The ML array consists of 64 subarray lenses which are scanned to different angles over a 2 GHz bandwidth centered at 10 GHz.

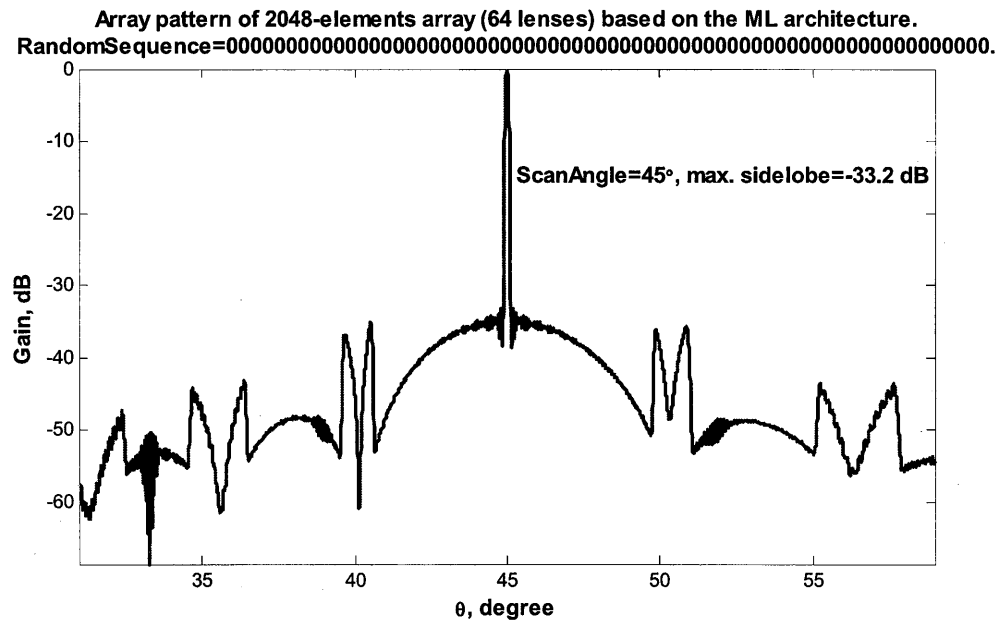


Figure 10b. Wideband array pattern for 45° scan.

D. Phase Quantization and Subarray Tapering.

In practice, there will be some amplitude tapering across the subarray. In addition, phase shifters generate only a finite number of discrete phase states. Using 4-bits phase shifters instead of ideal phase shifters in the ML array of Section 4B, causes the maximum grating lobe to rise by only a fraction of a dB. Although phase quantization does not have a significant effect on the maximum grating lobe level, subarray tapering will cause grating lobes to rise modestly with respect to the phase quantization case, especially in situations where random scanning cannot be used.

It is widely known that the significant effect of adding cosine tapering to a subarray is a widening of the subarray's beam width while its sidelobes are lowered. The elevated grating lobes in a tapered subarray system are caused by the shifts of the subarray pattern nulls away from the ideal locations where the grating lobes appear. Because of this misalignment, the subarray nulls are only able to partially suppress grating lobes. With greater shifting of the subarray pattern nulls, more misalignments occur and even higher grating lobe result.

At 35° scan, the peak sidelobe level of the cosine tapered array is about 2.7 dB higher than the peak sidelobe of the non-tapered array pattern, as shown in Figure 11a. The general sidelobes of the tapered array, however, are slightly lower than the sidelobes of the non-tapered array. The weights that were applied to the tapered array were computed from

$$c_n = \cos(\chi_n),$$

where

$$\chi_n = -35, -(35 + 70/31), -(35 + 140/31), \dots, 35 \text{ degree.}$$

c_n is the weight for the n^{th} element of the subarray.

The same random sequence, optimized for the non-tapered case, was used for both the tapered and non-tapered array. When optimized random sequences were used with both the tapered and non-tapered arrays, the peak quantization lobes in the two cases are about the same. However, without random scanning, the quantization lobes of the tapered array, shown in Figure 11b, are much higher than those of the non-tapered array. This example demonstrates another feature of the ML architecture with random scanning, which is not only able to smear out grating lobes due to periodic phase error but also due to periodic amplitude error. The amplitude error in this example is the difference between the ideal uniform taper and the cosine taper.

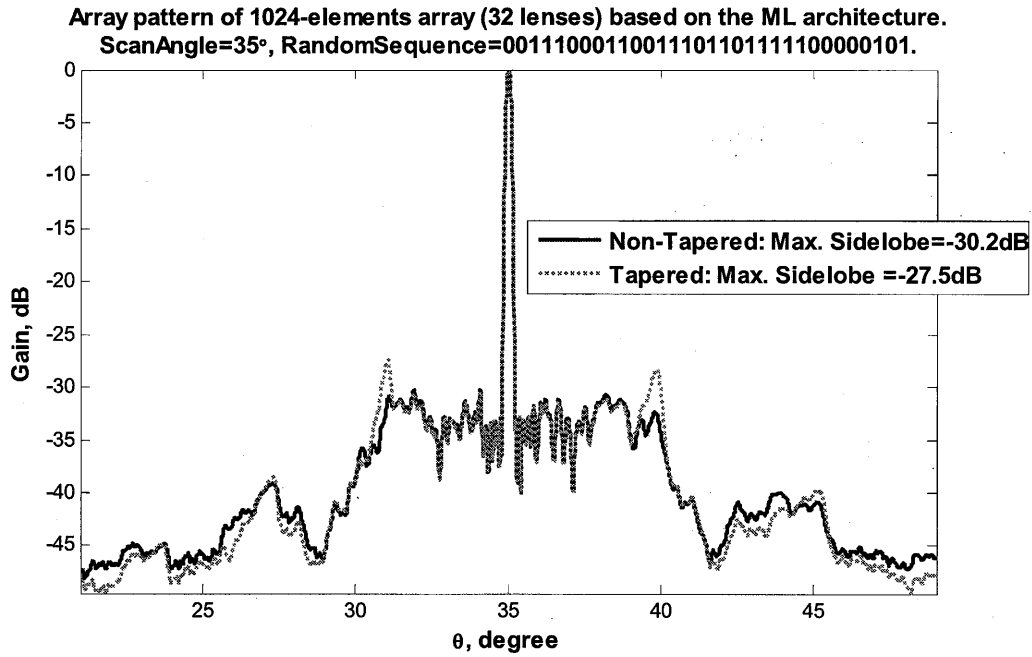


Figure 11a. The wideband array patterns of an array based on the ML architecture for 35° scan. The solid line corresponds to the ML array with uniform tapering across each subarray and the dashed line corresponds to the ML array with tapered subarrays.

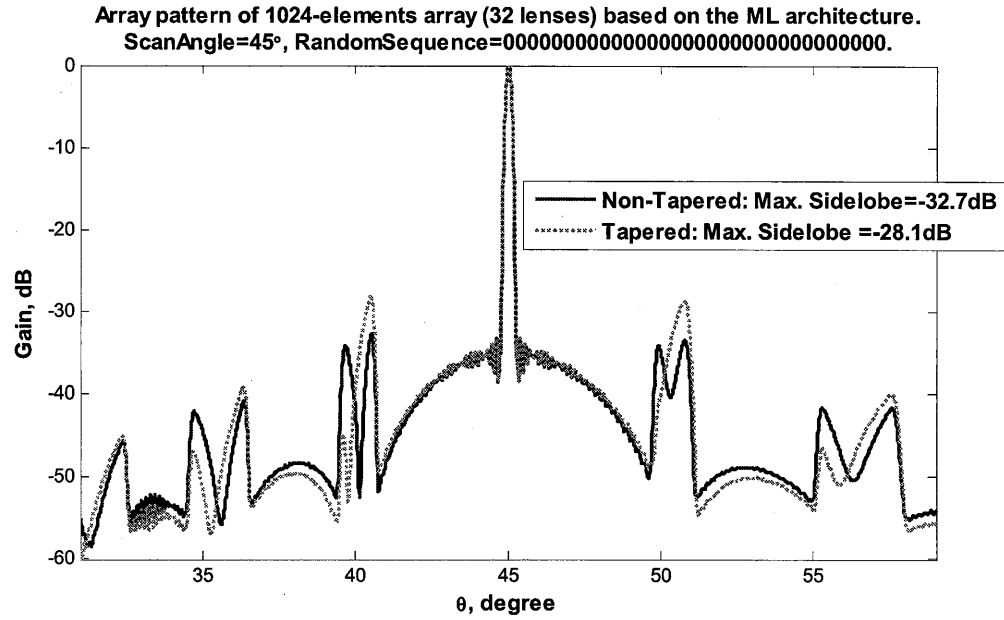


Figure 11b. Wideband array pattern for 45° scan.

5. CONCLUSION

The proposed Multi-Lens array architecture is modular, scalable and is ideally suited for very large arrays with wideband scanning requirements. Using ideal assumptions, (isotropic radiator, perfect Rotman lenses) it was shown that the quantization lobes of the ML array are much lower than the quantization lobes of a conventional subarray architecture since the ML array approximates an ideal time delay network having time delays at the subarray level, analog time delays in the Rotman lenses, and small phase approximations from phase shifters. Not only are the phase errors of the ML array much smaller than the phase errors of the conventional subarray, they are also non-periodic, which cause the grating lobes to be smeared out. To completely remove the phase errors in the ML architecture and to perhaps simplify the ML design, elements on surface 1 should be spaced closely such that phase scanning is not required. Although phase shifters can be removed from the ML architecture in this case, the complexity of the RF switching network must be increased to accommodate for the increasing number of elements on surface 1.

Examples that take into account phase quantization and amplitude tapering were considered. While phase quantization does not have a significant effect on the array pattern, the rising quantization lobe due to amplitude tapering can be smeared out using an optimized random sequence. Not all practical aspects of the multi-lens array architecture were considered. Among the important and practical details that were omitted are the locations for amplifiers (LNA) and the process for choosing the size of array and the size of the lens. Costs will dictate the locations and number of LNAs and desired gain, array's size and volume constraint will be used by array designers to choose size and the number of the lens in the array.

6. APPENDIX

A. Choosing a Random Sequence.

For the ML array in Section 4B with $N = 32$ subarrays, an exhausted search for the optimum random sequence requires the evaluation of 2^N scanning sequences. For large N , it is not practical to find the peak sidelobes for all 2^N different phase scan configurations and then select the optimum scan sequence that has the lowest sidelobe. Instead, a more tractable approach is to consider only a small subset of the 2^N scan sequences. A distribution of the peak sidelobes of the 2^N scanning sequences is first estimated to find out the size, K , of this subset and how the lowest sidelobe from the K randomly chosen sequences compared with the sidelobe of the globally optimum scan sequence. The histogram shown in Figure 12 for the array in section 4B is computed from 4200 randomly generated scanning sequences with the probability of "left" scan equal to the probability of "right" scan at each subarray.

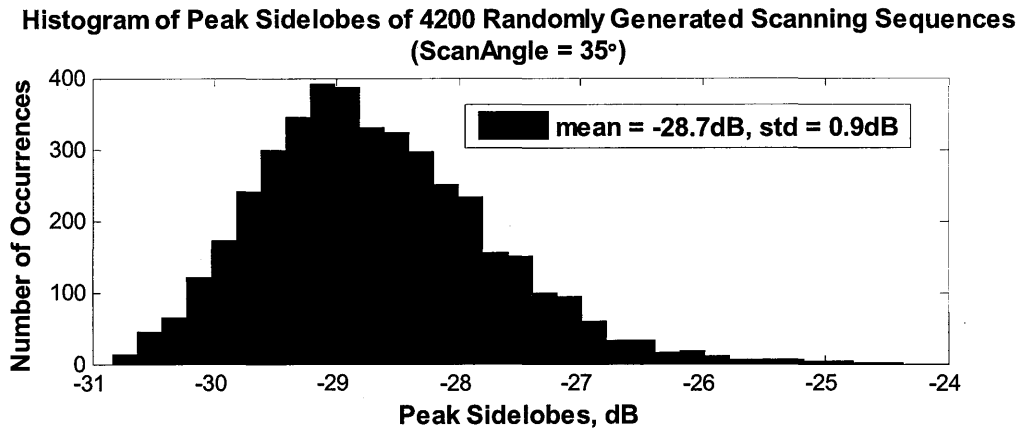


Figure 12. Histogram of the peak sidelobes of the ML array in Section 4B computed from 4200 random scanning sequences.

From the histogram, the probability of getting a random scan sequence with sidelobes level below -31 dB is very small. However, it is possible to obtain a sequence with sidelobes below -30 dB with relatively few trials. The number of trials that will be required can be determined by first estimating the probability, P_s , of a sequence with sidelobes below -30 dB. From the 4200 randomly generated sequences, a total of 264 scanning sequences exist which have sidelobes below -30 dB. The rough estimate of P_s is $264/4200 = 0.0629$ (99% margin error = $\pm 2\%$) and the estimated probability of having sidelobes greater than -30 dB is,

$$P_f = 1 - P_s = 0.937.$$

Assuming that the *probability of success*, P_s , is known, the number of trials, K , required to guarantee a desired probability, P_d , of having at least one success or having at least one scanning sequence with sidelobes below -30 dB must be determined. For independent trials and $P_d = 0.99$, K can be computed from

$$0.99 = 1 - P_f^K.$$

For $P_f = 0.937$, there is a 99% chance that from the $K = 71$ randomly generated sequence that at least one random scanning sequence will have peak sidelobe below -30 dB.

B. Choosing Random Sequences For a Range of Scan Angles.

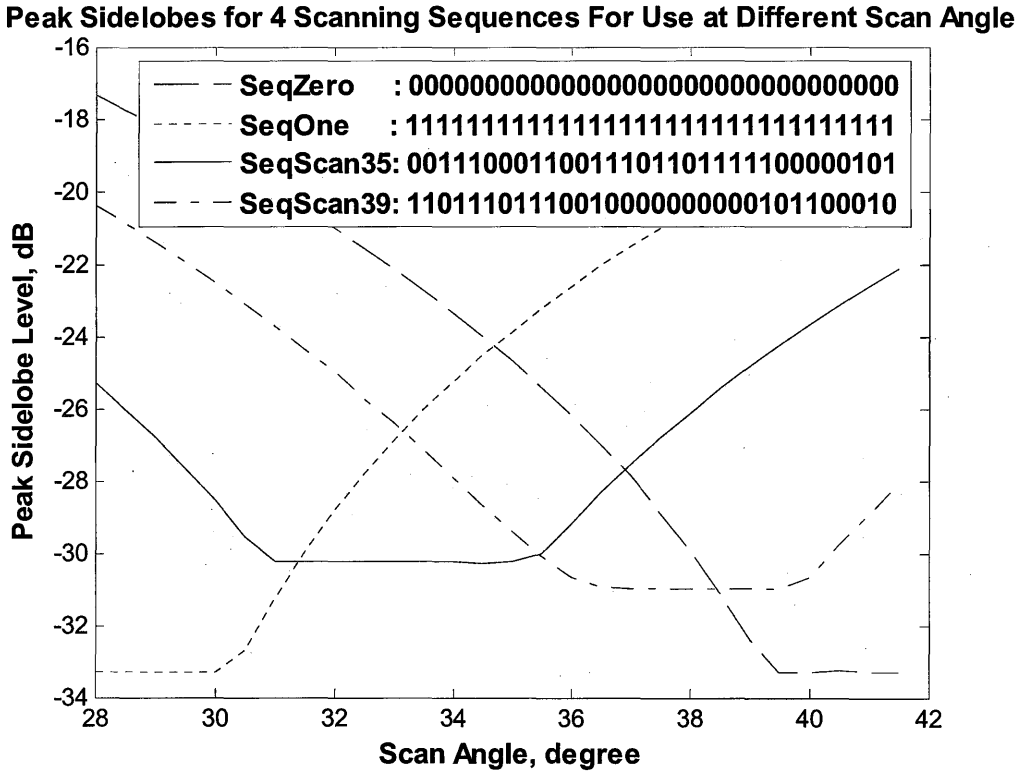


Figure 13. Peak sidelobes of an ML array scanned to different angles using a random sequence that was designed for any specific angle.

Although a random scanning sequence is chosen for a specific scan angle, it can be used for scan angles that are near the optimized angle. For example, in Figure 13, the scan sequence (“SeqScan35”) which was chosen for a 35° scan can be used for scan angles ranging from 31° to 35° and the resulting sidelobe level will still be below -30 dB. Two pre-computed random sequences are needed to cover 28 to 42 degrees scan for the array in Section 4B since different scan regions require different random sequences. *SeqScan35* is used for 32 to 35 degrees scanning and *SeqScan39* is used for 36 to 40 degree scanning. For scan angles ranging from 28 to 31 degrees, a left scan to the element at 28° is used at each subarray and a right scan to the element at 42° is always used for scan angle from 40 to 42 degrees.

ACKNOWLEDGEMENT

The author is grateful for the guidance and supports of Dr. Robert Mailloux whose inspiration and encouragements have helped the author through even difficult stages of the project. This paper is an accumulation of ideas from the numerous discussions with Dr. Mailloux, who has always been willing to spend time to meet and talk with the author.

about various aspects of the array architecture and provide constructive feedback. The previous sentence also applies to Dr. Hans Steyskal whose editing has greatly improved the quality of the paper. The author also has had stimulating discussions with Mr. David Curtis, Dr. Boris Tomasic and Dr. Peter Franchi.

REFERENCES

- [1] W. Rotman, P. Franchi, "Cylindrical Microwave Lens Antenna for Wideband Scanning Application", *Antennas and Prop. Int. Symposium*, vol. 18, pp. 564-567, Jun 1980.
- [2] H. L. Southhall, D. T. McGrath, "An Experimental Completely Overlapped Subarray Antenna", *IEEE Trans. On Antennas and Prop.* vol. AP-34, pp. 465-473, Apr 1986.
- [3] R. J. Mailloux, "A Low-Sidelobe Partially Overlapped Constrained Feed Network for Time-Delayed Subarrays.", *IEEE Trans. on Antennas and Prop.*, vol. AP-49, pp. 280-291, Feb 2001.
- [4] W. Rotman, R. F. Turner, "Wide-Angle Microwave Lens for Line Source Applications", *IEEE Trans. On Antennas and Prop.*, vol. AP-11, pp. 623-632, Nov 1963.
- [5] R. J. Mailloux, "Phased Array Antenna Handbook", Artech House, 1994.
- [6] T. I. Laakso, V. Valimaki, M. Karjalainen, and U. K. Laine, "Splitting the Unit Delay", *IEEE Signal Processing Mag.*, Vol. 13, Issue 1, pp. 30-60, Jan. 1996.
- [7] T. I. Laakso, T. Saramaki, and G. D. Cain. "Asymmetric Dolph-Chebyshev, Saramaki, and transitional windows for fractional delay FIR filter design", *Circuits and Systems. Proceedings of the Midwest Symposium on Meeting: August 13, 1995*, pp. 580-583.

Surface-Micromachined Ka-Band Phased-Array Antenna

Milan Lukic¹, Daniel Fontaine², Christopher Nichols³, Dejan Filipovic¹

¹Departemnt of Electrical and Computer Engineering
University of Colorado at Boulder, CO 80309-0425

²BAE Systems, Nashua, NH 03060

³Rohm and Haas Electronic Materials LLC, Blacksburg, VA 24060

Abstract: A rectangular coaxial line (RCL) fed cavity backed patch antenna element for a Ka-band phased array at 36GHz is presented in this paper. The antenna is fabricated by a sequential microfabrication surface micromachining process (PolyStrata™ process) with ten structural layers. Multiple beams are obtained by a Butler matrix beam forming network built from 50Ω RCLs and integrated on the same wafer with antenna elements. The unit cell of the array is a rectangular patch backed with a 700 μm tall, 3.64 x 3.64mm² footprint, air-filled cavity. The patch is 2.77mm long and 2.15mm wide and has two slits for impedance matching and eight holes for releasing the sacrificial photoresist. It is supported by two metal posts and firm attachment with the feeding coax. Individual antenna elements have measured impedance bandwidth of about 4.1% around 36GHz, with simulated gain and radiation efficiency of about 5.7dBi and 95%, respectively. Due to the metallic posts, the second band appears at 28GHz, and it is characterized with about 5.1% measured bandwidth. However the radiation pattern resembles that of a monopole. Modeling, analysis and design are conducted with the finite element code Ansoft HFSS and good agreement with measurements is demonstrated.

1. Introduction

Intense developments of radio-frequency micro-electromechanical systems (RF MEMS) components over the past decade (for broader review see [1]) have contributed to the development of enabling fabrication technologies for future, high-performance millimeter and sub-millimeter electromagnetic systems. Among these, special place belongs to the techniques aimed at building μ -coaxial lines and related components [2-6]. Though circular coaxial lines are desired (lowest loss), the micromachining fabrication is limited to the manufacturing of rectangular coaxial lines (RCLs). Low loss, wide single TEM and non-dispersive mode bandwidth, high turn ratios, possibilities for seamless single/multi-level integration with other passive and active components are just a few appealing properties associated with RCLs. In this paper we demonstrate a Ka-band antenna integrated with a μ -coaxial feed and aimed for the full passive integration with a Butler matrix beam-forming network and 4x4 phase array demonstration. To the best of our

knowledge, this is the first demonstration of an antenna/RCL configuration built using reported micro-fabrication techniques.

A number of surface micromachined patch antennas have been demonstrated in the past. In [7], Q-band micro-patch antennas were implemented on high resistivity silicon substrate using the surface micromachining technology composed of conventional thick photoresist lithography and copper metal plating process. An air-filled elevated microstrip antenna resonating at 25GHz based on surface micromachining technology is fabricated and characterized in [8]. The fabrication process used is a combination of the epoxy-core conductor technique, laser machining and electroplating bonding. The patch is fed by a vertical epoxy-core metal-coated micromachined probe and supported by several posts. In [9], a 60GHz 2x1 patch array antenna is designed and fabricated using micromachining technology fully compatible with commercial CMOS process. The antenna is supported with a feeding post and two additional supporting metal posts located at the virtual ground of the patch. Antenna elements separated by 0.8λ are fed by a corporate CPW based network.

In this paper, we demonstrate an all copper, air-cavity backed patch antenna designed for 36GHz operation within a 4x4 phased array. The patch is supported by two metallic posts, which along with the pulled-up cavity walls contribute to the emergence of another band at 28GHz. Interestingly, the lower band characteristics resemble the performance of a monopole, while in the higher band antenna performs as a cavity backed patch. The antenna is built using a sequential micro-fabrication technique, i.e. the *PolyStrataTM* process [10] developed by Rohm and Haas (see Fig. 1).

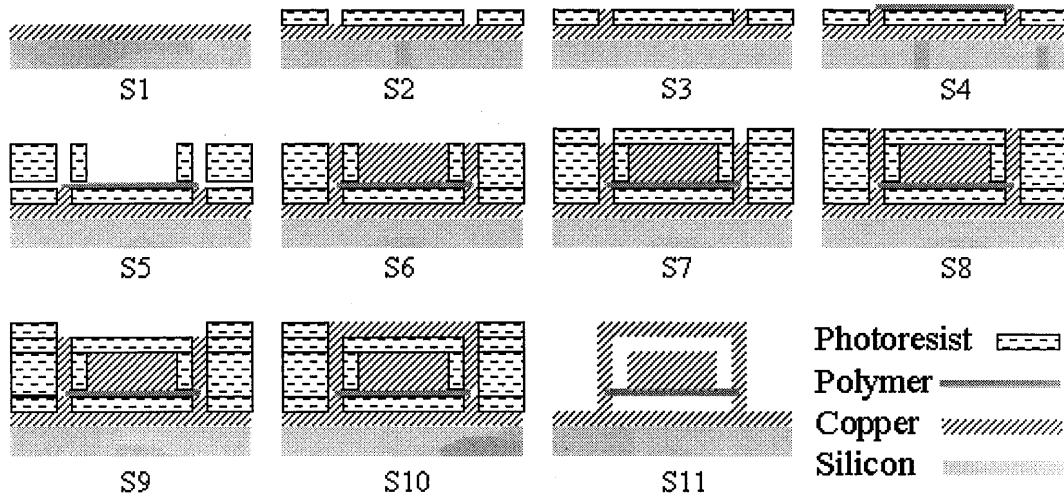


Figure 1. Simplified sketch of the steps undertaken in the sequential building process (left to right, top to bottom). The end result is a non-uniform air-polymer recta-coax comprised of 5 structural layers (extension to 10 layers is obvious).

As seen, the five level recta-coax structures are built up layer by layer by depositing a uniform copper stratum (layer 1), and sequence of strata comprised of photo-resist and copper (layers 2, 4, and 5). For this 5-layer process, the polymer support is a part of the 3rd layer. Once the structure is built, the resist is drained through the holes in the top and side walls. These openings are referred to as release holes. A single reticle of a 6" wafer built using the same process, however with 10 strata, is shown Fig. 2. Three prototypes of the designed antenna with the launch are in the top right corner.

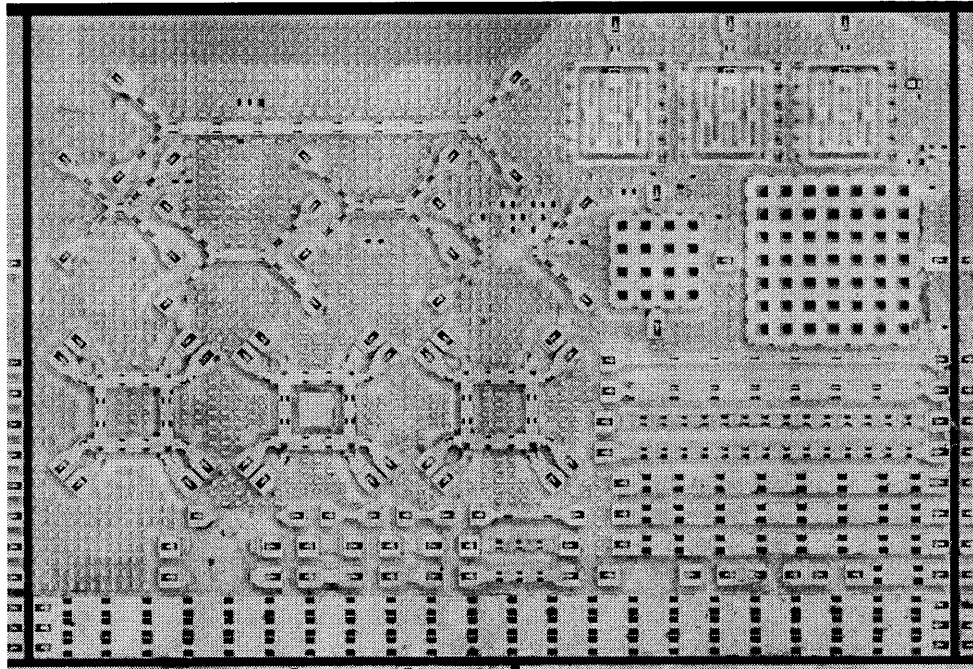
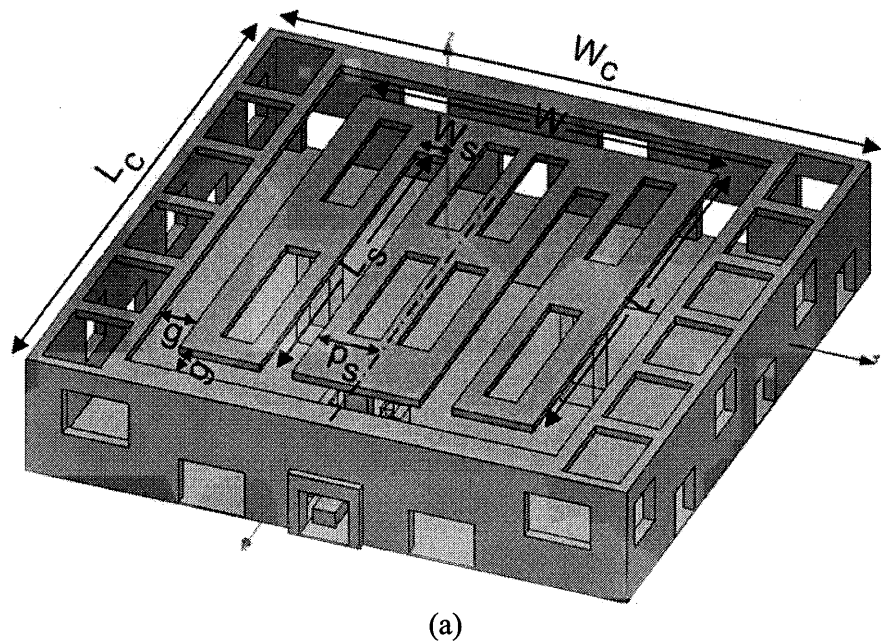


Figure 2. A single reticle on a fabricated 6" wafer. Antennas are in the top right corner.

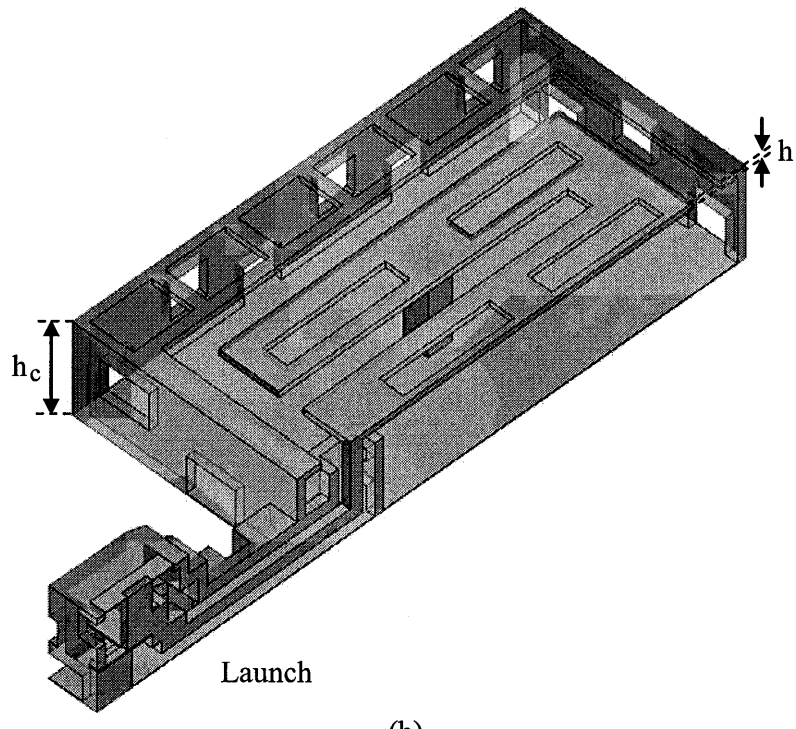
The paper is organized as follows. The designed antenna along with the parameters that define its structure are described in Section 2. In Section 3, a set of Ansoft's HFSS [17] based computational studies aimed to demonstrating effects of various parameters on the dual-band performance is provided. Measurements on the realized antenna, along with the computed far-fields are given in Section 4, while a brief description of the 4x4 phase array demonstration is given in Section 5.

2. Antenna Description

Structure and dimensional parameters of the proposed cavity backed patch antenna are shown in Fig. 3. Sacrificial photoresist is removed from the cavity through release holes in its walls and in the patch. There are 8 release holes on the patch, and a total of 34 holes in the pulled-up cavity walls.



(a)



(b)

Figure 3. Structure of the proposed antenna (a) without launch, (b) with launch (half of the geometry); $L_c=W_c=3640 \mu\text{m}$, $L=2770 \mu\text{m}$, $W=2150 \mu\text{m}$, $L_s=2350 \mu\text{m}$, $w_s=195 \mu\text{m}$, $p_s=390 \mu\text{m}$, $g=235 \mu\text{m}$, $h_c=760 \mu\text{m}$, $h=50 \mu\text{m}$.

Benefits of using a cavity backing for the patch antennas are explained in the details of [12], along with a comprehensive list of references. The following advantages of cavity backed patch antennas are of interest for our antenna design. In a phased array antenna, cavities can prevent scan blindness, yield less coupling and improve good matching over wider scan angles. Furthermore, a patch antenna in a cavity enclosure can improve the radiation near and beyond the horizon; thus, a truly omnidirectional radiation pattern can be achieved. Another important feature of the proposed patch antenna is the incorporation of the two slits in the design. These slits are $2350\mu\text{m}$ long, $195\mu\text{m}$ wide and offset $390\mu\text{m}$ from the antenna symmetry plane (x - z plane). They are utilized to achieve good 50Ω impedance matching with the feeding rectangular coaxial line. Detailed description of the effects obtained with this modification of the patch will be demonstrated in the next section.

It is important to note that the patch antennas with slits are commonly referred in literature as E-shaped patches [13-15]. They are typically used to achieve either wide-band (broadband) or dual-band operation. As an antenna given in [9], proposed patch is supported with a feeding post (extension of the inner conductor of the feeding RCL) and two additional supporting metal posts located on the plane with zero E-field (virtual ground of the patch). Thus, these supporting posts do not affect the electric performance of the antenna at the design frequency of 36GHz. However, due to their presence, the second band with good impedance match appears at about 28GHz. This will also be demonstrated in the following sections. The inner and outer conductors of the 50Ω feeding RCL have dimensions of 139×100 and $300 \times 300\mu\text{m}^2$, respectively. All vertical walls are $70\mu\text{m}$ thick. The remaining dimensions are given in the figure. A half of the antenna geometry is redrawn in Fig. 3b together with the launch used for landing the CPW probes during measurements of single antenna electric parameters.

3. Parametric Studies

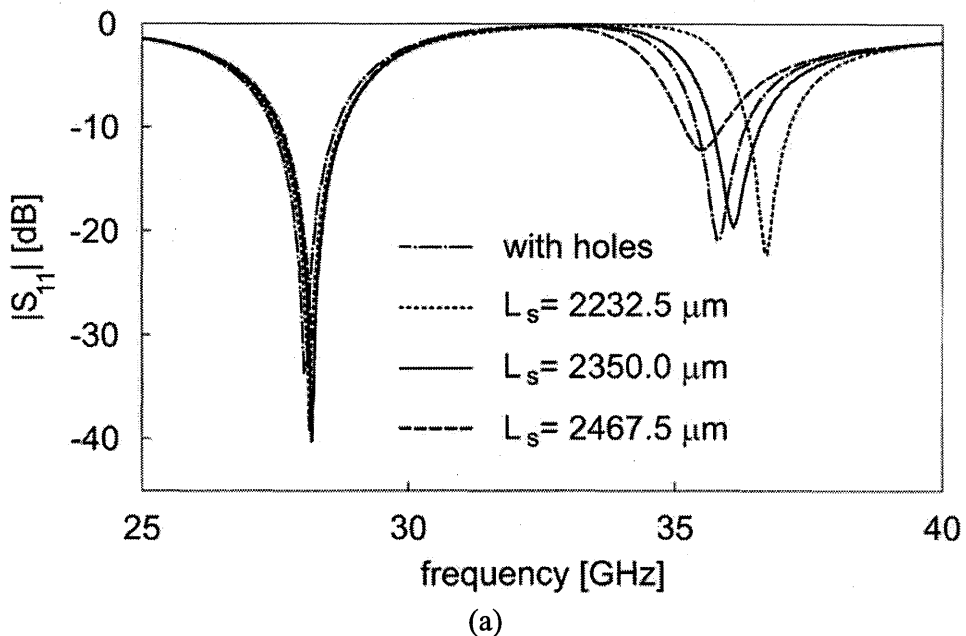
Several structural parameters are important for the performance of antenna shown in Fig. 3. In this section, the return loss variation as a function of following parameters is studied: slit length (L_s), slit width (w_s), slit position (offset) with respect to the antenna symmetry plane (p_s), width of the gap between the patch and the cavity top walls (g) and patch length (L). Antenna without release holes with dimensions given in Fig. 3 is denoted as reference antenna. Antenna with the same dimensions but having release holes (as shown in Fig. 3) is Antenna1. Remaining radiators, as listed in the first column of Table 1, have no release holes and all dimensions the same as reference antenna, except for one “unique” dimension which value is listed in the second column. The launch (shown in Fig. 3b) has not been included in these studies, however, its effects are considered in the following section.

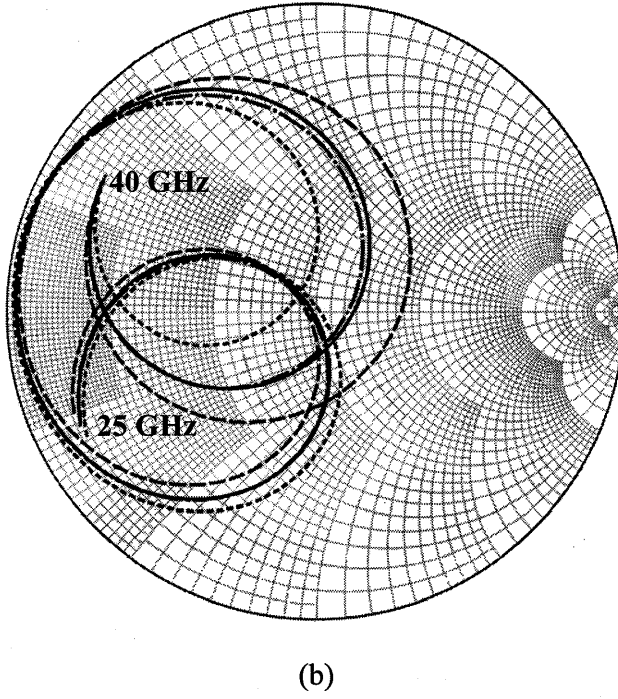
Table 1 Simulated dual-frequency performance of the antenna shown in Figure 3 †.

	unique dimension	f_1 (GHz), BW(GHz,%)	f_2 (GHz), BW(GHz,%)
Reference	none	28.20, 1.23, 4.36	36.10, 0.90, 2.49
Antenna1	release holes	28.05, 1.20, 4.28	35.80, 0.93, 2.60
Antenna2A	$L_s=2232.5 \mu\text{m}$	28.15, 1.25, 4.44	36.75, 0.75, 2.04
Antenna2B	$L_s=2467.5 \mu\text{m}$	28.20, 1.20, 4.26	35.50, 0.70, 1.97
Antenna3A	$w_s=300 \mu\text{m}$	28.00, 1.15, 4.11	36.55, 0.90, 2.46
Antenna3B	$w_s=100 \mu\text{m}$	28.40, 1.25, 4.40	35.55, 0.75, 2.11
Antenna4A	$p_s=440 \mu\text{m}$	28.40, 1.35, 4.75	36.05, 0.75, 2.08
Antenna4B	$p_s=340 \mu\text{m}$	27.95, 1.05, 3.76	36.20, 0.92, 2.54
Antenna5A	$g=300 \mu\text{m}$	29.00, 1.28, 4.41	36.00, 0.96, 2.67
Antenna5B	$g=150 \mu\text{m}$	26.50, 0.80, 3.02	36.25, 0.85, 2.34
Antenna6A	$L=2870 \mu\text{m}$	27.65, 1.17, 4.23	35.05, 0.81, 2.30
Antenna6B	$L=2670 \mu\text{m}$	28.70, 1.25, 4.36	37.20, 0.99, 2.66

† Antenna parameters are given in Figure 1 except for the “unique dimension“ specified in the table. The launch is not included in the simulations.

The first dimensional parameter to be studied is the slit length L_s ($L_s=2232.5 \mu\text{m}$ for Antenna2A and $L_s=2467.5 \mu\text{m}$ for Antenna2b; note that these two values for L_s are equal to $0.95L_{s0}$ and $1.05L_{s0}$, respectively, where $L_{s0}=2350 \mu\text{m}$ for the reference antenna). Simulated return loss versus frequency as well as complex reflection coefficient shown on the Smith chart, are given in Figure 4. Also shown are the results for Antenna1 (the only one with release holes).





(b)

Figure 4. Simulated (a) $|S_{11}|$ and (b) S_{11} shown on the Smith chart for Antenna1 (with release holes), Antenna2A ($L_s=2232.5 \mu\text{m}$) and Antenna2B ($L_s=2467.5 \mu\text{m}$) studied in Table 1. The solid lines are for the reference antenna ($L_s=2350.0 \mu\text{m}$).

The results for the two resonant frequencies and their corresponding return loss better than 10dB bandwidths, along with the results for all other studies of this section, are summarized in Table 1. It is noticed that the second resonance frequency f_2 for the Antenna1 is 35.8 GHz, slightly smaller than 36.1GHz for the reference antenna. The traces of S_{11} on the Smith chart for the two antennas (Antenna1 and reference) are very close to each other. To reduce computational time the holes are excluded from further studies reported in this section. Their effect on the antenna performance (for example on f_2) can be easily compensated for in the final design by fine tuning some of the parameters studied here. It is obvious from Fig. 4 that L_s can be effectively used to tune f_2 of the antenna, while the first resonant frequency f_1 remains almost unaffected by this parameter.

The next two studied parameters are slit width w_s (Antenna3A: $w_s=300\mu\text{m}$, Antenna3B: $w_s=100\mu\text{m}$, Reference: $w_s=195\mu\text{m}$), and slit position p_s (Antenna4A: $p_s=440\mu\text{m}$, Antenna4B: $p_s=340\mu\text{m}$, Reference: $p_s=390\mu\text{m}$). The results are shown in Figs. 5-7. The input impedance shown in Fig. 7 is de-embedded to the plane 100μm underneath the patch (at the end of the feeding RCL). It is observed that studied parameters w_s and p_s affect both frequencies (f_1 and f_2), and thus can be used for their tuning. Note also that for

the studied ranges of two parameters, the changes in f_2 are significantly larger for w_s while variation of f_1 is about the same. As seen in Fig. 7, larger variations of the antenna resistance (R) and reactance (X) are observed for larger values of p_s .

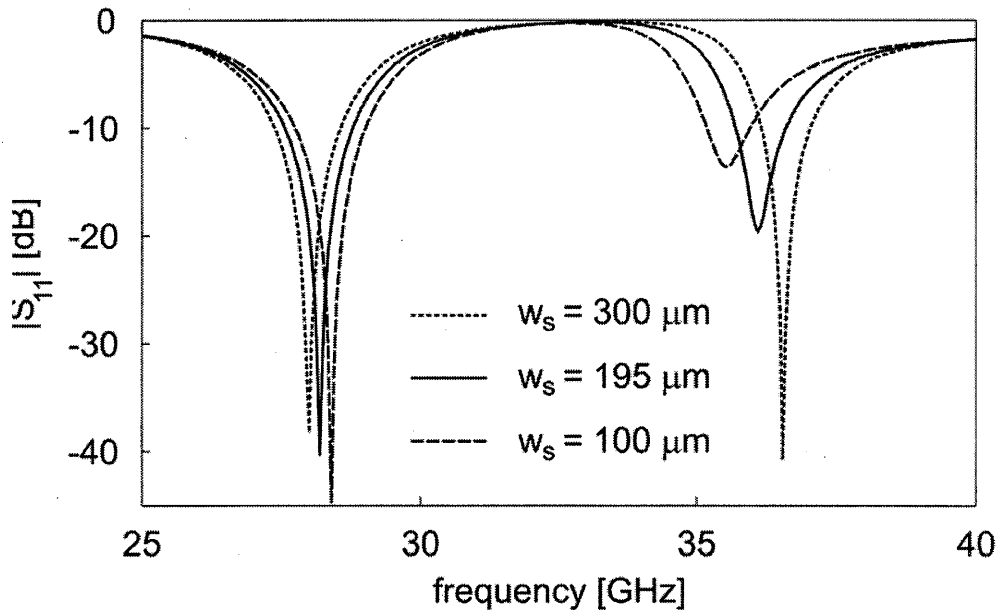


Figure 5. Simulated $|S_{11}|$ against frequency for Antenna3A ($w_s=300 \mu\text{m}$) and Antenna3B ($w_s=100 \mu\text{m}$) studied in Table 1. The solid line is for the reference antenna ($w_s=195 \mu\text{m}$).

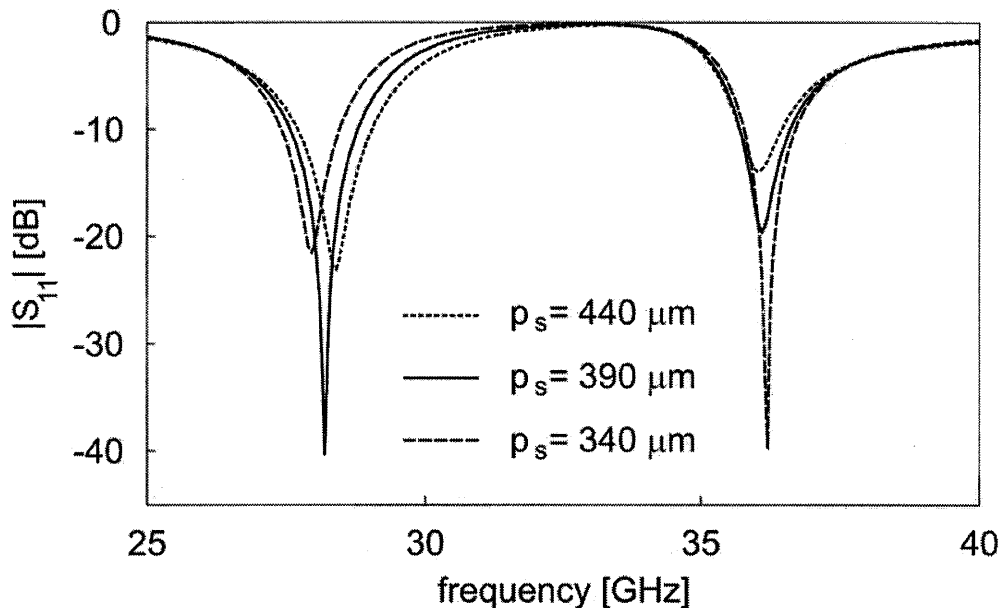


Figure 6. Simulated $|S_{11}|$ against frequency for Antenna4A ($p_s=440 \mu\text{m}$) and Antenna4B ($p_s=340 \mu\text{m}$) studied in Table 1. The solid line is for the reference antenna ($p_s=390 \mu\text{m}$).

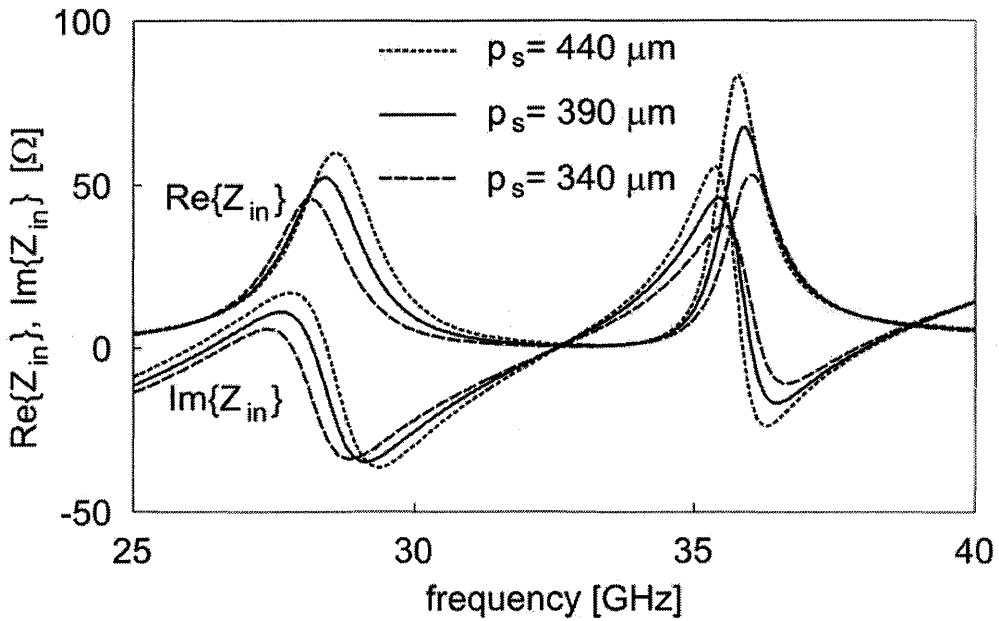


Figure 7. Simulated $\text{Re}\{Z_{\text{in}}\}$ and $\text{Im}\{Z_{\text{in}}\}$ against frequency for Antenna4A ($p_s=440 \mu\text{m}$) and Antenna4B ($p_s=340 \mu\text{m}$) studied in Table 1. The solid line is for the reference antenna ($p_s=390 \mu\text{m}$).

Finally, the last two studied parameters are the gap between the patch and the cavity top walls g (Antenna5A: $g=300\mu\text{m}$, Antenna5B: $g=150\mu\text{m}$, Reference: $g=235\mu\text{m}$) and patch length L (Antenna6A: $L=2870\mu\text{m}$, Antenna6B: $L=2670\mu\text{m}$, Reference: $L=2770\mu\text{m}$). The feeding point is maintained at the radiating edge of the patch for all three studied values of L . Effects on the return loss are depicted in Figs. 8 and 9. It is observed that f_2 is almost unaffected by g , while f_1 is very sensitive to this parameter value. Results of Fig. 9 demonstrate a well known fact that the longer patches have smaller resonant frequency (f_2 is decreased when L is increased). Note the same trends for f_1 and f_2 (they both decrease when L is increased) while these trends were opposite for the other parameters studied above.

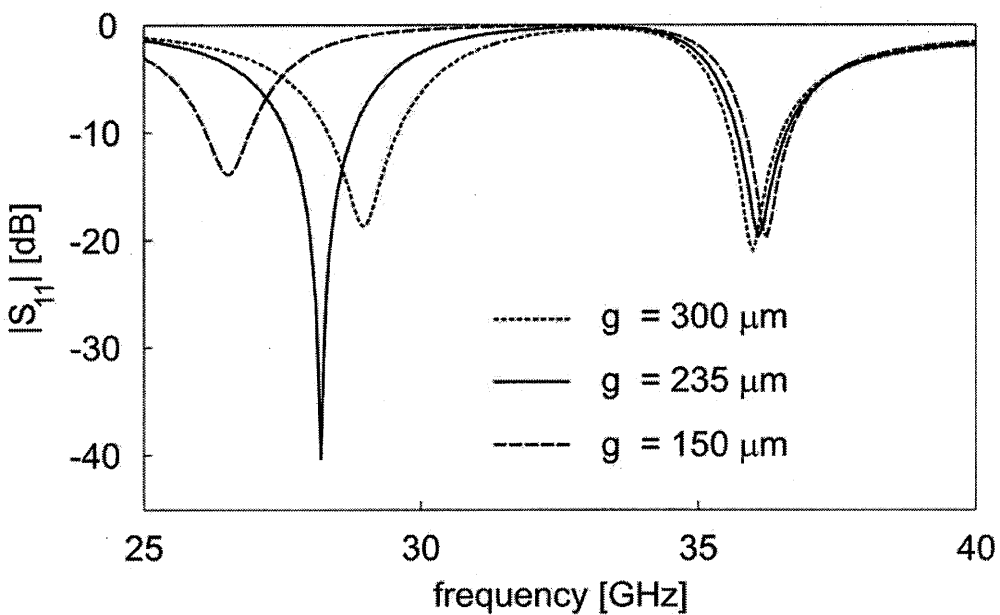


Figure 8. Simulated $|S_{11}|$ against frequency for Antenna5A ($g=300 \mu\text{m}$) and Antenna5B ($g=150 \mu\text{m}$) studied in Table 1. The solid line is for the reference antenna ($g=235 \mu\text{m}$).

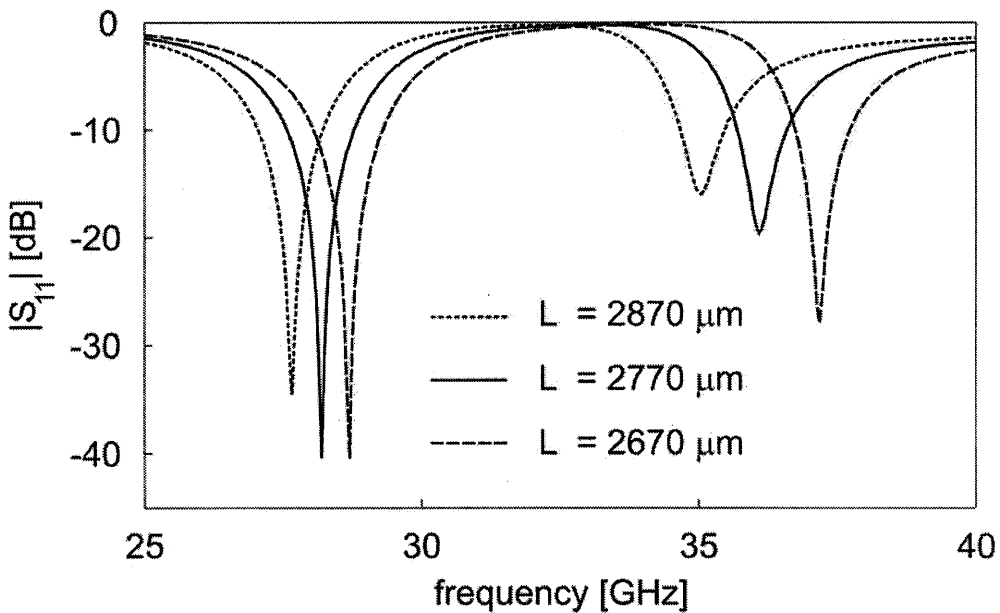


Figure 9. Simulated $|S_{11}|$ against frequency for Antenna6A ($L=2870 \mu\text{m}$) and Antenna6B ($L=2670 \mu\text{m}$) studied in Table 1. The solid line is for the reference antenna ($L=2770 \mu\text{m}$).

4. Performance of the Fabricated Antenna

Antenna described in sections 2 and 3 is fabricated using the PolyStrata™ [10] process. Comparison of measured and simulated return loss against frequency is shown in Fig. 10. As seen, the agreement is quite good. The measured and simulated results for resonance frequencies f_1 and f_2 and corresponding -10 dB bandwidths are summarized in Table 2.

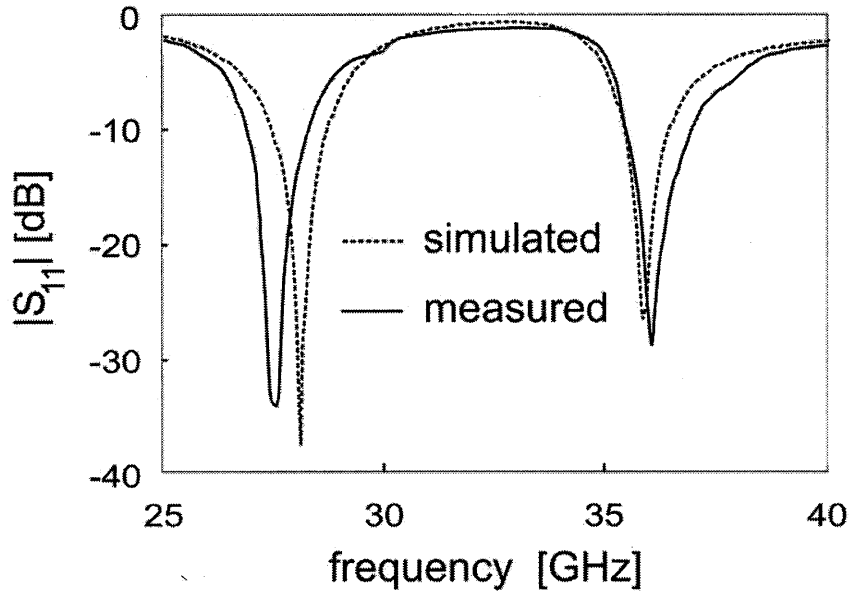


Figure 10. Measured and simulated $|S_{11}|$ against frequency for the fabricated antenna with the launch shown in Figure 3b.

Table 2 Comparison of measured and simulated dual-frequency performance of the antenna with the launch shown in Figure 3b.

	f_1 (GHz), BW(GHz,%)	f_2 (GHz), BW(GHz,%)
Measured	27.5, 1.40, 5.1	36.1, 1.50, 4.1
Simulated	28.1, 1.25, 4.4	35.9, 1.00, 2.8

Simulated E-plane (x-z plane) and H-plane (y-z) radiation patterns at two frequencies f_2 and f_1 for Antenna1 studied in Table 1 are shown in Figs. 11 and 12, respectively. The antenna is simulated above an infinite ground plane, thus there is no radiation into the lower half space (for $\theta < -90^\circ$ and $\theta > 90^\circ$). Maximum gains at frequencies f_2 and f_1 are 5.7dBi (at broadside) and 5.1dBi (at the horizon), respectively. Simulated E-plane cross-polarization radiations are negligible at f_2 . In the H-plane, the cross-polarization levels are below -15dB. The monopole like radiation pattern at f_1 is due to the currents flowing onto the supporting metal posts.

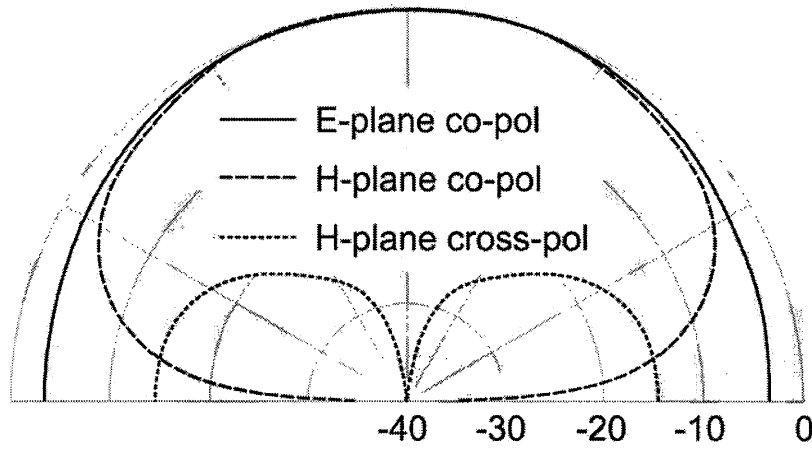


Figure 11. Simulated E-plane (x-z plane) and H-plane (y-z) radiation patterns at resonance f_2 for Antenna1 studied in Table 1. Gain=5.7 dBi.

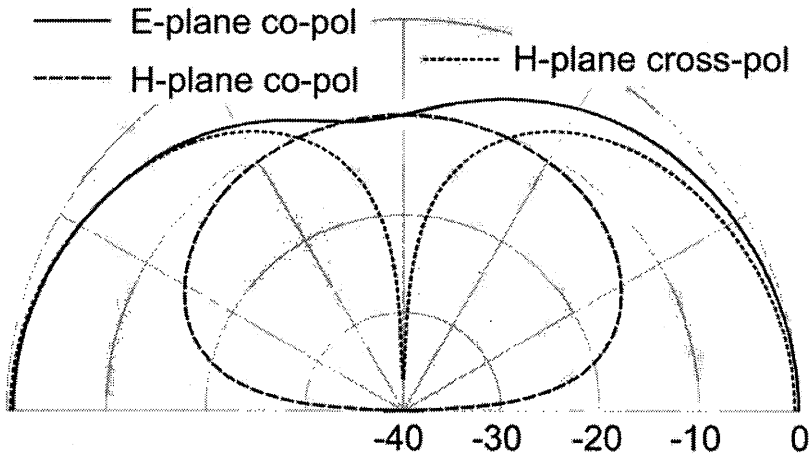


Figure 12. Simulated E-plane (x-z plane) and H-plane (y-z) radiation patterns at resonance f_1 for Antenna1 studied in Table 1. Gain=5.1 dBi.

5. Phased Array

The designed antenna is aimed to be a radiator for the 4x4 phased array operating at 36GHz. The array topology along with the RCL feeding network is shown in Fig. 13. Not shown in the figure is the RCL based 16x16 Butler matrix built with the two coaxial layers, total of 8 smaller 4x4 Butler matrices connected through the interconnecting and phase correction networks. The beam-forming of 16 independent beams, shown in Fig. 13b) imposes additional requirements on the antenna design. Specifically, it is desired that the radiation pattern in E- and H-planes be very similar. This minimizes the

differences in the total array gains measured on the beams furthest offset from broadside direction.

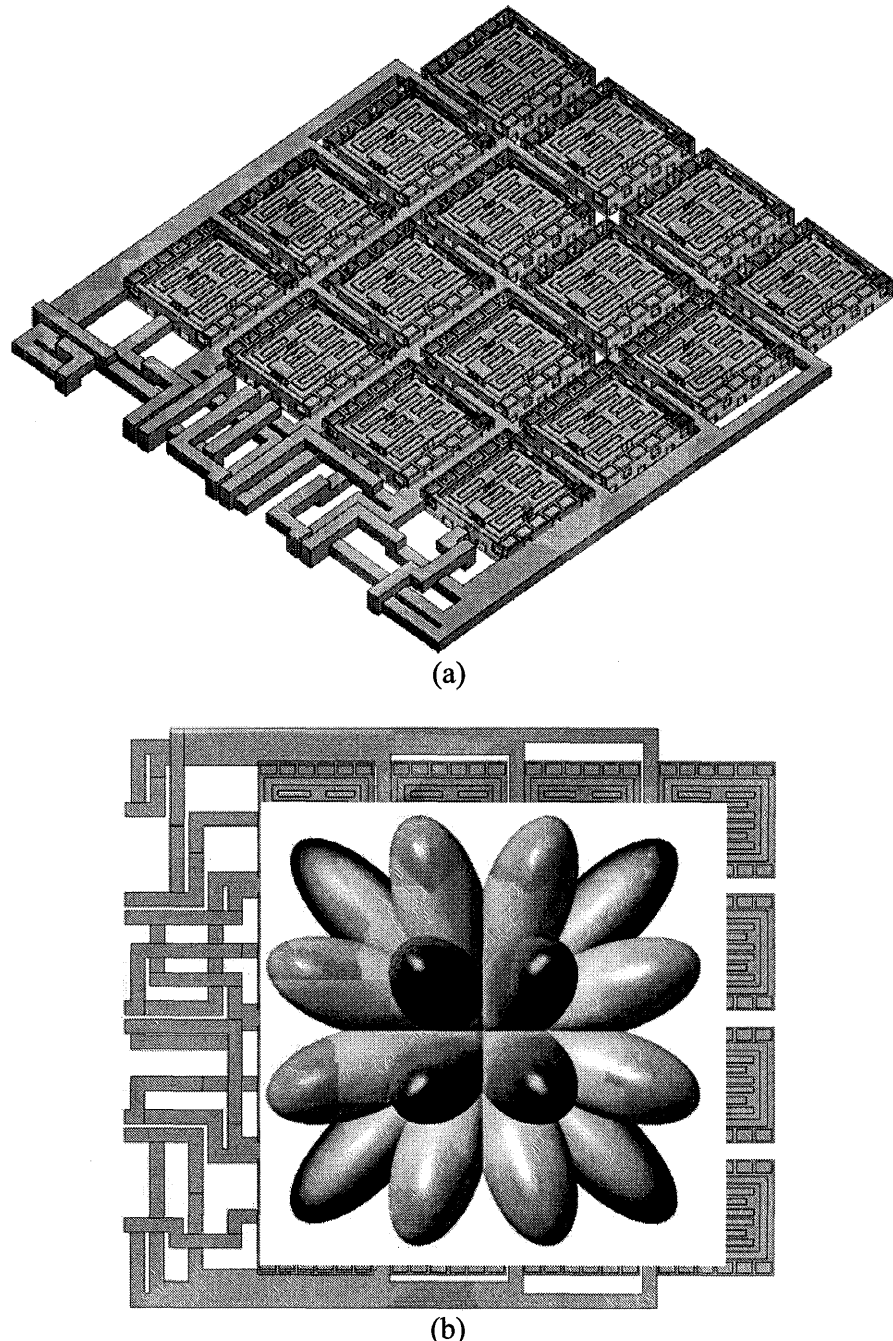


Figure 13. 4x4 antenna array with integrated RCL based feeding network (a) and computed 16 beams available through the 16x16 Butler matrix (b).

6. Summary

A surface micromachined cavity backed patch antenna operating at 36GHz is demonstrated in this work. The antenna is designed for integration with a recta-coax based 16x16 Butler matrix and subsequent phased array demonstration. Due to the requirements imposed by the PolyStrata™ surface micromachining process, the patch is fed by a recta-coax probe and it is supported by two metallic posts. The cavity is air filled, and several openings are integrated with the antenna to allow the release of sacrificial material. The whole structure is build from ten layers having overall height above the silicon of about 760 μ m. About 3% bandwidth (return loss better than 10dB) is measured, and excellent agreement with HFSS simulations verifies that the radiation pattern will be symmetric in both planes, with efficiency above 95%, low cross-polarization, and gain around 6dBi. Owing to the metallic supports and pulled-up cavity walls, a second band around 28GHz is also demonstrated. A monopole like pattern with excellent symmetry and cross-polarization for up to 30° above the ground, gain of about 5dBi and about 5% return loss bandwidth is obtained. Although lower frequency band is not aimed for the phased array, the detailed parametric study of the antenna for both bands is conducted and interesting findings are reported.

Acknowledgments

This work was supported by the DARPA-MTO under the 3D Micro-Electromagnetics Radio Frequency Systems (3d MERFS) program. Authors also acknowledge Mr. K. Vanhille, Mr. M. Buck, Prof. Z. Popovic, Dr. S. Rondineau, and Mr. Y. Saito from the University of Colorado at Boulder, Dr. G. Potvin from BAE Systems, Rohm and Haas microfabrication team, Dr. W. Wilkins from Mayo Foundation, Mr. E. Adler from ARL, and Dr. J. Evans from DARPA for numerous interactions and contributions to this work.

References

- [1] G.M. Rebeiz, *RF MEMS theory, design, and technology*. Hoboken, NJ: John Wiley & Sons, Inc., 2003.
- [2] R. Chen, "Micro-fabrication techniques," *Wireless Design and Development*, pp. 16-20, Dec. 2004.
- [3] J.-B. Yoon, B.-I. Kim, Y.-S. Choi, and E. Yoon, "3-D construction of monolithic passive components for RF and microwave ICs using thick-metal surface micromachining technology," *IEEE Trans. Microwave Theory Tech.*, vol. 51, no. 1, pp. 279-288, Jan. 2003.

- [4] I. Jeong, S.-H. Go, J.-S. Lee, and C.-M. Nam, "High-performance air-gap transmission lines and inductors for mm-wave applications," *IEEE Trans. Microwave Theory Tech.*, vol. 50, no.12, pp. 2850-2855, Dec. 2002.
- [5] I. Llamas-Garro, P. Hall, "A low loss wideband suspended coaxial transmission line," *Microw. Opt. Technol. Lett.*, vol. 43, pp. 93–95, Oct. 2004.
- [6] D. Filipovic, et. all, "Quasi-planar μ -coaxial structures for milimeter wave applications", *Proc. 2006 GomacTech*, San Diego, CA, Mar. 2006.
- [7] M.L. Ha, Y. Cho, C. Pyo, and Y. Kwon, "Q-band Micro-patch Antennas implemented on a High Resistivity Silicon substrate using the Surface Micromachining Technology," *Proc. of IEEE International Microwave Symposium*, Fort Worth, TX, pp.1189-1192, June 2004.
- [8] B. Pan, Y. Yoon, J. Papapolymerou, M.M. Tentzeris and M.G. Allen, "A High Performance Surface-Micromachined Elevated Patch Antenna," *Proc. of the IEEE-APS/URSI Symposium*, Washington, DC, pp. 397-400, July 2005.
- [9] J.G. Kim, H.S. Lee, H.S. Lee, J.B. Yoon, and S. Hong, "60-GHz CPW-Fed Post-Supported Patch Antenna Using Micromachining Technology," *IEEE Microwave and Wireless Components Letters*, pp. 635-637, Oct. 2005.
- [10] D. Sherrer and J. Fisher, "Coaxial waveguide microstructures and the method of formation thereof," *U.S. Patent Application Publication No. US 2004/0 263 290A1*, Dec. 30, 2004.
- [11] Ansoft Inc., High Frequency Structure Simulation (HFSS), Ver. 9.2, [Online] Available: <http://www.ansoft.com>
- [12] N. C. Karkamar, "Investigations into a cavity-backed circular-patch antenna," *IEEE Trans. Antennas Propag.*, vol. 12, pp. 1706–1715, Dec. 2002.
- [13] F. Yang, X.-X. Zhang, X. Ye, and Y. Rahmat-Samii, "Wide-band E-shaped patch antennas for wireless communications," *IEEE Trans. Antennas Propag.*, vol. 49, pp. 1094–1100, July 2001.
- [14] K. L. Wong and W. H. Hsu, "A broadband rectangular patch antenna with a pair of wide slits," *IEEE Trans. Antennas Propag.*, vol. 49, pp. 1345–1347., Sep. 2001.
- [15] Y. Ge, K. P. Esselle, and T. S. Bird, "E-shaped patch antennas for highspeed wireless networks," *IEEE Trans. Antennas Propag.*, vol. 52, no. 12, pp. 3213–3219, Dec. 2004.

Design and Development of Aircraft Antenna Interface Adapters – Conformal Couplers for USM-464 (EW) Test Applications

Thomas G. Campbell, M. C. Bailey and C. J. Reddy
Applied EM, Inc., 144 Research Drive, Hampton, VA 23666

ABSTRACT

An advanced Aircraft Antenna Interface Adapter (AAIA)-Conformal Coupler [1] concept was designed and developed to facilitate testing of aircraft electronic warfare (EW) antenna systems. This new concept eliminates the use of expensive, hard-to-handle antenna couplers (such as the ones with USM-464 systems) that require removal of aircraft radomes. The AAIA-Conformal Coupler design integrates near field EM analysis and testing methods along with conformal antenna materials technology to provide a lightweight, flexible and easy-to-use antenna coupler design approach. The feasibility of the AAIA-Conformal Coupler concept has been demonstrated and tested for the electronic warfare (EW) antennas on C-130 Combat Talon II, ALQ-172 systems. The AAIA concept includes radome “boots,” near field probes and reticulated radio frequency (RF) absorbing materials with Unishield® conductive coatings. The overall EM design of the AAIA-Conformal Coupler includes accurate positioning of the system in the near field of the aircraft antennas. The AAIA-Conformal Coupler exhibits absorption and shielding characteristics that reduces RF emissions on the flight line significantly below the permissible exposure levels (PEL) for antenna (EW) test operations. The AAIA design enables rapid checkout testing procedures with physical characteristics to withstand extreme environmental flight line conditions.

(1) *Introduction*

The design concept of Aircraft Antenna Interface Adapters (AAIA) enables maintenance personnel the capability to quantify and test aircraft RF antenna systems without removing aircraft components. The capability to provide accurate, quantitative, insitu radio frequency measurements will directly benefit the U. S. Air Force Special Operations Forces on Combat Talon and Gunship aircraft, and the Air Combat Command on the bomber fleets. The AAIA design concept exhibits flexible and lightweight conformal couplers that will support CTS/USM-464 testing through its projected life of 2042.

Currently, the AN/USM-464 countermeasures test set (CTS) provides end-to-end testing of aircraft antennas that are used for countermeasures systems, radar homing and warning systems, and integrated power-management systems. The C-130 Combat Talon II aircraft with EW antenna locations are shown in Figure 1 which includes forward and rear sector

coverage antennas and omni receive from both forward and rear locations on the aircraft. As shown in Figure 2, CTS procedures require attaching antenna couplers to the aircraft antennas and this procedure requires removal of aircraft radomes at all antenna locations except for the aft sector coverage antennas.

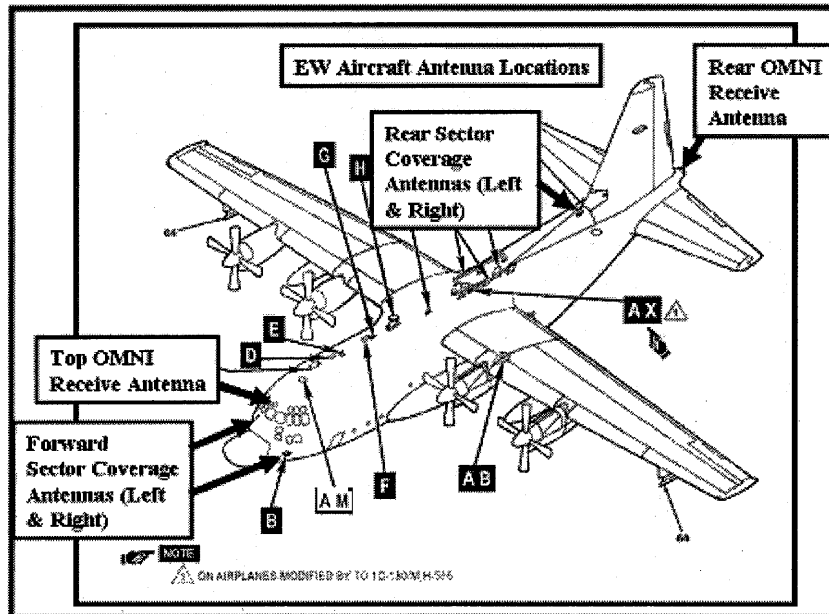


Figure 1 – C-130 Combat Talon II Aircraft showing antenna systems used for countermeasures.

Current antenna couplers for CTS testing are designed to attenuate, inject, and receive signals from the aircraft antennas during the various EW test procedures. The rear (aft) sector coverage antennas are flush mounted to the electronic enclosures as shown (in Figure 2). In this installation, the antenna couplers are attached directly to the antenna surfaces as shown. Even though the primary goal for all CTS testing is to provide efficient tools to accomplish all flight line testing, this process can take as many as 36 hours to perform.

The Aircraft Antenna Interface Adapters (AAIA)-Conformal Couplers will enable maintenance personnel the capability to quantify and test aircraft RF antenna systems without removing aircraft components. Therefore, the design and development of the AAIA will enhance test operations using the AN/USM-464 countermeasures test set.

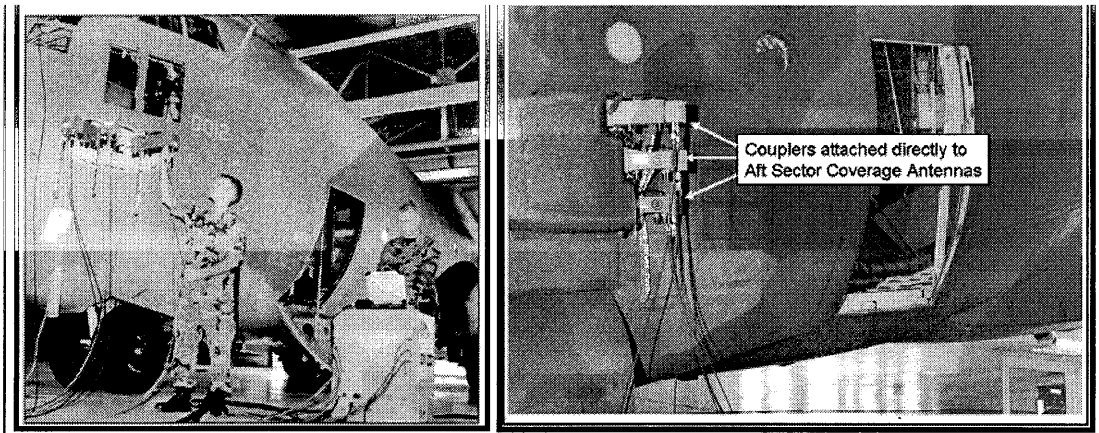


Figure 2 – Current test methods for USM-464 showing removal of aircraft radome and components for EW tests.

The currently fielded antenna couplers are designed for specific antenna locations on the aircraft and those designations are listed in Table I. Also listed are the three antenna (fielded) couplers that were provided to AEM in support the design and development of the AAIA-Conformal Coupler concept.

<i>Air Force Fielded Couplers Number</i>	<i>Forward Antenna Locations</i>	<i>Aft Antenna Locations</i>
#1 <i>(Tested by AEM)</i>	Top OMNI Receive Antenna	
#10		Rear OMNI Receive Antenna
#2 <i>(Tested by AEM)</i>	Forward Sector Antenna (AL)	Forward Sector Antenna (AL)
#4	Back Sector Antenna (BL)	Back Sector Antenna (BL)
#6 <i>(Tested by AEM)</i>	Center Sector Antenna (CL)	Center Sector Antenna (CL)

Table-I Coupler designations for Combat Talon II Aircraft antenna locations.

(2) Notional AAIA Design Approach

In order to conduct AAIA engineering designs, the EM characteristics of the aircraft (EW) antennas and the antenna coupler for the specific antenna locations, had to be determine. Supporting documents were obtained from Warner Robins AFB as well as access to typical antennas and couplers for the USM-464. Specifications such as frequency range, polarizations, power levels, isolation, and repeatability were considered within the limits of classification.

Notional design approaches for the AAIA were developed and reviewed with the Air Force and one of these approaches is shown in Figure 3. The basic concept consists of a radome “glove” that conforms to the shape and dimensions of the aircraft radome. The dimensions of the aircraft radomes were obtained from Air Force drawings and CAD mechanical drawings were used to fabricate radome mockups for AAIA development. A “blanket” of absorber is a major component of the AAIA design and is encapsulated by the AAIA envelope materials. The absorber materials are designed to provide EMI shielding and satisfy permissible emission standards for flight line personnel. The near field probes of the AAIA are integrated into the radome “glove” and properly positioned near the respective aircraft antenna. Silver laminated nylon, water proof materials could be provided for “blanket” materials and would be “breathable” and flexible. The AAIA must be capable of withstanding flight line operations and extreme environments.

Recognizing the main issues regarding RF absorber designs, the overall thickness of a multi-layer configuration is dependent upon the frequency range, size of the test antenna maximum radiated power levels, and test locations on the aircraft. Optimizing the design of the absorber “blanket” materials and the shielding characteristics of conductive the coatings, the RF leakage and signal radiation levels are reduced significantly.

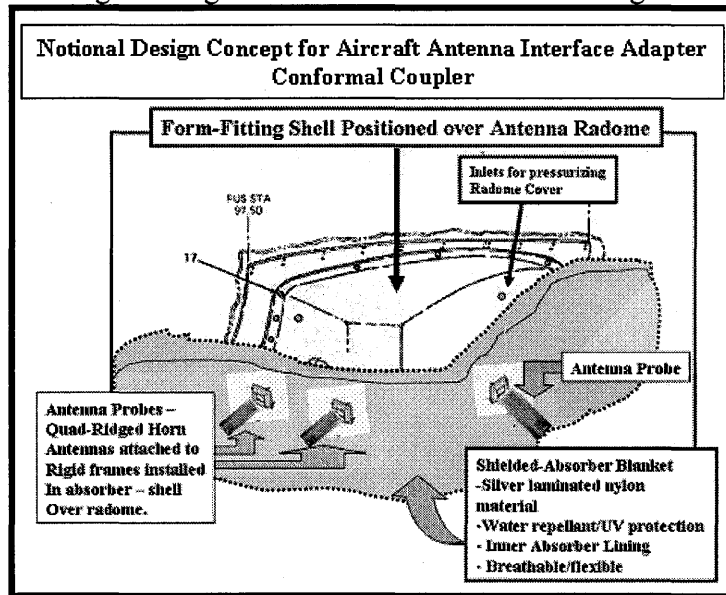


Figure 3 – AAIA design concept using shell cover over aircraft radome and anechoic material blanket to absorb and shield radiation.

An important feature of the AAIA design approach includes the use of Unitech's patented Unishield® conductive material coatings technology. The AAIA design features provide a conformal near-field anechoic-type covering that is used without removing aircraft components associated with the antenna system such as radomes, cables, etc. The AAIA will be a man-portable, state-of-the-art, covering that will “conform” to the aircraft surface, wing glove, nose radome, or section of the aircraft. The success of the AAIA-Conformal Coupler design provides an opportunity for a complete ‘overhaul’ of the antenna test procedures for EW aircraft, but the AAIA EM performance must always be

equal to or better than the currently fielded CTS antenna couplers. To demonstrate the AAIA design concept, two antenna positions for the C-130 Combat Talon II aircraft were selected for development – the *forward sector coverage antenna system* and the *top omni receive antenna*. Both of these antenna locations require removal of the radome, so the notional AAIA design approaches were directly applicable and beneficial for the associated test procedures.

(3) Near Field EM Performance of Sector Coverage and Top OMNI Receive Antennas for the C-130 Combat Talon II Aircraft

Before the design of the AAIA could be initiated, it was necessary to understand the EM performance of the aircraft antennas as well as the fielded antenna couplers used during CTS testing. Since the AAIA concept must operate in the near field environment of the aircraft antennas, the near field performance of each of the selected antenna systems had to be characterized. EM simulations were also conducted which provided valuable inputs in planning the experimental near field tests on the selected aircraft antennas.

Near Field Performance of Forward Sector Coverage Antennas

EM simulations (using FEKO) were conducted on the forward sector antennas that are positioned over a ground plane, and the orientations of the antennas (over the fuselage) were simulated using a ground plane configuration. The FEKO software provides the capability to analyze the near field in any of the three coordinate systems – planar, cylindrical and spherical. The EM analysis results established the parameters for planar near field tests that were conducted to verify EM predictions for AAIA designs. The radiation patterns of two (aircraft) horn antennas were measured and to simulate fuselage effects on the radiation pattern of the antennas. The experimental antenna is shown in Figure 4 along with photographs of the setup at VTAG. The assembly consisted of a trapezoidal ground plane with provisions for tilting each horn antenna.

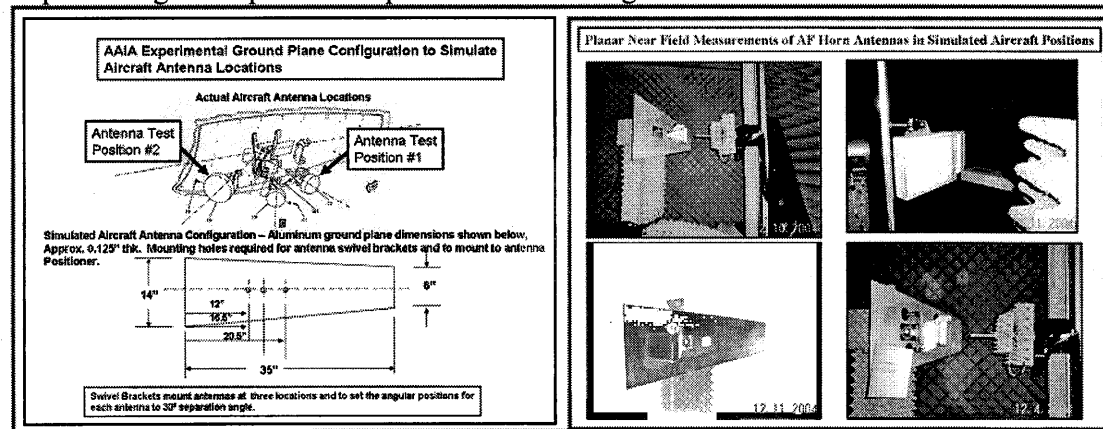


Figure 4 – Ground plane configuration for testing the aircraft EW antennas to determine near field effects.

A major objective of the near field experiments on the horn antennas was to determine if bifurcation occurred in the pattern amplitude at the desired probe position across the

entire frequency band of interest. These tests included near field scans, far field transformations (for gain and axial ration). Also, network analyzer (s-parameter) measurements were conducted for each horn antennas as well as actual aircraft antenna couplers provided by Warner-Robins AFB. Before measuring the near field patterns of the antennas over the ground plane, the frequency-impedance characteristics of the two horn antennas were measured.

Previous EM simulations (for the linearly polarized horn antenna) indicated that bimodal amplitude (bifurcation) effects will occur at certain frequencies and for specific near field conditions or probe positions. Near field measurement results were encouraging because bi-modal (bifurcation) effects did not occur for both horn antennas and for the (pre-selected) 8-cm probe position and as a function of frequency. The ground plane tests also determined that the proximity of the adjacent horn antennas did not affect the near field amplitude performance. In the first setup, the small horn antenna was positioned at the proper angular position with the ground plane. In the second ground plane setup, the large horn was positioned in the forward location very close to the ground plane, and in the third ground plane setup, both forward-looking horn antennas were tested together to determine interaction effects on near field radiation.

The sense of the polarization for each horn is right-hand circularly polarized as a meander line is used in the aperture plane. Eleven frequencies were scanned during each measurement for each waveguide band respectively and gain characteristics for each horn antenna were determined.

As indicated previously, preliminary EM simulations determined the sensitivity of the near field to power transfer as a sampling probe is positioned in the near field of the aircraft horn antennas. Finally, two probe positions were selected for near field checks; 4-cm and 8-cm away from the front face of the horn antennas. For experimental tests and upon closer inspection of pedestal positioning and probe controls, it was obvious that the 4-cm probe position could not be implemented. So, the 8-cm probe position was selected for all of the NF tests. These results for power density versus probe distance from the horn aperture are presented and discussed later in this report.

Examples of the near field test results on the antenna ground plane assembly are shown in Figures 5 and 6. In Figure 5, the ground plane effects on the near field amplitude are presented at several representative frequencies, 7GHz, 10 GHz, and 15 GHz. In Figure 6, near field characteristics for the three different antenna setups are presented at a single frequency, 7 GHz. In all of these tests, the quality of the amplitude (and phase) characteristics were maintained for all of the simulated positions for the forward sector coverage antenna system. The scattering that did occur and horn proximity produced minimal effects on the main amplitude and phase characteristics of the horn antennas. The fact that the horns are circularly polarized could be the primary reason for minimal effects on the near field patterns.

Comparison of Ground Plane Effects for Setup #1 versus Frequency

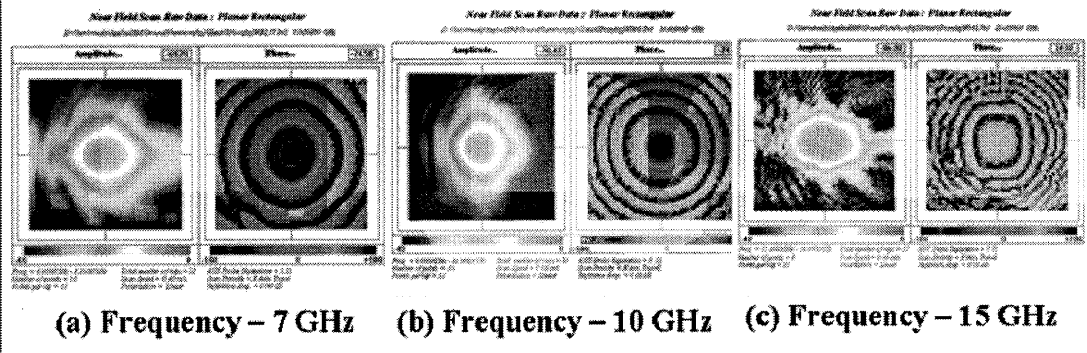


Figure 5 – Color plots of near field amplitude and phase for test setup #1 for three representative frequencies.

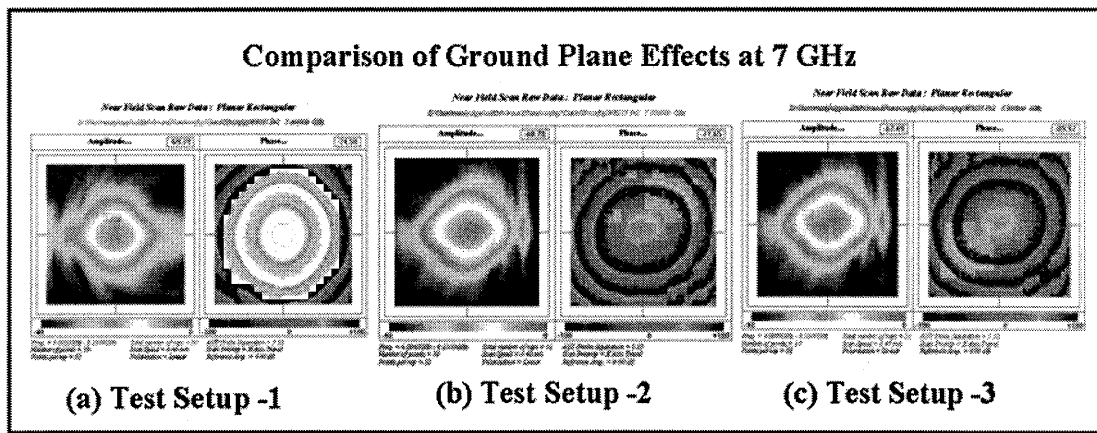


Figure 6 – Color plots of near field amplitude and phase for the three test setups at a single frequency – 7 GHz.

It can be seen that the amplitude lobe (at 8 cm) is well defined as well as the symmetry of the phase characteristics. Prior to testing these antennas, no information on the EM characteristics was available – especially in regard to gain, polarization, and bandwidth. So, these tests were very important to establish the basis for AAIA designs. The close proximity of the tilted ground plane did affect the pattern in one orthogonal plane more than the other but the effects are not severe.

Near Field Performance of Forward OMNI Receive (EW) Antenna

The forward OMNI receive aircraft antenna is located above the cockpit (as shown in Figure 1) and this antenna provides a wide angle radiation pattern that extends essentially 180-degrees centered on the nose of the aircraft. The tail OMNI receive antenna, which is located below the vertical fin, provides a similar pattern shape across the rear of the aircraft. Both antennas are classified so specific technical data on these antennas can not be provided. The general configuration of the forward antenna is shown in Figure 7 along with the S-parameter test results for that antenna.

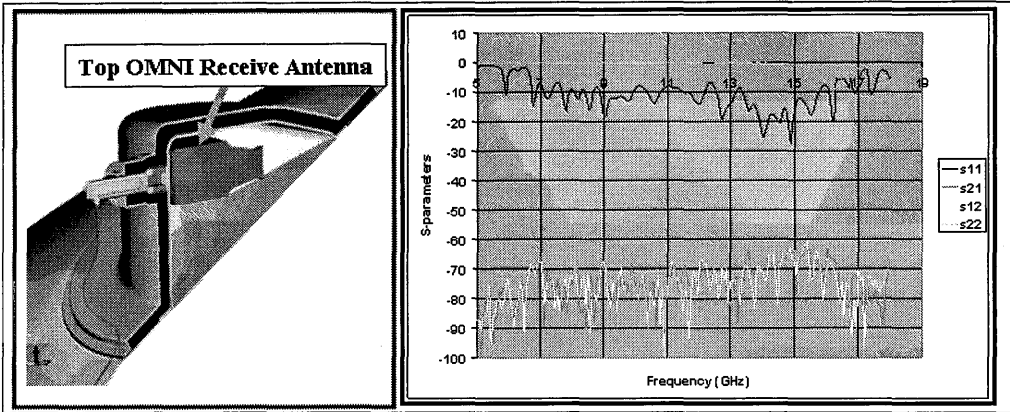


Figure 7 – General configuration of the top OMNI Receive aircraft antenna along with S-parameter test results.

Again as for the sector coverage horn antennas, the basic objective for this near field tests was to determine the near field amplitude characteristics of the OMNI Receive Antenna over the entire frequency range at a fixed probe position (of 8-cm) as selected previously during tests and simulations. After initial calibrations, the OMNI antenna was positioned on a vertical foam column and planar near field scans were conducted. The initial setup positioned the waveguide near field probe approximately 8-centimeters away from the front surface of the OMNI antenna. Test results verified that the 8-cm probe position is acceptable. Typical near field amplitude and phase plots at a representative frequency are shown in Figure 8. It can be noted that as observed for all the frequencies of interest, amplitude bifurcation effects did not occur for the 8-cm. probe position. Also, the phase distribution results indicated the polarization characteristics for the antenna.

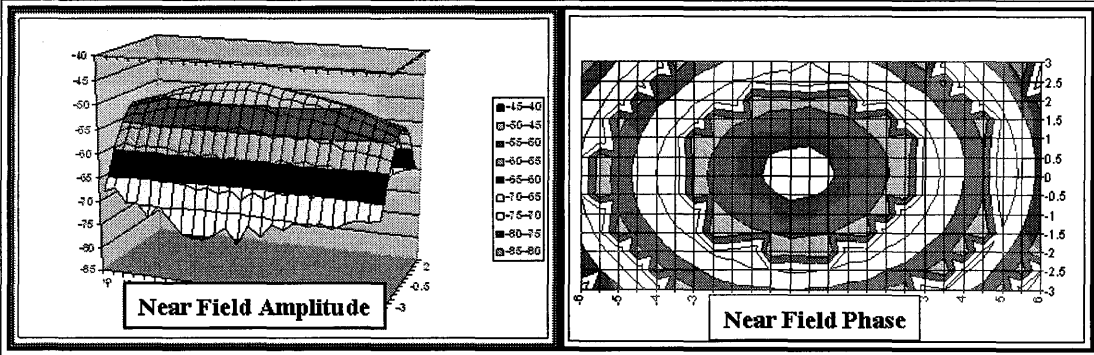


Figure 8 – Typical near field amplitude and phase characteristics for the top OMNI Receive aircraft antenna.

(4) EM Test Results on Selected Fielded Antenna Test Couplers

Fielded Antenna Couplers (#2 and #6) for the Sector Coverage Horn Antennas

Warner Robins AFB provided two fielded antenna couplers that are normally used for the forward sector coverage aircraft antennas and these couplers were used to provide

baseline EM performance characteristics for the AAIA design concept. EM tests included frequency response, insertion loss, and isolation characteristics. Photographs of the test setup at VTAG are shown in Figure 9.

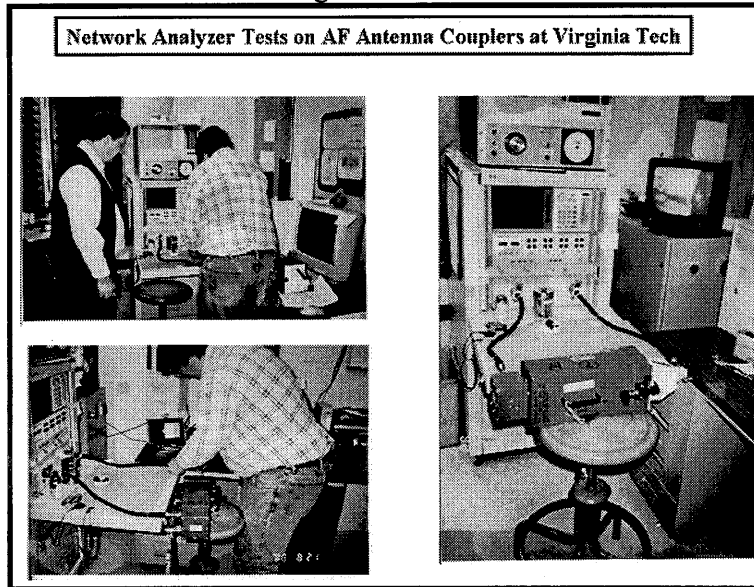


Figure 9 – Photographs of measurement setup at Virginia Tech for the antenna couplers for the countermeasures aircraft testing.

The isolation between ports J1 and J2 were measured while the appropriate horn antenna was attached for different combinations of 50-ohm terminations, etc. The test results indicated that signal variations could occur at specific frequencies due to detuning effects with the couplers directly attached to the horn antennas. Essentially, the basis for direct mounting the couplers to the horn antennas is to provide repeatable, calibrated, signal paths directly from the horn antennas to the couplers. But, signal variations during CTS tests are indeed possible depending upon the setup. Further tests indicated that the AF couplers are linearly polarized and not matched to the polarizations of the aircraft antennas. The insertion loss characteristics of the current AF couplers are presented in Figure 10 and the detuning effects can be noted in Figure 11. These results indicate that the couplers exhibit high loss characteristics across the frequency range and these effects were analyzed. S21 results indicated essentially the same bandwidth characteristics that were measured previously for the individual horns.

The S-parameters of small and large couplers are similar in characteristics. The average S11 (transmit port) and S22 (receive port) values are about -5dB (for the frequency range of interest). The worst case isolation between transmit and receive ports is about -10dB.

Insertion Loss Characteristics of the Large and Small Air Force Antenna Couplers – between horn antenna and J1 (Tx) and J2 (Rx) Ports

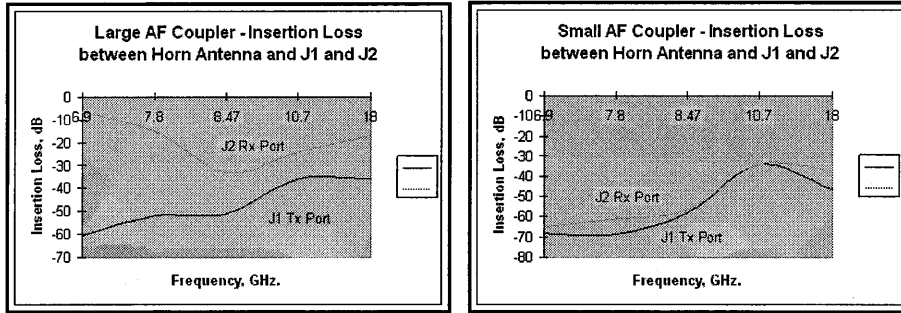


Figure 10 – Insertion loss characteristics of the large and small Air Force antenna couplers between horn antenna and J1 (Tx) and J2 (Rx) ports.

De-tuning Effects of Large and Small Air Force Couplers on the Aircraft Horn Antennas

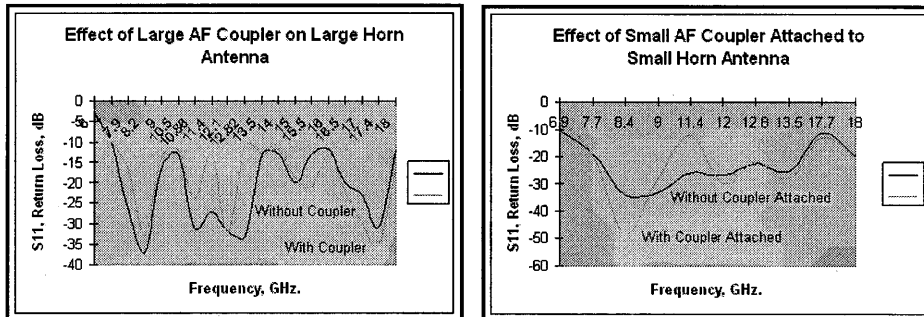


Figure 11 – De-tuning effects of the AF couplers when attached directly to the apertures of the aircraft horn antennas.

Fielded Antenna Coupler (#1) for the Forward OMNI Receive Antenna

Since the top OMNI Receive antenna is classified, it was necessary to conduct the EM near field tests at the Air Force Antenna Station – Ipswich, MA. The frequency response was measured with the forward OMNI antenna attached to the AF coupler and typical results are presented in Figure 12. These measurements were conducted primarily to determine the S12 (and S21) characteristics of the coupler and some detuning effects were also observed for this coupler attached to the test antenna.

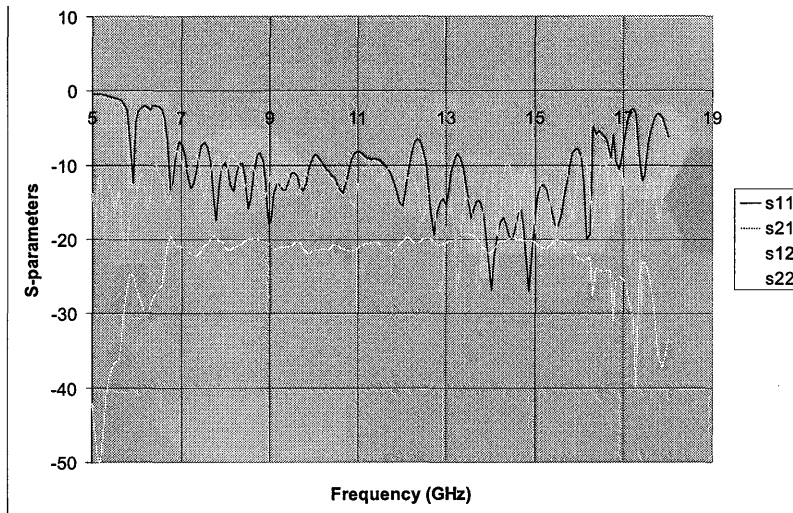


Figure 12 - S-parameter measurement results for top omni receive antenna attached to the antenna coupler.

(4) Aircraft Antenna Interface Adapter (AAIA)-Conformal Coupler Design

Near Field Probe Design

The overall AAIA design concept is analogous to a near field measurement system as its antenna probes will be in close proximity of the test antenna but stationary. As in near field measurements, the AAIA probes must exhibit minimal antenna interaction effects, must cover a wide frequency band (several WG bands), must exhibit high polarization purity, and have long-term stability and excellent repeatability. The antenna probes for the AAIA must satisfy the same performance specifications as already established for the fielded AF Antenna Couplers. So, in order to define the basic performance characteristics for the AAIA Antenna Probes, several near field probe designs were reviewed to determine design possibilities for the AAIA probe designs. Probes are used to sample the radiated EM fields of an antenna under test while minimally perturbing the incident field. Commercial probes are designed for minimum VSWR, long-term stability and repeatability.

Since right hand circular polarization is required for the AAIA, broadband, dual-ported probe designs were considered for the AAIA. Dual-ported probes provide orthogonal linear ports, high polarization purity, excellent port-to-port isolation, and can provide a thin-walled aperture to minimize probe-antenna interaction effects. The design reviewed emphasized a minimum thin-wall design to minimize probe to antenna interaction effects (low scattering aperture). Therefore, based on these requirements and probe design considerations, a quad-ridge waveguide design was selected as the near field probe for the AAIA-conformal coupler.

EM simulations were then conducted to determine the effect of the probe aperture size with probe positions from the horn antennas – especially in regard to power transfer and

coupling effects. Using the near field measurement results, EM simulation and modeling was conducted to determine the aperture size, orientation, position, and the overall configuration that will be required to ‘couple’ to the aircraft antennas as part of the AAIA design concept. The H-polarized near field at 8 centimeters from the large horn aperture was analyzed and the size of an aperture was determined that couples at the 3 dB contours of the near field amplitude levels. These results are presented in Figure 13 for the larger horn. Similar analysis was also conducted on the E-polarized near field at 8 centimeters and a corresponding study on the aperture size to capture the power radiated.

Essentially, a 4 to 6 inch square collecting area appeared to be about optimum for these conditions but smaller probe designs were desired to reduce the overall physical size of the AAIA. Additional analyses were conducted using a much smaller (1.3-inch) aperture size for the selected quad-ridge probe aperture. The power coupling was calculated as a function of frequency. It was determined the coupling power drops off linearly about 20 dB across the frequency range 6 to 18 GHz.

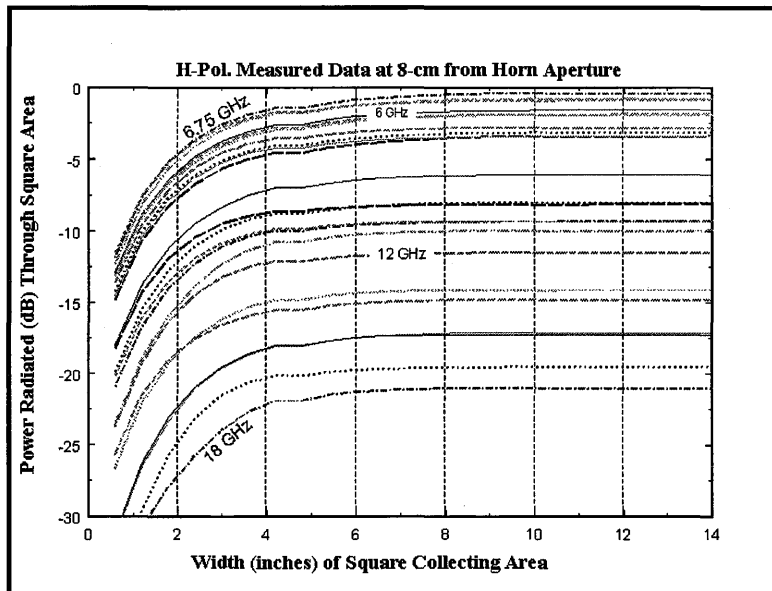


Figure 13 – Power radiated (dB) through square area positioned 8-centimeters from the large horn antenna.

Quad-Ridge EM Characteristics

Baseline S11 return loss measurements were conducted on the orthogonal ports (Horizontal and Vertical) across the bandwidth and with the quadrature hybrid connected for RHC polarization. The return loss measurement results for the RHC polarized configuration are presented in Figure 1 and it can be seen that the VSWR is less than 1.9.

Planar Near Field Measurements: The quad-ridge waveguide (configured for RHC) was mounted on the model tower and planar near field measurements were conducted to verify circular polarization, gain, and axial ratio. These measurements required three

waveguide probes to cover the 6-18 GHz band – {WR-137 (5.85-8.20 GHz)(Gain 22.1 dB); WR-90 (8.20-12.4 GHz)(Gain 22.1 dB); and WR-62 (12.4 – 18.0 GHz)(Gain 24.7 dB)}. Eleven frequencies were scanned during each measurement for each waveguide band respectively. Figure 14 shows typical near field amplitude and phase characteristics at 12.4 GHz and it can be seen that the fields are uniform and symmetrical.

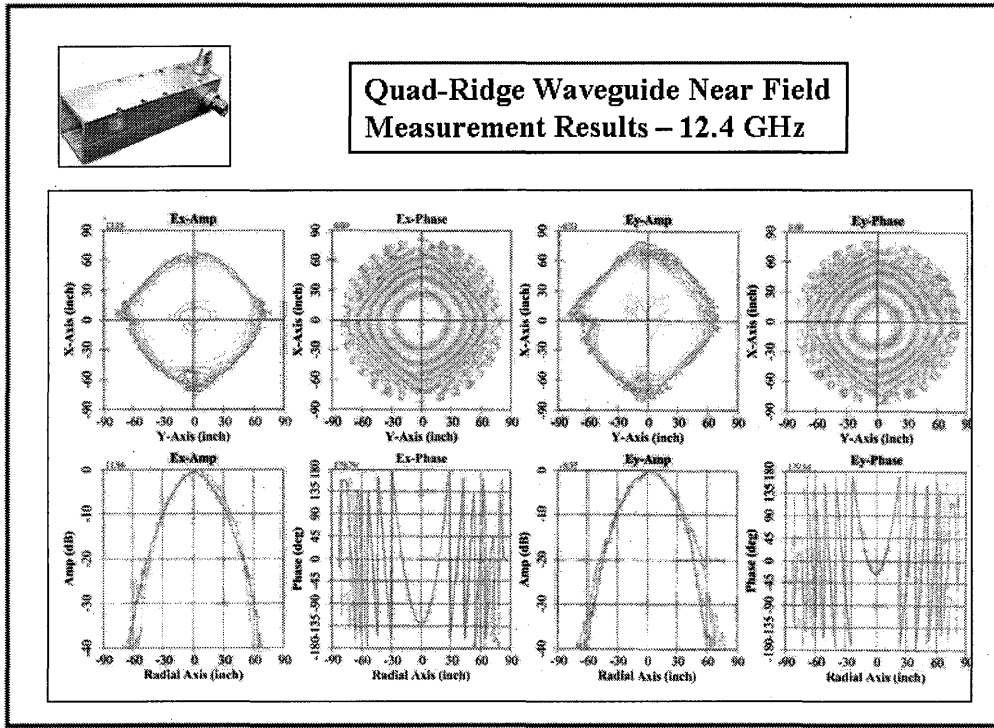


Figure 14 – Near field characteristics of the circularly polarized quad-ridge waveguide at 12.4 GHz.

Since the tests at Warner Robins would require circular polarization (RHC), the quad-ridge waveguide probe was equipped with a quadrature hybrid and phase-stable coaxial cables to provide that capability with the AAIA-Conformal Coupler. As described previously, the quad-ridge waveguide design was selected because it provides orthogonal ports and can provide linear or circular polarization depending upon the requirement. Since our near field probe had not been tested previously for circular polarization, tests were conducted at VTAG to measure both the near field and far field transformations for the quad-ridge waveguide assembled for RHC polarization. A 2-18 GHz quadrature hybrid and coaxial cables were purchased and assembled for this test configuration. The results of these tests at VTAG are presented in Figure 15 and the gain and circular polarization characteristics are essentially uniform across the band. The gain of the quad-ridge waveguide is compared to the gain of a spiral antenna (shown in blue).

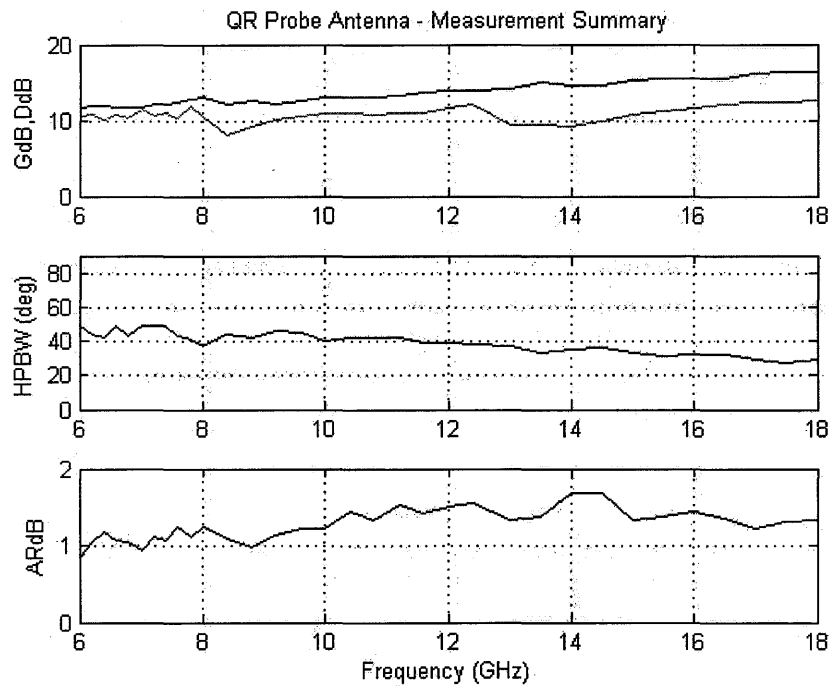


Figure 15 – Gain, HPBW, and Axial Ratio across the entire frequency band for the quad-ridge waveguide configured for RHC polarization.

The coupling power levels determined for the quad-ridged waveguide probe were used to calibrate the AAIA during actual EW laboratory tests at Warner Robins AFB and these test results are discussed later in this report.

Since the quad-ridge waveguide probe was selected for the AAIA, the RF characteristics must be compared to the fielded AF antenna couplers. These comparisons were useful in understanding the performance characteristics that are required and whether the AAIA probes would be acceptable for CTS tests. Performance comparisons are listed in Table II as the near field test results provided the data necessary for these comparisons.

The results indicate that even though the quad-ridged waveguide probe is much smaller than the earlier aperture considerations, there will be sufficient “coupling” to the aircraft antennas for accurate and reliable operational testing.

Parameter	AF Coupler #1 (large horn)	AF Coupler #2 (small horn)	Quad-Ridged Waveguide
Frequency (BW)	6-18 GHz	6-18 GHz	6-18 GHz
Power Gain (dB)	No gain	No gain	4-6 dBi
Axial Ratio	---	---	1.5 dB
Polarization	Linear	Linear	Dual Linear
Insertion Loss (J1- Tx Port)	-40 to -60 dB loss	-70 to -40 dB loss	
Insertion Loss (J2- Rx Port)	-30 to -8 dB loss	-65 to -40 dB loss	> 10 dB
De-tuning and scattering effects	-30 to -15 dB due to detuning in one frequency range	-30 to -10 dB due to detuning in one frequency range	
Isolation (port-port)	-15 dB	-15 dB	20 dB

Table II – Performance Comparisons with AF Antenna Couplers and Quad-Ridged Waveguides

Absorber Coating Designs

The baseline AAIA design provides an elastomer shell integrated with absorber materials. Additional embodiments would integrate the absorber materials directly into the elastomer rubberized design. Research has also been conducted using this type of design for EMI shielding gaskets for shipboard applications. Various flexible absorber materials were investigated for use in AAIA designs. The design approach selected used a flexible absorber / shielding “blanket” (shown in Figure 16). The material is a flexible open-cell lightweight foam that provides excellent broadband microwave absorption. This material can be bonded or mechanically attached as required. Therefore, the first AAIA engineering development model design consisted of absorber materials with a protective outercoverings to form an integrated “blanket” configuration. The rubber “boot” absorber blanket was fitted to the contour of the unit. The complete sandwich configuration is shown in Figure 14 with the Unishield coating, absorber, and outer vinyl liner.

Absorber material specimens were developed for EM properties measurements to determine absorption characteristics. Also, X-band waveguide specimens were prepared for further evaluation of the rubber shell material. The dielectric properties of the rubber material are important to determine the de-tuning effects when the material is placed directly over or near the horn antenna apertures. The dielectric constant of the rubber materials could cause some reflections and possible antenna detuning effects; so, these effects were considered as well. The next task was to investigate laminating techniques to incorporate the conductive coating systems, absorber materials and protective outer coverings to form the “blanket” configuration.

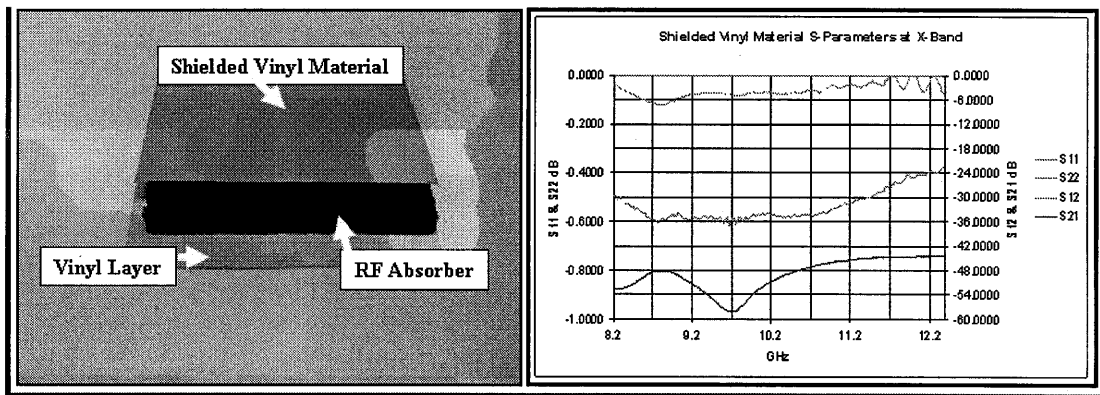


Figure 16 – Complete sandwich configuration for the AAIA absorber blanket showing the rubber layer, absorber, and outer layer of Unishield coated vinyl.

It is important that the overall RF shielding effectiveness is optimized so that the RF leakage between the AAIA and the aircraft structure is minimized. It was recognized that the amount of RF leakage between the AAIA and the aircraft is also dependent upon the fit between the AAIA and the aircraft radome. So, methods were designed into the (forward sector AAIA) that would provide a vacuum fit between the AAIA and the aircraft radome. The measurement results (using material samples)(shown in Figure 16) indicated that transmission loss greater than 54 dB could be exhibited by the absorber coating design approach. The absorber blanket design for the AAIA was later proved acceptable based on actual tests at Warner Robins AFB. The EM tests conducted later on the actual AAIA engineering development model demonstrated a shielding effectiveness greater than 50 dB which was considered significant.

(5) Engineering Development Models of AAIA-Conformal Couplers

AAIA-Conformal Coupler (EDM) for the Forward Sector Coverage Antenna System

CAD engineering renderings of the AAIA design concept are presented in Figure 16 along with a photograph of the engineering development model. The exploded views of the AAIA design indicate the number of components that are involved in the development effort. As described previously, the cover shell is shaped and oversized to fit over the antenna radome and adheres to the radome by vacuum pressurized fit. A radome mockup was fabricated and installed on a metal ground plane that “simulates” the aircraft installation. This experimental test demonstrated the capability for the AAIA to maintain position over the antenna radome with sufficient surface tension for flightline operations. In this manner, the geometry of the absorber materials was constant and, thereby, provided consistent EM performance results. The edging of the absorber blanket provided additional gasket shielding to reduce RF leakage around the edges of the AAIA boot. The auxiliary vacuum system is also shown in Figure 17 and test results indicated that the use of the vacuum pump was not necessary as the surface tension between the elastomer surface and the radome surface was sufficient to hold the “boot” in place.

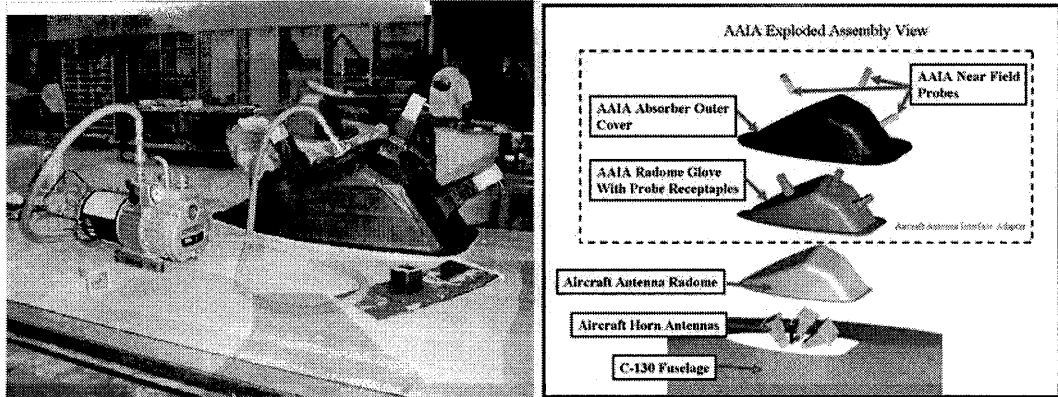


Figure 17 – Photograph and exploded assembly view of the AAIA engineering development model for the left forward radome antenna system.

EM shielding effectiveness tests were conducted on the AAIA-Conformal Coupler (EDM) for the forward sector coverage antennas and typical results are presented in Figure 18 (for horizontal polarization). Similar results were measured for vertical polarization. The shielding effectiveness test results shown are for antenna position #1 with and without the absorber boot over the antenna. Similar results were obtained for the other antenna locations. Approximately 25 dB of shielding was measured at that location at 6-18 GHz.

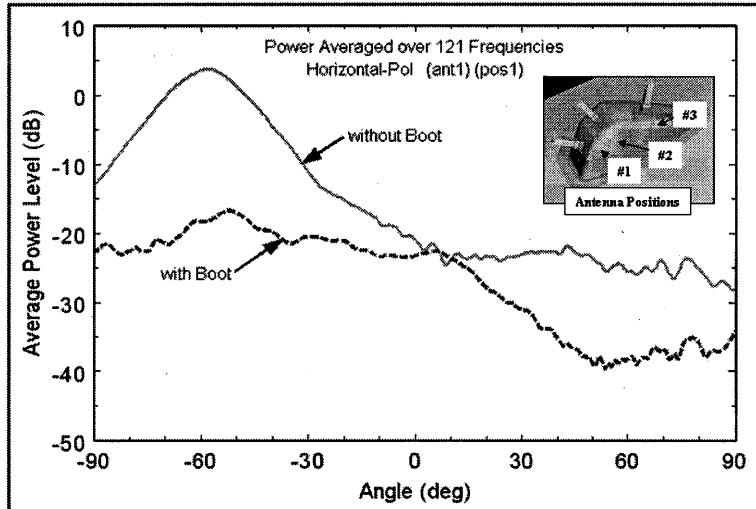


Figure 18 – Shielding effectiveness test results for the AAIA-Conformal Coupler (EDM) for the forward sector coverage antenna system.

After the EM characteristics of the quad-ridge waveguide were determined, the AAIA-Conformal Coupler for the left radome (transmit and receive) antennas was assembled at VTAG with the aircraft horn antennas provided. The purpose for this test was evaluate the overall frequency response for the AAIA EDM with actual aircraft horn antennas.

The test configuration is shown in Figure 19. One of the Air Force horn antennas was installed on a ground plane and the simulated aircraft radome was installed over the test

antenna. Then the AAIA was installed over the radome and EM performance measurements were conducted without and with (AAIA) absorber boot positioned over radome. S11 return loss measurements were conducted on the (proximity) quad-ridge waveguide probe installed in the AAIA and positioned over the horn antenna. Also, S11 measurements were conducted on the horn antenna to determine any appreciable detuning effects on the aircraft horn antennas due to the proximity of the probe/AAIA combination.

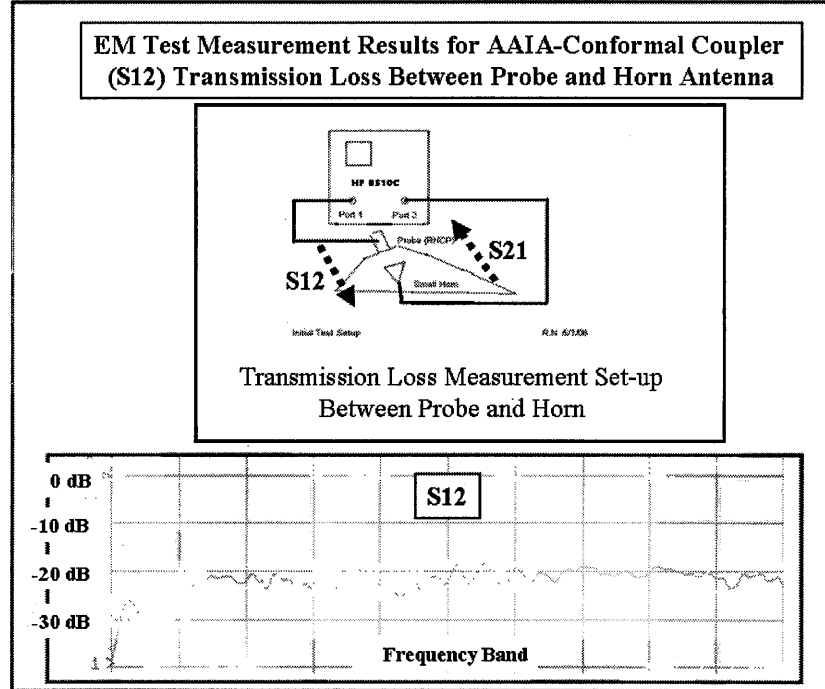


Figure 19 – S12 transmission loss characteristics between the AAIA and the aircraft horn antenna across the frequency band of interest.

Following these measurements, the overall frequency response of the AAIA-horn combination (S12 and S21) was measured across the frequency band of interest. In the event severe standing waves were measured between the AAIA probe and the aircraft horn antennas, small absorber plugs were made that were tested by placing them in front of the quad-ridge waveguide aperture. The primary results of all of these test configurations are listed in Figure 20.

Essentially, these tests indicated that there were no severe standing waves between the AAIA near field probe and the respective aircraft horn antenna. As a result, there was no appreciable effect of the absorber plugs in the frequency response of the AAIA except to attenuate the overall signal levels. Also, no major detuning effects were observed of the AAIA being placed over the aircraft horn antennas. The most significant measurement was S12 and S21 for the horn-to-probe and probe-to-horn test configurations. Before this test was conducted, it was extremely difficult to predict what the overall frequency response (transmission loss) was going to be for the AAIA-conformal coupler positioned over the simulated aircraft radome and horn antennas.

EM Test Measurement Results for AAIA-Conformal Coupler Performance - Return Loss, Proximity Effects, Standing Wave Effects	
AAIA Probe Configuration	VSWR (Return Loss)
1. Quad-Ridge Waveguide NF Probe	< 1.92 (across full band)
2. Horn-to-Probe Proximity Effects	< 1.67 (avg.)
3. Horn-to-Probe with absorber sample #1 in probe	< 1.22
4. Probe-to-Horn with absorber sample #1 in probe	< 1.22
5. Horn-to-Probe with absorber sample #2 in probe	< 1.92
6. Horn without Radome	< 1.92
7. Horn with Radome	< 1.92
8. Horn with Radome, AAIA, and NF Probe	< 1.92
9. S12 Horn-to-Probe in Position #1	approx. - 20 dB
10. S21 Probe-to-Horn in Position #1	approx. - 20 dB

Figure 20 – VSWR results of all of the various AAIA-Horn antenna combinations and with and without absorber plugs.

These measurement results were believed to be indicative as to what to expect of the AAIA performance for the next development -- the top OMNI receive antenna.

Since this AAIA EDM was the first model developed and tested, there were many lessons learned about ways to improve fabrication and especially ways to improve the RF shielding effectiveness. The ideas for improving the design were incorporated into the design and fabrication of the AAIA-Conformal Coupler for the forward top OMNI Receive antenna. It is recognized that the overall shielding effectiveness must be optimized to adhere to the shielding effectiveness levels specified in the Air Force Occupational Safety and Health Standard.

AAIA-Conformal Coupler (EDM) for the Forward Top OMNI Receive Antenna

The second engineering model that was developed was for the AAIA-Conformal Coupler for the forward top OMNI Receive Antenna on the C-130 Combat Talon II aircraft. The development of this AAIA was considered by the Air Force as a much better test case to really demonstrate the effectiveness of the AAIA design concept. So, steps were taken to improve upon the previous AAIA development and, especially, improve the RF shielding effectiveness of the absorber boot design.

Since the performance for this antenna is classified; near field tests were conducted at the Air Force Antenna Station at Ipswich, MA. As before, these test results verified the probe position (8-cm) for the boot design. The engineering design was completed for mounting the AAIA to the top omni receive antenna and this design included a ground plane configuration that simulated the 32-degree angle of the aircraft fuselage. Photographs taken during fabrication of the AAIA EDM are presented in Figure 21. The fabrication had been delayed until the probe position could be verified during the tests at Ipswich.

Based on the RF test results of AAIA #1 EDM, the overall thickness of the multi-layer absorber design for AAIA #2 was increased especially in the area where RF leakage could occur.

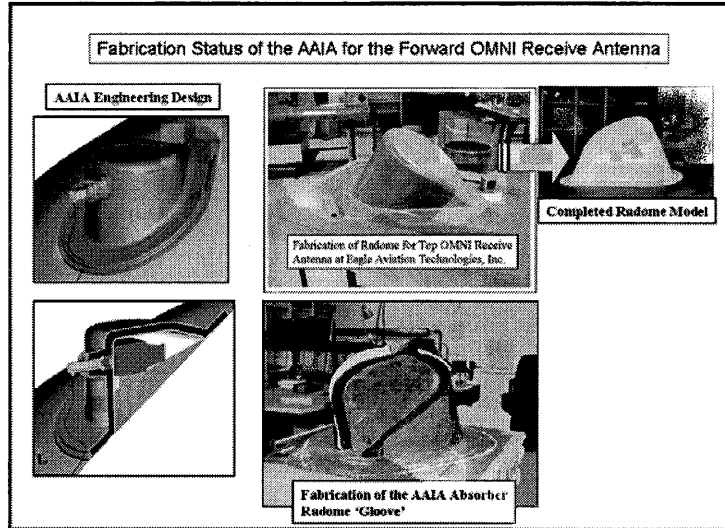


Figure 21 – Photographs of the fabrication stages in the development of AAIA (#2) for the forward top OMNI receive antenna.

EM shielding effectiveness tests were conducted on AAIA #2 at the Air Force Antenna Station in Ipswich, MA. The AAIA-Conformal Coupler is designed to fit over the antenna radome and position the quad-ridge probe directly in front of the aircraft antenna. The design and location of the near field probe provides the capability to transmit and receive RF signals to the respective aircraft antenna. In the case for the top OMNI Receive Antenna, the near field probe will be used to transmit signals to the aircraft receiving antenna. The basic objectives for this test were to determine the frequency response of the antenna and the frequency response when the antenna is attached to the AF coupler. These measurements were conducted primarily to determine the detuning effects (before and after) due to the attachment of the AF antenna coupler. A photograph of the test setup and shielding effectiveness test results are presented in Figure 22. It can be seen that major improvements in the shielding effectiveness were exhibited by AAIA #2 as compared with the previous design (for AAIA #1)

Network Analyzer (S11, S12, and S21) measurements with the Antenna Coupler attached to the OMNI Receive Antenna indicated that as expected, the antenna is detuned and approximately 20 dB of insertion loss is observed across the entire frequency band.

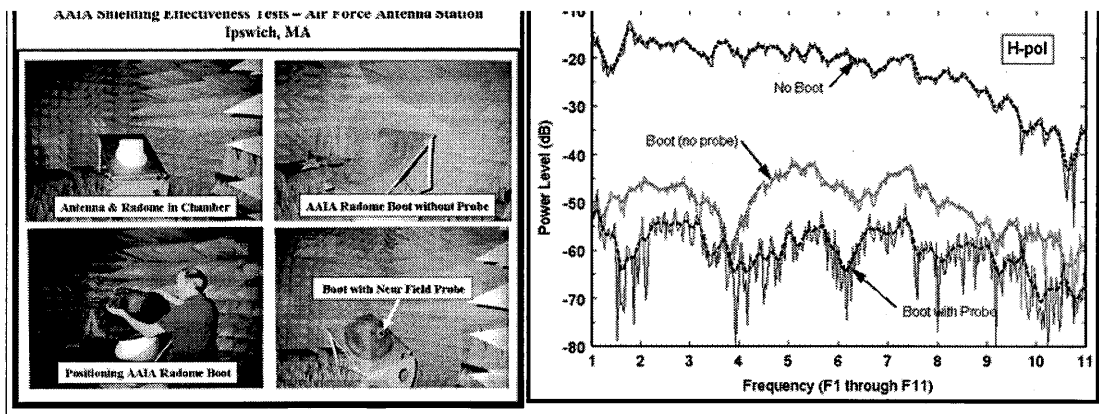


Figure 22 – Test setup at Ipswich, MA for the AAIA-Conformal Coupler for the top OMNI Receive Antenna.

Tests at Warner Robins AFB

The (Classified CONFIDENTIAL) C-130 Combat Talon II aircraft antenna was installed on ground plane in the laboratory at Warner Robins as shown in the photographs in Figure 23. After the alignment was verified, the simulated radome was removed and a test was conducted using the conventional coupler attached to antenna. A baseline set of measurements were conducted transmitting to the OMNI Receive Antenna using the AF fielded coupler – measuring frequency response, signal amplitude measurements across desired waveguide bands. Minimum and maximum signal levels recorded across the desired waveguide bands for this baseline test setup. These levels were then compared with the AAIA-Conformal Coupler.

The AF fielded coupler was then removed from the OMNI Receive Antenna and the simulated radome was installed over the antenna. The AAIA-Conformal Coupler was positioned over the radome and the quad-ridge waveguide near field probe was inserted into the “boot.” Coaxial cables and quadrature hybrid were connected to the probe to provide RHC polarization radiation characteristics. A test was conducted to verify that RHC polarization was correct as the cables on the hybrid were reversed to provide LHC polarization and the test result confirmed that the probe was indeed connected properly for RHC polarization. The signal levels were at least 20 dB lower when LHC polarization was connected.

In order to determine the reliability and repeatability of the AAIA Conformal Coupler, the near field probe was removed from the AAIA, rotated in 90-degree increments when re-inserted into the AAIA. Also, the entire AAIA absorber boot was removed and then re-positioned over the simulated radome. The signal levels were measured and compared to determine systematic repeatability errors. The results in Figure 23 show that the AAIA is very repeatable as the signal variation was less than 2 dB with changes in probe position.

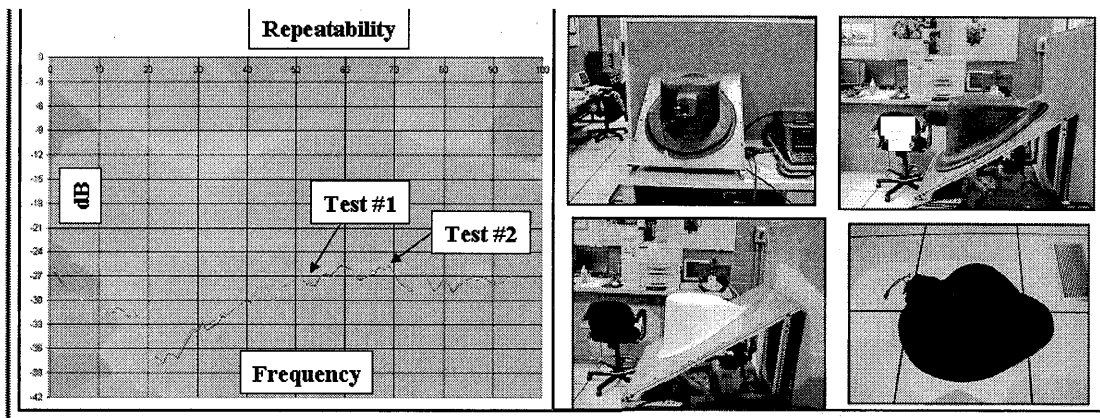


Figure 23 – AAIA-Conformal Coupler repeatability test results – removal of NF probe as well as entire AAIA absorber boot.

The WR test team suggested a leakage test should be conducted which consisted of an antenna probe “sniffer” that was connected to sensitive network analyzer. The AAIA-Conformal Coupler assembly was in-place on the bench and the “sniffer” was moved around the absorber boot of the AAIA. RF connections were made to transmit from the Top OMNI antenna (instead of receiving) and the relative signal levels were “sniffed” around the extremities of the AAIA boot. The signal level without the AAIA absorber boot was approximately – 20 dB level and when the boot was re-installed and “sniffed,” the signal level was essentially not measurable at the – 70 dB threshold level. Therefore, the shielding effectiveness of the AAIA-Conformal Coupler was outstanding.

A final summary of the RF performance of the AAIA-Conformal Coupler can best be described by comparing its S12 characteristics with the S12 tests on the AF fielded couplers. A sequence of test results are presented in Figure 16 with the AF fielded coupler; the comparisons with the AAIA, and the result of changing the relative position of the AAIA’s near field probe to the Top OMNI Receive Antenna. Comparing the AAIA with the AF fielded coupler, it can be seen that the AAIA exhibits approximately a 10 dB null at about the 25% into the frequency band of interest. Obviously, this was unexpected (especially based on all of the near field tests at Ipswich and VTAG); so a test was conducted to vary the position of the near field probe. These results are shown in the bottom trace (in Figure 24) and were obtained with the NF probe out of the AAIA absorber boot. This indicated that the AAIA probe had to be repositioned to improve the coupling efficiency to the top omni receive antenna and essentially the same level as the AF fielded coupler was measured.

Warner Robins Test Results for Air Force Field Coupler Compared with AAIA-Conformal Coupler for Top OMNI Receive Antenna

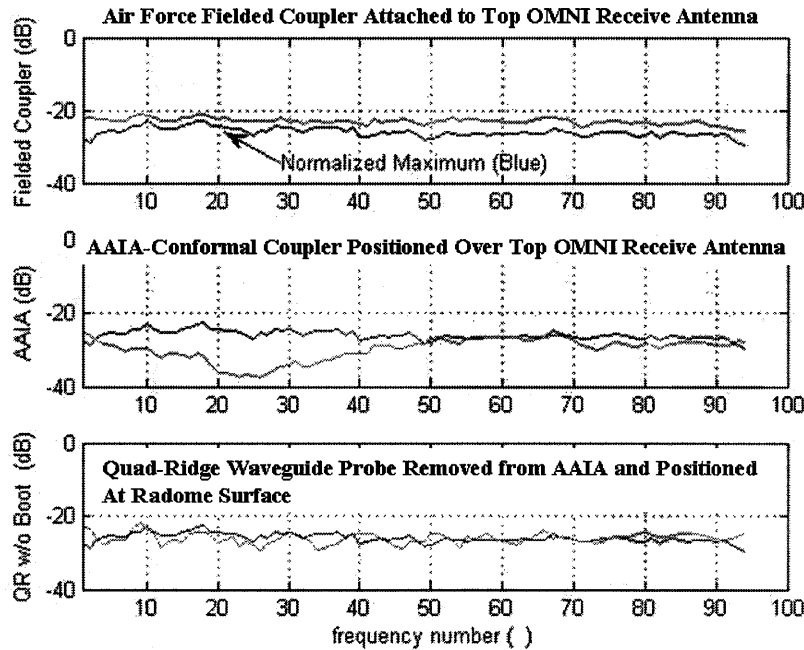


Figure 24 – Warner Robins test results with AF fielded coupler with AAIA-Conformal Coupler for Top OMNI Receive Antenna.

In addition to the need to change the position of the AAIA near field probe, is the possibility that the aperture and gain characteristics of the quad-ridge waveguide could have produced the signal “nulls” as measured at WR. So, in that regard, the VTAG test results were reviewed to see if that could be the case and the gain characteristics versus frequency were plotted and compared to the S12 WR test results. It was surprising to find two ‘dips’ in the gain characteristic generally ‘lined up’ with the nulls measured at WR.

The near field probe design is being re-analyzed to evaluate these effects as well as the aperture coupling parameters that will be used to design a modified near field probe. All of these experimental results are invaluable as a prototype AAIA is now being considered. The prototype AAIA design will improve the design of the coupling aperture and provide an increase of the system by 6-8 dB.

Since the AAIA-Conformal Coupler EDM was developed using a simulated aircraft radome, we were concerned how the AAIA “boot” would fit on an actual aircraft radome. Actually, the simulated radome was fabricated to fit onto a flat ground plane and the curvature of the aircraft fuselage was not simulated. This was done to reduce the fabrication cost for the simulated radome and associated components. Therefore, it was important that the overall fit with an actual aircraft radome be evaluated; so, this check was part of the tests at WR. Using flightline man lift capability, in the hangar at WR, a

C-130 was undergoing maintenance and that was the aircraft that we used to conduct the fit-check. Surprisingly, the AAIA "boot" did fit securely to the aircraft radome even though the bottom edge did not follow the curvature of the fuselage. Obviously, a prototype AAIA design will accurately follow the curvature of the fuselage.

While in the hangar, the aircraft maintenance technician was asked if we could get a closer look at the aircraft radome and he obtained one and we discussed the procedures for removal and re-installing the radomes during EW antenna tests. He indicated that the AAIA concept is a good way to proceed and will indeed save time on the flight line. Upon inspection of the radome, it was noticed that a metal plate was attached to the top to serve as a 'stiffener' to the radome and RTV-type sealants were used on top of the mounting screws for the radome. These features produced a rough exterior surface to the radome that must be accommodated when the AAIA's are used in normal testing procedures.

The actual exterior surface of the aircraft radome must be considered when a prototype AAIA design is conducted. For example, the interior surfaces of the AAIA must be adaptable to conform to the rough surface of the radome – at all times even if the exterior surfaces are changed due to additional radome sealants. This surface feature will be addressed in a new surface design.

(9) Summary and Future Developments

An advanced Aircraft Antenna Interface Adapter (AAIA)-Conformal Coupler design concept has been developed and demonstrated using engineering models (EDM) for two aircraft antenna systems on the C-130 Combat Talon II, ALQ-172. The EDM test results show that the AAIA concept is indeed both viable and practical for actual USM-464/CTS test operations. The AAIA #1 was developed for the forward sector coverage antenna system and the AAIA #2 was developed for the forward top OMNI receive antenna system. Since AAIA #1 was developed first, the lessons learned in the design and fabrication were improved upon in the design and fabrication of AAIA #2 and significant improvements were achieved – especially in the RF shielding effectiveness of the absorber boot design for AAIA #2. The AAIA-Conformal Coupler exhibits absorption and shielding characteristics that reduces RF emissions on the flight line significantly below the permissible exposure levels (PEL) for antenna (EW) test operations. Also, the RF test results for both designs also verified the concept as severe interaction effects between the AAIA near field probe and the aircraft antennas were not exhibited.

Therefore, the feasibility of the AAIA-Conformal Coupler concept has been demonstrated and tested for the electronic warfare (EW) antennas on C-130 Combat Talon II, ALQ-172 systems and ready for a prototype design and development effort. The AAIA design enables rapid checkout testing procedures with physical characteristics to withstand extreme environmental flight line conditions

(10) Acknowledgements

The outstanding support provided by Professor William Davis and Mr. Randall Nealy of the Virginia Tech Antenna Group (VTAG) for near field measurements and analysis is appreciated. Also, the contributions provided by Mr. Robert Boyd of Unitech, LLC and Mr. Bruce Bailey of Eagle Aviation Technologies, Inc. for engineering design support for developing the engineering development models.

(11) References

- [1] Contract No. F19628-03-C-0113, Engineering Task Addendum for Air Force Research Laboratory, Hanscom Air Force Base and Warner Robins Air Logistics Center, Combat Electronic Systems Directorate, Engineering Division. Jose Matos and Marlene Rogers are AF Sponsors at Warner Robins AFB.
- [2] Air Force Technical Manual, TO33D7-50-2007-1, 30 September, 1999.
- [3] F. H. Larson and J. E. Hanson, "A Dual-Polarized Probe System for Near-Field Measurements," Proceedings of the IEEE, 1979, APS Vo.2, pp. 557-560.
- [4] Air Force Occupational Safety and Health Standards, 48-9, dated 1 August 1997; Radio Frequency Radiation (RFR) Safety Program.